

## **Studies of Non-LTE Processes Relating to Atmospheric IR Backgrounds and Clutter**

**W. R. Pendleton  
J.A. Dodd  
M. J. Taylor  
P.S. Armstrong  
U. B. Makhoul**

**Stewart Radiance Laboratory, Utah State University  
139 The Great Road  
Bedford, MA 01730**

**October 2000**

**Final Report**

**APPROVED FOR PUBLIC RELEASE; DISTRIBUTION IS UNLIMITED.**


**20020510 203**



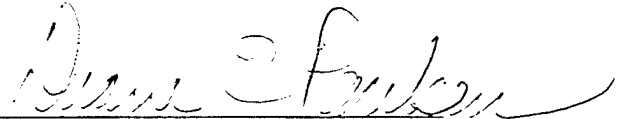
**AIR FORCE RESEARCH LABORATORY  
Space Vehicles Directorate  
29 Randolph Rd  
AIR FORCE MATERIEL COMMAND  
Hanscom AFB, MA 01731-3010**

---

This technical report has been reviewed and is approved for publication.



DEAN F. KIMBALL  
Contract Manager



DUANE E. PAULSEN  
Deputy Chief, AFRL/VSSS

This report has been reviewed by the ESC Public Affairs Office (PA) and is releasable to the National Technical Information Service (NTIS).

Qualified requestors may obtain additional copies from the Defense Technical Information Center (DTIC). All others should apply to the National Technical Information Service (NTIS).

If your address has changed, if you wish to be removed from the mailing list, or if the addressee is no longer employed by your organization, please notify PL/IM, 29 Randolph Road, Hanscom AFB MA 01731-3010. This will assist us in maintaining a current mailing list.

Do not return copies of this report unless contractual obligations or notices on a specific document require that it be returned.

REPORT DOCUMENTATION PAGE				Form Approved OMB No. 0704-0188	
<small>The public reporting burden for this collection of information is estimated to average 1 hour per response, including the time for reviewing instructions, searching existing data sources, gathering and maintaining the data needed, and completing and reviewing the collection of information. Send comments regarding this burden estimate or any other aspect of this collection of information, including suggestions for reducing the burden, to Department of Defense, Washington Headquarters Services, Directorate for Information Operations and Reports (0704-0188), 1215 Jefferson Davis Highway, Suite 1204, Arlington, VA 22202-4302. Respondents should be aware that notwithstanding any other provision of law, no person shall be subject to any penalty for failing to comply with a collection of information if it does not display a currently valid OMB control number.</small> <b>PLEASE DO NOT RETURN YOUR FORM TO THE ABOVE ADDRESS.</b>					
1. REPORT DATE (DD-MM-YYYY) 01-10-2000		2. REPORT TYPE Final		3. DATES COVERED (From - To) Sep 1993 - Dec 1999	
4. TITLE AND SUBTITLE Studies of Non LTE Processes Relating to Atmospheric IR Backgrounds and Clutter				5a. CONTRACT NUMBER F19628-93-C-0165	
				5b. GRANT NUMBER	
				5c. PROGRAM ELEMENT NUMBER 61102F	
6. AUTHOR(S) W.R. Pendleton, J.A. Dodd, M.J. Taylor, P.S. Armstrong, and U.B. Makhoulouf				5d. PROJECT NUMBER 2310	
				5e. TASK NUMBER GD	
				5f. WORK UNIT NUMBER AK	
7. PERFORMING ORGANIZATION NAME(S) AND ADDRESS(ES) Stewart Radiance Laboratory, Utah State University 139 The Great Road Bedford, MA 01730				8. PERFORMING ORGANIZATION REPORT NUMBER	
9. SPONSORING/MONITORING AGENCY NAME(S) AND ADDRESS(ES) Air Force Research Laboratory 29 Randolph Road Hanscom AFB, MA 01731-3010 Contract Manager: Dean Kimball/VSBM				10. SPONSOR/MONITOR'S ACRONYM(S)	
				11. SPONSOR/MONITOR'S REPORT NUMBER(S) AFRL-VS-TR-2000-1603	
12. DISTRIBUTION/AVAILABILITY STATEMENT Approved for Public Release; Distribution Unlimited					
13. SUPPLEMENTARY NOTES					
14. ABSTRACT This contractual effort consisted of three elements: laboratory studies of key chemical and transfer reactions which are of special interest to atmospheric IR emissions, ground-based field measurements of carefully selected infrared (IR) airglow and auroral emissions, and detailed modeling of the dynamics of atmospheric processes that are not in local thermodynamic equilibrium. Laboratory efforts centered on the production and detection of highly rotationally excited OH. Data sets obtained at the Bear Lake Observatory during MSX satellite data collection over the site were examined in depth. Conducted the preliminary analysis and interpretation of image data collected at Yucca Ridge, CO., during the SPRITES '96 campaign. A photochemical model for the sodium airglow emission was developed during this period. Work unit updated 5 MAR 98. During the update period, effort concentrated on the investigation of newly documented field observations of extreme non-local-thermodynamic-equilibrium (NLTE) (Continued)					
15. SUBJECT TERMS atmospheric IR emissions, atmospheric visible emissions, chemiluminescence, photochemical models, LABCEDE, gravity waves, turbulence, ALOHA-93, SPRITES'96, MSX					
16. SECURITY CLASSIFICATION OF:			17. LIMITATION OF ABSTRACT  SAR	18. NUMBER OF PAGES  81	19a. NAME OF RESPONSIBLE PERSON Gerald F. Zdyb
a. REPORT UNCL	b. ABSTRACT UNCL	c. THIS PAGE UNCL			19b. TELEPHONE NUMBER (include area code) 781 377-2089

UNCLASSIFIED

SECURITY CLASSIFICATION OF THIS PAGE

CLASSIFIED BY:

DECLASSIFY ON:

14. ABSTRACT (Continued):

phenomena in the IR airglow and auroral emissions. These new IR observations have significant systems implications. During this period, work continued on the development of the turbulent layer detection algorithm. This effort searched for the connection between the generation and breakdown of gravity waves into turbulence, resulting in spatial and temporal structure. Work also continued on the laboratory studies of NLTE atmospheric infrared emissions relating to the infrared background problem.

SECURITY CLASSIFICATION OF THIS PAGE

UNCLASSIFIED

## Table of Contents

1. Introduction	1
2. Analysis of hydroxyl earthlimb airglow emissions: Kinetic model for state-to-state dynamics of OH(v,N) J.A. Dodd, S.J. Lipson, et al.	5
3. Photochemical-dynamical modeling of the measured response of airglow to gravity waves. 1. Basic model for OH airglow U.B. Makhlof, R.H. Ricard, and J.R. Winick	32
4. Determination of horizontal and vertical structure of an unusual pattern of short period gravity waves imaged during ALOHA-93 M.J. Taylor, D.C. Fritts, and J.R. Isler	55
5. Vibrational relaxation of NO(v=2,3) by atomic oxygen J.A. Dodd, S.M. Singleton, et al.	59
6. Fractional population of NO(v-1) from vibrational relaxation of NO(v=2,3) by O and NO J.A. Dodd, R.B. Lockwood, et al.	65
7. A model for the response of the atomic oxygen 557.7 nm and the OH Meinel airglow to atmospheric gravity waves in a realistic atmosphere U.B. Makhlof, R.H. Picard, et al.	73

# STUDIES OF NON-LTE PROCESSES RELATING TO ATMOSPHERIC IR BACKGROUNDS AND CLUTTER

Final Report, 8 September 1993 -- 8 December 1999  
Contract F19628-93-C-0165

During this contractual period, field and laboratory experiments were performed on a variety of instruments to characterize various molecular processes in the atmosphere that are not in local thermodynamic equilibrium. In the modeling part, forward predicting models were developed and were validated against ground-based and space-based experiments. These models couple atmospheric dynamics with chemistry and radiative transfer, to characterize quantitatively the naturally occurring fluctuations in the atmospheric radiation fields.

## Laboratory Experiments:

In various studies, electron beams and laser light were used to excite atomic and molecular species, while infrared emission and laser-based techniques such as laser-induced fluorescence and multiphoton ionization were used for detection. Studies of nascent distributions from chemical reactions as well as collisional and radiative relaxation were performed. Rotational and vibrational energy transfer rates and pathways were also investigated. The laboratory and field experiments studied the  $\text{H}+\text{O}_3$  reaction and the subsequent rotational relaxation of highly excited levels of hydroxyl (OH), as well as a set of vibrational energy transfer studies of vibrationally excited nitric oxide (NO) by collisions with oxygen (O) atoms. In addition, analysis of field data from the CIRRIS-1A and MSX space-based experiments was performed to provide a context for the laboratory results, using computer code developed for the laboratory experiments.

The molecular infrared spectra generated by species in the upper mesosphere to lower thermosphere were collected by the CIRRIS 1A, EXCEDE III, and MSX experiments. These spectra were analyzed to determine the distribution of molecular states in these regions of the near-Earth environment. These state distributions comprised states in local thermodynamic equilibrium (LTE) and states that were not in local thermodynamic equilibrium (NLTE). The results of these field measurements led to several laboratory experiments to elucidate the production and relaxation processes controlling the molecular state distributions of several important molecules. These laboratory experiments were conducted at the LABCEDE facility, which was designed to simulate the appropriate background conditions for simulating the mesosphere and lower thermosphere.

The CIRRIS-1A mission used a cryogenic Michelson interferometer aboard the space shuttle to collect earthlimb spectra in the 2.5-25  $\mu\text{m}$  infrared band. The analysis of the fundamental band of nitric oxide (NO), centered near 5.3  $\mu\text{m}$ , determined that molecular states having very large amounts of angular momentum were populated, and the emissions from these rotationally excited states produced prominent spectral features that had not been observed in previous space experiments. The blue portion of the NO fundamental band includes several sharply peaked features produced by the R-branch band heads of the first three excited vibrational levels. Synthetic spectral fitting of the fundamental band determined the populations for up to five R-branch band heads in the

CIRRIS-1A data set (the first three are visible to inspection, and the last two ( $v=4,5$ ) are within the spectral domain of the  $v=1$  airglow). These R-branch band heads are observed in both daylight and auroral conditions, and are produced when sufficient population resides in states having large amounts of angular momentum ( $J \geq 75$ ). In addition to the R-branch band heads, these highly rotationally excited states radiate in the P-branch manifold, which is present in the red portion of the fundamental band. The spectral domain of these P-branch emissions is much wider than previously modeled in the atmospheric codes. For daylight and auroral conditions, the distribution of rotationally excited states was modeled using an effective temperature of 5000 K. This effective temperature is significantly higher than the local kinetic temperatures of the atmosphere as observed during the CIRRIS-1A experiment, which ranged from 250 K to 1000 K.

The EXCEDE III rocket experiment collected infrared spectral data showing emissions from highly vibrationally and rotationally excited nitric oxide (NO) generated by an artificial aurora. The rocket was comprised of two payloads. One module contained a high current electron beam source to generate the artificial aurora, and the second module contained the primary sensors, including a Michelson interferometer capable of recording both the fundamental and first overtone bands of NO. The interferometer collected 20 spectra on both the up-leg and down-leg sections of the rocket flight when the electron beam operated. Analysis of the spectral data utilized a synthetic spectral fitting code that determined absolute column densities for up to twelve vibrational states having a thermal rotational state distribution and up to nine vibrational states having a rotationally excited state distribution. The populations of the rotationally and vibrationally excited states depended on the overlap of the amount of electron energy deposited and the residence time of an excited molecule in the field of view of the interferometer.

The MSX satellite experiment collected spectra from highly excited hydroxyl (OH) in both the pure rotation emissions and the fundamental band emissions. These highly excited molecules were located in the mesopause region ( $\sim 85$  km altitude), and the local time of the data collection was just before sunrise. The MSX satellite contained a Michelson interferometer, where two detectors collected the emissions from the mesopause region. A third detector, where the field of view went to a tangent height of 72 km, also collected pure rotation band emissions. Synthetic spectral fitting determined the populations of the highly rotationally excited states that emit in the pure rotation band. These populations in the rotationally excited states are correlated with the populations from states emitting in the fundamental band from highly vibrationally excited states. This correlation was determined from two separate data collection events, where the interferometer scanned over a range of latitudes from  $20^\circ$  to  $65^\circ$  N twice in a relatively short period of time (20 minutes). Since the two detectors looking at the mesopause region did not share a common field of view, the third detector confirmed the population trend as a function of latitude. Because the altitude at which the peak populations of highly excited OH may vary with latitude, the results of the third detector were vital for the correlation between highly excited rotational states and highly vibrationally excited states. In addition, one of the data collection events showed that the population of the highly excited OH states varied by a factor of three over the range of latitudes, thus constraining the atmospheric chemistry models in regards to OH production.

A systematic study of these highly excited molecular states observed in the mesosphere and lower thermosphere was conducted using the LABCEDE facility located at the Air Force Research Laboratory at Hanscom Air Force Base. The collisional excitation and deactivation of highly rotationally excited states of nitric oxide (NO) and carbon monoxide (CO) were generated by electron excitation, and the state populations were measured by recording fundamental band emissions from these states by time-resolved Fourier transform spectroscopy. The ability to collect time-resolved spectra provided the capability to measure collisional relaxation rate constants that are required for models of vibrationally and rotationally excited state densities. The production of high rotationally excited states required collisional rather than radiative processes, due to the amount of angular momentum associated with these states. Two Michelson interferometers were used in this work, one providing  $3\text{ cm}^{-1}$  spectral and  $6\text{ }\mu\text{s}$  temporal resolution, and the second providing high sensitivity at  $0.3\text{ cm}^{-1}$  spectral resolution in continuous-wave mode. Rovibrational band heads were observed in both CO and NO, representing 80-100 quanta of rotational excitation and at least 2.5 eV in rotational and vibrational energy. While the NO spectra were optically thin, the CO spectra had a mixture of both optically thin and thick emissions, due to the large densities of ground state CO. Initial analysis of the data set excluded the optically thick emissions, and the effort was placed in the determination of the vibrationally excited states and the highly rotationally excited states. Later analysis included techniques to fit simultaneously both optically thick and thin emissions using a combination of synthetic basis functions and pattern recognition methods. Time-dependent vibrational populations were determined by synthetic spectral fitting, and the time histories of the vibrational populations following pulsed excitation were fitted using a model that includes collisional loss, radiation, and transport out of the field of view. A Stern-Volmer analysis of the total decay rates of the observed molecular states was applied to determine the collisional deactivation rate constants of rotationally excited CO by  $\text{N}_2$ , Ar, and CO. The rate constants for the quenching of high-J CO ( $v=1-5$ ) by  $\text{N}_2$  (local temperature near 100 K, due to cooling of the inner chamber within LABCEDE by liquid nitrogen) are on the order of  $10^{-13}\text{ cm}^3\text{ s}^{-1}$ , about 0.001 efficient.

A preliminary study of the interaction of small hydrocarbons with oxygen was also studied in the LABCEDE facility. Infrared radiation can be produced as a result of physical and chemical processes involving trace levels of hydrocarbons in the mesosphere and thermosphere. These processes include optical excitation and scattering, electron impact, and both reactive and non-reactive collisions with atomic oxygen. As a result, hydrocarbons and their reaction products can give rise to strong IR emission spectra, and contribute to IR backgrounds in the upper atmosphere. Using the LABCEDE facility, a series of laboratory experiments was conducted to study these phenomena. Selected hydrocarbons (including butane and ethylene) were mixed with  $\text{O}_2$  in a bath of  $\text{N}_2$  or Ar. The experiments used a pulsed electron beam as the energy source, and infrared spectra of the CO and OH products were collected using time-resolved Fourier transform spectroscopy. The observed spectra of vibrationally excited CO and OH were analyzed using synthetic spectral fitting to determine time-dependent molecular state distributions. Both excitation and relaxation processes were studied.

## MODELING AND FIELD MEASUREMENTS:



Several photochemical dynamical models were developed under this contract, including the OH(v) hydroxyl Meinel band model, the O(<sup>1</sup>S) green line atomic oxygen model, the O<sub>2</sub> (b) molecular oxygen atmospheric band model, and the sodium Na(<sup>2</sup>P) metallic emission. These models were used in conjunction with field measurements to study the transient response of the different airglow emissions due to atmospheric gravity waves and undular bores. The different airglow emissions originate from different altitudes, which synergistically define the importance of studying the vertical dynamical structure of the atmosphere.

One of the studies was conducted using data collected over the Hawaiian Islands during the ALOHA-93 campaign. The various photochemical-dynamical models were used to study a propagating undular bore observed by an all-sky CCD ground-based imager, which mapped several airglow emissions at different altitudes in the mesosphere and lower thermosphere region. The study investigated the mechanism and the sources of the travelling and ducted internal gravity waves and how these waves can interact with other internal gravity waves to generate the nonlinear phenomenon known as the undular bore, which is a sharp edge structure in the IR and visible background fields.

The Photochemical-Dynamical model in a Realistic atmosphere (PHDR) was developed and used to study the brightness and temperature fluctuations in the OH airglow, and to calculate the Krassovsky ratio, (which is a measure to the relative brightness fluctuations to the relative temperature fluctuations). This study was mainly concerned with the small scale internal gravity waves (IGW's). These small scale gravity waves become evanescent due to the sharp temperature gradient in the lower thermosphere, and, with the ground as a reflecting surface, resonant waves exist which influence the OH airglow structure. One interesting result was the zero phase between the brightness fluctuations and the temperature fluctuations which is supported by OH observations. A spectral capability was also added to the PHDR model to be able to compare radiances calculated by the model to those measured by different instruments with various band passes. A comparison of the 1.57  $\mu\text{m}$  emission measured on board the MAPWINE rocket, which was launched during a stratospheric warming event, yielded very good agreement between the measurements and model predictions.

The effects of doubling the CO<sub>2</sub> on the OH 2.7  $\mu\text{m}$  emission were also investigated, so as to understand the long-term effect of CO<sub>2</sub> on the IR background emission. The TIME-GCM (Thermosphere, Ionosphere, Mesosphere, Electrodynamics General Circulation Model) was used in this study in conjunction with the hydroxyl OH photochemical model. The models predicted a reduction in the OH 2.7  $\mu\text{m}$  emission when the amount of CO<sub>2</sub> was doubled in the atmosphere. Further investigation is necessary to assess this effect.

The combination of field measurements, laboratory experiments, and model simulations provide a powerful capability for pursuing quantitative visible and infrared studies and to investigate the structure of the atmospheric background emission and clutter that is associated with these structures. Understanding these basic physical processes that are the sources of the background clutter will help reduce this background noise and enhance detection capabilities.

## Analysis of hydroxyl earthlimb airglow emissions: Kinetic model for state-to-state dynamics of OH ( $v, N$ )

James A. Dodd,<sup>1</sup> Steven J. Lipson, John R. Lowell, Peter S. Armstrong,<sup>1</sup>  
William A. M. Blumberg, Richard M. Nadile, Steven M. Adler-Golden,<sup>2</sup>  
William J. Marinelli,<sup>3</sup> Karl W. Holtzclaw,<sup>3</sup> and B. David Green<sup>3</sup>

Phillips Laboratory/Geophysics Directorate, Optical Environment Division, Hanscom AFB, Massachusetts

**Abstract.** Detailed spectroscopic analysis of hydroxyl fundamental vibration-rotation and pure rotation emission lines has yielded OH( $v, N$ ) absolute column densities for nighttime earthlimb spectra in the 20 to 110-km tangent height region. High-resolution spectra were obtained in the Cryogenic Infrared Radiance Instrumentation for Shuttle (CIRRIS 1A) experiment. Rotationally thermalized populations in  $v=1-9$  have been derived from the fundamental bands between 2000 and 4000  $\text{cm}^{-1}$ . Highly rotationally excited populations with  $N \leq 33$  ( $\leq 2.3$  eV rotational energy) have been inferred from the pure rotation spectra between 400 and 1000  $\text{cm}^{-1}$ . These emissions originate in the airglow region near 85-90 km altitude. Spectral fits of the pure rotation lines imply equal populations in the spin-rotation states  $F_1$  and  $F_2$  but a ratio  $\Pi(A'')/\Pi(A'') = 1.8 \pm 0.3$  for the  $\Lambda$ -doublet populations. A forward predicting, first-principles kinetic model has been developed for the resultant OH( $v, N$ ) limb column densities. The kinetic model incorporates a necessary and sufficient number of processes known to generate and quench OH( $v, N$ ) in the mesopause region and includes recently calculated vibration-rotation Einstein coefficients for the high- $N$  levels. The model reproduces both the thermal and the highly rotationally excited OH( $v, N$ ) column densities. The tangent height dependence of the rotationally excited OH( $v, N$ ) column densities is consistent with two possible formation mechanisms: (1) transfer of vibrational to rotational energy induced by collisions with O atoms or (2) direct chemical production via  $\text{H} + \text{O}_3 \rightarrow \text{OH}(v, N) + \text{O}_2$ .

### Introduction

Vibrational nonlocal thermodynamic equilibrium (NLTE) effects have long been recognized in the upper atmosphere. For instance, Meinel [1950] correctly attributed the near-infrared nighttime airglow in the mesopause region to hydroxyl vibration-rotation emission, the vibrationally excited OH arising from the reaction of hydrogen atoms with ozone. Researchers have also formulated a chemiluminescent source for the excited vibrational states of ozone that radiate in the upper atmosphere in the 10 to 13- $\mu\text{m}$  wavelength region [Rawlins, 1985; Solomon *et al.*, 1986; Adler-Golden, 1987; Mlynarczyk and Drayson, 1990a, b]. Other production mechanisms, including earthshine and collision-induced pumping of the ground-state species, give rise to far less excitation of the corresponding excited vibrational levels.

In addition to vibrational NLTE effects in the upper atmosphere a number of recent reports have documented pronounced rotational NLTE effects. Very high rotational excitation in thermospheric nitric oxide has been inferred

from spectral analysis of the fundamental bands, both through extended  $P$ -branch emissions and  $R$ -branch band head emissions. Atmospheric emissions from rotationally excited NO( $v, J^*$ ) were first observed in the rocket-borne field-widened interferometer (FWI) experiment [Espy *et al.*, 1988] and positively identified in subsequent laboratory studies [Rawlins *et al.*, 1989]. High-resolution NO( $v, J^*$ ) fundamental spectra were observed more recently under a much wider range of conditions in the CIRRIS 1A experiment [Armstrong *et al.*, 1992], flown aboard the space shuttle, and also in the EXCEDE III rocket-borne auroral simulation experiment [Lipson *et al.*, 1992]. As much as 2 to 3-eV rotational energy in product NO( $v, J^*$ ) has been inferred from analyses of the field and laboratory data [Rawlins *et al.*, 1992].

Rotational NLTE has been observed in hydroxyl via pure rotation emission from high- $N$  levels in the CIRRIS 1A experiment [Dodd *et al.*, 1993a; Smith *et al.*, 1992; Baker *et al.*, 1991] and in the laboratory [Carleton *et al.*, 1990]. In CIRRIS 1A, OH( $v, N$ ) radiance was observed in the upper mesosphere/lower thermosphere region via limb measurements, providing a long pathlength to enhance the emission signals. Levels with rotational energies as high as 2.3 eV were inferred from OH( $v=0-6$ ) pure rotation emission lines. (Highly rotationally excited levels will hereafter be denoted OH( $v, N^*$ )). In the same experiment, rotationally thermalized OH( $v=1-9$ ) was monitored through fundamental band Meinel emission. The published studies have largely

<sup>1</sup>Stewart Radiance Laboratory, Bedford, Massachusetts.

<sup>2</sup>Spectral Sciences, Inc., Burlington, Massachusetts.

<sup>3</sup>Physical Sciences Inc., Andover, Massachusetts.

Copyright 1994 by the American Geophysical Union.

Paper number 93JD03338.

0148-0227/94/93JD-03338\$05.00

discussed the phenomenology of the spectra and outlined the analyses used to generate  $\text{OH}(\nu, N)$  column densities. At present, however, the production and quenching mechanisms of these high-energy states have not been determined and remain an intriguing problem.

In this paper we first describe in detail the analysis of the  $\text{OH}(\nu, N)$  emission spectra obtained in the CIRRIS 1A experiment. Spectral fitting was used to generate line-of-sight column densities, specific in the vibrational, rotational, and spin-sublevel degrees of freedom. In the second section we describe a first-principles kinetic model that semiquantitatively reproduces the  $\text{OH}(\nu, N)$  column densities and directly addresses many of the uncertainties concerning the origin of the high rotational excitation.

## Experiment

The CIRRIS 1A experiment was flown aboard the Space Shuttle Discovery as part of the STS-39 payload and obtained data during the 3-day period April 28-30, 1991 [Ahmadjian *et al.*, 1990; Bartschi *et al.*, 1992; Wellard *et al.*, 1992]. During this time, the shuttle executed a nearly circular orbit about the Earth, with a  $57^\circ$  inclination angle and a nominal altitude of 260 km. Limb-viewing data were obtained for tangent heights between 0 and 260 km as well as nadir and celestial views. The primary instrument consisted of a liquid-helium-cooled Michelson interferometer, in conjunction with a 0.3-m, high off-axis rejection telescope. Other instruments included a dual-plane radiometer with eight different filter passbands and photometers for narrowband detection of radiance at  $5577 \text{ \AA}$  ( $\text{O}({}^1\text{S} \rightarrow {}^1\text{D})$  transition) and  $3914 \text{ \AA}$  ( $\text{N}_2^+ \text{ B-X}(0-0)$  "first negative" band), in order to probe solar and auroral activity. The interferometer used a single detector plane consisting of five Si:As detectors of various sizes and sensitivities. The vertical field of view of the detectors at a 100-km tangent height ranged from 1.5 km to 15 km, the smaller field-of-view detectors having less sensitivity. To maximize the signal-to-noise ratio, our analysis was mainly limited to data from the largest detector (detector 2, with a 15-km vertical and horizontal field of view). However, hydroxyl pure rotation lines in the  $750\text{--}1000 \text{ cm}^{-1}$  region were easily observed using smaller detectors.

The Si:As detector had a significant spectral response between  $400$  and  $4000 \text{ cm}^{-1}$ . During the mission an eight-position optical filter wheel was used either in the open position or with one of seven short-, long-, and band-pass filters covering the detector plane. These filters served to eliminate intense emission from features such as the  $\text{CO}_2(\nu_2)$   $15\text{-}\mu\text{m}$  band and the  $\text{O}_3(\nu_3)$   $9.6\text{-}\mu\text{m}$  band and to decrease the noise level in spectra observed at other frequencies. Intense emission also gives rise to intensity oscillations ("ringing") superimposed on spectra generated from unapodized interferograms. Apodizing interferograms prior to transformation diminishes the ringing but also degrades the resolution. We will return to these points in conjunction with the filter 7 ( $770\text{--}1250 \text{ cm}^{-1}$  passband) data. Interferograms were obtained with three scan lengths: short (corresponding to  $8 \text{ cm}^{-1}$  nominal resolution spectra), medium ( $3 \text{ cm}^{-1}$ ), and long ( $1 \text{ cm}^{-1}$ ). A total of approximately 150,000 scans were obtained in the course of 18 hours of data acquisition. Our analysis is limited to the long interferograms, corresponding to the highest resolution data.

## Tangent Height Determination

The accurate determination of tangent heights is crucial in the case of OH emission at the mesopause, since the radiance occurs over such a small altitude range. As discussed previously [Smith *et al.*, 1992; Dodd *et al.*, 1993a], the observed  $\text{OH}(\nu, N)$  line intensities are very sensitive to the interferometer viewing angle. At the 100-km tangent height a change in pitch angle of  $10 \text{ mrad}$  ( $0.6^\circ$ ) results in a tangent height change of 15 km, providing a very sensitive means of discriminating against the possible effects of shuttle-induced radiance. Using detector 2,  $\text{OH}(\nu, N)$  emissions are never observed above 110-km tangent height. The  $\text{OH}(\nu, N)$  features are also not present above 110-km tangent height in spectra obtained from the other four detectors, within the limits of the (poorer) signal-to-noise ratio.

The interferometer pointing was monitored using several different methods over the course of the mission [Bartschi *et al.*, 1992]. First, the instrument gimbal mount angles with respect to the shuttle were monitored continuously ("gimbal" reading), with the shuttle's attitude determined via a laser gyroscope. The gimbal reading provided a low-noise measure of the pointing with a fast response time, albeit with a limited accuracy due to such factors as flexing of the shuttle and long-term drift of the gyroscope. Second, an IR horizon sensor (HS) was used to measure radiance at  $15 \text{ }\mu\text{m}$  (largely due to  $\text{CO}_2$  emission) by continually scanning a small cone angle about the center of the interferometer field of view. This instrument integrated the radiance signal as it scanned downward in tangent height, and was programmed to trigger when the integrated radiance was equal to a preset level corresponding to a nominal altitude of 40 km. The HS reading provides a higher pointing accuracy than the gimbal reading but with a slower response and higher noise level. A factor which limits the accuracy of the HS is the poorly understood seasonal and latitudinal dependence of the  $15\text{-}\mu\text{m}$  radiance intensity [Wertz, 1978]. The advantages of the two sets of pointing data were combined by fitting the differences between the gimbal and the HS elevation angles to a polynomial in mission time, then correcting the low-noise gimbal elevation angle to the more accurate but noisier HS angle. We estimate the accuracy of the pointing derived in this manner as  $\pm 5 \text{ km}$  at 100-km tangent height.

Recently, more accurate pointing information has become available. The celestial aspect sensor (CAS), also part of the CIRRIS 1A mission payload, obtained star images during the course of the mission using a film camera. Photographic analysis of these images has yielded a highly accurate measure of the pointing, largely for the nighttime portion of the mission. Fortunately in this case, almost all of the  $\text{OH}(\nu, N)$  data analyzed herein were obtained under nighttime conditions. We estimate the accuracy of the CAS pointing as  $\pm 2 \text{ km}$  at 100-km tangent height.

The gimbal and CAS pointing information were combined in a manner similar to that described above for the gimbal/HS pair. Elevation angle differences between the gimbal and CAS pointing data were fit to a second-order polynomial in mission time. This fit allows periodic "updating" of the continuous gimbal pointing angle such that it agrees with the CAS angle and provides an accurate, low-noise interpolation in time between CAS image acquisitions. For interferometer scan modes in which the instrument step/scans at sequentially increasing or decreasing tangent heights, a new CAS reading is generally obtained at each step. The CAS-corrected tangent heights were used for all of the nighttime data

analyzed in this report; the HS-corrected tangent heights were used for daytime data only.

### OH( $\nu, N$ ) Spectra and Column Densities

In this section we summarize the OH spectral data obtained from the CIRRIS 1A mission, and also the method whereby OH( $\nu, N$ ) column densities are obtained from line-of-sight spectra. A short description of angular momentum coupling in OH( $X^2\Pi$ ), together with the definitions of the labels used to denote the quantum state, is provided in the Appendix.

#### Conversion of Interferograms Into Spectra

Interferograms were obtained using a He-Ne reference laser monitor of the mirror retardation, each data point corresponding to an increment of the He-Ne 0.63299- $\mu\text{m}$  vacuum wavelength. Long scans nominally contain 700 data points left of center and 15,200 points right of center, where the center is the estimated zero-path-difference point. All but 256 data points left of center were discarded prior to processing. This procedure has no effect on the ultimate resolution of derived spectra, i.e. 0.63  $\text{cm}^{-1}$  full width half-maximum (FWHM) intensity with a sinc line shape, and serves to eliminate data taken before settling of the instrument. Interferograms thus truncated were subject to trapezoidal apodization about the center point to prevent frequency discrimination. No further apodization was performed, with the exception of the filter 7 data discussed below. Interferograms were zero filled by a factor of 8, giving a total of 128 K points, then subjected to fast Fourier transformation (FFT) using a standard computer routine [Press *et al.*, 1986]. Phase correction was accomplished by transforming the same interferogram, truncated to contain 256 points on either side of the center using triangular apodization [Mertz, 1967; Griffiths and de Haseth, 1986] and also zero filled to 128 K points. The resultant low-resolution phase was subtracted from the phase obtained by transforming the entire interferogram. Uncalibrated spectra in units of  $\text{V}/\text{cm}^{-1}$  were obtained by multiplying the magnitude of the FFT output by the cosine of the corrected phase, producing amplitude spectra with bipolar signal and noise. Spectrally calibrated data in units of  $\text{W cm}^{-2} \text{sr}^{-1}/\text{cm}^{-1}$  were then obtained by dividing the flight spectrum by the appropriate calibration spectrum.

Calibration interferograms were measured after completion of the mission using a 1200 K blackbody source. Interferograms were obtained for every detector/filter/detector-bias combination, for a total of  $5 \times 8 \times 2 = 80$  scans. Normalized spectral calibration curves were generated by a three-step process in which (1) calibration interferograms were transformed in a manner identical to flight interferograms, (2) calibration spectra were divided by a blackbody curve  $dE/d\sigma$  calculated for the appropriate source temperature (where  $\sigma$  is wavenumber), then (3) normalized to unity at the largest amplitude point in the filter passband.

Detector absolute response in volts was measured for several values of the blackbody temperature, i.e., as a function of the blackbody output in  $\text{W cm}^{-2} \text{sr}^{-1}$ , independently for each detector/filter/bias combination as before. Increasing blackbody photon flux gives rise to an increasing dc voltage offset  $V_{\text{DC}}$  in the interferogram. For a given detector/bias combination the nonlinear response was

constrained to have a filter-independent  $V_{\text{DC}}$  dependence. This constraint was imposed by least squares fitting the detector response as a filter-independent, smooth function of  $V_{\text{DC}}$ . This function was used to model the nonlinear absolute response for a given offset  $V_{\text{DC}}$ . Normalized calibration spectra were converted into units of  $\text{V}(\text{W cm}^{-2} \text{sr}^{-1})^{-1}$  by multiplying by the appropriate absolute calibration factor.

A number of raw interferograms were found to be corrupted, either by the presence of amplitude spikes or by a misregistration of interferogram point number. Several interferograms were repaired manually by removing 1-3 data points constituting obvious spikes, then replacing the points by linearly interpolating surrounding values. This latter operation was necessary to preserve the phase information in the interferogram and introduced no obvious frequency or intensity artifacts into resultant spectra. Other interferograms appeared problem free upon visual inspection but gave rise to spectra with egregious amplitude oscillations. These oscillations are indicative of a phase problem, resulting from a misregistration of the mirror retardation (i.e., missing points or extra points in the interferogram). The location of the interferogram point misregistration is not easily determined, however, preventing reconstruction of the interferograms. Thus these data were not used in further analyses.

#### Spectral Data Analysis

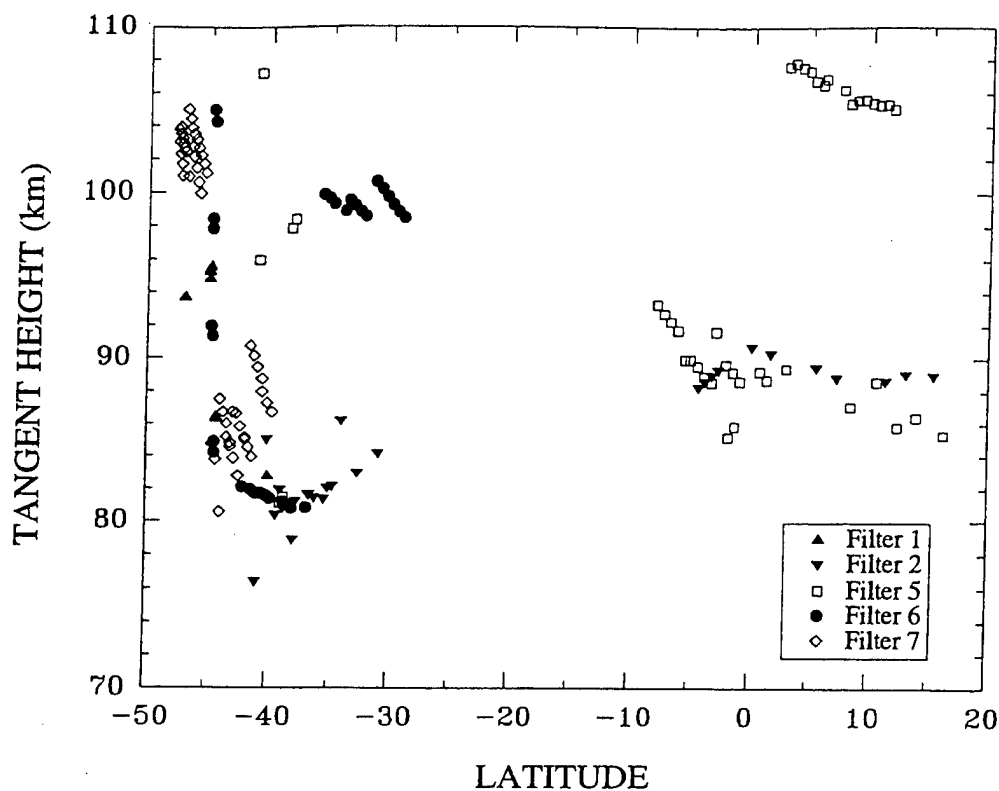
Table 1 details, as a function of filter passband, the type of spectrum observed and the total number of spectra used to derive OH( $\nu, N$ ) column densities. The table also lists the upper state  $\nu$  and  $N$  levels giving rise to the observed emissions. (For the pure rotation spectra the specific range of  $N$  depends on the  $\nu$  level.) The tangent heights and solar zenith angles at which the data were obtained, both as a function of latitude, are shown in Figures 1 and 2, respectively.

Figure 3 shows spectral data and the corresponding spectral fit for the OH vibration-rotation emission bands for  $\nu=1-9$  (obtained using filter 1). Note that the vertical scale for the left-hand side of Figure 3 has been expanded to show the details of the weaker emissions in the 2100-2750  $\text{cm}^{-1}$  region. Likewise, Figure 4 shows spectral data for two pure rotation passbands (obtained using filters 5 and 6), along with a plot of the synthetic spectrum generated from spectral fits performed separately to data in the corresponding passbands. The spectra in Figures 3 and 4 were taken at an 86-km tangent height. The details of the spectral fitting codes are described in the following sections.

**Table 1.** Filter Distribution of OH Spectral Data

Filter	Nominal Passband, $\text{cm}^{-1}$	Spectrum Type*	Upper State $\nu$ Range	Upper State $N$ Range	Scans Used
1	2040-4000	Vib-Rotn	1-9	1-4	12
2	2700-4000	Vib-Rotn	1-5	1-4	29
5	770-910	Pure Rotn	0-3	24-33	48
6	400-600	Pure Rotn	0-6	13-22	32
7	770-1250	Pure Rotn	0-3	24-33	53

\*Vib-Rotn, fundamental vibration-rotation bands; Pure Rotn, pure rotation bands.



**Figure 1.** Global coverage of the Cryogenic Infrared Radiance Instrumentation for Shuttle (CIRRIS 1A) OH scans used in the present analysis. The tangent height for each scan is plotted against the corresponding latitude at the tangent point. Scans obtained using five filter passbands are differentiated by symbol.

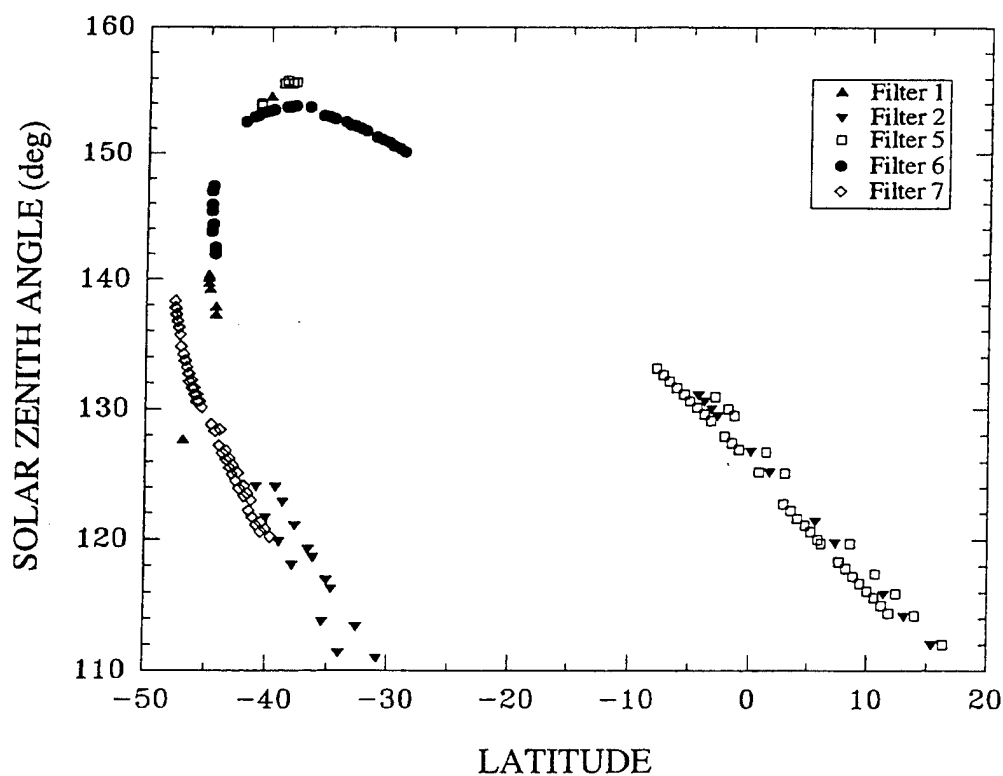


**Figure 2.** Global coverage of the CIRRIS 1A OH scans used in the present analysis. The solar zenith angle for each scan is plotted against the corresponding latitude at the tangent point. Scans obtained using five filter passbands are differentiated by symbol.

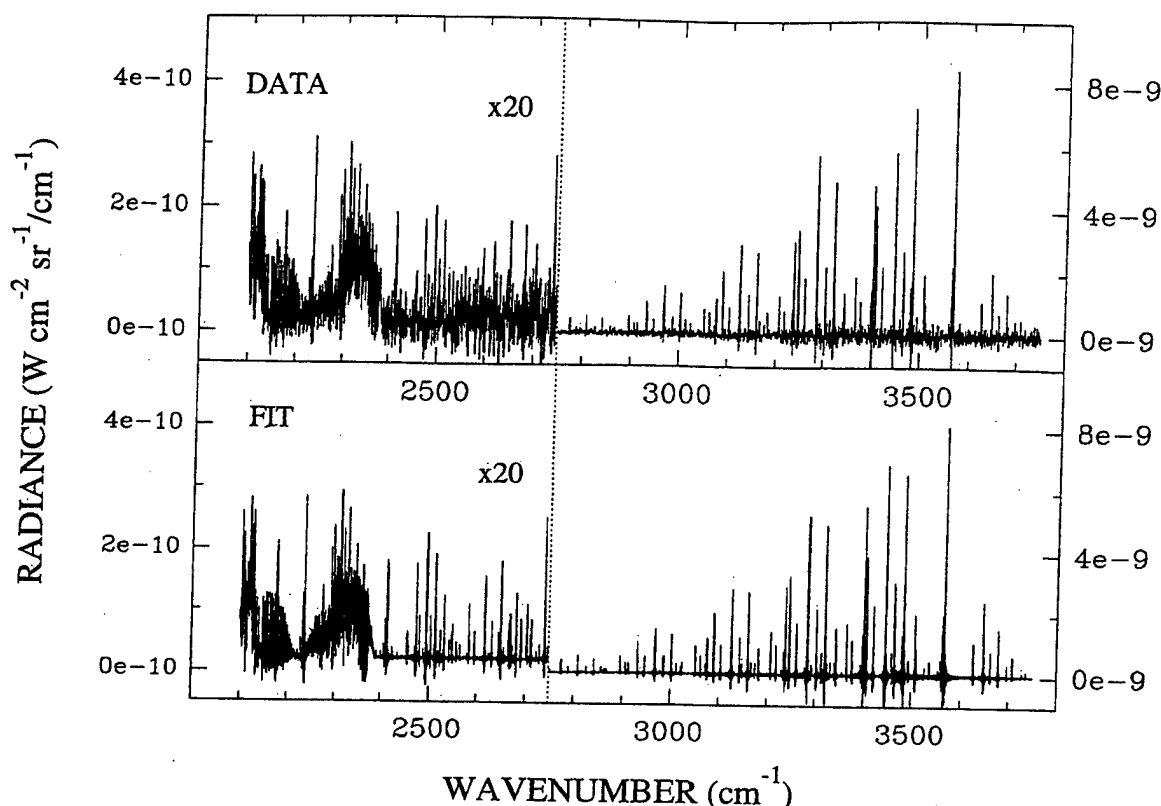


**Figure 3.** OH( $v \rightarrow v-1$ ) vibration-rotation spectrum obtained using filter 1 at 86-km tangent height. Note that the y scale has been expanded by a factor of 20 for wavenumber values less than 2750  $\text{cm}^{-1}$ . Radiance from  $\text{O}_3$ , CO, and  $\text{CO}_2$  is present in the 2100–2400  $\text{cm}^{-1}$  region; OH( $v \rightarrow v-1$ ) emission dominates the spectrum at higher wavenumber values. The data were fit in the 2100–3750  $\text{cm}^{-1}$  region, with the synthetic spectral fit shown at the bottom of the figure.

**Fundamental bands.** Above 2400  $\text{cm}^{-1}$  the OH fundamental vibration-rotation bands were the sole feature in nighttime spectra for a wide range of tangent heights. Between 2050 and 2400  $\text{cm}^{-1}$ , signal comparable in maximum amplitude to the OH(9–8)  $Q$  branch at 2236  $\text{cm}^{-1}$  was observed from three different emitters:  $\text{O}_3(v_1+v_3)$  in the 2050–2130  $\text{cm}^{-1}$  region;  $\text{CO}(1-0)$ , 2060–2220  $\text{cm}^{-1}$ ; and  $\text{CO}_2(v_3)$ , 2230–2390  $\text{cm}^{-1}$ . Notably, radiance from  $^{13}\text{CO}$  and  $\text{C}^{18}\text{O}$  was identified in the spectral data in addition to the main isotope [Dodd *et al.*, 1993b]. All of these features were accounted for in the spectral fitting algorithms.

Spectral data were modeled using a nonlinear fitting code developed earlier to model OH( $v \rightarrow v-1$ ) and ( $v \rightarrow v-2$ ) emission observed in the laboratory with a room-temperature interferometer [Dodd *et al.*, 1991]. Data were fit on a scan-by-scan basis. For an uncalibrated spectrum the noise level (units of  $\text{V}/\text{cm}^{-1}$ ) was taken to be constant over the appropriate wavenumber range. Thus the relative uncertainties in the spectral data points were scaled as the inverse of the spectral response function. The parameters  $w$ , for the effective FWHM of the sinc line shape function, and  $s$ , for the fractional wavenumber shift of the spectrum, were allowed to vary during each fit. The best fit value for  $w$  was generally equal to 0.63  $\text{cm}^{-1}$ , i.e., that calculated based on 15,200 fringes for the long leg of the interferogram. The parameter  $s$  accounts for experimental aspects such as finite detector size, nonuniform emission intensity in the field of view, and slight misalignment of the interferometer mirrors

or reference laser; its best fit value was typically equivalent to a  $1/10^4$  red shift.

OH vibration-rotation basis functions were synthesized using literature line positions [Coxon and Foster, 1982] and Einstein A coefficients [Nelson *et al.*, 1990]. The corresponding lines were then convolved with the interferometer sinc line shape function. Relative vibrational populations were allowed to vary independently as linear parameters in the fit. The relative rotational populations were taken to be independent of  $v$  and determined through a single adjustable parameter  $T$ , the rotational temperature. While other workers have observed Boltzmann nonequilibrium for OH rotational levels as low as  $N=4$  [Pendleton *et al.*, 1993], these observations typically enjoyed signal-to-noise ratios much higher than those in the present OH fundamental spectra, for which the signal-to-noise ratio equals 10:1 on the strongest lines. Transitions originating from levels higher than  $N=4$  are not visible in the OH fundamental spectra; no evidence of Boltzmann non-equilibrium for  $N=1-4$  is observed.

To fit the 2100–2400  $\text{cm}^{-1}$  region, radiance from ozone, carbon monoxide, and carbon dioxide must be taken into account. This was accomplished by generating normalized spectral profiles for each of the three species, then scaling the profiles independently of one another in the process of generating a best fit to the data. Spectral profiles for  $\text{O}_3$ , CO, and  $\text{CO}_2$  were synthesized using the strategic high-altitude radiance code (SHARC) in a limb-viewing geometry

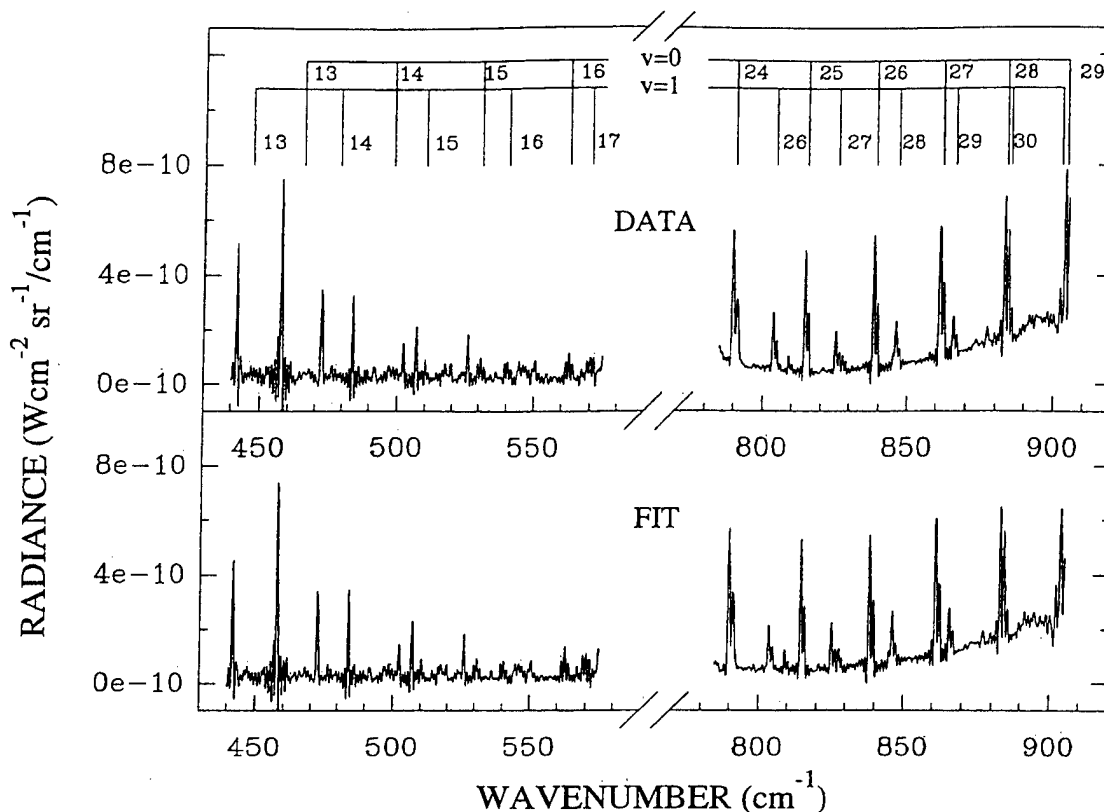


**Figure 4.** OH( $N \rightarrow N-1$ ) pure rotation spectra obtained using filters 6 (left) and 5 (right), both at 86-km tangent height. The wavenumber positions of the upper state  $N$  values for  $v=0,1$  are indicated above the plots. The strong lines seen in the filter 6 data are due to radiance from thermal  $H_2O$ . The data were fit in the 440–575  $cm^{-1}$  and 785–905  $cm^{-1}$  regions, respectively, with the corresponding synthetic spectral fits shown at the bottom of the figure.

[Sharma *et al.*, 1989]. The shapes of the normalized synthetic  $O_3$  and  $CO$  profiles were found to be relatively insensitive to tangent height in the 80 to 110-km region and were calculated assuming a tangent height of 85 km. Carbon dioxide, on the other hand, undergoes a much greater degree of self-absorption, the effect most pronounced at the lower tangent heights. To adequately model the  $CO_2$  emission, normalized  $CO_2$  spectral profiles were calculated independently at 80 and 95-km tangent heights. For each tangent height the model includes radiance from the  $CO_2$ ,  $^{13}CO_2$ , and  $CO^{18}O$  isotopes of carbon dioxide in fixed proportions. The  $^{13}CO$  and  $C^{18}O$  1-0 spectral profiles were modeled using line positions and emission intensities from the HITRAN line file [Rothman *et al.*, 1992], assuming the same rotational temperature  $T$  as determined for the OH  $N$  levels. The  $O_3$ , three  $CO$ , and two  $CO_2$  synthetic spectral profiles were then used as linearly independent basis functions in the fits to the filter 1 data, with the best fit multipliers determined by minimizing  $\chi^2$ .

A spectral fit to OH fundamental emission data is shown in Figure 3. The best fit multipliers for the various OH( $v \rightarrow v-1$ ) bands provide the absolute column densities for the line of sight in question. These fits yield the rotational state column densities for the upper state populations inferred from the OH( $v, N$ ) emission lines. Figure 5 shows the  $O_3$ ,  $CO$ , and  $CO_2$  basis functions, weighted proportionately by the best fit multipliers. Figure 6 shows a comparison of the data and fit from Figure 3, with the summed radiance from

$O_3$ ,  $CO$ , and  $CO_2$  (i.e., that shown in Figure 5) subtracted from both spectra. The residual radiance in the spectral data consists principally of the OH( $v \rightarrow v-1$ ) emission lines.

The spectral fits to the OH fundamental bands determine the line-of-sight column densities for the rotational levels of  $v=1-9$  which are at thermal equilibrium. These column densities are shown as a function of tangent height in Figure 7, in which the populations have been summed over both  $N$  and the four spin sublevels. The populations for  $v=6$  and 7 are poorly determined from the fits, especially for the higher tangent heights, owing to low transition probabilities in the fundamental bands. For clarity the populations in  $v=6$  and 7 have been omitted from the figure but generally fall within the range of the other higher  $v$  level populations. The column densities are seen to decrease by a large factor between 94-km and 96-km tangent height; they are not observed above 96 km within the signal-to-noise limit of the data. Taking into account the 15-km field of view of the interferometer, the 96-km tangent height corresponds to an upper bound altitude of about 89 km for the Meinel fundamental band radiance observed in the experiment.

For tangent heights below 75 km, nighttime limb spectra exhibit diminished OH fundamental band intensities, consistent with shorter pathlengths through the altitude region where the NLTE radiance occurs. For tangent heights below about 70 km, intense  $CO_2$  emission completely obscures the OH(9-8) band and the  $P$  branch of the OH(8-7) band. In the 2400–4000  $cm^{-1}$  region, however, OH fundamental band

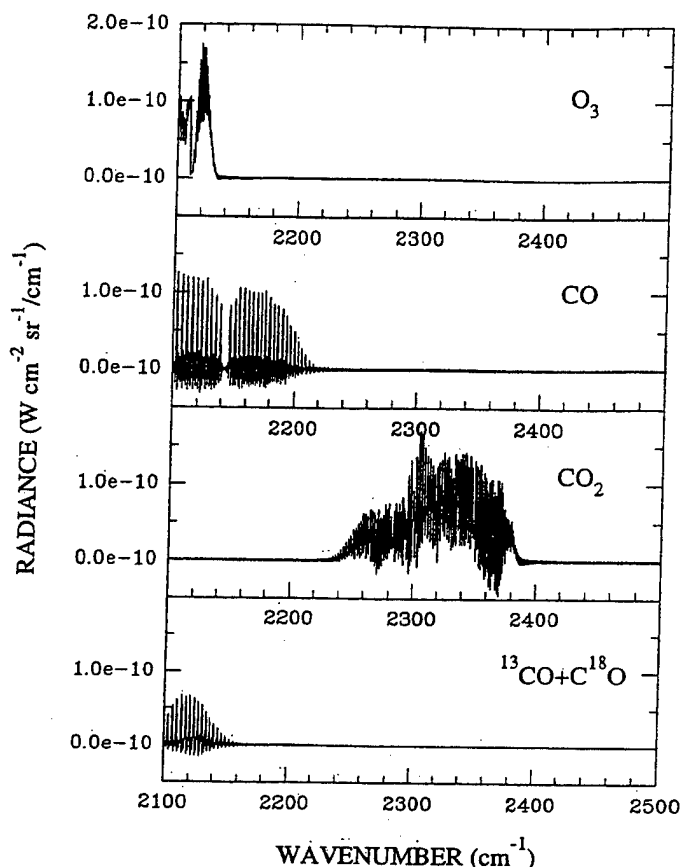


**Figure 5.** Basis functions for  $O_3$ ,  $CO$ ,  $CO_2$ , and  $^{13}CO + C^{18}O$ , respectively, weighted by the best fit factors according to the spectral fit to the data shown in Figure 3. The basis functions for  $O_3$ ,  $CO$ , and  $CO_2$  were calculated using the strategic high-altitude radiance code (SHARC) [Sharma et al., 1989]. The basis functions for  $^{13}CO$  and  $C^{18}O$  were calculated using line positions and intensities from the HITRAN line file [Rothman et al., 1992], with a rotational temperature  $T = 210$  K.

radiance dominates nighttime spectra for tangent heights as low as 20 km.

**Pure rotation bands.**  $OH(N \rightarrow N-1)$  pure rotation emission spectra from filters 5 and 6 are shown in Figure 4; spectral data from filter 7 are shown in Figure 8. All three of these filters removed the very intense  $CO_2(v_2)$  emission in the 600–750  $cm^{-1}$  range. Filters 5 and 6 also eliminated emission from the intense  $O_3(v_3)$  band in the 990–1070  $cm^{-1}$  region. Because filter 7 did not attenuate the  $O_3(v_3)$  band intensity, a significant amount of ringing is seen superimposed on the OH pure rotation lines in the 770–1000  $cm^{-1}$  region for unapodized interferograms. This ringing is difficult to model in the spectral fits, and a technique used to handle these data will be described below.

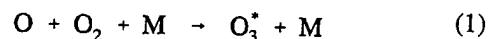
As in the case of the vibration-rotation spectral analysis, data were fit on a scan-by-scan basis, with the relative uncertainty in each spectral data point scaled as the inverse of the spectral response function.  $OH(N \rightarrow N-1)$  basis functions were synthesized in the same manner as the  $OH(v \rightarrow v-1)$  vibration-rotation basis functions, using literature line positions [Goldman et al., 1983] and Einstein A coefficients [Goorvitch et al., 1992; Holtzclaw et al., 1993].

The line width parameter  $w$  and line shift parameter  $s$  were allowed to vary in each fit, yielding best fit values similar to those obtained in the fits to the OH vibration-rotation spectra. Relative vibrational populations were allowed to vary freely in the fits, while relative spin sublevel populations were fixed at the best fit values obtained in the spin sublevel analysis, described below.

The rotational level distribution was parameterized using a Boltzmann distribution over  $N$ , with a single effective "temperature" parameter  $T$ , independent of  $v$  level. As was stated previously [Dodd et al., 1993a], the use of a Boltzmann distribution in this case is purely a convenience and does not imply that the rotational states are in thermal equilibrium. Because typical  $N$  distributions are approximately flat for the pure rotation region, the best fit parameter  $T$  was found to be very large, with both positive and negative values. The formal discontinuity in  $T$  at  $\pm\infty$  was removed by performing the fits using the parameter  $1/T$  in place of  $T$ . The value  $1/T$  equals zero for a flat distribution (after dividing by the degeneracies  $2(N+1)$  and  $2N$  for the  $F_1$  and  $F_2$  manifolds, respectively), with small positive and negative values for nearly flat distributions. The excellent agreement between the data and the model spectra (Figure 4) shows that this form for the  $N$  distribution provides an accurate representation of the line-of-sight populations. A line-by-line rotational level fit proved impossible owing to significant line overlap at the experimental resolution. We also attempted to fit the pure rotation data using a set of  $v$ -dependent temperature parameters  $1/T_v$ . However, because the signal-to-noise ratio degrades with increasing  $v$ , the error in the best fit  $1/T_v$  parameters increases rapidly with  $v$ . The vibration level-independent parameter  $1/T$  is determined largely by the  $v=0$  and  $v=1$  pure rotation data.

For the filter 6 data, radiance from  $H_2O$  pure rotation lines was seen to contribute to the spectra, as predicted from the SHARC model [Sharma et al., 1989]. This emission arises primarily from the  $H_2O$  ground vibrational state, with the rotational level population in thermal equilibrium with the local kinetic temperature, i.e., 200 K. Below 90-km tangent height these lines are stronger than the OH pure rotation lines, while above 90 km the OH lines are stronger, with the total radiance decreasing with increasing altitude. Normalized  $H_2O$  spectral profiles, calculated using the SHARC model, were found to be sensitive to the assumed tangent height. Thus two synthetic  $H_2O$  profiles were calculated assuming 80 and 95-km tangent heights, then used as linearly independent basis functions, analogous to the method used to analyze the 2100–2400  $cm^{-1}$  region. The fitting routine determined the best fit multipliers optimizing the contributions made by the two  $H_2O$  profiles. Figure 9 replots the data and fit from Figure 4 for the 400–600  $cm^{-1}$  region, with the best fit  $H_2O$  radiance subtracted from both spectra. The residual amplitude in the data consists of the weaker  $OH(N \rightarrow N-1)$  transitions.

For the filter 5 data a diffuse baseline radiance level is present, with an integrated intensity about equal in magnitude to the summed intensity of the  $OH(N \rightarrow N-1)$  pure rotation lines. This baseline emission is attributed to  $O_3(v_3)$  hot band radiance. Vibraluminescent ozone arises through the three-body recombination reaction [Rawlins, 1985],





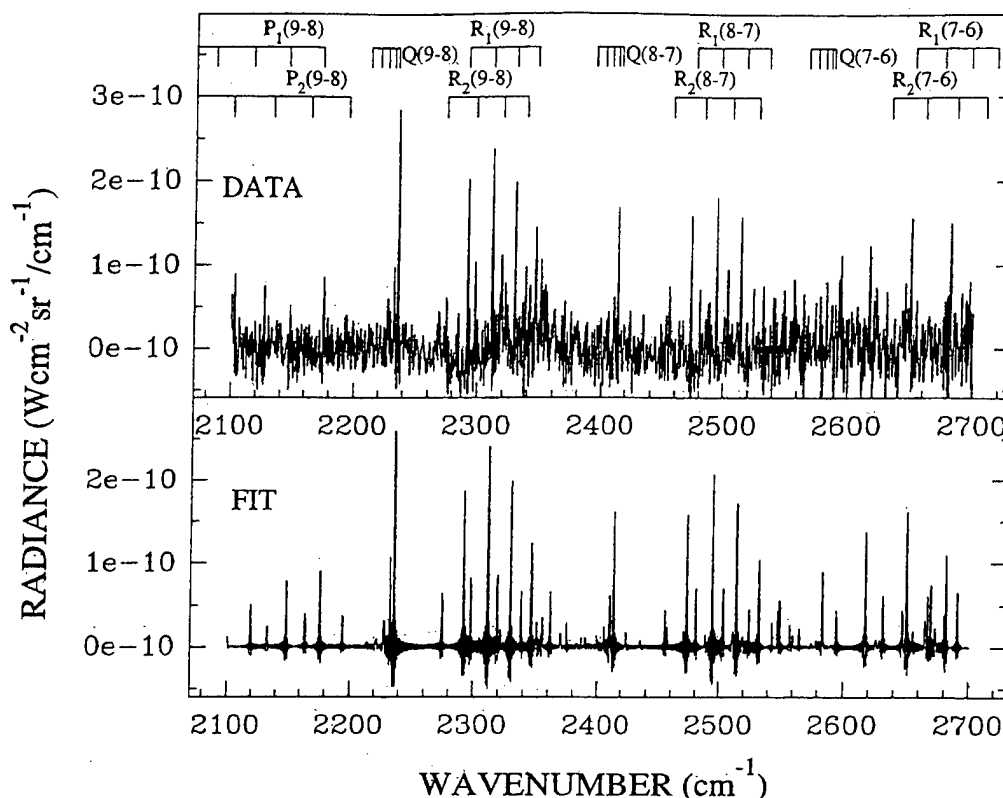


**Figure 6.** Identical filter 1 spectra from Figure 3, except that the modeled  $O_3$ ,  $CO$ , and  $CO_2$  radiance has been subtracted from both the data and the fit. This process more clearly shows the  $OH(v \rightarrow v-1)$  lines in both spectra. Wavenumber positions for the first few  $P$ ,  $Q$ , and  $R$  emission lines for the two spin-orbit manifolds are indicated above the plot. Corresponding  $Q_1$  and  $Q_2$  transitions are not resolved under the experimental resolution and are labeled simply as " $Q$ "-branch lines on the figure.

where  $M$  is any species that can carry off a portion of the excess energy. Following this assumption, the intensity of the  $O_3(v_3)$  hot bands is proportional to the product  $[O] \times [O_2] \times [M]$ , of which only  $[O]$  has a clear diurnal variation and only for altitudes below the  $OH$  airglow layer [Philbrick,

1985]. If the loss is dominated by infrared photon emission, the hot band intensity should not display a significant diurnal variation, as observed in the SPIRE rocket-borne experiment [Green *et al.*, 1986]. The fundamental  $O_3(v_3)$  band at  $9.6 \mu m$ , on the other hand, results largely from earthshine pumping of the ground state. Thus the  $v_3$  band intensity is a measure of the total ozone concentration and diminishes greatly during daytime hours owing to  $O_3$  solar photodissociation.

Examination of daytime spectra with similar tangent heights showed that the  $O_3(v_3)$  hot band radiance has no significant diurnal variation, while the  $OH$  pure rotation lines and the intense  $O_3(v_3)$  band at  $9.6 \mu m$  decrease in intensity by a factor of 10. As discussed above, these observations are consistent with a radiative loss term dominating the overall disappearance of the upper states giving rise to the

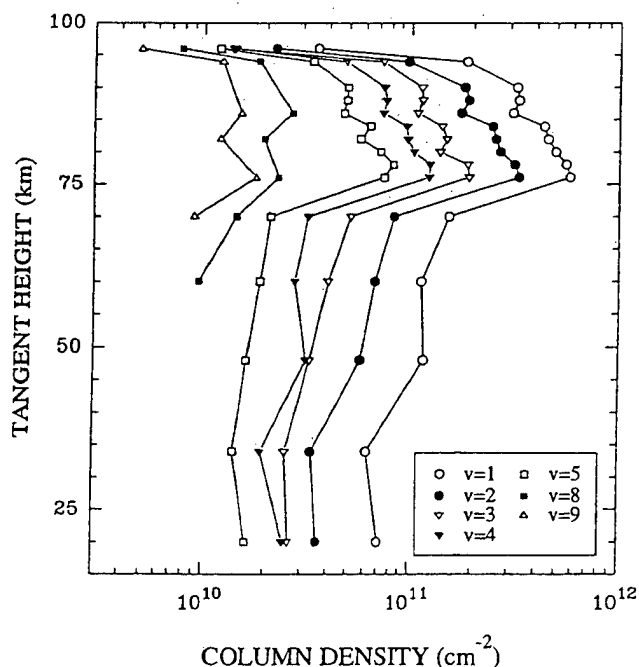


**Figure 7.** Thermal  $OH(v)$  column densities as a function of tangent height, summed over  $N$  and the four spin sublevels. The values were derived from spectral fitting of the fundamental bands. For clarity, column densities for  $v=6$  and  $7$  are not shown; those values have much larger error bars due to weaker radiance. No emission above the noise level was observed in the fundamental bands for tangent heights above  $96 km$ . The derived  $OH(v)$  column densities decrease below  $78 km$  tangent altitude, consistent with shorter pathlengths through the mesopause region where the excited  $v$  levels occur.

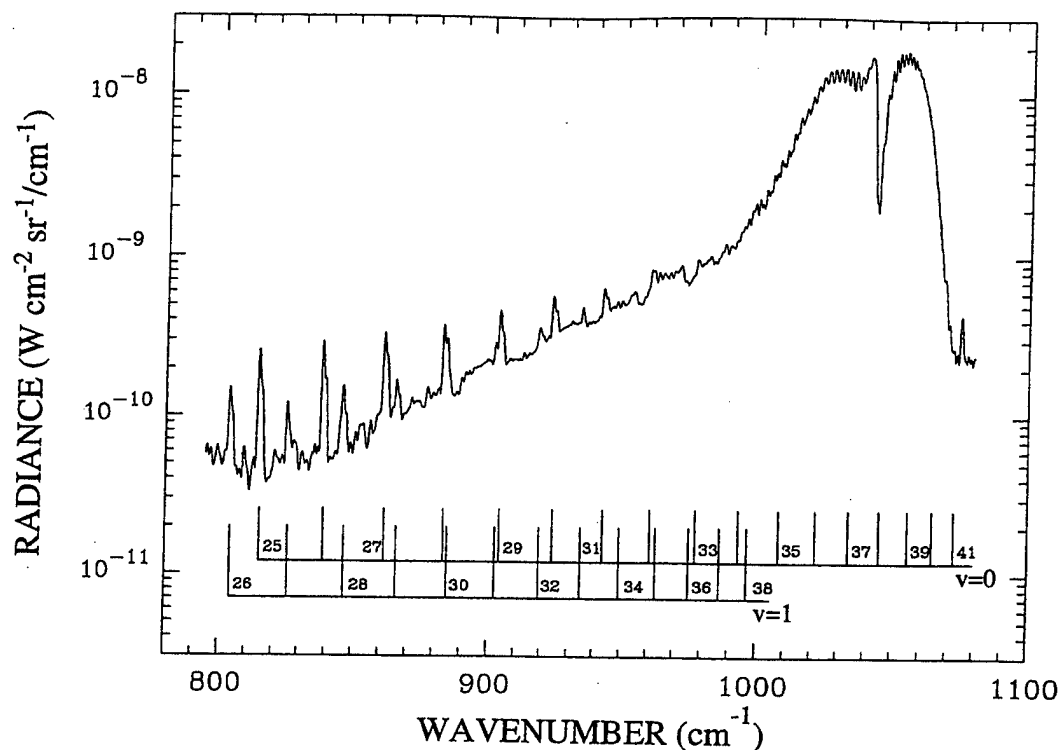


**Figure 8.** Semilog plot of an  $\text{OH}(N \rightarrow N-1)$  pure rotation spectrum from filter 7 ( $770\text{--}1250\text{ cm}^{-1}$  passband), obtained at 86-km tangent height. The interferogram was triangularly apodized to diminish ringing (see text). The  $\text{O}_3(\nu_3)$  band obscures possible OH pure rotation lines in the  $1000\text{--}1070\text{ cm}^{-1}$  region. The small peak visible at  $1075\text{ cm}^{-1}$  is also due to ozone emission. The highest OH rotational level inferred from the spectrum is  $N=33$ ; no  $\text{OH}(N \rightarrow N-1)$  emission lines are observed at wavenumber values higher than  $1070\text{ cm}^{-1}$ . Wavenumber positions for upper state  $N$  levels for  $v=0,1$  are shown beneath the plot.

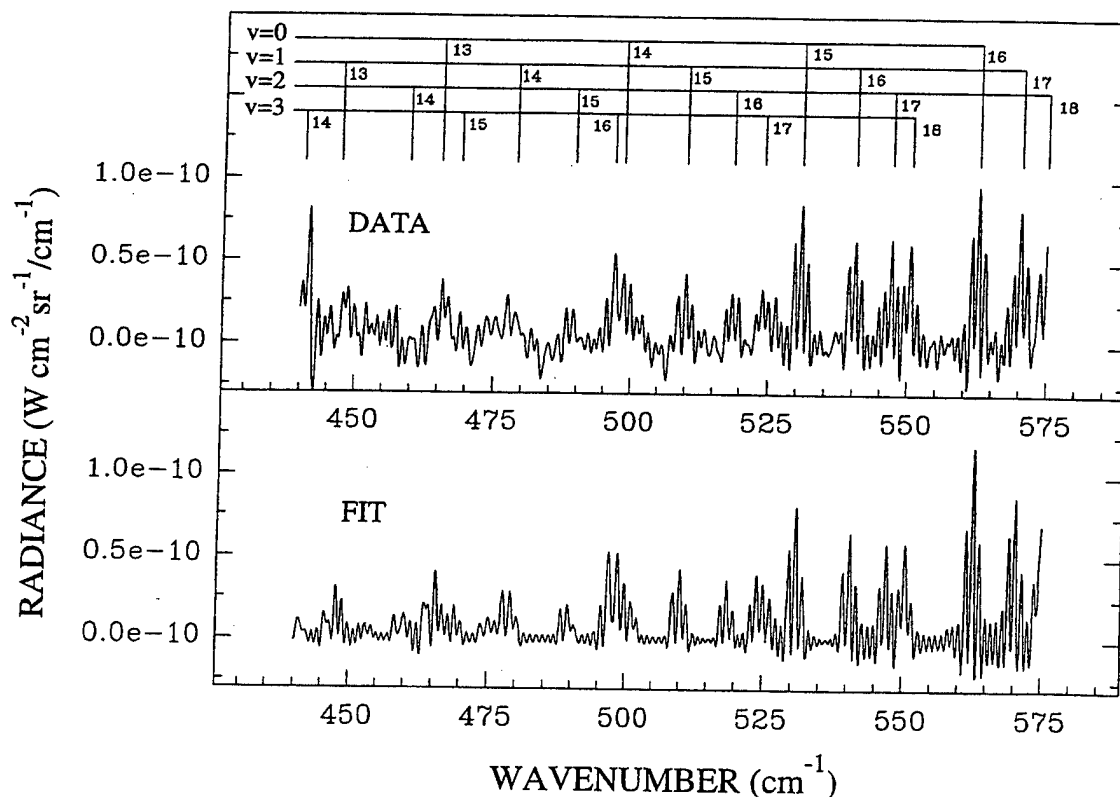


**Figure 9.** Identical filter 6 spectra from Figure 4, except that the modeled  $\text{H}_2\text{O}$  radiance has been subtracted from both the data and the fit. This process more clearly shows the  $\text{OH}(N \rightarrow N-1)$  lines in both spectra. Wavenumber positions for upper state  $N$  levels for  $v=0\text{--}3$  are indicated above the plot.

$O_3(v_3)$  hot bands. The intensity decrease in the  $OH(N \rightarrow N-1)$  lines and fundamental  $O_3(v_3)$  band are consistent with photodissociative loss of ozone during daylight hours and with  $O_3$  being a precursor of the  $OH(v, N)$ . To model the diffuse  $O_3(v_3)$  hot band radiance in nighttime spectra, daytime spectra were averaged in two separate tangent height bins (79-81 km and 94-96 km), reducing the noise. The two composite spectra were then used as independent basis functions in fits to the nighttime data. The best fit multipliers for these basis functions provide a measure of the  $O_3$  hot band contribution to the total radiance in this passband.

For filter 7 data, daytime data could not be subtracted from nighttime data, owing to the strong diurnal variation of the  $O_3$  9.6- $\mu$ m band intensity and to the presence in the daytime spectra of the  $CO_2$  "laser" bands, i.e., the  $v_3-2v_2$  and  $v_3-v_1$  bands with origins at 9.4  $\mu$ m and 10.4  $\mu$ m, respectively. In addition, Fourier transformation of unapodized interferograms gives rise to large amplitude

ringing superimposed on the  $OH$  pure rotation lines. To fit filter 7 spectra, interferograms were apodized prior to transformation using a triangular function, with unit contribution at the center of the interferogram and zero contribution at the furthestmost data point. This apodization both smoothed out the ringing and broadened the  $OH$  pure rotation features, effectively converting the  $OH$  lines to singlets from the doublet structure observable under maximum resolution (i.e., with no apodization). The baseline in this case was modeled using a second-order polynomial in wavenumber, with adjustable parameters multiplying each of the polynomial functions. Figure 8 shows a spectrum in the 770-1250  $cm^{-1}$  region resulting from a triangularly apodized interferogram. Spectral data were fit between 795 and 985  $cm^{-1}$ .

Lower-resolution (4  $cm^{-1}$ ) spectral data in the 750-1000  $cm^{-1}$  region have been obtained from the SPIRIT 1 rocket-borne interferometer experiment [Adler-Golden *et al.*, 1990]. These spectra exhibit instrumentally broadened features

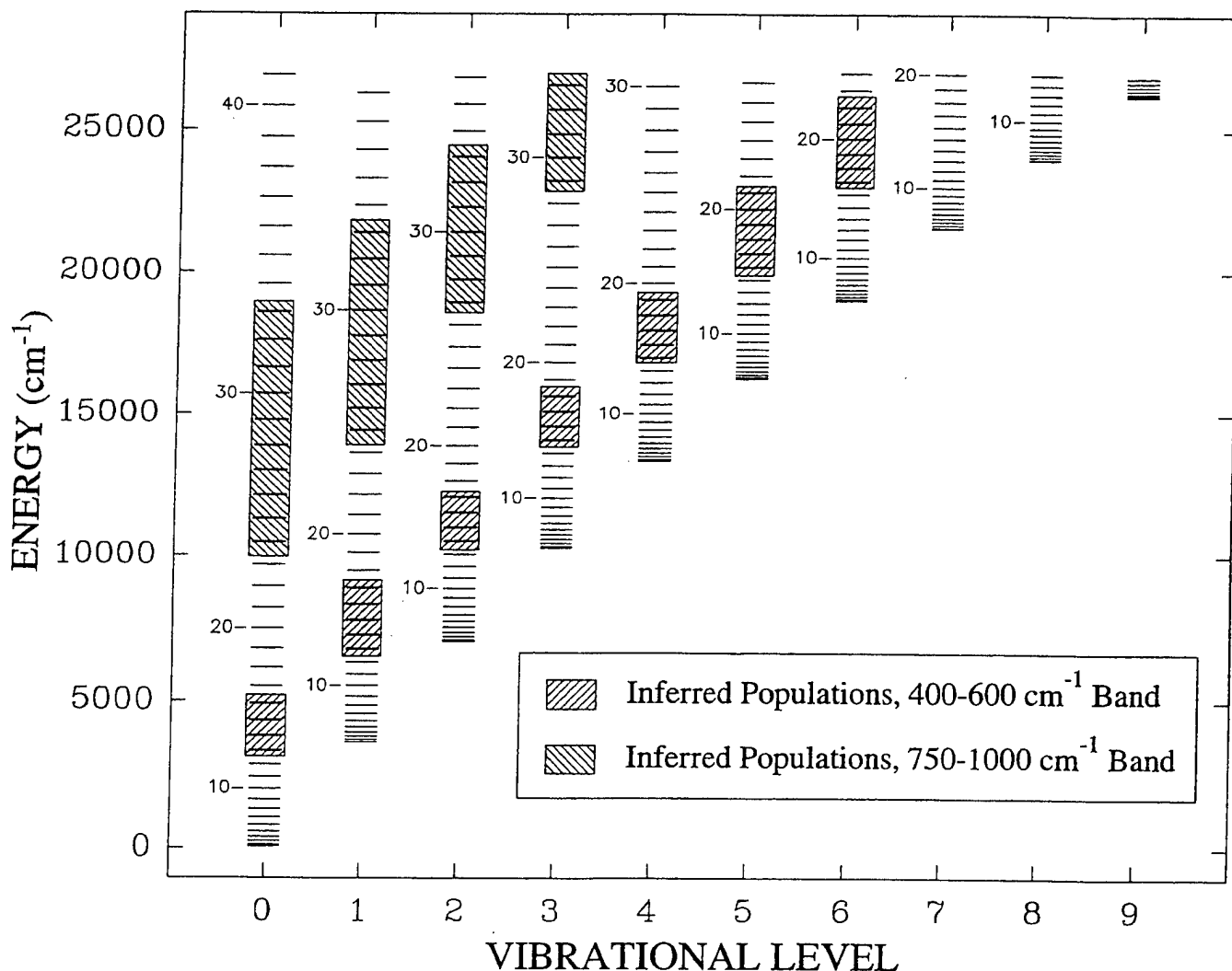


**Figure 10.** Total energy of  $OH(v, N)$  levels, for all levels with energies less than the available energy of the  $H + O_3 \rightarrow OH + O_2$  reaction, i.e., 27,000  $cm^{-1}$ . The energies of the four spin sublevels have been averaged for each  $v, N$  pair. Levels for which the populations were inferred from the pure rotation spectra are shaded. In addition, populations for  $v=1-9, N=1-4$  were inferred from the vibration-rotation spectra. No emission was observed from levels with energy greater than 27,000  $cm^{-1}$ .

superimposed on a diffuse baseline and were at first analyzed assuming that  $O_3$  gives rise to all of the observed radiance [Adler-Golden *et al.*, 1990; Adler-Golden and Smith, 1990]. These data were recently reanalyzed by Rawlins *et al.* [1993], who showed that the broad features coincide with the known positions of the OH pure rotation lines, as documented in the initial report on highly excited OH( $v, N^*$ ) from CIRIS 1A [Smith *et al.*, 1992]. The spectral data shown herein provide more substantial evidence that the ozone hot band radiance is almost featureless, even at  $1\text{ cm}^{-1}$  resolution.

The OH( $v, N^*$ ) emission intensities were also modeled in the  $750\text{--}1000\text{ cm}^{-1}$  region assuming a steady state radiative population distribution over  $N$ . Under this assumption the relative population of any two adjacent  $N$  levels is given by

$$\frac{\text{pop}_N}{\text{pop}_{N-1}} = \frac{A_{N-1}}{A_N}, \quad (2)$$

where the Einstein  $A$  coefficients are those for pure rotation emission. In equation (2) we approximate the radiative

distribution by ignoring the vibration-rotation  $A$  coefficients: for  $v=0$ , downward vibration-rotation transitions do not exist; for  $v=1$ , the fundamental ( $\Delta v=1$ ) emission rates from  $N=24\text{--}33$  are about a factor of 10 smaller than the corresponding pure rotation rates [Holtzclaw *et al.*, 1993]. We find that the OH( $N \rightarrow N-1$ ) line intensities are accurately modeled using a radiative distribution over  $N$ , implying that OH( $v, N^*$ ) formation and loss is dominated by pure rotation emission in this range of  $N$  and not by physical or chemical mechanisms. Figure 10 shows the states to which these observations apply. We will return to this discussion in the kinetic model section of the paper.

As mentioned above, the pure rotation spectra do not contain information for several  $N$  levels of interest. For instance, considering transitions for  $v=0$ , filter 6 data provide column densities for OH  $N=13\text{--}16$ , while filters 5 and 7 data provide column densities for  $N=24\text{--}33$ . Attempts were made to obtain OH column densities for  $N$  levels below, above, and between these two sets of values. For  $N \leq 12$ , the OH pure rotation lines either occur at a wavenumber lower than the nominal filter 6 passband or occur in the passband but

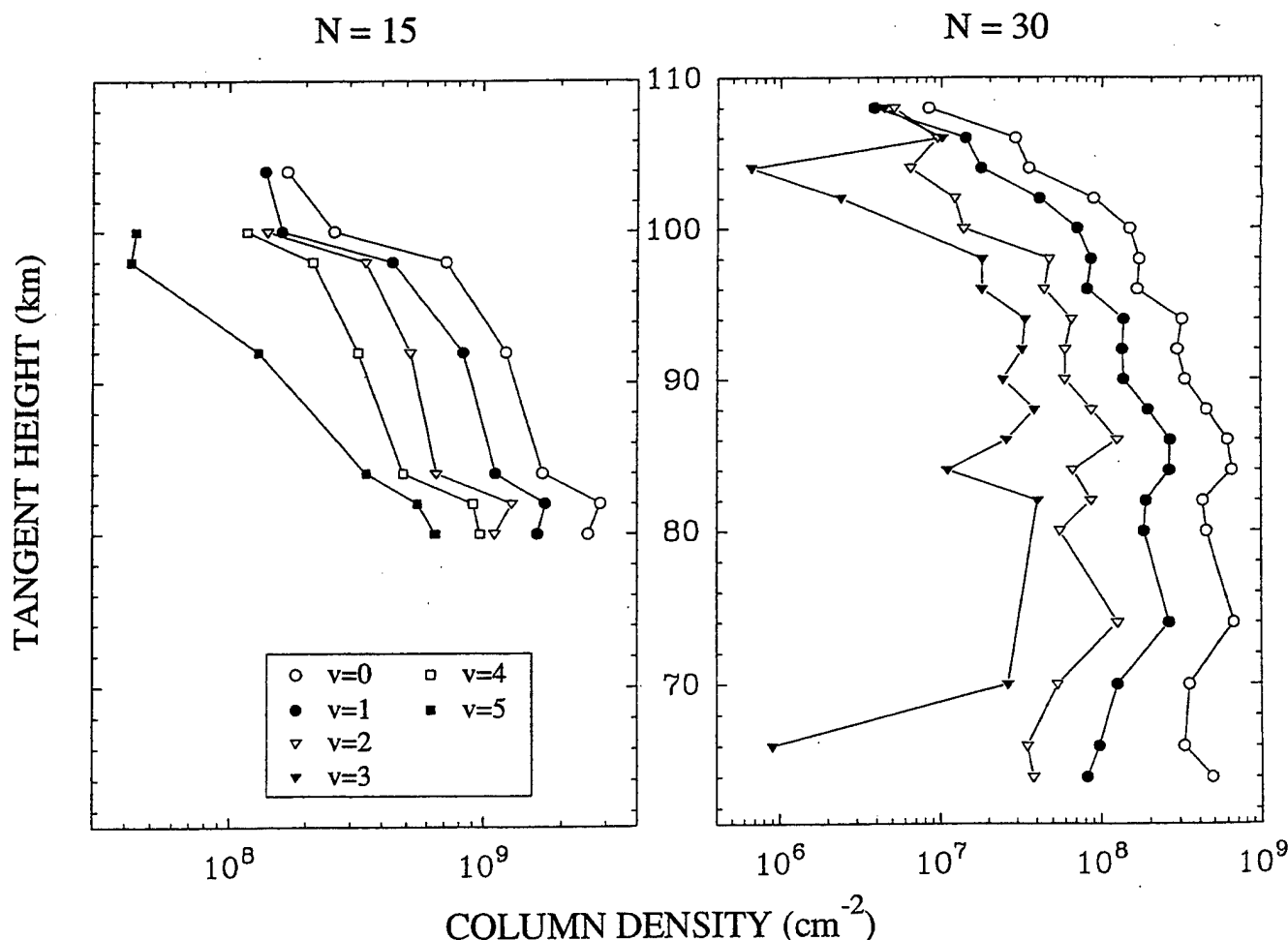


**Figure 11.** Derived OH( $v, N=15$ ) and OH( $v, N=30$ ) column densities, shown as a function of tangent height, summed over the four spin sublevels. For clarity, OH( $v=3, N=15$ ) column densities are not shown. Like the OH( $v$ ) column densities (Figure 7) the OH( $v, N=30$ ) column densities decrease below about 80 km tangent altitude, consistent with shorter pathlengths through the mesopause region. The OH pure rotation emissions could not be analyzed for tangent heights below 80 km ( $N=15$  data, from  $400\text{--}600\text{ cm}^{-1}$  passband) or 60 km ( $N=30$  data, from  $750\text{--}1000\text{ cm}^{-1}$  passband) due to intense overlying radiance from other emitters.

are too weak to observe. For  $N \geq 34$ , the lines are not seen owing to the intense  $O_3(v_3)$  feature ( $990\text{--}1070\text{ cm}^{-1}$ ). No OH pure rotation lines are observed for wavenumber values in the range  $1070\text{--}1250\text{ cm}^{-1}$ , i.e., at higher wavenumber values than the  $O_3(v_3)$  band. Finally, open filter (filter 0) spectra were studied to look for evidence of OH pure rotation lines for  $17 \leq N \leq 23$ . No further lines in addition to those already observed in filters 5, 6, and 7 data were identified, due to the intense  $CO_2(v_2)$  feature extending from  $600$  to  $750\text{ cm}^{-1}$ . The noise level was also significantly greater in the open filter case than when the  $CO_2(v_2)$  band is attenuated; for instance, the  $OH(v, N^*)$  pure rotation lines in the  $400\text{--}600\text{ cm}^{-1}$  band are below the noise level when open filter data are used.

Figure 11 shows  $N=15$  and  $N=30$  column densities for various  $v$  levels, derived from the  $400\text{--}600\text{ cm}^{-1}$  and  $750\text{--}1000\text{ cm}^{-1}$  passband data, respectively. Like the  $OH(v \rightarrow v-1)$  fundamental bands, OH pure rotation lines are observed for tangent heights significantly below the airglow layer. In the  $750\text{--}1000\text{ cm}^{-1}$  region,  $OH(N \rightarrow N-1)$  emissions

are visible for tangent heights as low as  $50\text{ km}$ . Below about  $80\text{ km}$  the lines are diminished in intensity, consistent with shorter pathlengths through the airglow layer. With decreasing tangent height, neighboring emitters (notably, the  $O_3(v_3)$  band as well as the  $CO_2 v_1+v_2-2v_2$  band at  $791\text{ cm}^{-1}$ ) become increasingly intense, eventually obscuring the OH emissions. In the  $400\text{--}600\text{ cm}^{-1}$  region,  $H_2O$  emissions quickly become very intense, obscuring OH emission lines below  $80\text{ km}$ .

**Column density binning.** For the purposes of the kinetic model,  $OH(v, N)$  column densities derived from the experiment were averaged over  $2\text{-km}$  vertical bins, for tangent heights between  $20\text{ km}$  and  $108\text{ km}$ . Most of the column density data lie in the  $75$  to  $110\text{-km}$  region (Figures 7 and 11), although the lower tangent height data provide an additional constraint on the kinetic model, described below. In the averaging process, column densities were weighted by the reciprocal variance determined from the corresponding spectral fit. For the uppermost tangent heights the  $OH(v, N)$  radiance is detected only in the lower part of the field of

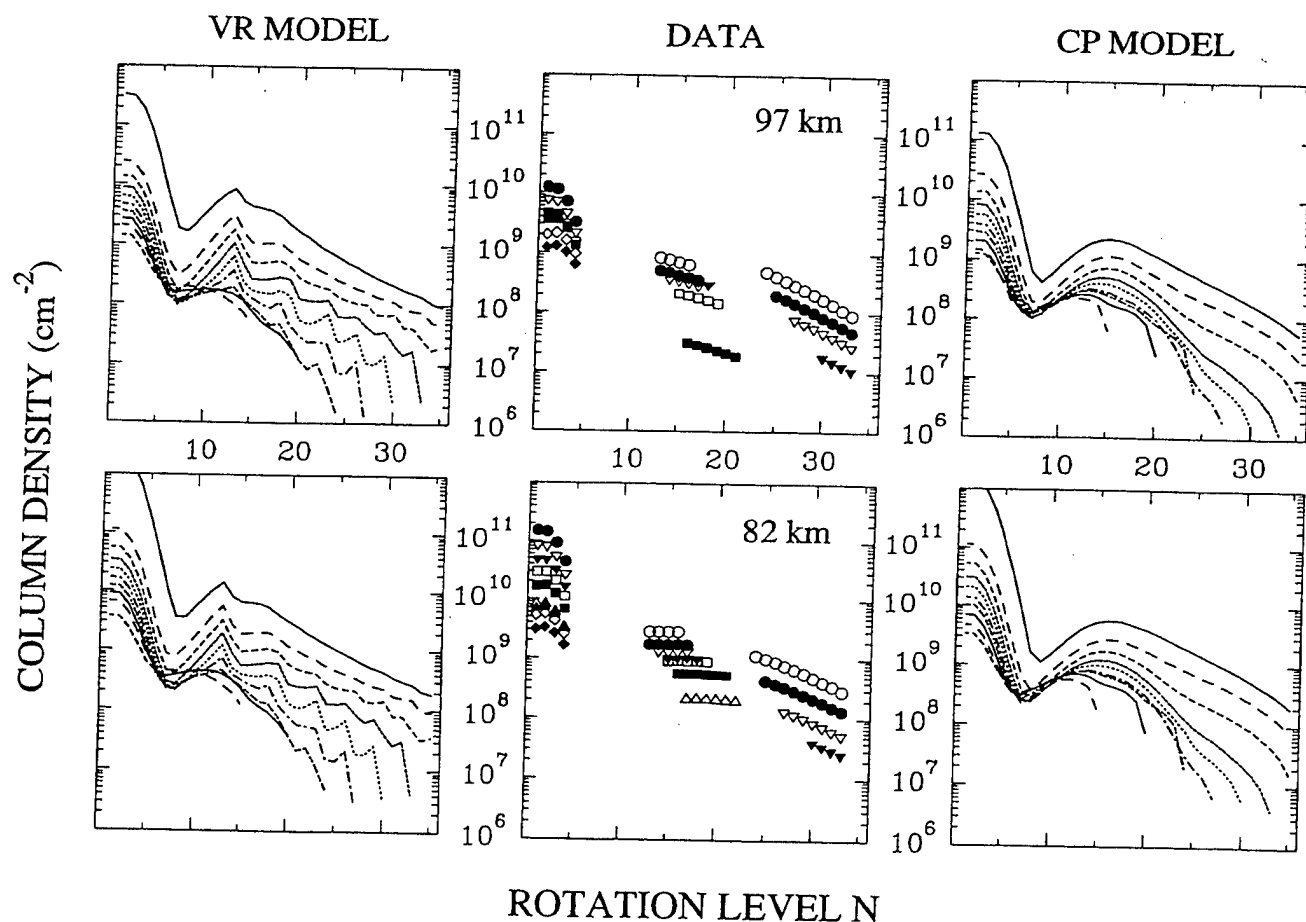


**Figure 12.**  $OH(v, N)$  column densities for two different tangent heights:  $97\text{ km}$  for the top plots, and  $82\text{ km}$  for the bottom plots. Column densities derived from the spectral data are shown in the center plots, for  $v=1\text{--}9$  in the low- $N$  range,  $v=0\text{--}6$  in the mid- $N$  range, and  $v=0\text{--}3$  in the high- $N$  range. Some of the column densities have been omitted from the  $97\text{-km}$  data for clarity. Symbols used: circles,  $v=0$  (open),  $v=1$  (solid); downward pointing triangles,  $v=2$  (open),  $v=3$  (solid); squares,  $v=4$  (open),  $v=5$  (solid); upward pointing triangles,  $v=6$  (open),  $v=7$  (solid); diamonds,  $v=8$  (open),  $v=9$  (solid). The best fit VR model is shown on the left-hand side, and the best fit CP model on the right-hand side, both for  $v=0\text{--}9$ .  $OH(v, N)$  model column densities are differentiated by line type according to vibrational level. For both models the low- $N$  column densities decrease monotonically as the vibrational level increases from  $v=0$  to  $v=9$ .

view. A description of the populations determined in the fits, for all  $v$  and  $N$ , is shown in Figure 12 for tangent height ranges centered at 82 km and 97 km. For a given  $v$  level, the ratio of the low- $N$  to the high- $N$  populations is 100-1000 at 82 km but only 10-100 at 97 km, indicating a greater degree of rotational excitation (relative to the low- $N$  populations) at the higher altitudes.

**OH spin sublevels.** As discussed in the Appendix, angular momentum coupling among the molecular rotation, electron spin, and electron orbital angular momentum vectors gives rise to a quadruplet line structure for each  $\text{OH}(v,N)$  vibration-rotation or pure rotation transition. For the low- $N$  vibration-rotation transitions, the  $F_1$  and  $F_2$  transitions are widely separated in wavenumber, but the splitting due to  $\Lambda$  doubling is small (a few hundredths of a wavenumber) and cannot be resolved in the instrument-broadened data. Thus assuming the Einstein  $A$  coefficients for each pair of  $\Lambda$ -doublet transitions are nearly equal, the vibration-rotation bands do not contain any information concerning the relative populations of the  $e$  and  $f$  parity states. Spectral fits show that the spin-orbit states  $\Pi_{3/2}$  and  $\Pi_{1/2}$  are in equilibrium at the kinetic temperature of the mesopause for low  $N$ .

In the case of the high- $N$  levels probed by the pure rotation bands, the spin-rotation and  $\Lambda$ -doublet energy level splittings are of comparable magnitude, i.e., about  $20 \text{ cm}^{-1}$ . The energy levels and dipole-allowed pure rotation transitions are shown in Figure 13 for the  $(v=0, N=26 \rightarrow N=25)$  transition. Under the dipole selection rules,

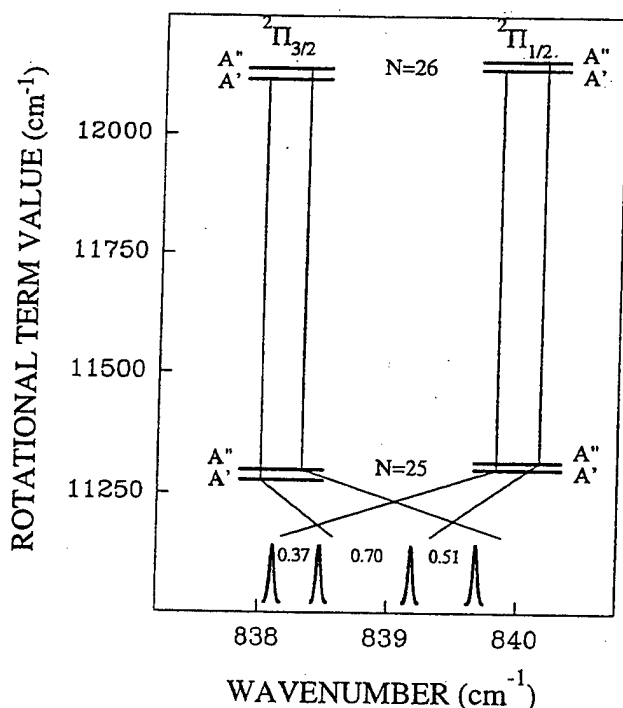


**Figure 13.** Diagram of the four allowed spin sublevel transitions comprising the  $\text{OH}(v=0, N=26 \rightarrow N=25)$  pure rotation transition. The wavenumber positions of the four transition lines are indicated at the bottom of the plot. The lines are resolved only as doublets under the CIRIS 1A experimental resolution.

pure rotation transitions connecting different spin-rotation ( $F_1$  and  $F_2$ ) or electronic parity ( $A'$  and  $A''$ ) states are forbidden. Thus to the extent that the lifetimes for the  $\text{OH}(v,N^*)$  levels are limited by pure rotation emission (or that  $v$ - and  $N$ -changing collisions are ineffective in mixing the components), the relative spin sublevel populations are preserved during the radiative cascade downward in  $N$ . This phenomenon in turn preserves the memory of any sublevel selective formation or decay mechanisms, whether of physical or chemical nature.

Holtzclaw *et al.* [1993] have shown that the  $P$ - and  $R$ -branch ( $\Delta N = \pm 1$ ) fundamental band emission rates can be significant relative to the high- $N$  pure rotation rates. For  $\text{OH}(v=1-3, N \geq 15)$ , the pure rotation transitions are 1-10 times faster than the fundamental transitions from the same upper state, with the fundamental transitions more important for  $v=3$  and the lower range of  $N$ . However, the  $P$ - and  $R$ -branch vibration-rotation transitions, like the pure rotation transitions, preserve the spin-sublevel identities of the initial and final states. The  $Q$ -branch ( $\Delta N = 0$ ) transitions, which connect the  $A'$  and  $A''$  parity states, have negligible rates for high  $N$ .

The pure rotation rates are also faster than computed collisional relaxation rates in the 80 to 110-km altitude range. Figure 14 compares the pure rotation and the collision-induced rotational relaxation rates for two different altitudes, the latter values calculated from the kinetic model, described below. Conceivably, every collision could serve to populate each of the four spin sublevels of a given  $\text{OH}(v,N)$  state with equal probability. Limited data are available on this phenomenon in OH. Copeland and Crosley [1984] found that the collisional transfer rate between  $\Lambda$  components is approximately  $1/3$  to  $1/2$  of the total rate for collisions between  $\text{OH}(\Pi_{3/2}, J=3/2-7/2)$  and  $\text{H}_2\text{O}$ . For higher values of the rotational quantum number, however, Sears *et al.* [1989] estimated a 10:1 propensity to preserve the  $\Lambda$ -doublet identity during rotational relaxation of  $\text{OD}(v=0, N=37-40)$  in a 10:1  $\text{D}_2/\text{O}_3$  mixture. The  $\Lambda$ -doublet energy level separation for those  $N$  values in OD is 13-14  $\text{cm}^{-1}$ , approximately equal to the separation for  $N=20$  in OH. Figure 14 shows that collisional scrambling will most effectively compete with radiative cascade for the lowest  $N^*$  levels and at the lowest altitudes.

As discussed previously [Dodd *et al.*, 1993a], the instrumental resolution is not quite adequate to resolve the quadruplet structure of the  $\text{OH}(v,N^*)$  pure rotation transitions. Instead, the transitions are seen as triplets in the 400-600  $\text{cm}^{-1}$  region and doublets in the 750-1000  $\text{cm}^{-1}$  region. To determine four independent sublevel populations, it was assumed that sublevel population ratios are preserved as the OH population radiatively cascades, over all of the  $N$  levels inferred from spectra in the two pure rotation passbands. Pure rotation spectra from the two passbands could then be spectrally fit together to determine a set of spin sublevel populations, in effect determining four population values from a set of five intensities. This procedure is partially justified by two observations discussed by Dodd *et al.* [1993a], i.e., that within each passband the spin sublevel intensity ratios are independent of  $N$  and that for a given value of  $N$  the effective temperature for the spin sublevel population distribution is vastly different from the kinetic temperature of the mesopause (200 K).

Spectral fits to determine spin sublevel populations

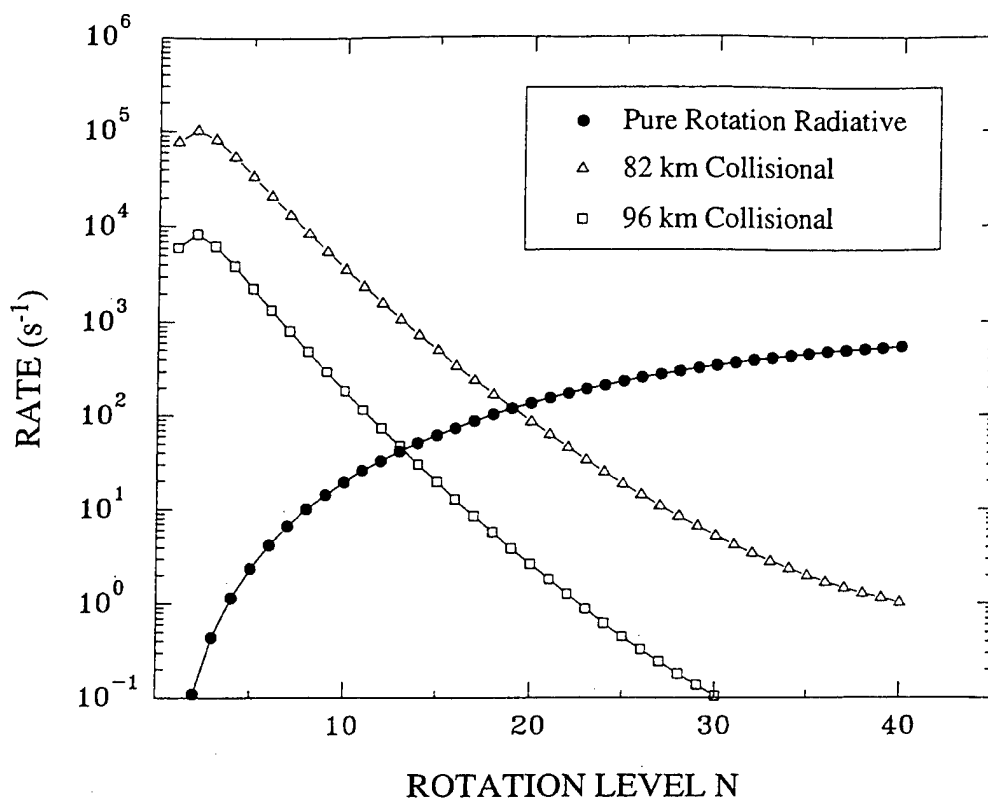


**Figure 14.** Pure rotation radiative rates for  $\text{OH}(N \rightarrow N-1)$  as a function of  $N$ , for the  $v=0$  manifold. Also shown are the model collision-induced rotational relaxation rates, calculated as the product of  $k_{\text{ROT}}(N)$  (equation (12)) and the total number density at 82-km and 96-km altitudes, respectively. Collisional relaxation dominates  $\text{OH}(N)$  loss for low  $N$ , while radiative decay dominates the loss for high  $N$ .

utilized the global fit method, developed earlier in an analysis of laboratory OH emission data [Dodd *et al.*, 1991]. Using this method, numerous scans were fit simultaneously to a total of  $5 + 10 \times n_6 + 7 \times n_5$  parameters, where  $n_6$  and  $n_5$  are the number of scans in the filter 6 and filter 5 regions, respectively, included in the fit. (Filter 7 data could not be used in the sublevel population determination due to the large ringing in unapodized spectra.) The five "global" parameters are the FWHM parameter  $w$ , the line shift parameter  $s$ , and three spin sublevel population ratios, all of which are taken to be constant over all of the scans. (The absolute scaling of the sublevel intensities is determined by the  $v$  multipliers.) The 10 "local" parameters for filter 6 are  $1/T$  and multipliers for the two  $\text{H}_2\text{O}$  and seven OH vibrational level ( $v=0-6$ ) basis functions. The seven parameters for filter 5 are  $1/T$  and multipliers for the two ozone hot band and four OH vibrational level ( $v=0-3$ ) basis functions. Aside from  $w$  and  $s$  the local parameters are identical to those used in the scan-by-scan fits to the spectra, described above. Uncertainties in the spectral data were estimated from out-of-band noise levels and scaled as the inverse of the spectral response function. A simultaneous fit to spectra from both passbands yields model spectra in excellent agreement with the data [Dodd *et al.*, 1993a], despite the redundancy in the spin sublevel intensities (five) relative to the population multipliers (four).

As a further check on the validity of the assumption concerning sublevel population preservation, pure rotation data were fit separately in five different tangent height bins, as shown in Figure 15. For the three tangent height bins

located at 90 km and above, the best fit populations do not vary outside their respective (statistical) error bars. On the other hand, for the two tangent height bins below 90 km the  $A'$  populations change significantly. We interpret this result to indicate that the spin sublevel populations are affected by collisional scrambling in the lower tangent height bins. Thus all of the spectral data above 90 km were refit together, yielding the spin sublevel distribution  $\Pi_1(A') : \Pi_1(A'') : \Pi_2(A') : \Pi_2(A'') = 33 : 18 : 31 : 18$  reported previously [Dodd *et al.*, 1993a]. The filter 6 and filter 5 spectral data were also fit separately for tangent heights above 90 km to determine spin sublevel population distributions, assuming only that the relative populations are constant within each separate range of  $N$ . For the filter 6 region the distribution  $[\Pi_1(A') + \Pi_2(A'')] : \Pi_2(A') : \Pi_1(A'')$  equals  $52 : 29 : 19$ , while for the filter 5 region the distribution  $[\Pi_1(A') + \Pi_2(A')] : [\Pi_1(A'') + \Pi_2(A'')]$  equals  $64 : 36$ .

The effects of  $L$  uncoupling could conceivably result in a significant difference between the  $\Lambda$ -doublet transition probabilities for a given upper state level  $\text{OH}(v, N, F)$ .  $L$  uncoupling results from a small amount of mixing of the  $\text{OH}(A^2\Sigma^+)$  wave function into the  $\text{OH}(X^2\Pi)$  wave function. Holstclaw *et al.* [1993], following Mies [1974], have estimated the perturbative effect of wave function mixing on the  $A$  coefficients of the OH vibration-rotation bands. They estimate the effect as of the order of  $\leq 10\%$  for  $\text{OH}(N \leq 40)$   $P$ - and  $R$ -branch transition dipole moments, with the magnitude of the perturbation scaling roughly as  $N$ . Transition dipole moments for pure rotation transitions, however, are governed

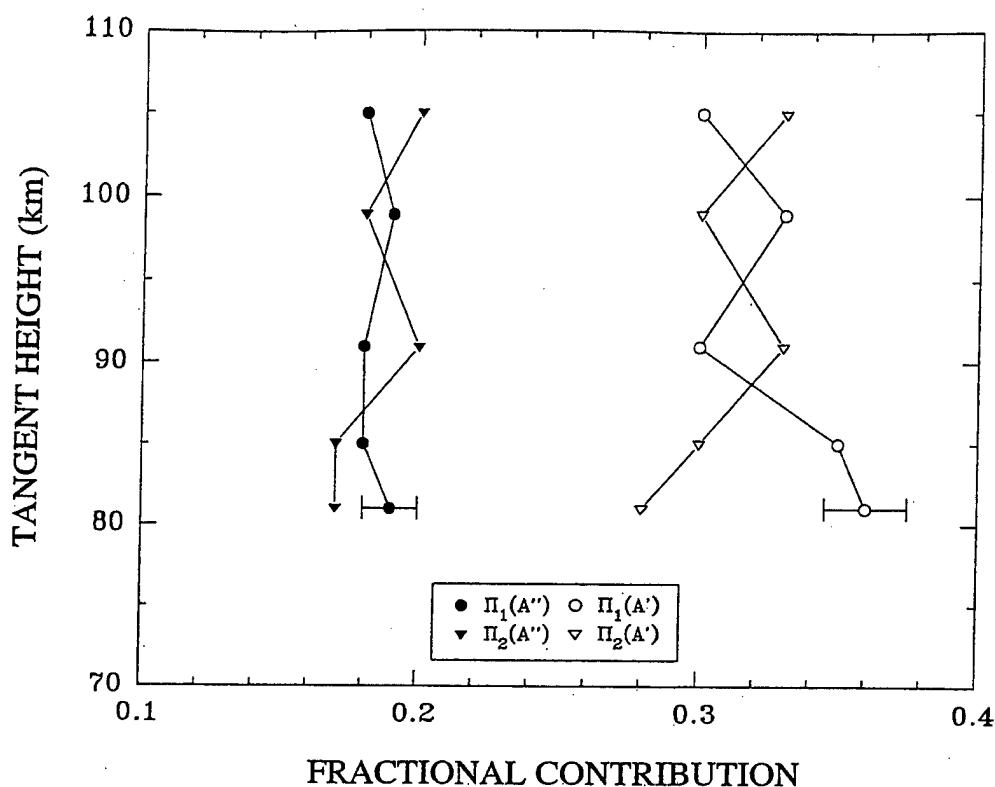


Figure 15. Best fit relative populations of the  $\Pi_1(A')$ ,  $\Pi_2(A')$ ,  $\Pi_1(A'')$ , and  $\Pi_2(A'')$  spin sublevels. Best fit populations were determined by fitting pure rotation spectra from filters 5 and 6, grouped into five different tangent height bins. Typical  $2\sigma$  statistical error bars are shown for one tangent height bin.

mainly by the large permanent dipole moment  $\mu(r_e) = 1.7$  D. This value is at least an order of magnitude greater than the corresponding vibration-rotation transition moments. Thus the perturbation introduces uncertainty of the order of  $\leq 1\%$  in the OH pure rotation transition dipole moments (or  $\leq 2\%$  in the A coefficients) and is ignored in the present analysis.

### Origin of OH( $v, N$ ) Populations

As the next step in the analysis of the OH( $v, N$ ) emissions, we consider possible chemical and physical sources of the OH( $v, N$ ), especially the novel highly rotationally excited element of the population. First, it is conceivable that the OH high- $N$  levels are populated via radiative cascade from nascently produced vibration-rotation levels. A number of workers have measured the OH nascent vibrational distribution from  $H + O_3 \rightarrow OH(v) + O_2$  in cells [Charters *et al.*, 1971; Streit and Johnston, 1976; Klenerman and Smith, 1987] and in a molecular beam apparatus [Ohoyama *et al.*, 1985]. As discussed by Dodd *et al.* [1991], these experimental measurements of the branching fractions  $\chi_v$  suggest that the  $H + O_3$  reaction feeds OH( $v \geq 6$ ) exclusively. Assuming that to be the case, OH( $v=6, N=24$ ) is the highest nascent rotational level, given the reaction exothermicity of  $27,000 \text{ cm}^{-1}$  (see Figure 10). The  $\Delta N=0, \pm 1$  selection rule for dipole-allowed transitions places constraints on the levels accessible through radiative cascade. The highest  $N$  levels that can be produced via radiative cascade from the OH( $6, 24$ ) state are  $N = 30, 29$ , and  $28$  for  $v = 0, 1$ , and  $2$ , respectively. Nevertheless, significant emissions are observed in the spectral data for levels up to  $N=33$  for  $v=0-2$ .

The radiative feed mechanism cannot account for these emissions.

Three further possible sources of the highly rotationally excited OH( $v, N$ ) have been mentioned [Smith *et al.*, 1992]: first, excitation of thermal OH( $v=0$ ) by translationally excited oxygen atoms ( $O_{\text{fast}}$ ); second, direct chemical production through the  $H+O_3$  reaction; and third, collision-induced transfer of vibrational to rotational energy (VR transfer) from nascent OH high- $v$  states. We consider the first mechanism, upumping of OH( $0$ ) by ambient  $O_{\text{fast}}$ , unlikely. The OH( $v, N^*$ ) radiance is observed to decrease by about a factor of 10 on progressing from nighttime to daytime conditions [Dodd *et al.*, 1993a], commensurate with current model predictions for the diurnal variation of the thermal OH concentration [Makhlouf *et al.*, 1990]. On the other hand, the chemical reactions which give rise to  $O_{\text{fast}}$  in the mesopause region, such as  $O_3$  solar photodissociation, as well as dissociative recombination of  $NO^+$  and  $O_2^+$  with electrons, are many orders of magnitude faster during daylight hours [Philbrick, 1985]. Thus assuming that the rate of thermalization of  $O_{\text{fast}}$  is independent of local time, the steady state  $O_{\text{fast}}$  concentration is predicted to be much higher during the daytime. These estimates of the daytime concentrations of  $O_{\text{fast}}$  and OH are inconsistent with OH( $v, N^*$ ) production by  $O_{\text{fast}}$  pumping of thermal OH.

Published studies of the  $H + O_3$  reaction do not rule out direct chemical production of high- $N$  OH. To our knowledge, all of these studies made use of overtone ( $\Delta v \geq 2$ ) emission spectra for detection of the nascent OH( $v, N$ ) levels [Charters *et al.*, 1971; Streit and Johnston, 1976; Ohoyama *et al.*, 1985; Klenerman and Smith, 1987]. However, due to



relatively small Einstein  $A$  factors [Holtzclaw *et al.*, 1993], the OH overtones are insensitive to the presence of a small amount of population in high- $N$  levels. Moreover, two of the groups [Streit and Johnston, 1976; Ohoyama *et al.*, 1985] used  $\Delta v \geq 4$  multiquantum transitions to probe the OH emissions, precluding detection of OH( $v < 4$ ). Another group [Kleerner and Smith, 1987] does not state whether emissions from OH( $v < 6$ ) were observed. Polanyi and Sloan [1975] have shown that the  $H + O_3$  reaction produces OH( $v=7-9$ )  $F_1$  and  $F_2$  spin sublevels in a statistical population ratio, i.e.,  $N+1$  to  $N$ . This ratio is near unity for high  $N$ , consistent with the spin sublevel distribution derived for low  $v$  from the CIRIS pure rotation spectra.

The resonant VR energy transfer mechanism has much precedent in the literature. The VR mechanism has been invoked to explain pure rotational lasing from highly excited rotational levels of OH [Smith and Robinson, 1978] and HF [Sirkin and Pimentel, 1981]. In their experiment, Sirkin and Pimentel [1981] observed particularly strong laser oscillation from the  $J=14$  rotational level of HF( $v=0-3$ ), which is nearly resonant with several low- $J$  levels of the next higher vibrational level (see Figure 10; HF and OH have similar vibrational and rotational energy level spacings). Lasing from  $J$  values as high as 31 in  $v=0$  and 1 was also observed, suggesting multiquantum resonant VR transfer from low- $J$  levels of  $v=4-6$ . The kinetic model employed by Sirkin and Pimentel required substantial changes in the HF vibrational and rotational levels ( $\Delta v$  as large as 5,  $\Delta J$  as large as 26) upon collision with buffer gas molecules. More recent measurements of HF( $v=1$ ) relaxation by HF [Haugen *et al.*, 1984] have further substantiated the resonant VR transfer mechanism. Those researchers estimated that 20-40% of the molecules relax through the  $v=0$ ,  $J=10-14$  set of levels, which are closely resonant with  $v=1$ , low  $J$ . Moreover, quasi-classical trajectory studies at higher energies ( $\geq 0.2$  eV) [Thompson, 1982a, b] demonstrated that collisional relaxation of OH( $v, J$ ) by Ar is governed by resonant VR transfer. While resonant VR energy transfer is known from laboratory experiments and from calculations, we know of no case where the mechanism has been shown to be operative in the Earth's atmosphere.

Clearly, neither the direct chemical production mechanism nor the resonant VR transfer mechanism can be dismissed based on prior knowledge. Thus both mechanisms were investigated in detail using a first-principles kinetic code to predict OH( $v, N$ ) distributions as a function of tangent height. These studies are discussed below.

### Kinetic Model

We have formulated an OH( $v, N$ ) state-specific kinetic model using the minimum number of OH formation and quenching pathways consistent with current understanding of mesopause conditions and pertinent OH reaction and energy transfer rate constants. Predictions made by any viable scheme must be consistent with observation, including the energies of the inferred OH( $v, N^*$ ) (as high as 23,000  $\text{cm}^{-1}$ ), the  $v$  and  $N$  distribution, and the tangent height dependence of the populations. We consider a detailed investigation into sublevel-dependent production and loss rates, as well as the collisional coupling of the four sublevel states, beyond the scope of the current model. In the following we discuss the elements of the model, which include the following in order:

methods of computation and comparison with data, the hydroxyl quantum energy level description, the model atmosphere, OH chemical production and loss, pure rotation and vibration-rotation radiative decay, and collisional (i.e., nonreactive) deactivation.

### Line-of-sight Column Density Predictions

OH( $v, N$ ) number densities were calculated by successively integrating the appropriate kinetic equations until negligible changes occurred in the calculated steady state number densities for all OH( $v, N$ ). The Gear backward differentiation algorithm was used to integrate the coupled set of "stiff" equations [Hindmarsh, 1980]. Stiff sets of equations occur for processes occurring under very different timescales. The equations were derived from the kinetic processes described in detail below. Number densities were calculated for altitudes between 78 km and 106 km, in 2-km bins; below and above these limits the OH( $v, N$ ) populations were negligible.

Limb line-of-sight column densities from field experiments can often be inverted to yield altitude-dependent number densities for comparison with models. In this study we have instead chosen to model the hydroxyl column density data directly, generating forward predicting column densities from model number densities using the following procedure. Calculated OH( $v, N$ ) number densities were multiplied by pathlengths determined from the shell size (2 km) and line of sight viewing angle, for each of several paths within the detector 2 vertical field of view (shown in Figure 16). The derived column densities were then averaged over the field of view using the known sensitivity profile of the detector.

Two main variations of the kinetic model, as described below, were used to generate a set of OH( $v, N$ ) column density predictions. Several elements of the model, including the altitude-dependent species concentrations and kinetic temperature, OH chemical production and loss rates, and OH( $v, N$ ) rotation-vibration and pure rotation radiative decay rates, were taken without adjustment from the literature. However, several kinetic parameters describing collisional relaxation are poorly known and thus were varied to determine their effects on column density predictions as well as the sensitivity of the predictions to their variation. To facilitate comparisons between the model and the data for all OH( $v, N$ ) at each tangent height, the kinetic model was automated, such that the poorly determined parameters were allowed to vary freely. For a given set of model constraints the best fit kinetic parameters were determined by minimizing  $\chi^2$ , defined as

$$\chi^2 = \sum_i \left[ \frac{\log(D_i / M_i)}{\sigma_i / D_i} \right]^2, \quad i = (v, N), \quad (3)$$

where  $D_i$  and  $M_i$  are the data and model column densities, respectively, for OH vibration-rotation state  $i$  at a given tangent height, and the  $\sigma_i$  are the corresponding uncertainties. The use of logarithms was required to correctly weight the data points, given the orders-of-magnitude dynamic range of the column densities. The  $\sigma_i$  are defined as

$$\sigma_i^2 = \sigma_{\text{DATA},i}^2 + \sigma_{\text{MODEL}}^2, \quad (4)$$

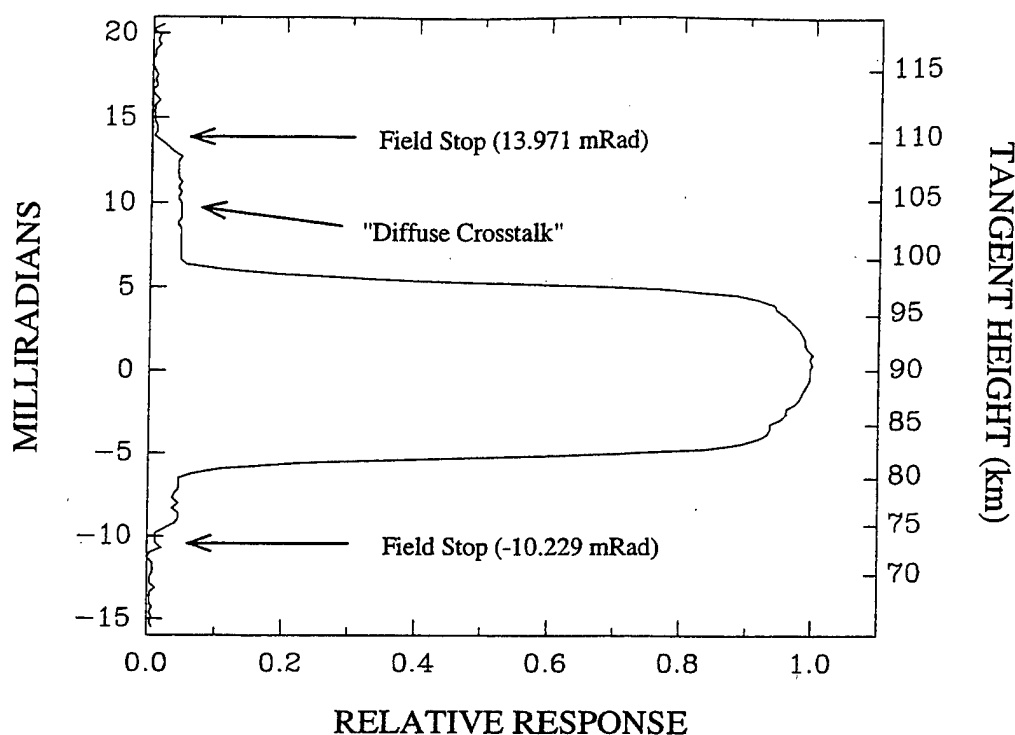


**Figure 16.** Relative response for the detector 2 field of view (FOV) in the vertical dimension, plotted against milliradian offset from the center of the FOV. The right-hand y axis shows the corresponding tangent heights, assuming that the FOV is centered at 90 km. The field stops are also indicated. The "diffuse cross-talk" response plateau results from nonnegligible signal from photons impinging outside the nominal FOV. This cross-talk is taken into account in the kinetic modeling of  $\text{OH}(v,N)$  column densities.

where the  $\sigma_{\text{DATA},i}$  are the uncertainties in the derived  $\text{OH}(v,N)$  column densities and  $\sigma_{\text{MODEL}}$  is an estimate of the uncertainty in the model column density predictions. The quantity  $\sigma_{\text{MODEL}}$  results from uncertainty in the kinetic model input parameters, e.g., the altitude-dependent number densities and reaction rate constants, and is estimated to be 30% of the corresponding  $\text{OH}(v,N)$  column density. This additional uncertainty is added independently of the value of  $\sigma_{\text{DATA},i}$ . Typical values for  $\sigma_{\text{DATA},i}$  range from 5% of the column density  $D_i$  for low- $N$  populations derived from the fundamental spectra (filters 1 and 2) to 50% of  $D_i$  for high- $N$  populations derived from the 400–600  $\text{cm}^{-1}$  pure rotation band (filter 6).

#### **$\text{OH}(v,N)$ Energy Levels**

Our conventions concerning the labeling of ground electronic state hydroxyl energy levels are discussed in the Appendix. The manifold of  $\text{OH}$  vibration-rotation levels as a function of total energy is shown in Figure 10 [Coxon and Foster, 1982; Goldman *et al.*, 1983]. In the figure, all of the levels with total energy less than the exothermicity of the reaction  $\text{H} + \text{O}_3 \rightarrow \text{OH}(v,N) + \text{O}_2$ , i.e., 27,000  $\text{cm}^{-1}$ , are shown. Thus all of the levels shown are energetically accessible by that reaction. For each  $\text{OH}(v,N)$  energy level the energies of the four spin sublevels have been averaged. For simplicity, in the kinetic model the sublevels have also been consolidated into a single effective state for each  $v,N$  combination, with the mean energy and degeneracy  $(2N+1)$  of the four sublevels.

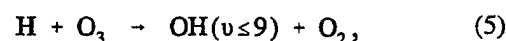
#### **Model Atmosphere**

Altitude-dependent kinetic temperatures and number densities for  $\text{N}_2$ ,  $\text{O}_2$ ,  $\text{O}$ , and  $\text{H}$  were generated using MSISE-90 [Hedin, 1991], using the appropriate calendar date, local midnight, and a latitude of 40° S. The chosen latitude and local time were assumed to adequately represent the ranges of the latitudes and solar zenith angles in the data set. As seen in Figure 1, most of the data were obtained between -30° and -50° latitude. Nighttime data were used with solar zenith angles between 110° and 160° (Figure 2).

The MSISE-90 atmosphere model does not include  $\text{O}_3$  number densities. Thus an ozone number density profile was generated from the MSISE-90 kinetic temperature and  $\text{N}_2$ ,  $\text{O}_2$ ,  $\text{O}$ , and  $\text{H}$  profiles, assuming that the nighttime  $\text{O}_3$  production and destruction mechanisms are given by  $\text{O} + \text{O}_2 + \text{M} \rightarrow \text{O}_3 + \text{M}$  and  $\text{H} + \text{O}_3 \rightarrow \text{OH} + \text{O}_2$ , respectively, for altitudes near the  $\text{OH}$  airglow layer. Temperature-dependent rate constants for the two processes were taken from DeMore *et al.* [1990]. The resultant  $\text{O}_3$  profile, along with the temperature and species profiles taken directly from MSISE-90, is shown in Figure 17.

#### **$\text{OH}$ Chemical Production and Loss**

The sole production term for hydroxyl was taken to be



with the nascent vibrational distribution  $v=9 : v=8 : v=7 : v=6$  equal to 1 : 0.55 : 0.35 : 0.17, as

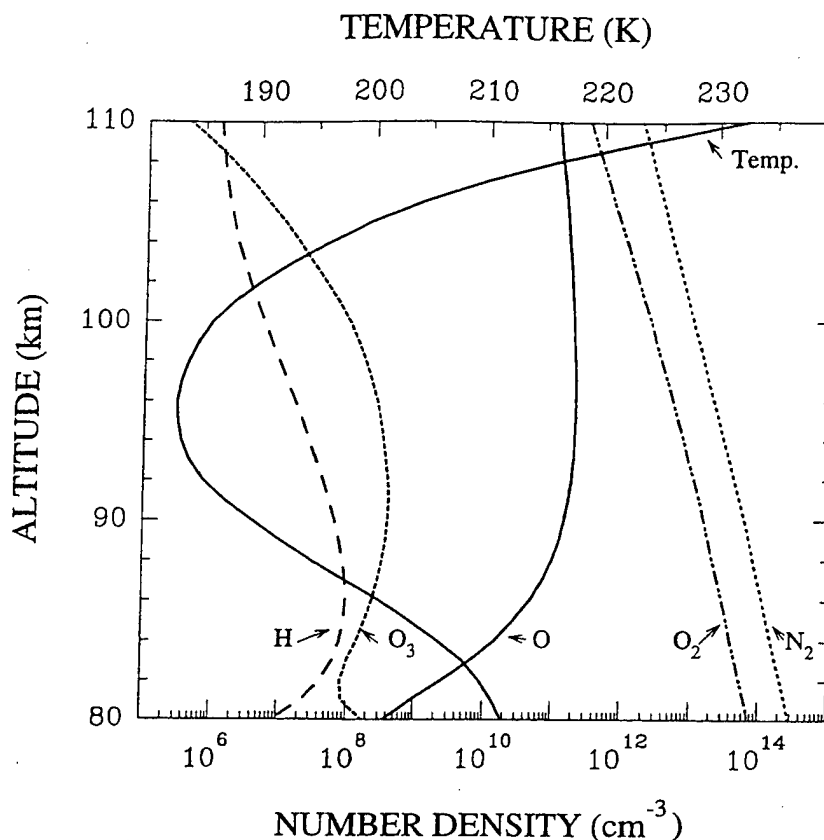
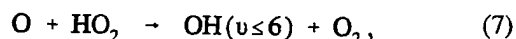


**Figure 17.** Kinetic temperature and species altitude profiles used in the kinetic model. Altitude profiles for  $N_2$ ,  $O_2$ ,  $O$ ,  $H$ , and temperature were taken from the MSISE-90 atmosphere model [Hedin, 1991]; the  $O_3$  profile was determined from the other profiles, as explained in the text. Assumed conditions: April 30, midnight local time,  $40^\circ$  S latitude.

measured recently by Kleernerman and Smith [1987]. The overall rate constant for reaction (5) was assumed to have the temperature dependence [DeMore et al., 1990] given by

$$k_5 = 1.4 \times 10^{-10} e^{-\frac{470}{T(K)}} \text{ cm}^3 \text{ s}^{-1}. \quad (6)$$

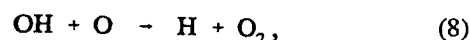
The  $N$  distribution for the nascent product of  $H + O_3$  was parameterized through the use of a Boltzmann distribution, with the  $v$ -dependent effective temperatures equal to 760 K, 1230 K, and 1940 K for  $v=9$ , 8, and 7, respectively [Llewellyn and Long, 1978]. The effective temperature for  $v=6$  was taken to be equal to 2600 K by extrapolation. Another reaction,



has been discussed as a possible source of chemiluminescent  $OH(v)$  at the mesopause [Kaye, 1988; Sivjee and Hamwey, 1987; McDade and Llewellyn, 1987]. However, it has not been established that reaction (7) plays a significant role in the nighttime airglow. Lack of knowledge concerning the radiational and collisional quenching of nascently formed  $OH(v)$  has hindered resolution of this question. Nevertheless, reasonable choices can be made for the quenching rates which obviate the need for a secondary source of  $OH(v)$  via reaction (7) [McDade and Llewellyn, 1987]. In addition, about half of the observed  $OH$  high- $N$

lines arise from molecules containing more internal energy than is available to the products of reaction (7). Because of these considerations we exclude reaction (7) from the source term.

Chemical destruction of  $OH$  was assumed to be dominated by reaction with  $O$  atoms, namely



with the temperature-dependent rate constant [DeMore et al., 1990] given by

$$k_8 = 2.2 \times 10^{-11} e^{-\frac{120}{T(K)}} \text{ cm}^3 \text{ s}^{-1}. \quad (9)$$

The model  $O$  atom densities in the 80 to 110-km range, when multiplied by the rate constant  $k_8$ , yield an  $OH$  chemical destruction rate of the order of  $10 \text{ s}^{-1}$ . This rate limits the lifetimes of the longest-lived  $OH(v, N)$  levels, i.e., the low- $N$  and low- $v$  states, particularly the low- $N$  levels of  $OH(v=0)$ . The calculated steady state populations of the low- $N$  levels of  $OH(v=0)$  are inversely proportional to the  $O + OH$  reaction rate. Spencer and Glass [1977] measured a factor of 2 to 3 rate enhancement for the reaction of  $OH(v=1)$  with  $O$  atoms over that for  $OH(v=0)$ , the  $O + OH(v=1)$  reaction occurring on every second collision. Thus the reaction rate of  $O$  atoms with  $OH(v \geq 1)$  was increased by a factor of 2.5 over the  $OH(v=0)$  reaction rate. This modification has only a minor effect on the low- $N$

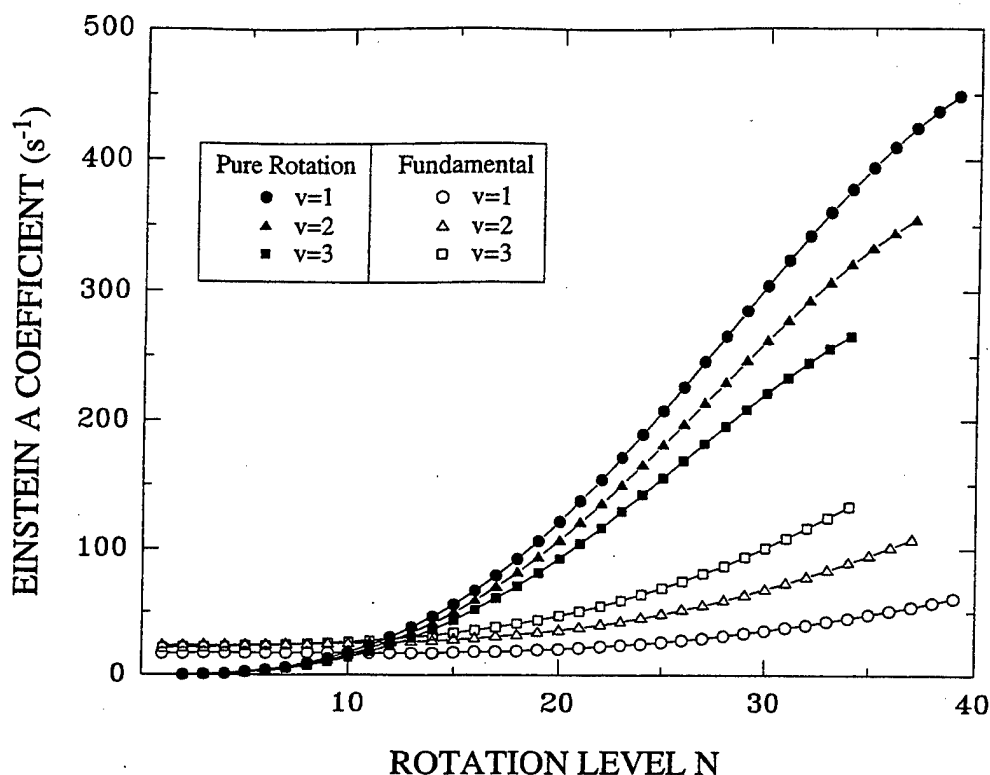


**Figure 18.** Einstein A coefficients for OH( $v=1-3, N$ ) fundamental and pure rotation transitions [Holtzclaw *et al.* 1993], where  $v$  and  $N$  refer to the upper state. The fundamental A coefficients have been summed over the P, Q, and R branches. Both sets of A coefficients refer to the  $F_1$  manifold; the  $F_2$  A coefficients are similar.

populations for the low- $v$  levels and a negligible effect on the other levels.

#### Radiative Cascade

**Pure rotation.** OH pure rotation radiative decay has been incorporated using the Einstein coefficients calculated independently by Holtzclaw *et al.* [1993] and Goorvitch *et al.* [1992]. Both of these groups used the OH dipole moment function  $\mu(r)$  determined by Nelson *et al.* [1990] and calculated transition probabilities which agree to within 1% for all  $v, N$ . For large values of  $N$  the pure rotation rates equal several hundred per second and represent the single largest loss term for the atmospheric OH( $v, N^*$ ).

**Vibration-rotation.** OH vibration-rotation cascade has been included using the values for  $v=1-9$ ,  $\Delta v=1-5$ ,  $N=1-15$  determined by Nelson *et al.* [1990] and extended to higher  $N$  levels by Holtzclaw *et al.* [1993]. The Holtzclaw *et al.* calculation used the dipole moment function  $\mu(r)$  and the nonrotating molecule potential  $V_{\text{RKR}}$  from Nelson *et al.* and assumed a case b rotational kinetic energy term. As discussed in the Appendix, the case b approximation is certainly valid for  $N$  values as large as 15. Holtzclaw *et al.* point out that the major uncertainty in the vibration-rotation transition probabilities results from ignoring mixing of the OH( $A^2\Sigma^+$ ) wave function into the OH( $X^2\Pi$ ) wave function, as discussed above for the OH  $\Lambda$ -doublet analysis. Uncertainties were estimated as  $\pm 15\%$  in the P and R branches for  $N=30$ , scaling roughly as  $N$ . Uncertainties were estimated to be far larger in the Q branches; however, the Q branches are very weak for large  $N$  and thus a negligible loss term for the atmospheric OH( $v, N^*$ ).

As mentioned above, the fundamental band emission rates can be significant relative to the high- $N$  pure rotation emission rates, while the overtone ( $\Delta v \geq 2$ ) rates are less important. Figure 18 shows the  $v=1-3$  fundamental band emission rates, summed over the P, Q, and R branches, together with the pure rotation emission rates. The substantial radiative rates in the fundamental bands have been taken into account in the kinetic model.

#### Collisional Relaxation

**Rotational relaxation.** Rotational relaxation rates were derived by modeling the air broadening of absorption line widths in terms of the lifetimes of the rotational states involved in the transition. Because air-broadening data for OH are scarce, the HF molecule was used as a model. HF and OH have similar dipole moments (1.8 D for HF versus 1.7 D for OH) and rotational constants  $B_0$  (21  $\text{cm}^{-1}$  for HF versus 19  $\text{cm}^{-1}$  for OH) and may well have similar line-broadening properties. Khayar and Bonamy [1982] have compared measured Ar-broadened HF pure rotation line widths to values calculated for Ar broadening of OH line widths and found that the broadening is about 50% larger in the case of OH; this result is taken into account below.

Rates were calculated by fitting HF(1-0) vibrational fundamental air-broadening coefficients, measured at 202 K [Pine and Looney, 1987], to the following formula:

$$\gamma = \frac{L(T)}{2\pi c} [k(N_i) + k(N_j)], \quad (10)$$

where  $\gamma$  is the broadening coefficient of the absorption line

half width at half-maximum intensity, in units of  $\text{cm}^{-1} \text{atm}^{-1}$ ,  $L(T)$  is Loschmidt's number, and  $k(N_i)$  and  $k(N_f)$  are rate constants summed over all of the collision-induced loss mechanisms for the initial and final rovibrational levels, respectively, connected by the infrared transition.

The collision-induced loss terms were taken to be

$$k(N) = k_{\text{COLL}} + k_{\text{ROT}}(N), \quad (11)$$

where  $k_{\text{COLL}}$  is a constant collisional dephasing term, and

$$k_{\text{ROT}}(N) = \alpha \sum_{N'=N} (2N'+1) e^{-\frac{\beta|\Delta E|}{k_B T}} \quad (12)$$

is the rate constant for collision-induced rotational energy transfer. The sum is over all rotational states  $N'$  not equal to the initial state value  $N$ , and  $\Delta E$  is the energy difference between the initial and final states. The "exponential-gap" dependence for rotational energy transfer rates was first used by Polanyi and Woodall [1972] to model HF rotational relaxation. The  $2N+1$  degeneracy factor takes into account microscopic reversibility [Brunner and Pritchard, 1982]. The dephasing rate constant  $k_{\text{COLL}}$ ,  $\alpha$ , and  $\beta$  are adjustable parameters in the fit.

The fit reproduced the values  $\gamma$  for air broadening of the HF(1-0)  $P(1)$ - $P(9)$  and  $R(0)$ - $R(8)$  lines to within the estimated experimental uncertainty. Using the best fit values for  $\alpha$  ( $6.6 \times 10^{-10} \text{ cm}^3 \text{ s}^{-1}$ ) and  $\beta$  (1.7), the quantities  $k_{\text{ROT}}(N)$  were determined for HF( $v=0$ ), then adjusted upward by 50% in accord with the calculation of Khayar and Bonamy [1982]. Rate constants  $k_{\text{ROT}}(N)$ , assumed to be independent of OH  $v$  level, were then fixed in the subsequent least squares fits to the OH( $v, N$ ) populations. Rates for collisional transfer out of a specific  $N$  level, plotted in Figure 14, were calculated as the product of  $k_{\text{ROT}}(N)$  and the total number density at 82-km and 96-km altitudes. As seen in Figure 14, rotation level-changing collisions limit the OH( $v, N$ ) lifetimes for low  $N$ , while spontaneous emission limits the lifetimes for high  $N$ , the crossover occurring in the range  $N=10$ -20.

Very recently, Schiffman and Nesbitt [1993] measured OH( $v=1 \leftarrow 0$ ) room-temperature air-broadening coefficients, for  $N'=1$ -4. For a given value of  $N$  the OH broadening coefficients are about 2 times larger than HF coefficients measured at 295 K [Pine and Looney, 1987]. Scaling the  $k_{\text{ROT}}(N)$  values upward to agree with the OH air-broadening measurements does not qualitatively change the results of the kinetic modeling. Indeed, the model uncertainty introduced by extrapolating either data set to much higher values of  $N$  is a more serious concern than the absolute scaling.

**Vibrational relaxation.** Two separate models for the OH( $v, N$ ) vibrational relaxation were considered, one which takes the high- $N$  levels to be the product of vibration-to-rotation energy transfer from energy resonant states in higher  $v$  levels ("VR" model) and one which takes the high- $N$  states to be nascent products of the  $\text{H} + \text{O}_3 \rightarrow \text{OH} + \text{O}_2$  reaction ("chemical production," or "CP" model).

**VR model:** This model incorporates collisional quenching of OH( $v, N$ ) by  $\text{O}_2$  with rate constants  $k_v$  given by

$$\ln k_v = av + b, \quad (13)$$

with  $a$  and  $b$  determined through a least squares fit to the values  $k_{v=1-6}(\text{O}_2)$ , determined by Dodd et al. [1991]. The rate constants thus generated range from  $1.0 \times 10^{-13} \text{ cm}^3 \text{ s}^{-1}$  for  $v=1$  to  $1.5 \times 10^{-11} \text{ cm}^3 \text{ s}^{-1}$  for  $v=9$ . The extrapolated rate constant  $k_{v=9}(\text{O}_2)$  is equal to a value recently measured by Chalamala and Copeland [1993], i.e.,  $(1.7 \pm 1.1) \times 10^{-11} \text{ cm}^3 \text{ s}^{-1}$ , within the uncertainty in the measurement. Multiquantum quenching is incorporated into the model using a parameterization similar to that introduced previously [Dodd et al., 1991], in which the probability of a downward transition  $v_i \rightarrow v_f$  is taken to be proportional to  $1/(v_i - v_f)^{n-v}$ , with an adjustable multiquantum parameter  $n$ . A value  $n=9$  denotes collisional relaxation of  $v_i=9$  to produce a flat distribution of final states  $v_f=0$ -8, with increasing single quantum character as  $v_i$  decreases. Larger values of  $n$  (e.g.,  $\geq 12$ ) denote single quantum relaxation for all  $v$  levels. We find that the  $\chi^2$  value is not sensitive to the chosen value of  $n$ , for  $n \geq 9$ ; for  $n < 9$ ,  $\chi^2$  worsens appreciably. Thus we have assumed single quantum relaxation of OH( $v$ ) by  $\text{O}_2$ , consistent with the findings of laboratory measurements of the vibrational relaxation of OH( $v$ ) by  $\text{O}_2$  [Dodd et al., 1991].

Vibrational relaxation of OH( $v$ ) by  $\text{N}_2$  is known to be much slower than relaxation by  $\text{O}_2$ . For  $v=2$  the relaxation rate constant  $k_v(\text{N}_2)$  is at least 26 times smaller than  $k_v(\text{O}_2)$  [Rensberger et al., 1989]; for  $v=9$ ,  $k_v(\text{N}_2)$  was found in one study to be at least 20 times smaller than  $k_v(\text{O}_2)$  [Finlayson-Pitts and Kleindienst, 1981] and in another to be at least 34 times smaller [Chalamala and Copeland, 1993]. Thus despite the fourfold greater abundance of  $\text{N}_2$  versus  $\text{O}_2$  in the mesopause region, relaxation of OH( $v=1$ -9) by  $\text{N}_2$  is at most one-fifth the rate for  $\text{O}_2$ -mediated relaxation. In addition, the mechanism of relaxation of OH( $v$ ) by  $\text{N}_2$  has not been studied in any detail, at least partly due to the small values for  $k_v(\text{N}_2)$ . Thus  $\text{N}_2$ -mediated relaxation is ignored in the present model.

Under the VR model, the assumption is made that the reaction between H atoms and  $\text{O}_3$  produces OH( $v=6$ -9) only. For each initial level  $i$  in vibrational manifold  $v$ , a set of  $v-1$  final levels  $f$  most closely coincident in total energy to  $E_i$  was identified, with the proviso that  $E_f \leq E_i + 140 \text{ cm}^{-1}$  (i.e.,  $k_B T$  at 200 K). The collision-induced resonant VR transfer mechanism was assumed to connect the initial state with these final states only. The VR transfer process corresponds to a right-to-left horizontal transition of OH( $v, N$ ) in Figure 10, conserving the total energy of the hydroxyl molecule.

Trial models were generated using various species, such as  $\text{N}_2$ ,  $\text{O}_2$ , and O, to induce resonant VR transfer in OH( $v, N$ ). In the model atmosphere the major atmospheric constituents  $\text{N}_2$  and  $\text{O}_2$  decrease in density by 2 orders of magnitude between 80 and 110-km altitude, while the O-atom density rises an order of magnitude between 80 and 95 km, then remains approximately constant (Figure 17). We find that the OH( $v, N^*$ ) column density predictions based on  $\text{N}_2/\text{O}_2$ -induced VR transfer are wholly inconsistent with the data, predicting far too much OH( $v, N^*$ ) at the lower tangent heights and far too little OH( $v, N^*$ ) at the higher tangent heights. On the other hand, O-atom-induced transfer is much more consistent with the data. The less prevalent species (e.g.,  $\text{O}_3$ , H) would require a physically unreasonable collision cross section in order to effect the necessary transfer.

Transfer of multiple vibrational quanta for O-atom quenching is provided through an expression similar to that presented above for O<sub>2</sub> quenching. In this case, the probability of a downward transition  $v_i \rightarrow v_f$  is taken to be  $1/(v_i - v_f)^n$ , for which  $n=0$  denotes a flat distribution of final  $v_f$  levels, and increasing positive values of  $n$  denote increasing single-quantum character. In addition, a second parameter  $C$  was introduced as a constant multiplier (units of  $\text{cm}^3 \text{s}^{-1}$ ) for the  $v, N$  level-independent rate constant governing O-atom induced collisional energy transfer. The parameters  $n$  and  $C$  were allowed to vary in the fit to the OH( $v, N$ ) column density data. The best fit value  $n$  is equal to 0, corresponding to a flat final state  $v_f$  distribution. The best fit value  $C$  equals  $4 \times 10^{-11} \text{ cm}^3 \text{s}^{-1}$ , which corresponds to the measured rate of the  $\text{O} + \text{OH} \rightarrow \text{O}_2 + \text{H}$  reaction at 200 K. Thus the dominant product channel for O + OH collisions may involve bond-breaking for low- $v$  OH but energy transfer for high- $v$  OH.

A complicating issue in the case of O + OH collisions involves possible formation of an intermediate HO<sub>2</sub> complex. HO<sub>2</sub> is bound by 3.1 eV with respect to the separated O + OH reactants [Varandas and Marques, 1992] and thus could be sufficiently long lived as to lose all memory of reactant quantum state. According to unimolecular reaction rate theory, such a complex would be predicted to decompose into O + OH and H + O<sub>2</sub> fragments, with a statistical product state distribution governed by quantum state densities at the total energy of the complex. This prediction is inconsistent with the much more restrictive VR model product state prediction. On the other hand, the reaction  $\text{O}(^1D) + \text{H}_2 \rightarrow \text{OH}(v, N) + \text{H}$  also proceeds through a stable intermediate but gives rise to a highly nonstatistical distribution of rotationally excited OH( $v=0-4$ ) [Sloan, 1988]. Studies of the reaction

dynamics on the H<sub>2</sub>O(<sup>1</sup>A') potential energy surface have shown that production of high- $N$  OH is enhanced through a long-range H-OH' product transition state and a large exit impact parameter [Rynerfors et al., 1985]. Thus it is possible that unanticipated dynamics control the outcome of inelastic collisions between OH and O(<sup>3</sup>P).

The left-hand side of Figure 12 shows the prediction made by the VR model for the OH( $v, N$ ) column densities for two different tangent heights. The cusps, or local maxima, observed in the populations for certain values of  $N$  result from energy resonances of the cusp level with the low- $N$  levels of a higher vibrational state (see Figure 10). The VR model dictates that resonant VR transfer from the closely spaced low- $N$  levels into a given vibrational manifold populates a unique  $N$  level, producing a surplus of population in that level. The cusps could be evened out by relaxing the uniqueness condition of the resonant VR transfer mechanism. Even in the present model, the cusps are largely smoothed by the high rate of pure rotation radiative cascade, especially for the low- $v$ , high- $N$  states.

**CP model:** The CP model incorporates collisional quenching of OH( $v$ ) by O<sub>2</sub> in a manner identical to the VR model. However, feed into the high- $N$  levels occurs not through resonant VR transfer but instead through direct chemical production via the H + O<sub>3</sub> reaction. In the CP model, the OH( $v=6-9$ ) nascent distribution given by Klenerman and Smith [1987] is amended to include low- $v$  levels. The rotational level dependence of the model OH( $v=0-5$ ) chemical production rates can not be determined independently from the pure rotation data. Thus we have parameterized the feed rates according to a probability  $P(N)$  assuming a statistical distribution of nascent  $N$  levels, namely

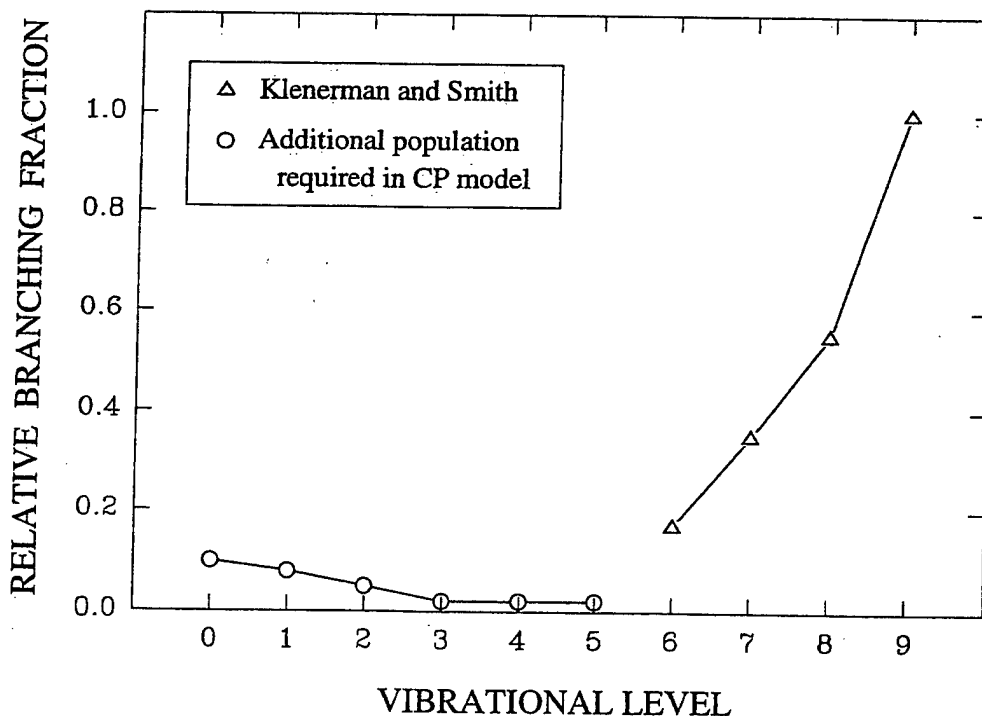


Figure 19. Product OH vibrational level branching fraction for  $\text{H} + \text{O}_3 \rightarrow \text{OH}(v) + \text{O}_2$ . Points marked by triangles are taken from Klenerman and Smith [1987]; points marked by circles represent additional population of the low- $v$  levels required by the CP model. See text for discussion.

$$P(N) = (2N+1) \sqrt{E_{\text{TOT}} - E_{\text{VIB}} - E_{\text{ROT}}}, \quad (14)$$

where  $E_{\text{TOT}}$ ,  $E_{\text{VIB}}$ ,  $E_{\text{ROT}}$  are the total, vibrational and rotational energies, respectively, and  $E_{\text{TOT}}$  is equal to the 27,000 cm<sup>-1</sup> exothermicity of the H + O<sub>3</sub> reaction. The  $2N+1$  term gives the rotational degeneracy of product OH( $v,N$ ), while the square root term is proportional to the product translational partition function. Clearly we have not proved that the statistical model is correct in this case; instead, we will show that a simple model can be used to reproduce the data. For the CP model, the only parameters adjusted in the fit to the OH( $v,N$ ) column densities are the fractions  $\chi(v)$  denoting the relative feed rates into the lower  $v$  levels. The amount of feed into the lower  $v$  levels required in order to match the data is indicated in Figure 19. It is seen that the level of feed into  $v=0$  determined by the CP model is about 10% of that for  $v=9$ , with smaller percentages required for  $v=1-5$ .

The OH( $v,N$ ) population distribution predicted by the CP model is shown on the right-hand side of Figure 12; it is seen to be similar to the VR model prediction. The CP model does not predict the cusps for certain values of  $N$  both because it has no resonant transfer mechanism and because it uses a smooth function for the  $N$  dependence of the chemical feed.

## Discussion

### Hydroxyl Vibrational-Rotational Distributions

As seen from Figure 12, both the VR and the CP models predict an inversion in the rotational level populations in the range  $N=8-13$ , even after dividing by the degeneracies  $2N+1$ . This inversion is strongest for the lowest  $v$  levels and gradually diminishes with increasing  $v$ . A bimodal form for the rotational distribution is a well-known outcome of the exponential-gap form for the rotational relaxation rates [Polanyi and Woodall, 1972]. Under the exponential-gap model, high- $N$  levels are relaxed very slowly, while mid- $N$  levels are depleted more quickly but are only slowly populated from above. Typically, a population minimum occurs, with the value of  $N$  at the minimum determined by the steepness of the exponential decay in the rates. If the OH rotational relaxation rates are made a weaker function of  $N$ , the magnitude of the population inversions seen in Figure 12 is reduced. At the same time, the predictions made for low- $N$  and high- $N$  populations are little affected by variation of the exponential-gap parameter  $\beta$  (equation (12)). For any reasonable value of  $\beta$ , the closely spaced low- $N$  levels are always strongly coupled through  $N$ -changing collisions, while production and loss of the high- $N$  levels are always dominated by pure rotation emission. Thus a best fit value for  $\beta$  cannot be determined unequivocally in the absence of population data for  $N=5-12$ .

Both models are consistent with the pure rotation radiative cascade dominating the feed and loss for the high- $N$  levels. This was ascertained by computing the flux of OH molecules (units of cm<sup>-3</sup> s<sup>-1</sup>) into each  $N$  level of  $v=0$ , at an altitude of 90 km. The flux was calculated for each of five mechanisms: pure rotation radiative cascade, vibration-rotation radiative cascade, collision-induced rotational energy transfer, collision-induced vibrational energy transfer, and resonant VR transfer (VR model only) or feed from H + O<sub>3</sub>

(CP model only). For both models the flux due to pure rotation cascade is found to dominate over the other mechanisms by an order of magnitude in the range  $N=18-35$ . Pure rotation radiative cascade remains the most important feed mechanism for  $N$  values as low as 15.

Very recently, Pendleton *et al.* [1993] reported more detailed OH( $v,N$ ) distributions obtained through ground-based FWI observations of  $\Delta v=2$  and 3 Meinel band emissions. In particular,  $P$ -branch emissions for  $v'=3, 6$ , and 7, and  $N'=1-12$  were analyzed in detail. For those values of  $N$  the inferred rotational state populations decrease monotonically with increasing  $N$ , as opposed to the distinct population minimum predicted by the VR and CP models. The inferred populations for OH( $v,N=1-12$ ) may be useful in discriminating between the exponential-gap and alternative models [Brunner and Pritchard, 1982] of OH( $N_i \rightarrow N_j$ ) collision-induced rotational relaxation. Pendleton *et al.* [1993] derive the population ratios  $(v=3,N=1):(v=3,N=9) = 60, (6,1):(6,11) = 50$ , and  $(7,1):(7,12) = 35$ , indicating a greater degree of rotational excitation (relative to  $N=1$ ) for the higher  $v$  levels. These ratios are consistent with the CIRRIS limb column densities, taken near the OH  $\Delta v=1$  peak emission altitude (e.g., the 82-km populations shown in Figure 12). This consistency provides a valuable check on the methods and resulting populations obtained from both experiments. Further analysis taking the ground-based observations into account is in progress.

### OH( $v,N$ ) Model Altitude Distributions

The VR and CP kinetic models predict similar altitude distributions. Figure 20 shows CP model number densities for the thermal and rotationally excited components. For the purposes of the figure, the thermal and rotationally excited distributions were generated by summing the rotational level populations over  $N=1-7$  and  $N \geq 11$ , respectively. For the excited distributions,  $N$  levels are included up to 27,000 cm<sup>-1</sup> total energy (Figure 10). Altitude distributions are shown for thermal OH(0-9), and for rotationally excited OH(0-6). Figure 20 shows that for the thermal component the  $v=1$  number densities peak at about 87 km, while those for  $v=9$  peak at about 89 km. McDade [1991] has summarized the available data concerning the altitude distribution of the various OH( $v$ ) levels. OH Meinel band emissions have been observed using rocket-borne broadband radiometers and have also been extensively modeled. Both the data and the models suggest that the peak OH( $v$ ) number densities should occur at higher altitudes for higher  $v$  levels. The model calculations of McDade [1991] show that the altitude spread in the peak OH( $v=1-9$ ) number densities should not exceed 1-2 km, consistent with the present results.

The rotationally excited distribution peaks 0-2 km higher in altitude than the thermal component, depending on the  $v$  level. The rotationally excited component also displays less dependence of the peak altitude on  $v$ , with all levels peaking at about 89 km. To our knowledge, no other models of the altitude distributions of the only recently discovered [Smith *et al.*, 1992] OH high- $N$  populations have been reported.

### Sources of Angular Momentum

The OH levels observed in the pure rotation spectra contain a substantial amount of angular momentum, the origin of which must be rationalized under any viable

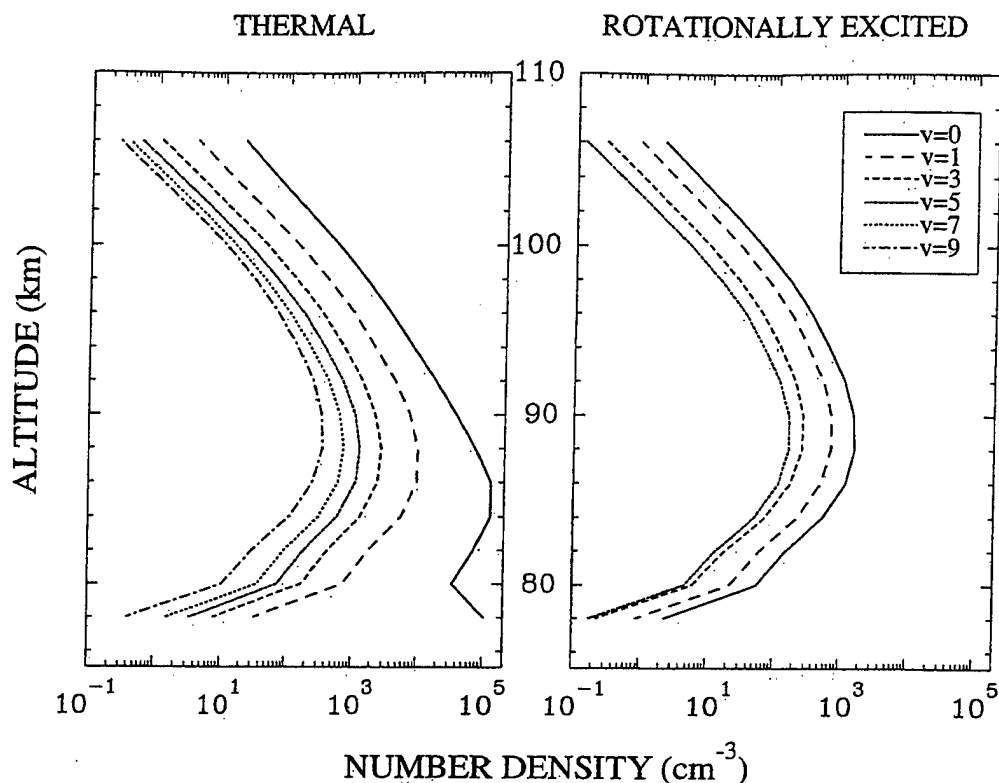


**Figure 20.** OH( $v$ ) number density predictions from the CP kinetic model for the thermal and rotationally excited components. The thermalized populations have been summed over  $N=1-7$ , while the excited populations have been summed over all  $N \geq 11$ , consistent with total energy less than  $27,000 \text{ cm}^{-1}$ . In both cases the populations have been summed over the four spin sublevels. OH( $v, N$ ) model number densities are differentiated by line type according to the vibrational level. Vibrational levels  $v=2, 4, 6$ , and  $8$  have been omitted for clarity.

mechanistic model. In the case of the VR model, a large amount of angular momentum transfer necessarily occurs during O-OH collisions. For instance, a large proportion of the low- $v$ , high- $N$  population results from direct transfer from  $v=9, N=1-7$ , since  $v=9$  is the most highly populated nascent vibrational state of the  $\text{H} + \text{O}_3$  reaction. Thus transfer from  $v=9$  to the low- $v$  levels requires typical  $\Delta N$  values of 30. The angular momentum imparted to the highly rotationally excited OH molecule must arise chiefly from the orbital angular momentum of the OH + O constituents, in either the reactant or the product channels [Mikulecky and Gericke, 1992]. The orbital angular momentum  $L\hbar = \mu v b$ , where  $\mu$  is the reduced mass of the system,  $v$  is the relative velocity, and  $b$  is the impact parameter. To impart maximum angular momentum to the product OH, the reactant and product  $\mathbf{L}$  vectors are assumed to be antiparallel, such that the vector equation

$$\begin{aligned} \Delta N &\approx L_{\text{PRODUCTS}} - L_{\text{REACTANTS}} \\ &= \frac{\mu(\mathbf{v} \times \mathbf{b}_P - \mathbf{v} \times \mathbf{b}_R)}{\hbar} \end{aligned} \quad (15)$$

holds. Setting the average relative velocity equal to  $720 \text{ m s}^{-1}$  at 200 K, the average impact parameter can be estimated assuming a hard-sphere potential, namely

$$b = \sqrt{\frac{k}{\pi v}}, \quad (16)$$

where the rate constant  $k$  is taken to be  $4 \times 10^{-11} \text{ cm}^3 \text{ s}^{-1}$ , the value obtained by the kinetic fit to the population data. The parameter  $b$  is calculated to be  $1.3 \text{ \AA}$ , i.e., slightly larger than the OH bond length of  $1.0 \text{ \AA}$ . Using these values for  $v$  and  $b$  along with  $\mu = 8.2 \text{ amu}$ ,  $\Delta N \leq 24$  is calculated, roughly consistent with the  $\Delta N$  value required for the VR model.

For the CP model, the OH angular momentum must arise in the course of the  $\text{H} + \text{O}_3$  reaction, the dynamics of which have been studied theoretically [Chen *et al.*, 1981; Dupuis *et al.*, 1986]. Two low-energy pathways for the reaction have been identified, one involving colinear approach of the H atom along an O-O bond and a planar transition state and the other involving perpendicular approach of the H atom, directed at one of the terminal O atoms. Chen *et al.* [1981] point out that for the planar transition state, violent oscillation in the incipient OH bond would likely transfer momentum into (counterpropagating) rotation of the OH and  $\text{O}_2$  products. This momentum transfer would be less likely in the case of perpendicular approach of the H atom. If at least a portion of the reactive trajectories proceed via a coplanar transition state, this mechanism could serve to populate the OH high- $N$  states. The counterrotating  $\text{O}_2$  molecule would help provide conservation of angular



momentum. The small rotation constant of  $O_2$  ( $B_0 = 1.4 \text{ cm}^{-1}$ ) allows the production of high- $J$  levels with only modest investments of energy. For instance, production of  $O_2(J=25)$  requires only  $940 \text{ cm}^{-1}$  of energy, which is about the rotational level spacing in high- $N$  OH.

### $\Lambda$ -Doublet Distribution

As discussed above, the  $\Lambda$ -doublet ratio  $\Pi(A')/\Pi(A'') = 1.8 \pm 0.3$  was determined from the pure rotation emission intensities for the range  $N=13$ –33 [Dodd *et al.*, 1993a]. For high  $N$  the O-atom  $p\Pi$ -orbital containing the unpaired electron is in the plane of rotation in the  $\Pi(A')$  case and perpendicular to the plane of rotation in the  $\Pi(A'')$  case [Alexander *et al.*, 1988]. Preference for the  $\Pi(A')$  component has been observed in chemical reactions that form OH, such as  $H + O_2$  [Kleinermaun and Wolfrum, 1984],  $O(^1D) + H_2$  [Mikulecky and Gericke, 1992], and  $O(^1D) + H_2O$  [King *et al.*, 1992], and from inelastic collisions of OH with  $H_2$  [Andresen *et al.*, 1984a]. Preference for the  $\Pi(A'')$  component has been observed in the photodissociation of  $H_2O$  [Andresen *et al.*, 1984b]. To our knowledge, published accounts do not address the nascent OH  $\Lambda$ -doublet population distribution in the  $H + O_3$  reaction. The populations could be probed experimentally, for instance through LIF detection on the OH  $A-X$  transition [Sloan, 1988].

It was mentioned above that a planar  $H-O_3$  transition state could favor formation of high- $N$  OH. A planar  $H-O_3$  transition state could also favor production of the  $\Pi(A')$   $\Lambda$  doublet, according to arguments made in the literature for similar reactions [Andresen and Rothe, 1985]. For planar  $H-O_3$  the incipient OH  $p\Pi$  orbital containing the unpaired electron is oriented in the plane of the complex. If the torques responsible for rotational excitation of the product OH also lie in the plane, preferential population of the  $\Pi(A')$   $\Lambda$  doublet occurs. It is possible, then, that the two separate channels of the  $H + O_3$  reaction suggested by Kaye [1988] preferentially populate high- $v$  OH and high- $N$  OH, respectively. Clearly, the  $H + O_3$  reaction bears further study.

Finally, two groups have attempted to calculate a "prior" expectation for the population ratio  $\Pi(A')/\Pi(A'')$  in high- $N$  levels of OH resulting from a chemical reaction. These models assume no dynamical constraints to the motions of the nuclei in the transition state for the reaction  $H + OX \rightarrow HO + X$ . Bronikowski and Zare [1990], using a very simple geometrical argument, predict  $\Pi(A')/\Pi(A'')=2$ . Hanazaki [1993], on the other hand, argues that the former study contains flaws and predicts  $\Pi(A')/\Pi(A'')=1$  for an unconstrained  $H + OX$  reaction. No attempts are made here to interpret the observed  $\Lambda$ -doublet ratio in terms of a prior expectation, pending the outcome of this disagreement.

### Implications for Energy Budget

Population of the OH high- $N$  levels, by any mechanism, could have a significant effect on models of the energy budget of the mesopause [Mlynczak and Solomon, 1993]. OH( $v,N^*$ ) levels will radiate much of their initial energy back out into space. Thus they provide an additional cooling mechanism for the mesopause region, the magnitude of the effect depending on the flux through those levels. The measured nascent product distribution for  $v=6$ –9 [Kleinermaun and Smith, 1987] accounts for roughly 90% of the available

exothermicity of the  $H + O_3$  reaction. The remaining 10% feeds into the kinetic energy of the fragments and rotation of the  $O_2$  molecule, thus heating the atmosphere. If the CP mechanism is correct, models of the nascent product distribution for the  $H + O_3$  reaction would have to be revised, possibly resulting in a significant difference in estimates for the amount of residual energy feeding into those degrees of freedom. This difference would also have to be taken into account in a calculation of the effects of chemical production of OH( $v,N^*$ ) on atmospheric heating.

### Summary

A large number of OH( $v,N$ ) pure rotation and vibration-rotation earthlimb spectra have been obtained through the CIRIS 1A space shuttle experiment. These spectra have been analyzed to yield OH( $v,N$ ) column densities in the Earth's airglow region between 20 and 110 km. Partially resolved pure rotation emission from OH levels with up to 2.3 eV of rotational energy has been observed, as well as fundamental emission from OH( $v=1$ –9). The pure rotation emission has been analyzed to determine the relative spin sublevel populations, indicating equal amounts of the spin-rotation states but an approximately 2:1  $\Pi(A')/\Pi(A'')$  ratio in the  $\Lambda$  components.

A first-principles kinetic model has been developed to predict OH( $v,N$ ) altitude-dependent number densities, which are convolved with the detector field of view for direct comparison with the data. The model incorporates laboratory values for the OH( $v=6$ –9, $N$ ) relative branching fractions from the  $H + O_3$  reaction. Two adaptations of the model have been shown to be consistent with all aspects of the OH( $v,N$ ) column density data set. The first adaptation is a resonant VR energy transfer mechanism, under which vibrational energy in nascently produced OH( $v=6$ –9) is exchanged for rotational energy in product OH(low  $v$ , high  $N$ ) upon inelastic collisions with O atoms. In the second adaptation the observed high- $N$  levels are taken to be nascent, chemiluminescent product states of the  $H + O_3$  reaction. Neither mechanism can be discounted based on considerations of angular momentum, nor on the basis of the observed  $\Lambda$ -doublet population ratio. The identification of the correct mechanism would provide great insight into the dynamics of highly rotationally excited hydroxyl in the upper atmosphere and better quantify the effects on energy budget models of the mesopause.

### Appendix: Angular Momentum Coupling in OH( $X^2\Pi$ )

For small values of the molecular rotation the OH wave functions are well approximated assuming Hund's case a angular momentum coupling. For case a, both the electron orbital angular momentum vector  $L$  and the electron spin vector  $S$  are strongly coupled to the internuclear axis. This coupling results in the two "spin-orbit" manifolds  $F_1$  ( $\Omega=3/2$ ) and  $F_2$  ( $\Omega=1/2$ ). The quantum number  $J$ , representing the total angular momentum, is used to label the rotational levels.

With increasing rotation,  $S$  rapidly uncouples from the internuclear axis and couples instead to the end-over-end rotation vector  $R$ , a situation described by Hund's case b. The resultant "spin-rotation" wave functions, also labeled  $F_1$

and  $F_2$ , can be described as linear combinations of the case a spin-orbit wave functions [Zare, 1988]. The rotational quantum levels are labeled by  $N$ , which is the total angular momentum apart from electron spin. A labeling scheme for OH rotational levels independent of the angular momentum coupling case uses the formal correspondence  $N = J - 1/2$  for the  $F_1$  manifold and  $N = J + 1/2$  for the  $F_2$  manifold. Thus the positive integer values  $N$  are used to label rotational states for both case a and case b, with  $N=1$  the lowest energy level for both  $F_1$  and  $F_2$  manifolds. For convenience we have adopted this convention.

For nonzero values of the rotational angular momentum the electronic orbital angular momentum  $L$  is slightly uncoupled from the internuclear axis, removing a further degeneracy and resulting in "A doubling." The  $e$  and  $f$  A-doublet states have opposite total electronic-rotational parity and can be used to label the OH levels regardless of coupling case. In the case b (high  $N$ ) limit for  $^2\Pi$  diatomic molecules such as OH, the parity states have a definite physical interpretation:  $1e$  and  $2f$  levels are symmetric with respect to reflection of the electronic coordinates in the plane of rotation ( $\Pi(A')$  symmetry) and  $2e$  and  $1f$  levels are antisymmetric ( $\Pi(A'')$ ) [Alexander et al., 1988; Zare, 1988]. Like the  $N$  labeling, the  $\Pi(A')/\Pi(A'')$  nomenclature can be used to formally label the A-doublet states for both coupling cases, even though it has a strict symmetry interpretation only in the case b limit. The relative population of the two A components provides a clue as to the dynamics involved in OH formation (see Discussion section).

**Acknowledgments.** We gratefully acknowledge support from the entire CIRIS 1A team at the Optical Environment Division of the Phillips Laboratory/Geophysics Directorate, as well as at the Utah State University Space Dynamics Laboratory and the Boston College Institute for Space Research. We would especially like to thank the following individuals for their contributions to this work and to the CIRIS program: M. Ahmadjian, Captain D. A. Dean, E. R. Huppi, S. M. Miller, R. H. Picard, R. D. Sharma, D. R. Smith, N. B. Wheeler, J. R. Winick, and J. O. Wise (PL), G. E. Bingham and W. R. Pendleton, Jr. (USU), E. N. Richards and B. F. Sullivan (BC), U. B. Makhlof (Stewart Radiance Laboratory), C. Trowbridge (PhotoMetrics, Inc.), and R. J. Healey (Yap Analytics Inc.). We also thank A. Schiffman and D. J. Nesbitt for sharing their unpublished OH air-broadening data. P. S. A. acknowledges support provided by the Geophysics Scholarship program, administered by the Northeast Consortium for Engineering Education under contract with the Air Force Office of Scientific Research. Funding was provided by the Ballistic Missile Defense Organization/DTNS (formerly the Strategic Defense Initiative Organization/TNS) under Program Element 63215C/task 110501, the Defense Nuclear Agency/RAAE under DNA MIPR #92-586 and Work Unit 00002, and the Air Force Office of Scientific Research under task 2303EP1/PL007.

## References

- Adler-Golden, S. M., Analysis of SPIRIT LWIR emission: An ozone  $\nu_3$  model, *Rep. TR-122*, 26 pp., Spectral Sci., Inc., Burlington, Mass., 1987.
- Adler-Golden, S. M., and D. R. Smith, Identification of 4- to 7-quantum  $\nu_3$  bands in the atmospheric recombination spectrum of ozone, *Planet. Space Sci.*, **38**, 1121, 1990.
- Adler-Golden, S. M., M. W. Matthew, D. R. Smith, and A. J. Ratkowski, The 9- to 12- $\mu$ m atmospheric ozone emission observed in the SPIRIT 1 experiment, *J. Geophys. Res.*, **95**, 15243, 1990.
- Ahmadjian, M., R. M. Nadile, J. O. Wise, and B. Bartschi, CIRIS 1A space shuttle experiment, *J. Spacecr. Rockets*, **27**, 669, 1990.
- Alexander, M. H., et al., A nomenclature for A-doublet levels in rotating linear molecules, *J. Chem. Phys.*, **89**, 1749, 1988.
- Andresen, P., and E. W. Rothe, Analysis of chemical dynamics via A doubling: Directed lobes in product molecules and transition states, *J. Chem. Phys.*, **82**, 3634, 1985.
- Andresen, P., D. Hausler, and H. W. Luff, Selective A-doublet population of OH in inelastic collisions with  $H_2$ : A possible pump mechanism for the  $^2\Pi_{1/2}$  astronomical maser, *J. Chem. Phys.*, **81**, 571, 1984a.
- Andresen, P., G. S. Ondrey, B. Titze, and E. R. Rothe, Nuclear and electron dynamics in the photodissociation of water, *J. Chem. Phys.*, **80**, 2548, 1984b.
- Armstrong, P. S., S. J. Lipson, J. R. Lowell, W. A. M. Blumberg, D. R. Smith, R. M. Nadile, and J. A. Dodd, Analysis of CIRIS 1A nitric oxide spectra (abstract), *Eos Trans. AGU*, **73**(43), Fall Meeting Suppl., 430, 1992.
- Baker, D. J., A. J. Steed, and R. M. Nadile, Limb measurements of OH fundamental band sequence airglow IR spectrum from Discovery orbital vehicle (STS-39) (abstract), *Eos Trans. AGU*, **72**(44), Fall Meeting Suppl., 358, 1991.
- Bartschi, B., A. Steed, J. Blakeley, M. Ahmadjian, J. Griffin, and R. Nadile, Cryogenic infrared radiance instrumentation for shuttle (CIRIS 1A): Instrumentation and flight performance, *Proc. SPIE Int. Soc. Opt. Eng.*, **1765**, 64, 1992.
- Bronikowski, M. J., and R. N. Zare, Simple model for A-doublet propensities in bimolecular reactions, *Chem. Phys. Lett.*, **166**, 5, 1990.
- Brunner, T. A., and D. Pritchard, Fitting laws for rotationally inelastic collisions, *Adv. Chem. Phys.*, **L**, 589, 1982.
- Carleton, K. L., W. J. Marinelli, K. W. Holtzclaw, B. D. Green, S. J. Lipson, and W. A. M. Blumberg, OH( $X, \nu$ ) rotational relaxation by nitrogen and oxygen (abstract), *Eos Trans. AGU*, **71**(43), Fall Meeting Suppl., 1490, 1990.
- Chalamala, B. R., and R. A. Copeland, Collision dynamics of OH( $X^2\Pi, v=9$ ), *J. Chem. Phys.*, **99**, 5807, 1993.
- Charters, P. E., R. G. Macdonald, and J. C. Polanyi, Formation of vibrationally excited OH by the reaction  $H + O_3$ , *Appl. Opt.*, **10**, 1747, 1971.
- Chen, M. M. L., R. W. Wetmore, and H. F. Schaefer III, Mechanism of the  $H + O_3$  reaction, *J. Chem. Phys.*, **74**, 2938, 1981.
- Copeland, R. A., and D. R. Crosley, A-doublet transfer and propensities in collisions of OH( $X^2\Pi, v=2$ ) with  $H_2O$ , *J. Chem. Phys.*, **81**, 6400, 1984.
- Coxon, J. A., and S. C. Foster, Rotational analysis of hydroxyl vibration rotation emission bands: Molecular constants for OH  $X^2\Pi$ ,  $6 \leq v \leq 10$ , *Can. J. Phys.*, **60**, 41, 1982.
- DeMore, W. B., S. P. Sander, D. M. Golden, M. J. Molina, R. F. Hampson, M. J. Kurylo, C. J. Howard, and A. R. Ravishankara, Chemical kinetics and photochemical data for use in stratospheric modeling, *JPL Publ. 90-1*, 217 pp., Jet Propulsion Laboratory, Calif. Inst. Tech., Pasadena, Calif., 1990.
- Dodd, J. A., S. J. Lipson, and W. A. M. Blumberg, Formation and vibrational relaxation of OH( $X^2\Pi, v$ ) by  $O_2$  and  $CO_2$ , *J. Chem. Phys.*, **95**, 5752, 1991.
- Dodd, J. A., W. A. M. Blumberg, S. J. Lipson, J. R. Lowell, P. S. Armstrong, D. R. Smith, R. M. Nadile, N. B. Wheeler, and E. R. Huppi, OH( $v, N$ ) column densities from high-resolution earthlimb spectra, *Geophys. Res. Lett.*, **20**, 305, 1993a.
- Dodd, J. A., J. R. Winick, W. A. M. Blumberg, S. J. Lipson, P. S. Armstrong, and J. R. Lowell, CIRIS 1A observation

- of  $^{13}\text{C}^{16}\text{O}$  and  $^{12}\text{C}^{18}\text{O}$  fundamental band radiance in the upper atmosphere, *Geophys. Res. Lett.*, **20**, 2683, 1993b.
- Dupuis, M., G. Fitzgerald, B. Hammond, W. A. Lester, Jr., and H. F. Schaefer III, Theoretical study of the  $\text{H} + \text{O}_3 \leftrightarrow \text{OH} + \text{O}_2 \leftrightarrow \text{O} + \text{HO}_2$  system, *J. Chem. Phys.*, **84**, 2691, 1986.
- Espy, P. J., C. R. Harris, A. J. Steed, J. C. Ulwick, and R. H. Haycock, Rocket-borne interferometer measurement of infrared auroral spectra, *Planet. Space Sci.*, **36**, 543, 1988.
- Finlayson-Pitts, B. J., and T. E. Kleindienst, The reaction of hydrogen atoms with ozone as a source of vibrationally excited  $\text{OH}(X^2\Pi_{1/2})_{v=9}$  for kinetic studies, *J. Chem. Phys.*, **74**, 5643, 1981.
- Goldman, A., J. R. Gillis, and J. A. Coxon, Spectral line parameters for the pure rotation bands of solar OH, *J. Quant. Spectrosc. Radiat. Transfer*, **29**, 1983. (OH line positions were obtained from the file on record at the Department of Physics, University of Denver.)
- Goorvitch, D., A. Goldman, R. H. Tipping, C. Chackerian, and H. Dothe, Hydroxyl  $X^2\Pi$  pure rotational transitions, *J. Geophys. Res.*, **97**, 20,771, 1992.
- Green, B. D., W. T. Rawlins, and R. M. Nadile, Diurnal variability of vibrationally excited mesospheric ozone as observed during the SPIRE mission, *J. Geophys. Res.*, **91**, 311, 1986.
- Griffiths, P. R., and J. A. de Haseth, *Fourier Transform Infrared Spectrometry*, pp. 25-33, John Wiley, New York, 1986.
- Hanazaki, I., Formation of lambda-doublet components of OH in the bimolecular reactions:  $\text{H} + \text{OX} \rightarrow \text{OH} + \text{X}$ , *Chem. Phys. Lett.*, **201**, 301, 1993.
- Haugen, H. K., W. H. Pence, and S. R. Leone, Infrared double resonance spectroscopy of V-T,R relaxation of  $\text{HF}(v=1)$ : Direct measurement of the high- $J$  populations, *J. Chem. Phys.*, **80**, 1839, 1984.
- Hedin, A. E., Extension of the MSIS thermosphere model into the middle and lower atmosphere, *J. Geophys. Res.*, **96**, 1159, 1991.
- Hindmarsh, A. C., *Livermore Solver for Ordinary Differential Equations (Program LSODE)*, Lawrence Livermore Laboratory, Livermore, Calif., 1980.
- Holtzclaw, K. W., J. C. Person, and B. D. Green, Einstein coefficients for emission from high rotational states of the  $\text{OH}(X^2\Pi)$  radical, *J. Quant. Spectrosc. Radiat. Transfer*, **49**, 223, 1993.
- Kaye, J. A., On the possible role of the reaction  $\text{O} + \text{HO}_2 \rightarrow \text{OH} + \text{O}_2$  in OH airglow, *J. Geophys. Res.*, **93**, 285, 1988.
- Khayar, A., and J. Bonamy, Calculation of mean collision cross sections of free radical OH with foreign gases, *J. Quant. Spectrosc. Radiat. Transfer*, **28**, 199, 1982.
- King, D. S., D. G. Sauder, and M. P. Casassa, Product kinetic energies, correlations, and scattering anisotropy in the bimolecular reaction  $\text{O}(^1D) + \text{H}_2\text{O} \rightarrow 2 \text{OH}$ , *J. Chem. Phys.*, **97**, 5919, 1992.
- Kleinermaun, K., and J. Wolfrum, Hot atom-laser induced fluorescence experiments on the reaction of  $\text{H}(^2S)$  with  $\text{O}_2$ , *J. Chem. Phys.*, **80**, 1446, 1984.
- Klenerman, D., and I. W. M. Smith, Infrared chemiluminescence studies using a SISAM spectrometer, *J. Chem. Soc., Faraday Trans. 2*, **83**, 229, 1987.
- Lipson, S. J., P. S. Armstrong, J. R. Lowell, W. A. M. Blumberg, D. E. Paulsen, M. E. Fraser, W. T. Rawlins, B. D. Green, R. E. Murphy, and J. A. Dodd, EXCEDE III observations of emissions from highly vibrationally and rotationally excited nitric oxide (abstract), *Eos Trans. AGU*, **73**(43), Fall Meeting Suppl., 419, 1992.
- Llewellyn, E. J., and B. H. Long, The OH Meinel bands in the airglow--the radiative lifetime, *Can. J. Phys.*, **56**, 581, 1978.
- Makhlouf, U., R. H. Picard, and J. R. Winick, Modulation of the hydroxyl emission by a monochromatic gravity wave in a realistic, non-isothermal atmosphere (abstract), *Eos Trans. AGU*, **71**(43), Fall Meeting Suppl., 1496, 1990.
- McDade, I. C., The altitude dependence of the  $\text{OH}(X^2\Pi)$  vibrational distribution in the nightglow: Some model expectations, *Planet. Space Sci.*, **39**, 1049, 1991.
- McDade, I. C., and E. J. Llewellyn, Kinetic parameters related to sources and sinks of vibrationally excited OH in the nightglow, *J. Geophys. Res.*, **92**, 7643, 1987.
- Meinel, A. B., OH emission bands in the spectrum of the night sky I, *Astrophys. J.*, **111**, 555, 1950.
- Mertz, L., Auxiliary computation for Fourier spectrometry, *Infrared Phys.*, **7**, 17, 1967.
- Mies, F. H., Calculated vibrational transition probabilities of  $\text{OH}(X^2\Pi)$ , *J. Molec. Spectrosc.*, **53**, 150, 1974.
- Mikulecky, K., and K.-H. Gericke, The influence of vibrational and translational motion on the reaction dynamics of  $\text{O}(^1D) + \text{H}_2(^1\Sigma_g^+, v)$ , *J. Chem. Phys.*, **96**, 7490, 1992.
- Mlynczak, M. G., and S. R. Drayson, Calculation of infrared limb emission by ozone in the terrestrial middle atmosphere, 1. Source functions, *J. Geophys. Res.*, **95**, 16,497, 1990a.
- Mlynczak, M. G., and S. R. Drayson, Calculation of infrared limb emission by ozone in the terrestrial middle atmosphere, 2. Emission calculations, *J. Geophys. Res.*, **95**, 16,513, 1990b.
- Mlynczak, M. G., and S. Solomon, A detailed evaluation of the heating efficiency in the middle atmosphere, *J. Geophys. Res.*, **98**, 10,517, 1993.
- Nelson, D. D., Jr., A. Schiffman, D. J. Nesbitt, J. J. Orlando, and J. B. Burkholder,  $\text{H} + \text{O}_3$  Fourier-transform infrared emission and laser absorption studies of  $\text{OH}(X^2\Pi)$  radical: An experimental dipole moment function and state-to-state Einstein A coefficients, *J. Chem. Phys.*, **93**, 7003, 1990.
- Ohoyama, H., T. Kasai, Y. Yoshimura, H. Kimura, and K. Kuwata, Initial distribution of vibration of the OH radicals produced in the  $\text{H} + \text{O}_3 \rightarrow \text{OH}(X^2\Pi_{1/2,3/2}) + \text{O}_2$  reaction. Chemiluminescence by a crossed beam technique, *Chem. Phys. Lett.*, **118**, 263, 1985.
- Pendleton, W. R., Jr., P. J. Espy, and M. R. Hammond, Evidence for nonlocal thermodynamic equilibrium rotation in the OH nightglow, *J. Geophys. Res.*, **98**, 11,567, 1993.
- Philbrick, C. R., Atmospheric composition: The oxygen constituents, in *Handbook of Geophysics and the Space Environment*, edited by A.S. Jursa, pp. 21:42-21:44, Air Force Geophysics Laboratory, Hanscom AFB, Mass., 1985.
- Pine, A. S., and J. P. Looney,  $\text{N}_2$  and air broadening in the fundamental bands of HF and HCl, *J. Molec. Spectrosc.*, **122**, 41, 1987.
- Polanyi, J. C., and K. B. Woodall, Mechanism of rotational relaxation, *J. Chem. Phys.*, **56**, 1563, 1972.
- Polanyi, J. C., and J. J. Sloan, Detailed rate constants for the reactions  $\text{H} + \text{O}_3 \rightarrow \text{OH}(v', J') + \text{O}_2$ , and  $\text{H} + \text{NO}_2 \rightarrow \text{OH}(v', J') + \text{NO}$ , *Int. J. Chem. Kinet. Suppl.*, **1**, 51, 1975.
- Press, W. H., B. P. Flannery, S. A. Teukolsky, and W. T. Vetterling, *Numerical Recipes*, pp. 390-407, Cambridge University Press, New York, 1986.
- Rawlins, W. T., Chemistry of vibrationally excited ozone in the upper atmosphere, *J. Geophys. Res.*, **90**, 12,283, 1985.
- Rawlins, W. T., M. E. Fraser, and S. M. Miller, Rovibrational excitation of nitric oxide in the reaction of  $\text{O}_2$  with metastable atomic nitrogen, *J. Phys. Chem.*, **93**, 1097, 1989.
- Rawlins, W. T., M. E. Fraser, L. G. Piper, W. A. M. Blumberg, and S. M. Miller, The aeronomy of aurorally excited infrared fluorescence from rovibrationally excited nitric oxide (abstract), *Eos Trans. AGU*, **73**(43), Fall Meeting Suppl., 430, 1992.
- Rawlins, W. T., A. M. Woodward, and D. R. Smith, Aeronomy of infrared ozone fluorescence measured during an aurora by the SPIRIT 1 rocket-borne interferometer, *J. Geophys. Res.*, **98**, 3677, 1993.

- Rensberger, K. J., J. B. Jeffries, and D. R. Crosley, Vibrational relaxation of  $\text{OH}(X^2\Pi_1, v=2)$ , *J. Chem. Phys.*, **90**, 2174, 1989.
- Rothman, L. S., et al., The HITRAN molecular database: Editions of 1991 and 1992, *J. Quant. Spectrosc. Radiat. Transfer*, **48**, 469, 1992.
- Rynefors, K., P. A. Elofson, and L. Holmlid, Monte Carlo simulation of  $\text{O}(^1D) + \text{H}_2$  and  $\text{O}(^1D) + \text{HCl}$ -Rotational excitation of product OH radicals, *Chem. Phys.*, **100**, 53, 1985.
- Schiffman, A., and D. J. Nesbitt, Pressure-broadening and collisional narrowing in  $\text{OH}(v=1 \leftarrow 0)$  rovibrational transitions with Ar, He,  $\text{O}_2$ , and  $\text{N}_2$ , *J. Chem. Phys.*, *in press*, 1993.
- Sears, T. J., G. E. Hall, and J. J. F. McAndrew, Rotational populations in OD formed in the reaction  $\text{O}(^1D) + \text{D}_2$  investigated by infrared rotational absorption spectroscopy, *J. Chem. Phys.*, **91**, 5201, 1989.
- Sharma, R. D., A. J. Ratkowski, R. L. Sundberg, J. W. Duff, L. S. Bernstein, P. K. Acharya, J. H. Gruninger, D. C. Robertson, and R. J. Healey, Description of SHARC, the strategic high-altitude radiance code, *Rep. GL-TR-89-0229*, 218 pp., Geophysics Laboratory, Hanscom AFB, Mass., 1989.
- Sirkin, E. R., and G. C. Pimentel, HF rotational laser emission through photoelimination from vinyl fluoride and 1,1-difluoroethene, *J. Chem. Phys.*, **75**, 604, 1981.
- Sivjee, G. G., and R. M. Hamwey, Temperature and chemistry of the polar mesopause OH, *J. Geophys. Res.*, **92**, 4663, 1987.
- Sloan, J. J., On the dynamics of abstraction, insertion, and addition-elimination reactions in the gas phase, *J. Phys. Chem.*, **92**, 18, 1988.
- Smith, J. H., and D. W. Robinson, The OH and OD laser: Collision-induced energy transfer pumping, *J. Chem. Phys.*, **68**, 5474, 1978.
- Smith, D. R., W. A. M. Blumberg, R. M. Nadile, S. J. Lipson, E. R. Huppi, N. B. Wheeler, and J. A. Dodd, Observation of high- $N$  hydroxyl pure rotation lines in atmospheric emission spectra by the CIRIS 1A space shuttle experiment, *Geophys. Res. Lett.*, **19**, 593, 1992.
- Solomon, S., J. T. Kiehl, B. J. Kerridge, E. E. Remsburg, and J. M. Russell III, Evidence for nonlocal thermodynamic equilibrium in the  $\nu_3$  mode of mesospheric ozone, *J. Geophys. Res.*, **91**, 9865, 1986.
- Spencer, J. E., and G. P. Glass, The production and subsequent relaxation of vibrationally excited OH in the reaction of atomic oxygen with HBr, *Int. J. Chem. Kinet.*, **11**, 97, 1977.
- Streit, G. E., and H. S. Johnston, Reactions and quenching of vibrationally excited hydroxyl radicals, *J. Chem. Phys.*, **64**, 95, 1976.
- Thompson, D. L., Vibrational-rotational-translational energy transfer in Ar + OH. Quasiclassical trajectory state-to-state cross sections, *J. Phys. Chem.*, **86**, 2538, 1982a.
- Thompson, D. L., Quasiclassical trajectory state-to-state cross sections for energy transfer in Ar + OH( $v=9, J=0,4,8$ ) collisions, *Chem. Phys. Lett.*, **92**, 383, 1982b.
- Varandas, A. J. C., and J. M. C. Marques, A detailed state-to-state low-energy dynamics study of the reaction  $\text{O}(^3P) + \text{OH}(^2\Pi) \rightarrow \text{O}_2(X^3\Sigma_g^-) + \text{H}(^2S)$  using a quasiclassical trajectory-internal-energy quantum-mechanical-threshold method, *J. Chem. Phys.*, **97**, 4050, 1992.
- Wellard, S., J. Blakeley, S. Brown, B. Bartschi, and E. R. Huppi, Cryogenic Michelson interferometer on the space shuttle, paper presented at SPIE International Symposium on Optical Applied Science and Engineering, Soc. of Photo-Opt. Instrum. Eng., San Diego, July 23-24, 1992.
- Wertz, J. R., Appearance of the earth at infrared wavelengths, in *Spacecraft Attitude Determination and Control*, edited by J.R. Wertz, pp. 90-98, D. Reidel, Norwell, Mass., 1978.
- Zare, R. N., *Angular Momentum*, pp. 297-317, Wiley-Interscience, New York, 1988.
- S. M. Adler-Golden, Spectral Sciences, Inc., 111 South Bedford Street, Burlington, MA 01803.
- P. S. Armstrong and J. A. Dodd, Stewart Radiance Laboratory, 139 Great Road, Bedford, MA 01730.
- W. A. M. Blumberg, S. J. Lipson, J. R. Lowell, and R. M. Nadile, Phillips Laboratory, Geophysics Directorate/GPO, 29 Randolph Road, Hanscom Air Force Base, MA 01731.
- B. D. Green, K. W. Holtzclaw, and W. J. Marinelli, Physical Sciences Inc., 20 New England Business Center, Andover, MA 01810.

(Received May 7, 1993; revised November 24, 1993; accepted November 24, 1993.)

# Photochemical-dynamical modeling of the measured response of airglow to gravity waves

## 1. Basic model for OH airglow

U.B. Makhoul,<sup>1</sup> R.H. Picard, and J.R. Winick

Phillips Laboratory, Geophysics Directorate, Hanscom Air Force Base, Massachusetts

**Abstract.** A photochemical-dynamical model for the OH Meinel airglow is developed and used to study the fluctuations in OH emission due to atmospheric gravity waves propagating through the mesosphere. The linear response of the OH Meinel emission to gravity wave perturbations is calculated assuming realistic photochemistry and gravity wave dynamics satisfying Hines (1960) isothermal windless model. The current model differs from prior models in that it considers fluctuations in vibrationally excited hydroxyl populations [OH( $\nu$ )] instead of fluctuations in the production rate of OH( $\nu$ ). Two types of correction terms to the latter class of models are found, one involving advection of excited-state populations by the gravity wave and one involving quenching of OH( $\nu$ ) by collisions with perturber molecules. Effects of these additional terms are expressed in terms of the so-called Krassovsky ratio  $\eta$ , which relates relative fluctuations in the column intensity measured by a passive optical instrument to relative fluctuations in the ambient temperature. The extra wave advection term is found to be unimportant under typical conditions, but quenching is important and has two major effects: (1) It makes  $\eta$  a vibrational-level-dependent quantity, and (2) it can lower  $\eta$  by more than 50% depending on the wave period. A typical range for  $\eta$  over a reasonably chosen range of wave parameters was found to be from less than 1 up to 9. The measuring instrument was also explicitly considered in the model formulation. Instead of simply assuming that the instrument measured the brightness-weighted temperature, as is commonly done in gravity wave response models, two common instruments for determining temperature from passive column-integrated measurements were explicitly modeled. The instruments modeled consisted of (1) a moderate-resolution instrument, such as a Michelson interferometer, which infers the temperature from the ratio of two rotational lines in a vibrational band (the rotational temperature) and (2) a high-resolution instrument, such as a Fabry-Pérot interferometer, which uses the Doppler width of a single line to infer the temperature (the Doppler temperature). For gravity waves with large phase velocity (large-scale waves), calculations by both of these methods are found to be generally in agreement with each other and with the brightness-weighted temperature. However, for gravity waves with small phase velocity (small-scale waves) the two realistic simulations can differ from simulations using the brightness-weighted temperature by as much as 35%. The effect of vertical standing waves is considered by modifying the Hines model to include a rigid ground boundary. It is found that the standing waves have a profound effect on the phase of the gravity wave response. Values of  $\eta$  generated from the model are compared with published ground-based OH Meinel measurements of a quasi-sinusoidal short-period gravity wave by Taylor et al. (1991) from Sacramento Peak, New Mexico, at 15° elevation, as well as with the Svalbard polar-night data of Viereck and Deehr (1989). The agreement was found to be reasonable in both amplitude and phase for standing waves.

## 1. Introduction

Many observations of the hydroxyl airglow emissions reveal evidence of temporal and spatial structures in these emissions [e.g., Krassovsky, 1972; Peterson and Kieffaber, 1973; Krassovsky et al., 1977; Noxon, 1978; Takahashi et al., 1985; Taylor et al., 1987; Viereck and

Deehr, 1989; Taylor and Hill, 1991; Taylor et al., 1991]. Since such structures have been related to the passage of atmospheric internal gravity waves (IGWs) [Hines, 1960] through the emitting layer, their observation in the OH emission layer can be used as a probe to study the IGWs and their role in the dynamics of the middle atmosphere.

The so-called Krassovsky ratio  $\eta$  [Krassovsky, 1972] is a measure of the airglow response to a periodic dynamical perturbation such as an IGW and relates the observed relative fluctuations in the airglow brightness to the relative fluctuations in the ambient temperature averaged over the emission layer,

$$\eta_{\nu} = \frac{\Delta B_{\nu\nu'}/B_{0\nu\nu'}}{\Delta T/T_0} \quad (1)$$

<sup>1</sup>Now at Stewart Radiance Laboratory, Bedford, Massachusetts.

where  $B_{0v}$  is the steady state unperturbed column brightness on the transition between vibrational level  $v$  and level  $v'$ ,  $\Delta B_{vv'}$  is the fluctuation in this brightness, and  $T_0$  and  $\Delta T$  are the steady state temperature and its fluctuation. (The subscript  $v$  in  $\eta$  is used only to emphasize vibrational level dependency.)

The value of  $\eta$  is independent of the amplitude of the perturbation in the regime where the response is linear. In addition, it has been shown, in principle, to depend on the airglow photochemistry and dynamics. Krassovsky [1972] showed that  $\eta$  was dependent upon the order of the rate-limiting reaction and wrote

$$\eta = \frac{2}{\gamma - 1} - \mu \quad (2)$$

where  $\gamma = c_p/c_v$  is the specific heat ratio and  $\mu$  is the coefficient of temperature dependence  $T^{-\mu}$ , of the rate constant  $k(T)$  for the rate-limiting reaction (in the case of the OH Meinel bands, this is the three-body formation reaction for  $O_3$ ). This relation was revisited recently by Hines and Tarasick [1987].

When the IGW period is much longer than the photochemical lifetimes, the chemical production and loss rates are determined by the instantaneous species concentrations, and one would expect Krassovsky's expression for  $\eta$ , equation (1), to be approximately correct. However, Walterscheid *et al.* [1987] showed that when the IGW period shortens enough to become comparable to the photochemical lifetime, the simple Krassovsky result given by equation (2) is modified due to coupling of the chemistry and dynamics, which makes the response dependent on wave period. They formulated an Eulerian photochemical-dynamical model for the hydroxyl airglow IGW modulation problem by coupling a five-reaction photochemical model from a set of  $O_x/HO_x$  reactions described by Winick [1983] with Hines [1960] dynamical model for an IGW in an isothermal windless atmosphere.

The Krassovsky ratio  $\eta$  that Walterscheid *et al.* [1987] calculated pertained to a single atmospheric height level, since they did not integrate across the OH emission layer, and hence their results were applicable only when the vertical IGW wavelength was large compared with the layer thickness (that is for a large-scale wave or a thin emitting layer). In a later publication, Schubert and Walterscheid [1988] extended the calculations to an airglow layer with a finite thickness. They used a brightness-weighted temperature (BWT) [Weinstock, 1978; Noxon, 1978] to obtain an  $\eta$  value applicable to a column-integrated measurement. Schubert *et al.* [1991] incorporated eddy diffusivity and molecular viscosity effects [Hickey, 1988a, b] into the model. The latter were shown to have an effect on long-period, small-vertical-scale gravity waves.

These models have been extended to other radiating states including the  $O_2 b^1\Sigma_g^+$  state, source of the  $O_2$  atmospheric bands [Tarasick and Shepherd, 1992a; Zhang *et al.*, 1992; Hickey *et al.*, 1993], and the sodium nightglow [Plane and Hickey, 1993].

Nevertheless, there still remain important effects which have been neglected in the existing models. In particular, most OH airglow models have ignored the effects of quenching [Walterscheid *et al.*, 1987; Schubert and Walterscheid, 1988; Schubert *et al.*, 1991]. Quenching is well known to have a significant effect on the steady state OH emission profile and integrated column radiance. We will show in this paper that quenching also has a profound effect on the response of the OH Meinel emission to IGW forcing. A recent paper by Tarasick and Shepherd [1992b] also included quenching of individual vibrational levels but made approximations that avoided solving the full set of photochemical-dynamical equations. In particular, one of their approximations was to drop two members of the reaction set of Walterscheid *et al.*, [1987], denoted here by (R2) and (R4) below. By contrast, in this paper we solve the fully coupled photochemistry and dynamics to determine the role of quenching and find no need to reduce the reaction set or introduce further simplifying assumptions.

When defining temperature for an inhomogeneous atmospheric emission layer, modelers have universally assumed that the BWT is the quantity of interest. However, no instrument measures the BWT directly, and in this paper we compare  $\eta$  values based on the BWT to  $\eta$  values determined from experimentally observable temperature measures, namely, the rotational temperature ( $T_{rot}$ ), based on the ratio of line intensities in a rovibrational band, and the Doppler temperature ( $T_{Dop}$ ), based on the width of a single Doppler-broadened emission line.

Other researchers have often tended to use generic unperturbed atmospheric profiles, including density profiles for reactive species such as  $O_3$ , O, H, and  $HO_2$ , instead of profiles appropriate to the season, latitude, and time of day of the measurements to which they were comparing their model results. An exception is Hickey *et al.* [1992], who have used minor species profiles output from the two dimensional photochemical model of Garcia and Solomon [1985] for the month and latitude of interest. Since there can be a significant seasonal/latitudinal dependence [Le Texier *et al.*, 1987, 1989] to the unperturbed OH Meinel emission profile, as well as a diurnal variation, in this paper we have chosen profiles for the major species in the background atmosphere from an existing climatological model [Summers, 1993], then adapted a diurnal photochemical model [Winick *et al.*, 1985] to determine the profiles of the reactive minor species.

In addition, our model is formulated to allow for an oblique line of sight (LOS). Using a flat-Earth approximation, following Tarasick and Hines [1990], we compare our model results with oblique-looking data on a quasi-sinusoidal wave event recorded by Taylor *et al.* [1991] from Sacramento Peak, New Mexico.

In our model we have followed closely the approach of Walterscheid *et al.* [1987] in linearizing the coupled continuity equations for the response of major and minor species of interest to the applied IGW including all photochemical couplings. Unlike Walterscheid *et al.*, however, we have calculated the photon emission rate from

each vibrational transition separately rather than assuming that the emission rate is equal to the production rate of the vibrationally excited OH. Our kinetic scheme then couples fourteen species: the five of Walterscheid et al. plus the nine lowest vibrationally excited states of OH. This formalism enables us to identify vibrational-level-dependent loss effects. In addition, we add a few minor, but nonnegligible, reactions from *Winick* [1983] to the photochemical scheme which they used.

Although we focus on the OH Meinel airglow in this paper, many of the methods we use and points we make are quite general and would apply equally well to other radiating species. This is true, for example, of the method of incorporating quenching and of the nature of effects due to inhomogeneous atmospheres.

We continue in the next section (section 2) by describing the model used for the background atmospheric composition along with the diurnal photochemical model for the reactive minor species. Section 3 describes the chemistry of the production and loss processes used to calculate the OH vibrational level populations,  $[\text{OH}(v)]$ , including both their steady state values and their response to IGW perturbations. We write the continuity equations for the populations of the nine relevant vibrationally excited levels of OH, plus the five reactive  $\text{O}_x/\text{HO}_x$  species, and briefly discuss their steady state solution, including the impact of quenching. Section 4 describes the IGW isothermal windless model and the calculation of the first-order response of the OH vibrational populations coupled to the reactive minor species. In section 5 we compare different methods used to infer the effective temperature in an inhomogeneous atmosphere from airglow observations, among themselves and with the BWT customarily used in models. We use the comparison to assess the influence of atmospheric stratification and of the temperature determination method on the amplitude and phase of the Krassovsky ratio. We discuss the effect of quenching on the linear emission perturbation in section 6. In section 7 we introduce the isothermal model with a ground boundary condition, yielding vertical standing waves. Section 8 discusses interference effects occurring in the short-vertical-wavelength limit for an isothermal atmosphere, and we compare the results of model calculations with experimental data and with other models. After comparing our results with the measurements of *Taylor et al.* [1991] and *Viereck and Deehr* [1989], we find that our simulations are in general agreement with many features of the data, especially for IGWs with periods less than 1 hour. In the case of the latter data, we find that vertically standing gravity waves were required in the model to obtain better agreement. We conclude in the last section (section 9) by recapitulating the main points and discussing requirements for future work.

In a follow-on paper we will consider the effects of background winds and of a non isothermal atmosphere on the IGW and, in turn, on the  $\text{OH}(v)$  dynamical response. We will also perform more detailed comparisons with data.

## 2. Background Atmospheric and Diurnal Models

We start with a simple one-dimensional (1-D) diurnal photochemical model to generate photochemically self-consistent number-density profiles for reactive minor species in the atmosphere, in particular for  $[\text{O}]$ ,  $[\text{H}]$ ,  $[\text{OH}]$ ,  $[\text{O}_3]$ , and  $[\text{HO}_2]$ . The diurnal model generates profiles for a specified latitude, day of the year, and time of day, and was used previously by *Winick et al.* [1985] to predict the time dependence of  $[\text{O}_3]$  and  $\text{O}_2(^1\Delta_g)$  emission near the dawn terminator for the SPectral Infrared Rocket Experiment (SPIRE) [*Stair et al.*, 1985]. The model includes  $\text{O}_x$ ,  $\text{HO}_x$ ,  $\text{NO}_x$ , and  $\text{ClO}_x$  chemistry and allows eddy transport of  $\text{O}_x$  and  $\text{HO}_x$ . The time-dependent continuity equations for the minor species are solved by the family technique [e.g., *Winick*, 1983]. Chemical reaction rates in the model were updated from the latest *Jet Propulsion Laboratory* [1990] compilation, supplemented by rates from recent publications as described in the next section. Eddy-diffusion coefficients have been updated from *Strobel et al.* [1987]. The major species density profiles,  $[\text{O}_2(z)]$  and  $[\text{N}_2(z)]$ , as well as profiles for temperature  $T(z)$ , pressure  $p(z)$ , methane density  $[\text{CH}_4(z)]$ , and water-vapor density  $[\text{H}_2\text{O}(z)]$  are taken from the trace constituent climatological model of *Summers* [1993]. This climatological model was compiled from data and is supplemented by output from a two-dimensional photochemical model. Profiles for every month and all latitudes, in multiples of  $+10^\circ$ , are contained in the model. Background atmospheric profiles of  $[\text{N}_2]$ ,  $[\text{O}_2]$ , and  $[\text{H}_2\text{O}]$ , in addition to the temperature  $T$ , are shown in Figures 1 (a) and (b) for June at  $30^\circ\text{N}$  latitude. This specific latitude and time are chosen because below we compare our model with observations made from the White Sands Missile Range Tracking Station at Sacramento Peak ( $30^\circ\text{N}$ ,  $105.8^\circ\text{W}$ ), New Mexico, during the new-moon period on day 165 in 1983 near local midnight [*Taylor et al.*, 1991].

The profiles from the model of *Summers* [1993] (Figures 1) are entered into the 1-D diurnal model, initial starting profiles for the reactive minor species are assumed, and the simulation is run through 15 diurnal cycles until the initial transient dies away and a diurnally reproducible steady state results. Minor species density profiles are calculated from 30 to 120 km. The results for the density profiles of reactive species in the  $\text{O}_x$  and  $\text{HO}_x$  families from 70 to 100 km with the input from Figure 1 are shown in Figure 2.

## 3. Steady State Vibrational Level Production and Loss Processes

The minor species profiles, generated from the 1-D diurnal model, are used as an input to our kinetic model for vibrational level populations  $\text{OH}(v)$ , which includes an expanded reaction set for production and loss of OH



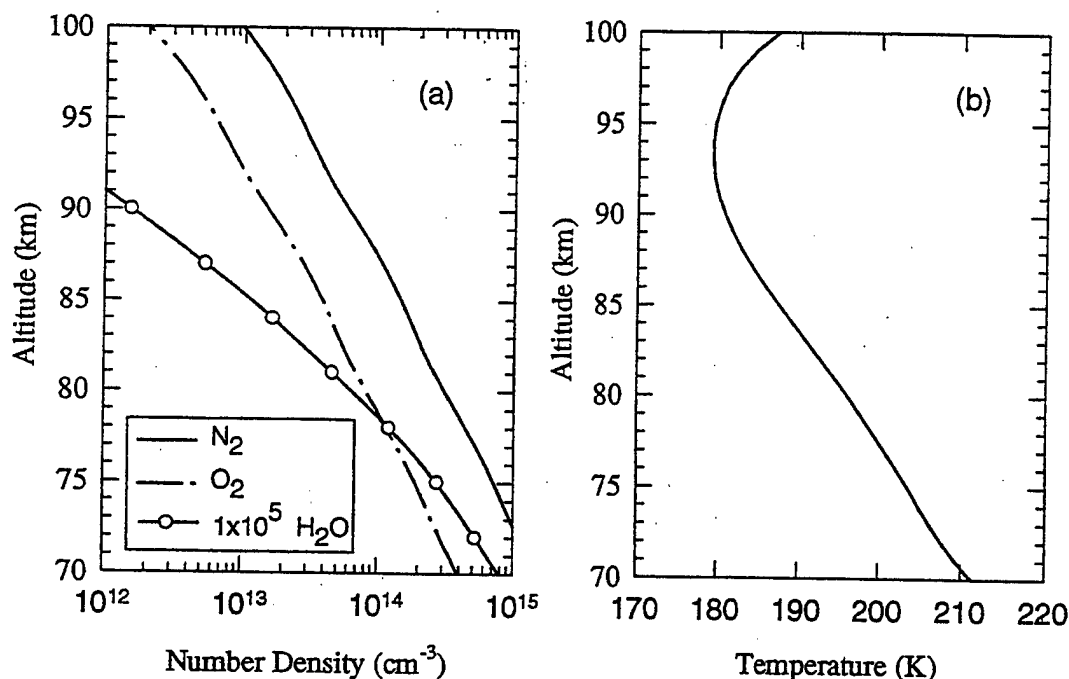


Figure 1. Background atmospheric profiles for June, 30°N latitude from the climatological model of Summers [1993] used as input to the 1-D photochemical model. Altitude range plotted is restricted to range of interest for OH airglow. (a) Altitude profiles of  $[\text{N}_2]$ ,  $[\text{O}_2]$ , and  $[\text{H}_2\text{O}]$ . (b) Temperature profile.

vibration. This reaction set includes chemical quenching of  $\text{OH}(v)$  by atomic oxygen and collisional quenching by the molecular species  $\text{O}_2$  and  $\text{N}_2$ . The following reactions are used in our OH vibrational kinetic model:

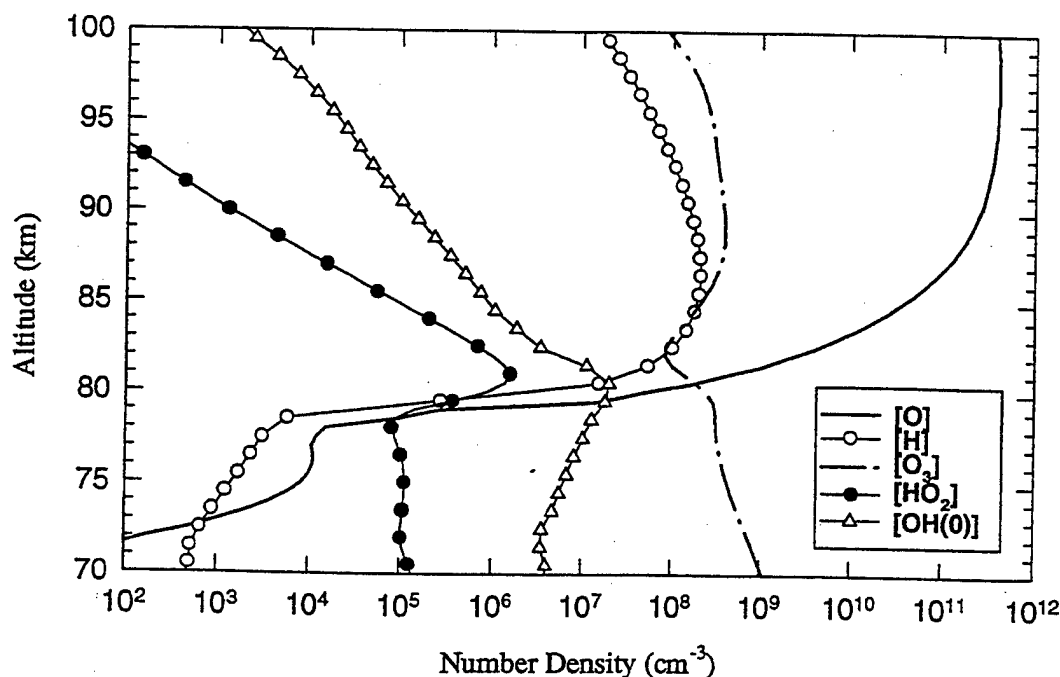
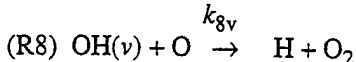
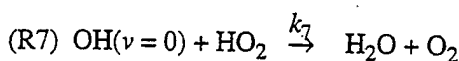
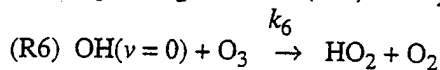
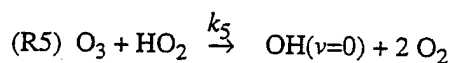
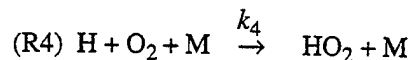
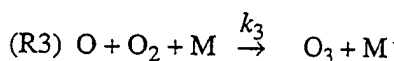
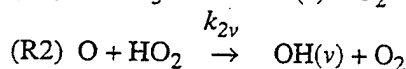
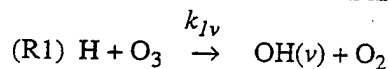
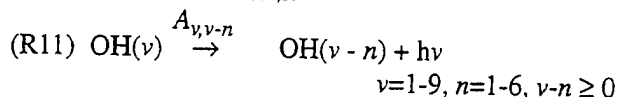
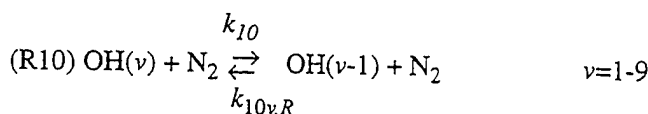
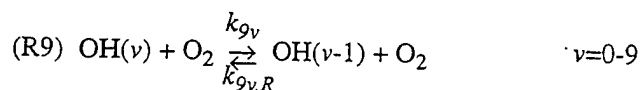


Figure 2. Minor-species profiles generated by the 1-D photochemical model for local midnight, day 165 at 30°N latitude.





The rate constants  $k_1, \dots, k_{10}$  are listed in Table 1. The rates of the reverse reactions,  $k_{9v,R}$  and  $k_{10v,R}$ , resulting in collisional excitation, are determined from  $k_{9v}$  and  $k_{10v}$  by detailed balance; for example  $k_{9v,R} = k_{9v} \exp[-(E_v - E_{v-1})/k_B T]$ , where  $E_v$  is the energy of vibrational level  $v$  and  $k_B$  is Boltzmann's constant. The band-averaged Einstein A coefficients  $A_{v,v-n}$  are from Table 1 of *Turnbull and Lowe* [1989], although an alternate set of A coefficients is available from *Nelson et al.* [1990].

The basic five-reaction kinetic scheme for total [OH] employed by *Walterscheid et al.* [1987], selected from the reactions of *Winick* [1983], consists of reactions (R1) - (R4), plus reaction (R8). To extend the reaction set to OH( $v$ ) kinetics, we have added to these reactions (1)

quenching of OH( $v$ ) by O<sub>2</sub> and N<sub>2</sub> (reactions (R9) and (R10)), (2) radiative decay (reaction (R11)), and less importantly, (3) additional sources and sinks of OH( $v=0$ ) (reactions (R5) - (R7)). In addition, we have introduced vibrational level dependence in a number of reactions. For example, we have allowed reaction (R2) to be a source of vibrationally excited OH and have used the OH destroying reaction (R8) to chemically quench OH( $v$ ).

Since the work of *Bates and Nicolet* [1950], reaction (R1) between atomic hydrogen and ozone has been known to be the primary reaction producing OH( $v$ ). The vibrational levels  $v=6-9$  are populated using the branching ratios of *Klenerman and Smith* [1987]. The secondary OH production reaction (R2) in our model is assumed to produce OH( $v$ ) in  $v=0-3$  in our model, although all levels  $v \leq 6$  are energetically accessible in the reaction. Significant differences of opinion exist in the literature concerning the role of this secondary reaction. Some researchers [*Llewellyn et al.*, 1978; *McDade and Llewellyn*, 1987] believe that reaction (R2) does not produce vibrationally excited OH. *Lunt et al.* [1988] cite laboratory evidence that vibrationally excited OH is produced in reaction (R2), but they were unable to measure the vibrational branching ratios. *López-Moreno et al.* [1987]

Table 1. Rate Constants for OH( $v$ ) Production and Loss Processes

Rate constant	Value <sup>a</sup>	Comments
$k_{1v}$	$1.4 \times 10^{-10} \exp(-470/T) b(v)$	$b(v)$ is branching ratio for reaction (R1), <sup>b</sup> $b(9) = 0.48, b(8) = 0.27, b(7) = 0.17,$ $b(6) = 0.08, b(v) = 0.$ for $v = 0-5$ .
$k_{2v}$	$3.0 \times 10^{-11} d(v)$	$d(v)$ is the branching ratio for reaction (R2), <sup>c</sup> $d(0) = 0.52, d(1) = 0.34, d(2) = 0.13,$ $d(3) = 0.01, d(v) = 0.$ for $v = 4-9$
$k_3$	$6.0 \times 10^{-34} (300/T)^{2.3}$	three-body O <sub>3</sub> production
$k_4$	$5.7 \times 10^{-32} (300/T)^{1.6}$	three-body HO <sub>2</sub> production
$k_5$	$1.1 \times 10^{-14}$	production of OH(0) only
$k_6$	$1.6 \times 10^{-12} \exp(-940/T)$	chemical loss of OH(0) only
$k_7$	$4.8 \times 10^{-11}$	chemical loss of OH(0) only
$k_{8v}$	$a_8(v) \times 10^{-11}$	$a_8(0)=3.9, a_8(1)=10.5, a_8(v)=25.$ for $v = 2-9$
$k_{9v}$	$a_9(v) \times 10^{-13}$	$a_9(1)=1.3, a_9(2)=2.7, a_9(3)=5.2, a_9(4)=8.8, a_9(5)=17.,$ $a_9(6)=30., a_9(7)=54., a_9(8)=98., a_9(9)=170.$
$k_{10v}$	$a_{10}(v) \times 10^{-14}$	$a_{10}(1)=0.58, a_{10}(2)=1.0, a_{10}(3)=1.7, a_{10}(4)=3.0,$ $a_{10}(5)=5.2, a_{10}(6)=9.1, a_{10}(7)=16., a_{10}(8)=27.,$ $a_{10}(9)=48.$
$A_{v,v-n}$	Band-averaged Einstein A coefficients from Table 1 of <i>Turnbull and Lowe</i> [1989]	

<sup>a</sup> Here T is the temperature in Kelvin. Reaction rate constant units are s<sup>-1</sup> for a unimolecular reaction, cm<sup>3</sup> s<sup>-1</sup> for a two-body reaction, and cm<sup>6</sup> s<sup>-1</sup> for a three-body reaction.

<sup>b</sup> *Klenerman and Smith* [1987].

<sup>c</sup> *Kaye* [1988].

assumed that this reaction produces  $\text{OH}(\nu)$  in the vibrational states  $\nu = 3 - 6$ , while *Kaye* [1988] allowed it to produce OH only in low vibrational levels  $\nu = 0 - 3$ . Overall, however, this secondary reaction is believed to be of relatively minor importance as a production mechanism for vibrationally excited OH at night [*Kaye*, 1988; *R.P. Lowe*, private communication 1991], by contrast to its paramount influence in that role under sunlit conditions [*Le Texier et al.*, 1987]. Consequently, we have found that the assumption made concerning its vibrational yield, namely, whether it is assumed to produce only ground state hydroxyl or vibrationally excited OH to varying degrees; will have bearing on the calculated Krassovsky ratio at night only near the terminator. Nevertheless, there will be some effect on the altitude profile of volume emission from the assumption made concerning the  $\text{O} + \text{HO}_2$  vibrational yield. Moreover, reaction (R2) will remain important in determining the partitioning of odd oxygen between  $\text{HO}_2$  and OH, since it is the primary loss mechanism for  $\text{HO}_2$ .

The most important additions to the kinetic scheme are the collisional quenching and radiative loss reactions, reactions (R9) - (R11). The last reaction (R11), representing radiative loss for the various vibrational levels, includes both single quantum and multi quantum transitions. Multi quantum transitions are strong due to the large anharmonicity of the vibrating molecule, and the largest rate is the first overtone ( $\Delta\nu = 2$ ) when  $\nu > 2$ . Even higher overtones ( $\Delta\nu \geq 3$ ) often exceed the fundamental. The total radiative loss rates,  $\sum_\nu A_{\nu\nu'}$ , scale roughly with  $\nu$ , increasing from  $22.74 \text{ s}^{-1}$  for  $\nu = 1$  to  $275.9 \text{ s}^{-1}$  at  $\nu = 9$  at  $T = 200 \text{ K}$  [*Turnbull and Lowe*, 1989].

Many of the quenching rate constants required in reactions (R9) and (R10) are uncertain. Existing experimental measurements are incomplete, and there are few theoretical guides. Quenching by the molecular species is generally assumed to proceed by single-quantum transitions, in accord with the results of Schwartz, Slawsky, Herzfeld (SSH) theory for vibrational relaxation, although there is some question concerning the validity of this assumption, especially for higher  $\nu$  [*Dodd et al.*, 1990]. The rate constants for quenching by molecular oxygen, reaction (R9), are taken from *Dodd et al.* [1991] for  $\nu = 1 - 6$ , from *Knutsen and Copeland* [1993] for  $\nu = 7 - 8$ , and from *Chalamala and Copeland* [1993] for  $\nu = 9$ . The rates increase by more than 2 orders of magnitude between  $\nu = 1$  and  $\nu = 9$  (see Table 1). *Sappey and Copeland* [1990] have also measured the rate for  $\nu = 12$ , which is about the same as the rate for  $\nu = 9$ . The quenching rate constants for molecular nitrogen, reaction (R10), were obtained in a similar manner by interpolating and extrapolating logarithmically between measurements at  $\nu = 2$  [*Rensberger et al.*, 1989] and  $\nu = 12$  [*Sappey and Copeland*, 1990] (see Table 1). The  $\text{N}_2$  quenching rates increase almost as much between  $\nu = 1$  and  $\nu = 9$  as do the corresponding  $\text{O}_2$  rates, but quenching by  $\text{N}_2$  is much less important, since its rates are a factor of 20-35 less than the corresponding  $\text{O}_2$  rates. The effect of quenching by both

$\text{O}_2$  and  $\text{N}_2$  on the OH Meinel band volume emission profiles will be felt most strongly at lower altitudes, manifesting itself as an attenuation of the bottom side of the profile and a raising of the peak altitude.

Reaction (R8) represents sudden-death chemical quenching by atomic oxygen. Its treatment is also quite important, in spite of the fact that the rates for this reaction are somewhat controversial. For  $\nu=0$  the rate constant was taken from *Hampson and Garvin* [1977], and for  $\nu=1$  the value of *Spencer and Glass* [1977] was used. The latter authors noted a factor of 2 - 3 enhancement of the reaction rate constant for  $\nu = 1$  compared to  $\nu = 0$ , so that every other collision resulted in a reaction for  $\nu = 1$ . For  $\nu = 2 - 9$ , there are no experimental values available for  $k_{8\nu}$ . However, *Sivjee and Hamwey* [1987] noted that it is not possible to explain the results on the  $\nu$  dependence of OH Meinel altitude profiles [*Rogers et al.*, 1973; *Baker*, 1978] unless the values of  $k_{8\nu}$  remain large for higher  $\nu$ . They chose a rate constant of  $4.0 \times 10^{-10} \text{ cm}^3/\text{s}$  to fit their data. However, we refrain from using *Sivjee and Hamwey's* value, since it exceeds the gas kinetic collisional limit ( $2.5 \times 10^{-10} \text{ cm}^3/\text{s}$ ) in the OH airglow layer. At the end of this section we examine the effect of the choice of the chemical quenching rate constant  $k_{2\nu}$  on the steady state  $[\text{OH}(\nu)]$  profiles.

We also add to the vibrational-kinetic model further production and loss processes for  $\text{OH}(\nu=0)$ . Reactions (R5) - (R7), although only small contributors, are added to make the reaction set more complete and attempt to bring the sum of  $[\text{OH}(\nu)]$  calculated by the kinetic model into closer agreement with the total [OH] calculated by the 1-D diurnal model.

The procedure is now to insert the reactions (R1) - (R11) into the Eulerian continuity equation for the  $[\text{OH}(\nu)]$ ,  $\nu = 0, \dots, 9$ :

$$\frac{\partial N_\nu}{\partial t} = Q_\nu - L_\nu N_\nu - \text{div}(N_\nu \mathbf{V}) \quad (3)$$

where

- $N_\nu$  number density of  $\text{OH}(\nu) \equiv [\text{OH}(\nu)]$ ;
- $Q_\nu$  photochemical production rate for level  $\nu$ ;
- $L_\nu$  photochemical loss frequency for level  $\nu$ ;
- $\mathbf{V}$  gravity wave velocity field and its Cartesian components ( $u, 0, w$ ).

These equations are coupled to similar continuity equations for the other  $\text{O}_x$  and  $\text{HO}_x$  species involved in OH photochemistry. The values of  $Q_\nu$  and  $L_\nu$  are determined from reactions (R1) - (R11) along with the rate constants in Table 1. The volume emission rates  $I_{\nu\nu'}$  are easily calculated by multiplying the vibrational-level populations  $N_\nu$  by the corresponding Einstein A coefficients,

$$I_{\nu\nu'} = A_{\nu\nu'} N_\nu$$

Our main purpose is to investigate the IGW response of this system, which we do in the next section. However, in the remainder of this section we briefly examine the

solution of equation (3) in the unperturbed steady state, with no IGW present. In the steady state, with no background wind ( $V_0 = 0$ ), the divergence term in equation (3) vanishes, and the resulting equations describe photochemical equilibrium with production equals loss. We obtain

$$0 = Q_{v0} - L_{v0}N_{v0} \quad (4)$$

whose solution is

$$[OH(v)]_0 \equiv N_{v0} = \frac{Q_{v0}}{L_{v0}} \quad (5)$$

The unperturbed volume emission rates  $I_{vv'0}$  are then obtained by replacing  $N_v$  by  $N_{v0}$  from equation (5),

$$I_{vv'0} = A_{vv'} [OH(v)]_0 \quad (6)$$

Using the reactions (R1) - (R11) and the results in Figure 2 for the case mentioned above (day 165, 30°N, local midnight), we have carried out a sensitivity study to show the influence of quenching on the steady state solutions (equation (5)). To do this we employed both a fast gas kinetic rate ( $2.5 \times 10^{-10} \text{ cm}^3/\text{s}$ ) and a slow rate ( $2.2 \times 10^{-11} \text{ cm}^3/\text{s}$ ) for quenching by atomic oxygen of  $OH(v)$  with  $v = 2 - 9$ . A large difference was found as a result of using the fast and slow rates, especially for the lower vibrational states. The results are illustrated in Figure 3, where we show the effect of the choice of the rate constant  $k_{8v}$  on a high ( $v = 9$ ) and a low ( $v = 3$ )  $OH$  energy level. Although atomic oxygen is a minor species compared to  $N_2$  and  $O_2$  around the peak of the emission layer

near 88 km, it is still an important quencher of  $OH$ , especially on the top side of the layer and for the lower vibrational levels, as can be seen in Figure 3. Quenching has a greater effect on the lower vibrational levels, since they are longer-lived. For example, the radiative lifetime for  $OH(9)$  is 3.6 ms at 200 K whereas the  $OH(1)$  lifetime is 44 ms. Notice that the  $[OH(v)]$  peak altitude is lowered slightly as the quenching is increased, in accord with rocket measurements [Rogers *et al.*, 1973; Baker, 1978]. For our model calculations, we have chosen to use the fast rate ( $2.5 \times 10^{-10} \text{ cm}^3/\text{s}$ ) for  $v = 2-9$ . Thus every collision of an  $OH(v)$  molecule with atomic oxygen destroys the  $OH$ .

We also solved equations (5) for all the  $OH$  excited vibrational populations  $N_{v0}$  ( $v = 1 - 9$ ) with inclusion of quenching. The results are shown in Figure 4 and indicate that (1) the  $OH(v)$  vibrational distribution is not strongly altitude dependent and (2) the peaks of the vibrational level populations for  $v = 1 - 9$  fall within a 2-km span of altitude, with the  $v = 9$  peak at a slightly higher altitude than the  $v = 1$  peak. This is attributed to quenching by atomic oxygen, which occurs preferentially on the topside of the layer and affects the longer-lived state  $v = 1$  more than the shorter-lived state  $v = 9$ .

In the next section we consider the IGW model and the linear response of the  $OH$  Meinel bands to the IGW.

#### 4. Internal Gravity wave Dynamical Model and Airglow Linear Response

We assume that a monochromatic IGW perturbs the photochemical system described in section 3. We further assume that the IGW amplitude is small enough so that the wave and the corresponding airglow response can be

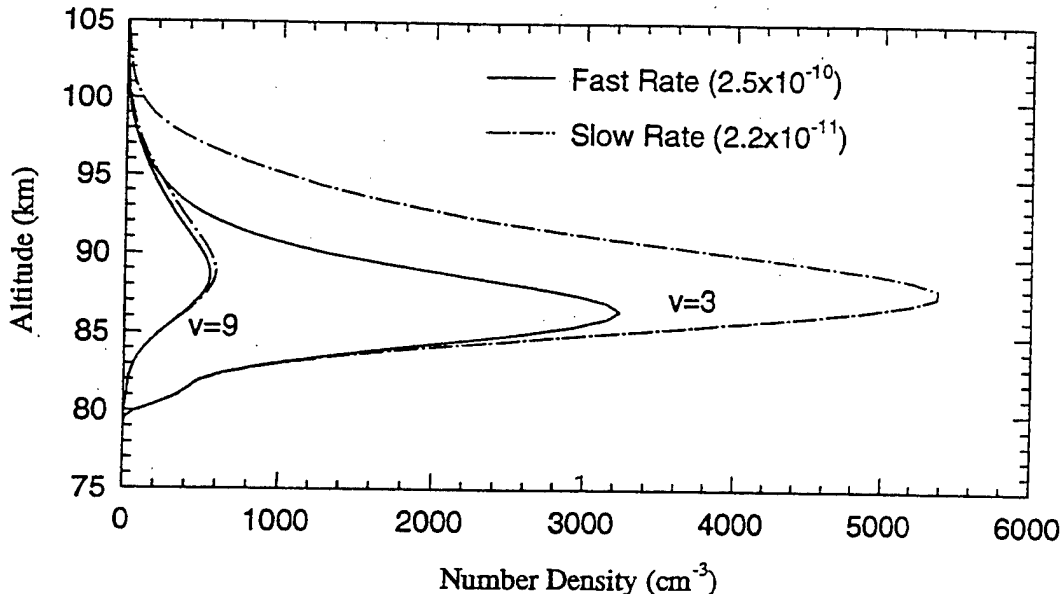


**Figure 3.** Effect of choice of rate constant for chemical quenching of  $OH$  vibration by atomic oxygen [reaction (R8)] on photochemical equilibrium profiles of  $[OH(v=3)]$  and  $[OH(v=9)]$  generated by  $OH$  vibrational kinetic model. The profiles are shown for a fast rate of  $2.5 \times 10^{-10} \text{ cm}^3/\text{s}$  and for a slow rate an order of magnitude less ( $2.2 \times 10^{-11} \text{ cm}^3/\text{s}$ ).

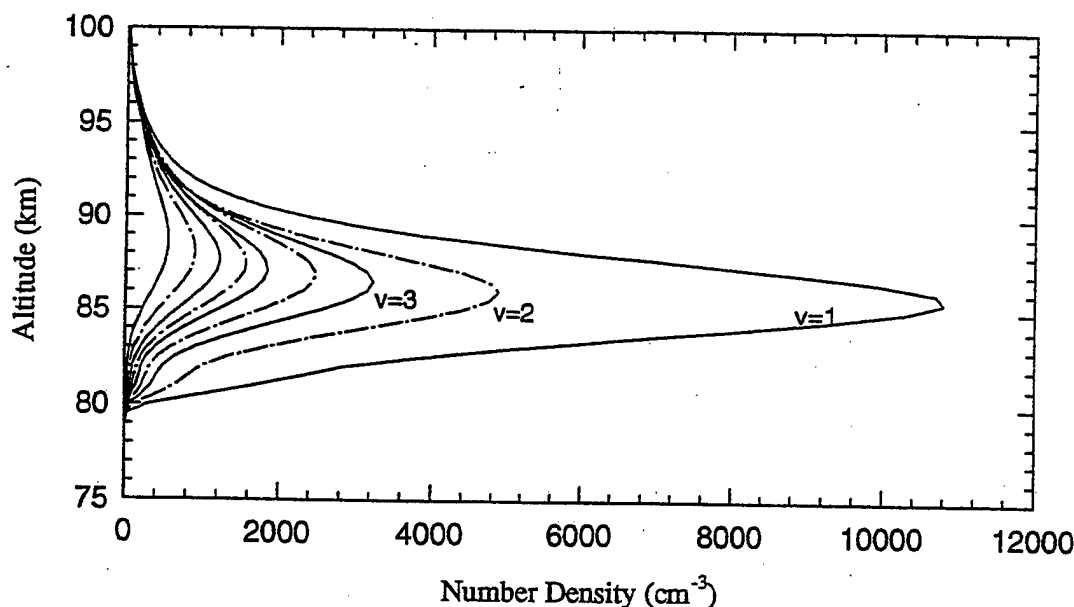


Figure 4. Photochemical equilibrium altitude profiles of  $[\text{OH}(v)]$   $v = 1-9$ , generated by OH vibrational kinetic model using input profiles for day 165, local midnight, 30°N and fast O chemical quenching rate.

treated in the linear approximation [Hines, 1960; Walterscheid *et al.*, 1987]. We calculate the perturbation due to the IGW in the total molecular number density  $N_{\text{tot}}$ , the temperature  $T$ , and the horizontal and vertical components  $u$  and  $w$  of the velocity  $V$ , using Hines' [1960] windless isothermal IGW model.

The Hines model is used in this paper because (1) it yields simple analytic solutions and (2) it allows us to compare our results with those of other investigators who have used it extensively. We have also modeled the effect on airglow of a wave in a non isothermal atmosphere with a sheared background wind [Makhlouf *et al.*, 1990, 1991]. This is a more realistic model for wave propagation that can support waves ducted by the thermal structure of the atmosphere, as well as being a more consistent one. However, this model is less convenient, since it requires a numerical solution of the primitive equations. Since a number of important features can be illustrated without including background wind and non isothermal effects and we wish to perform meaningful comparisons with prior work which used the windless Hines model, we treat only the isothermal, windless case in this paper. The effect of using a realistic gravity wave model in a non isothermal atmosphere with background winds will be considered further in a follow-on publication.

The next step is to linearize equation (3), along with similar continuity equations for the species O,  $\text{O}_3$ , H, and  $\text{HO}_2$ , about the zero-order steady state solution of equation (5), plus the corresponding steady state solutions for the other species. We consider each vibrational level of OH as a separate chemically active species, so that we have a total of 14 species. The corresponding densities are denoted by  $N_i$  ( $i=0, 1, \dots, 13$ ), representing in turn  $[\text{OH}(v)]$  ( $v = 0-9$ ),  $[\text{O}_3]$ ,  $[\text{O}]$ ,  $[\text{H}]$ , and  $[\text{HO}_2]$ , while the corresponding production and loss rates are denoted by  $Q_i$  and

$L_i$ . The number densities of  $\text{O}_2$  and  $\text{N}_2$  are assumed to change only negligibly due to photochemistry and to be affected by the IGW dynamics only.

With no background wind,  $u$  and  $w$  then have no steady state component and are strictly first-order quantities. We expand the remaining variables in the continuity equations to first order about their steady state values by writing, for example,  $X = X_0 + \Delta X$ , for a generic variable  $X$ , where the subscript 0 denotes the steady state value and  $\Delta X$  is the difference from the steady state. Assuming horizontal homogeneity, the first-order linearized form of equation (3) is then

$$\frac{\partial \Delta N_i}{\partial t} = \Delta Q_i - N_{i0} \Delta L_i - L_{i0} \Delta N_i - N_{i0} \left( \frac{\partial u}{\partial x} + \frac{\partial w}{\partial z} \right) - \frac{\partial N_{i0} w}{\partial z} \quad (7)$$

In the Hines IGW model, fluid-parameter perturbations have space-time dependences given by the factor  $\exp[i(\omega t - k_z z - k_x x)]$ , where  $x \neq 0$  will be necessary later to describe an oblique LOS. Moreover, all perturbations in minor-species densities and related quantities will be proportional to this same factor in a linear response model. Putting the space-time factor into equation (7) and dividing by  $N_{i0}$ , we obtain a set of coupled equations for the relative fluctuations in  $N_i$ ,

$$(L_{i0} + i\omega) \frac{\Delta N_i}{N_{i0}} = \frac{\Delta Q_i}{N_{i0}} - \Delta L_i + i k_x u - \frac{\partial w}{\partial z} - \frac{1}{N_{i0}} \frac{\partial N_{i0} w}{\partial z} \quad (8)$$

Substituting the zero-order number density, the perturbed production and loss rates for each species, and the IGW particle velocity in equation (8), we obtain 14 linear algebraic equations for the 14 unknown species density perturbations  $\Delta N_i$  driven by the IGW velocity. Solving

these equations, we obtain, in particular, the desired perturbations in the OH level populations  $\Delta[\text{OH}(\nu)] = \Delta N_{i=\nu}$ ,  $\nu = 1 - 9$ . The perturbed volume emission rate is then  $I_{\nu\nu'} = I_{\nu\nu'0} + \Delta I_{\nu\nu'}$ , to first order, where

$$\Delta I_{\nu\nu'} = A_{\nu\nu'} \Delta[\text{OH}(\nu)] \quad (9)$$

Dividing equation (9) by equation (6), we see that  $\Delta I_{\nu\nu'}/I_{\nu\nu'0} = \Delta N_{\nu}/N_{\nu0}$ . Since the  $A$  coefficients have cancelled, we see that the fractional fluctuation in the emission rate is the same for all bands originating in the same upper level  $\nu$ . Using equation (8) for  $\Delta N_{\nu}/N_{\nu0}$  and noting from equation (4) that  $L_{\nu0} N_{\nu0} = Q_{\nu0}$ , we obtain an equation for the relative fluctuation in the emission rate,

$$\frac{\Delta I_{\nu\nu'}}{I_{\nu\nu'0}} \left( 1 + \frac{i\omega}{L_{\nu0}} \right) = \frac{\Delta Q_{\nu}}{Q_{\nu0}} - \frac{\Delta L_{\nu}}{L_{\nu0}} + \frac{1}{L_{\nu0}} \left( ik_x u - \frac{\partial w}{\partial z} - \frac{1}{[\text{OH}(\nu)]} \frac{\partial [\text{OH}(\nu)]}{\partial z} \right) \quad (10)$$

In the gravity wave branch at least, we have  $\omega < \text{Brunt-Väisälä (BV) frequency } \omega_b \approx 2\pi/[5 \text{ min}]$  near the mesopause, while  $L_{\nu0} \geq \sum_{\nu'} A_{\nu\nu'} \geq 22 \text{ s}^{-1}$ . Hence the second term on the left-hand side of equation (10), which arises from the time derivative, could be ignored in the continuity equations of the hydroxyl level population fluctuations  $\Delta[\text{OH}(\nu)]$  for  $\nu > 0$ . The corresponding term could also be ignored in the continuity equations for  $[\text{OH}(\nu=0)]$  and  $[\text{HO}_2]$  over most of the altitude range of interest (80 - 100 km). This is apparent from Figure 5, which is a plot of the chemical lifetime  $L_{i0}^{-1}$  of the reactive  $i$ th species versus altitude. Nevertheless, even though

the terms in question are small, they will be retained for completeness in both numerical and analytical solutions.

It is also apparent from Figure 5 that the lifetimes of  $\text{OH}(\nu=0)$  and  $\text{HO}_2$  are very nearly the same and track each other over the whole range of interest. This is because reaction with atomic oxygen is the dominant loss channel for each of these species, so that for  $z > 80\text{--}85\text{ km}$ , the ratio of the lifetimes is  $\tau_{\text{HO}_2}/\tau_{\text{OH}(0)} = L_{\text{OH}(0)}/L_{\text{HO}_2} = k_{8,0}/[\Sigma_{\nu} k_{2\nu}] \approx 1.3$ .

Equation (10) shows that the fractional first-order perturbed volume emission rate is a sum of three terms, which represent (1) production rate fluctuations  $\Delta Q_{\nu}/Q_{\nu0}$ , (2) loss-rate fluctuations  $\Delta L_{\nu}/L_{\nu0}$ , and (3) fluctuations that arise from the divergence term of the continuity equation and represent wave transport, that is, advection and compression, of  $[\text{OH}(\nu)]_0$ . In the model of *Walterscheid et al.* [1987] and the extended model of *Schubert and Walterscheid* [1988], fluctuations in the loss rate and in the divergence term were not considered. That is, only the first of the three terms in equation (10) was included, so that  $\Delta I_{\nu\nu'}/I_{\nu\nu'0}$  was equal to  $\Delta Q_{\nu}/Q_{\nu0}$ . These authors allowed production of excited OH only by the  $\text{H} + \text{O}_3$  reaction (R1). Since the branching ratio  $b(\nu)$  for this reaction cancels in the numerator and denominator of  $\Delta Q_{\nu}/Q_{\nu0}$ , they obtained relative emission rate fluctuation  $\Delta I/I_0 \propto \Delta Q/Q_0$  which were independent of the vibrational level  $\nu$ . By contrast, our approach treats the population of each vibrational level separately, considering the effect of quenching, production from other OH levels, and transport on its fluctuations. This is a major difference between our approach and that of *Walterscheid et al.* [1987] and leads to a vibrational level dependence of the response to an IGW, as we will see further in section 6.

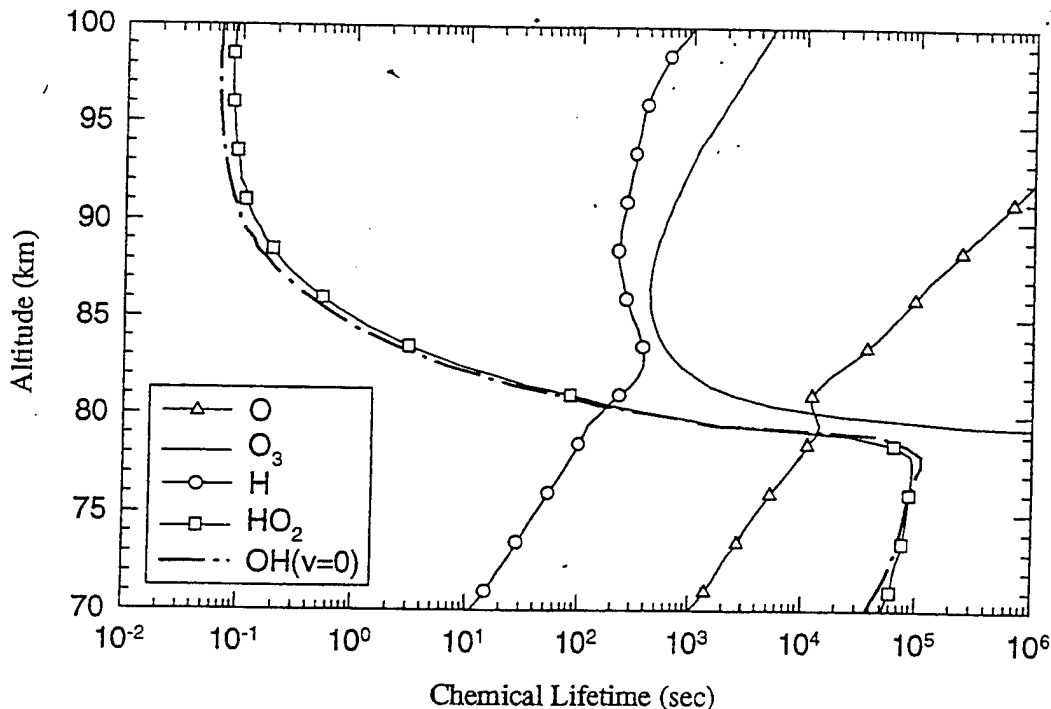


Figure 5. Chemical lifetime versus altitude from the 1-D photochemical model for photochemically active odd-hydrogen and odd-oxygen species.

The scale of the transport term, which is the last term in equation (10), is the ratio of two lengths, namely, (1) the distance which a typical IGW velocity will move a parcel in the  $[\text{OH}(\nu)]$  lifetime and (2) either the IGW wavelength or the  $[\text{OH}]$  scale height. This means it could be ignored in the equations for  $\Delta I_{\nu\nu'}$  and  $\Delta[\text{OH}(\nu)]$  ( $\nu \neq 0$ ), since the  $\text{OH}(\nu)$  lifetime is so short (although we keep it). Hence it will have little direct effect on the Krassovsky ratio. Note, however, from Figure 5 that it cannot be neglected in the determination of the fluctuations of  $[\text{O}]$  and  $[\text{O}_3]$ , which are long-lived species and which drive the chemical fluctuations of  $[\text{OH}(\nu)]$ . Thus the transport term has an indirect effect on the OH brightness fluctuations.

## 5. Inferring Temperature From Airglow Emission

Experimenters have used measurable airglow properties to calculate the effective temperature of the radiating region in a number of ways. For example, they have inferred the temperature from the measured ratio of rotational line intensities in a band or from the measured half width of a Doppler-broadened emission line. The Krassovsky ratio  $\eta$  is commonly computed from temperatures inferred from remotely sensed airglow data in this way. In an isothermal atmosphere or for an infinitesimally thin emission layer, such techniques measure the local temperature; however, for an extended layer in a non isothermal atmosphere, what is measured is some average of the atmospheric temperature over the emission layer. Modelers (as well as some experimenters) have typically assumed that the BWT is the quantity measured [e.g., Weinstock 1978; Hines and Tarasick, 1987; Walterscheid et al., 1987; Schubert et al., 1991], in which the local temperature is weighted by the local band volume emission rate and integrated over the layer. We show that a realistic model should consider the method of temperature measurement which will affect the results obtained. This will avoid errors which can occur when  $\eta$  values computed from the BWT are compared with data.

We calculate  $\eta_{\nu}$  using three different methods to specify an effective temperature: the brightness weighted temperature and two methods used in field temperature measurements, the rotational temperature and the Doppler temperature. We intend the experimental methods implemented in this section to be merely illustrative of the class of measurement techniques and not to mimic any particular investigator's method. However, it is possible to simulate all the details of a particular method, should the goal of the investigation be a detailed comparison of a particular data set with the model. In each method we evaluate the steady state effective temperature and its fluctuation occurring in the denominator of equation (1).

**Brightness-weighted temperature.** Theoreticians and modelers have typically used the BWT to calculate

$\eta_{\nu}$ . The brightness  $B_{\nu\nu'}$  seen by a column-integrating airglow instrument, which occurs in the numerator of the definition of  $\eta_{\nu}$  (equation (1)), is defined as the integral of the volume emission rate along the LOS:

$$B_{\nu\nu'} = \int I_{\nu\nu'}(x, z) dl = B_{\nu\nu'0} + \Delta B_{\nu\nu'} \quad (11)$$

where the integral has been expanded to first order in IGW parameters and

$$dl = dz \sec \theta$$

where

$\theta$  is the LOS zenith angle

$$I_{\nu\nu'} = I_{\nu\nu'0} + \Delta I_{\nu\nu'}$$

$$B_{\nu\nu'0} = \int I_{\nu\nu'0}(z) dz,$$

$$\Delta B_{\nu\nu'} = \int \Delta I_{\nu\nu'}(x, z) dz$$

The plane-parallel assumption for the atmosphere has been made. Then the BWT is defined

$$\langle T \rangle_{\nu} = \frac{\int I_{\nu\nu'}(x, z) T(x, z) dz}{B_{\nu\nu'}} = \langle T \rangle_{\nu 0} + \Delta \langle T \rangle_{\nu} \quad (12)$$

Thus we see that "volume-emission-weighted temperature" would be a more accurate name for the BWT.

Expanding equation (12) to first order, we find that the steady state BWT and the fluctuation in the BWT are given by

$$\langle T \rangle_{\nu 0} = \frac{\int I_{\nu\nu'0}(z) T_0(z) dz}{B_{\nu\nu'0}} \quad (13)$$

and

$$\Delta \langle T \rangle_{\nu} = T_{1\nu} + T_{2\nu} - T_{3\nu} \quad (14)$$

where

$$T_{1\nu} = \frac{\int I_{\nu\nu'0}(z) \Delta T(x, z) dz}{B_{\nu\nu'0}}$$

$$T_{2\nu} = \frac{\int \Delta I_{\nu\nu'}(x, z) T_0(z) dz}{B_{\nu\nu'0}}$$

$$T_{3\nu} = \langle T \rangle_{\nu 0} \frac{\Delta B_{\nu\nu'}}{B_{\nu\nu'0}}$$

We find that for small-scale waves, the terms  $T_{1\nu}$  arising from the temperature perturbation  $\Delta T$  and  $T_{2\nu} - T_{3\nu}$  arising from  $\Delta I_{\nu\nu'}$  are comparable in size, whereas for larger scale waves, the term  $T_{1\nu}$  dominates.

**Rotational Temperature.** The rotational temperature is inferred by measuring the brightness on a minimum of two rotational lines in one of a molecular emitter's rovibrational bands and assuming that these rotational lines conform to a Boltzmann distribution.

From the line-pair ratios, an effective  $T_{rot}$  can be determined.

In a realistic atmosphere, the ratio of the intensities of two rotational lines, denoted by subscripts a and b, respectively, in a single vibrational band can be written as:

$$\frac{B_a}{B_b} = \frac{A_a \int N_a(x, z) dl}{A_b \int N_b(x, z) dl} \quad (15)$$

where  $N_a(x, v)$ , the population of rotational state  $a$ , is determined from the total vibrational level population  $N_v(x, z)$  by thermal equilibrium at the local temperature,

$$N_a(x, z) = \frac{N_v(x, z) g_a \exp[-E_a/k_B T(x, z)]}{Z_v[T(x, z)]} \quad (16)$$

with a similar expression for  $N_b$ , where

$A_a, A_b$  rovibrational Einstein coefficients;

$g_{a,b}$  degeneracy factors of the specified rotational lines;

$E_{a,b}$  energy of specified rovibrational level; referred to energy of lowest rotational state in level  $v$ ;

$k_B$  Boltzmann's constant;

$Z_v(T)$  rotational partition function in band

$v = \sum g_a \exp(-E_a/k_B T)$  (sum over all rotational states in band).

In the case of an isothermal atmosphere,  $T(z) = T_0$ , we see from equation (15) that  $R \equiv B_a A_b / B_b A_a = g_a / g_b \exp[-(E_a - E_b)/k_B T_0]$  is Boltzmann distributed. Clearly, when  $T(z)$  is not constant,  $R$  is not Boltzmann distributed, but assuming that it is we can define an effective  $T_{rot}$  for the emitting region by

$$T_{rot} = \frac{E_b - E_a}{k_B \ln(B_a A_b g_b / B_b A_a g_a)} \quad (17)$$

where  $B_a/B_b$  is the measured line pair brightness ratio. The steady state rotational temperature  $T_{rot,0}$  is obtained by replacing  $B_a/B_b$  in equation (17) by its steady state value  $B_{a0}/B_{b0}$ . Assuming now that the atmosphere is perturbed by an IGW, we expand equation (17) to first order in the wave amplitude and find that the relative temperature fluctuation is proportional to the difference of the relative brightness fluctuations of the two lines being measured; that is,

$$\begin{aligned} \frac{\Delta T_{rot}}{T_{rot,0}} &= \frac{k_B T_{rot,0}}{(E_a - E_b)} \left\{ \frac{\Delta B_a}{B_{a0}} - \frac{\Delta B_b}{B_{b0}} \right\} \\ &= \left\{ \frac{\Delta B_b}{B_{b0}} - \frac{\Delta B_a}{B_{a0}} \right\} / \left\{ \ln \left( \frac{B_{a0} A_b g_b}{B_{b0} A_a g_a} \right) \right\} \end{aligned} \quad (18)$$

where  $B_a/B_{a0}$  is obtained by expanding  $B_a$  to first order in the numerator of equation (15) and is given in the appendix. The ratio  $\Delta B_b/B_{b0}$  is obtained in a similar fashion from the denominator of equation (15). Once the relative temperature fluctuation is calculated, it is used with the

relative brightness fluctuation of the corresponding vibrational band from equation (11) to calculate the Krassovsky ratio  $\eta_v$ .

**Doppler Temperature.** The Doppler temperature is inferred from the spectral width of a single emission line, for example, a single rotational line in a hydroxyl rovibrational band. Such measurements can be made by highly dispersive instruments such as Fabry-Pérot interferometers [Hernandez, 1980, 1986] or special-purpose Michelson interferometers [Thuillier and Hersé, 1991; Shepherd et al., 1993]. At sufficiently high altitude the emission line shape is Gaussian due to the Doppler line broadening and the Maxwellian velocity distribution, and the spectral volume emission of the line is [Goody and Yung, 1989; Hernandez, 1986]

$$I(v, x, z) = \frac{A_a N_a(x, z)}{\sqrt{\pi} \alpha(x, z)} \exp \left[ - \left( \frac{v - v_0}{\alpha(x, z)} \right)^2 \right] \quad (19)$$

where  $v_0$  is the center frequency of the line and  $\alpha$  is the Doppler line width from line center to the  $1/e$  point, given by

$$\alpha(x, z) = \frac{v_0}{c} \sqrt{\frac{2k_B T(x, z)}{m}} \quad (20)$$

(the full width at half-maximum (FWHM) is  $2(\ln 2)^{1/2} \alpha$ );  $c$  is the speed of light,  $m$  is the molecular mass of the emitting species, and  $N_a$  is given by equation (16). The peak of the profile  $v_0$  will be a function of  $x$  and  $z$  if there is a wind, since it will be Doppler shifted by an amount proportional to the radial component of the particle velocity. Determining the peak of the profile enables wind measurements to be made. Application of the basic techniques to OH rovibrational bands is discussed, for example, by Hernandez and Smith [1984] and Shepherd et al. [1993]. Since wind measurement is not our purpose in this paper, we ignore the spatial dependence of  $v_0$ .

The spectral brightness and its expansion to first order are,

$$B(v) = \int I(v, x, z) dl = B_0(v) + \Delta B(v) \quad (21)$$

where

$$B_0(v) = \int I_0(v, z) dl \quad (22)$$

$$\Delta B(v) = \int \Delta I(v, x, z) dl \quad (23)$$

Here  $I_0(v, z)$  is obtained by making the substitutions  $N_{a0}(z)$  for  $N_a$ ,  $\alpha_0(z)$  for  $\alpha$ , and  $T_0(z)$  for  $T$  in equations (19) and (20), while perturbing these same equations yields

$$\begin{aligned} \frac{\Delta I(v, x, z)}{I_0(v, z)} &= \left[ \frac{(v - v_0)^2}{\alpha_0^2(z)} - \frac{1}{2} \right] \\ &\quad + \frac{\Delta T(x, z)}{T_0(z)} + \frac{\Delta N_a(x, z)}{N_{a0}(z)} \end{aligned} \quad (24)$$

where  $\Delta N_a/N_{a0}$  is given in the appendix and we have used

$$\frac{\Delta \alpha(x, z)}{\alpha_0(z)} = \frac{1}{2} \frac{\Delta T(x, z)}{T_0(z)} \quad (25)$$

The steady state and perturbed spectral brightness profiles, obtained by substituting  $I_0$  and  $\Delta I$  from equation (24) into equations (22) and (23), are clearly not Gaussian. We would expect  $I_0(v, z)$  to be Gaussian only in an isothermal atmosphere, since the weighted sum of a Gaussian shaped line of different widths obtained by line-of-sight integration through a varying temperature field will not be Gaussian. We assume that the observer measures an effective Doppler width by assuming that the spectral profile is close to Gaussian, that is,

$$B(v) = B(v_0) \exp\left(-\frac{(v - v_0)^2}{\alpha_{eff}^2}\right) \quad (26)$$

Substituting  $\alpha_{eff}$  as mentioned above, any detailed measurement scheme can be implemented in the model, and the results will depend on the details. For illustrative purposes, we assume that measurements of  $B(v)$  are made at  $v_0$  and at some other frequency, say  $v_1$ . Then  $\alpha_{eff}$  can be obtained by solving equation (26), using  $B(v_0)$  and  $B(v_1)$ , and the effective Doppler temperature  $T_{Dop}$  follows by substituting  $\alpha_{eff}$  into equation (20):

$$T_{Dop} = \frac{m}{2k_B} \left( \frac{c\alpha_{eff}}{v_0} \right)^2 \quad (27)$$

To obtain the unperturbed values of Doppler width and Doppler temperature,  $\alpha_{eff,0}$  and  $T_{Dop,0}$ , we substitute the steady state values of spectral brightness,  $B_0(v_0)$  and  $B_0(v_1)$ , into equation (26). The first-order perturbed values,  $\Delta \alpha_{eff}$  and  $\Delta T_{Dop}$ , are obtained by expanding equations (26) and (27) to first order to obtain

$$\frac{\Delta T_{Dop}}{T_{Dop,0}} = \left( \frac{\Delta B(v_1)}{B_0(v_1)} - \frac{\Delta B(v_0)}{B_0(v_0)} \right) / \ln \left( \frac{B_0(v_0)}{B_0(v_1)} \right) \quad (28)$$

In the model simulation the quantities appearing in equation (28) are evaluated using equations (22)-(24).

The  $\eta$  is evaluated using the  $T_{Dop}$  fluctuation from equation (28). To determine the line brightness fluctuation  $\Delta B$  and the background brightness  $B_0$  in the numerator of the ratio, we integrate equations (22) and (23) over the line, obtaining

$$B_{a0} = \int B_0(v) dv \quad (29)$$

$$\Delta B_a = \int \Delta B(v) dv \quad (30)$$

If, as is the case for the OH Meinel emission, the line is part of a molecular band, we have a choice. We can use either the total band brightness fluctuation  $\Delta B_{vv}$ , equation (11), in the numerator of  $\eta_v$ , or the line brightness of equations (29) and (30), which refers to a single rotational line

in the band. We choose the latter procedure here because the line brightness is more likely to be known by measurements with a highly dispersive instrument capable of resolving the structure within a Doppler line. Notice, however, that these are not equivalent procedures. The population of rotational state  $a$ , given by equation (16) not only fluctuates when the band population  $N_v$  fluctuates, but also fluctuates when the temperature  $T$  does. Consequently, the values of  $\eta_v$  calculated will be different. The relation between these inequivalent response functions  $\eta_v$  can be calculated using the equation for  $\Delta N_a/N_{a0}$  in the appendix.

To illustrate the differences between these distinct definitions of  $\eta_v$ , we assume a wave with a horizontal phase velocity  $V_{phx} = \omega/k_x$  of 40 m/s, propagating in the midlatitude atmosphere described in section 2, the same atmospheric conditions for which Figures 1-5 were plotted. Figure 6 shows the amplitude of  $\eta_{v=6}$  calculated from the model OH(6-2) band radiance for zenith viewing, as a

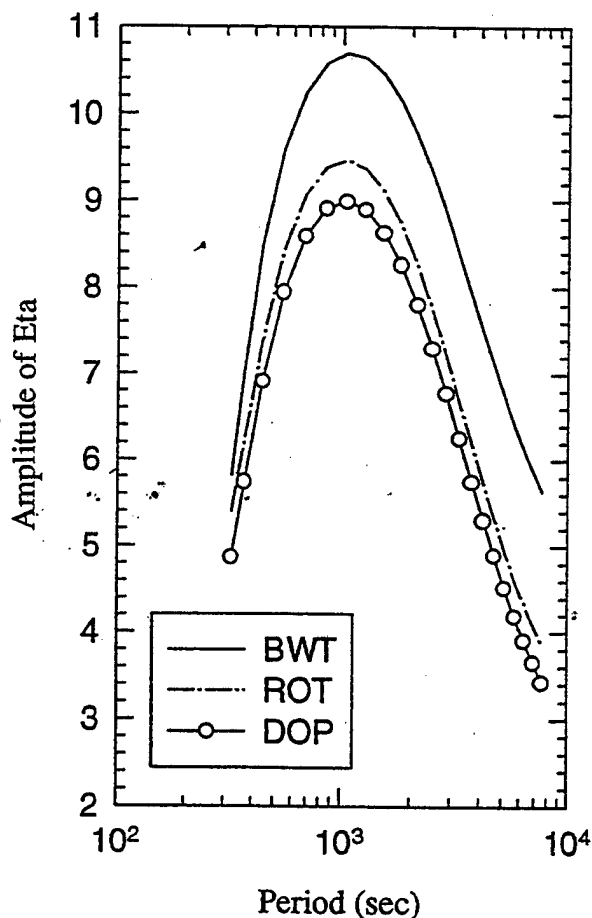


Figure 6. Amplitude of Krassovsky's  $\eta$ , airglow response function to a gravity wave, for the OH(6-2) Meinel band generated by photochemical-dynamical (PHD) model and for a vertical line-of-sight. The wave is a small-scale wave with a horizontal phase speed  $V_{phx}=40\text{m/s}$ . Curves are plotted for three different definitions of an effective temperature in a non isothermal atmosphere: a brightness-weighted temperature (BWT), a rotational temperature ( $T_{rot}$ ), and a Doppler temperature ( $T_{Dop}$ ). The curves are shown from the short-period cut-off at the BV frequency to a period near 3 hours.



function of wave period  $\tau$ , using the temperature definitions described above for the BWT, the  $T_{rot}$  and the  $T_{Dop}$ . It is seen that  $|\eta_{v=6}|$  can differ by 20-50% over the range of periods shown, with the  $|\eta_{BWT}|$  being an overestimate and  $|\eta_{Dop}|$  yielding the lowest values. Figure 7 is the same as Figure 6, except that a larger-scale wave with a horizontal phase velocity of 140 m/s is used. There is an overall reduction in the value of  $|\eta_{v=6}|$ , but qualitatively the results are similar to those shown in Figure 6, with perhaps slightly smaller percentage differences for the larger-scale gravity waves.

Since  $\eta_v = |\eta_v| \exp(i\phi_v)$  is a complex quantity, it is also interesting to compare its phase values  $\phi_v$  calculated by the three procedures. Figures 8 and 9 show plots of the phases for the BWT,  $T_{rot}$  and  $T_{Dop}$  cases, for the small-scale and large-scale waves of Figures 6 and 7. The phase values between  $0^\circ$  and  $180^\circ$  indicate that the OH brightness leads the gravity wave temperature variation. The phases in Figure 8 increase from  $45^\circ$  to  $80^\circ$  with increasing period. The order of the phase results is reversed from the amplitude results, with the BWT underestimating  $\phi_v$  by about  $10^\circ$ . While  $\phi_v$  is smaller at a fixed period for the results shown in Figure 9 compared to those of Figure 8, varying from  $20^\circ$  to  $55^\circ$ , the general increase

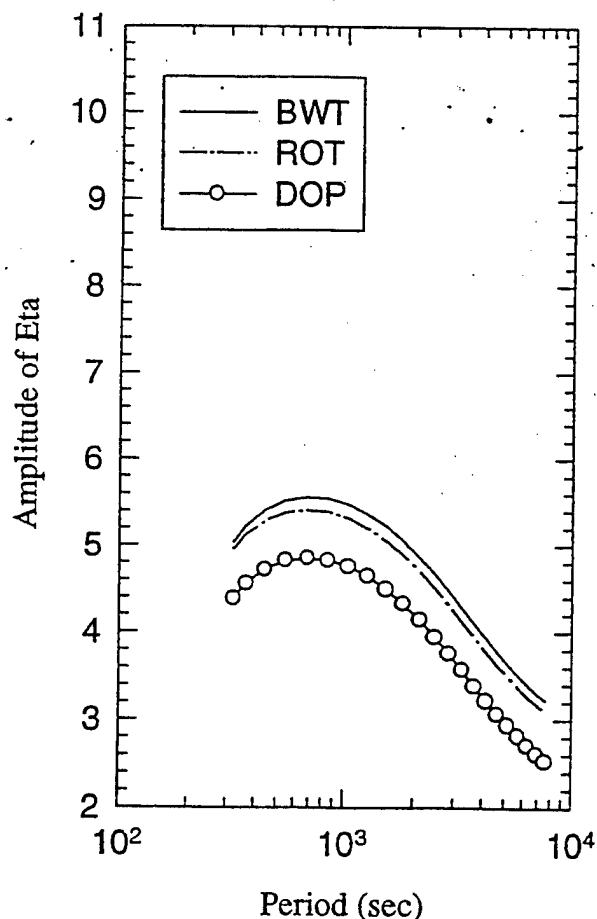


Figure 7. Same as in Figure 6, but for a large-scale wave with  $V_{phx} = 140$  m/s.

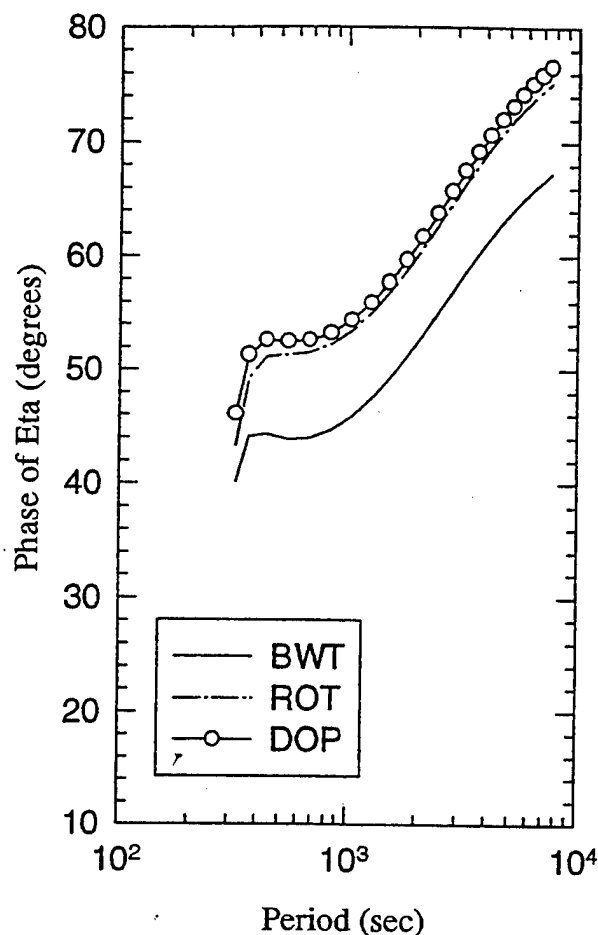


Figure 8. As in Figure 6, but showing the phase of the response function  $\eta_{v=6}$  to the small-scale wave  $V_{phx} = 40$  m/s.

of  $\phi_v$  with increasing period in the two cases is qualitatively similar.

In the next section we explore the effect of quenching on the value of  $|\eta_v|$  and  $\phi_v$  and look at the resulting vibrational-level dependence of  $\eta_v$ .

## 6. Effect of Quenching on Gravity Wave Response

The effect of quenching on  $\eta$  is considerable, especially for small-scale waves, which can have vertical wavelengths comparable to the thickness of the airglow emission layer. Figure 10 shows a plot of  $|\eta_{v=1}|$  employing the BWT as a function of period, with and without quenching by  $[O]$ ,  $[O_2]$ , and  $[N_2]$  as described in the quenching model of section 3, a vertical line-of-sight, and the small-scale wave case considered above ( $V_{phx} = 40$  m/s). When quenching is neglected,  $|\eta_{v=1}|$  increases by 40 to 130%, with larger changes occurring at longer periods. Quenching also causes  $\eta_v$  to become dependent on the vibrational level  $v$ . Figure 11 repeats the  $v = 1$  result for  $|\eta_v|$  from Figure 10, along with the corresponding results for  $v = 6$  and  $v = 9$ . The  $v = 6$  curve has already been plotted as the BWT result in Figure 6. The response function

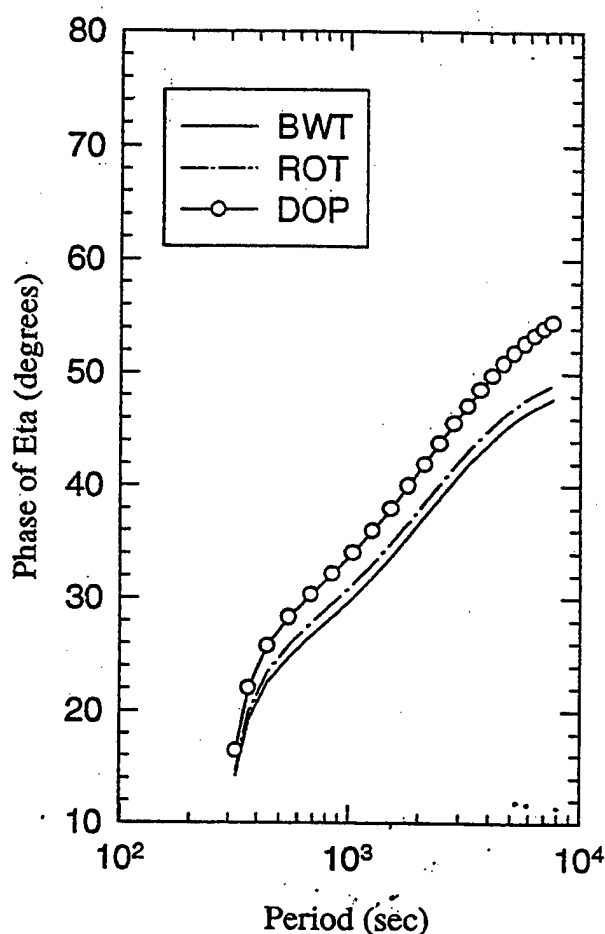


Figure 9. As in Figure 7, but showing the phase of the response function  $\eta_{v=6}$  to the large-scale wave  $V_{phx}=140$  m/s.

peaks near periods of 15 min in all cases, but there is a 25-35% variation in amplitude for the different vibrational levels. In general, values of  $|\eta_v|$  are larger for the higher vibrational levels than for the  $v=1$  level. There is little difference between  $|\eta_{v=6}|$  and  $|\eta_{v=9}|$ , except at longer periods where  $|\eta_{v=9}|$  drops rapidly and approaches  $|\eta_{v=1}|$ . The results for the phases  $\phi_v$  of the response functions, corresponding to the amplitude results in Figure 11, are shown in Figure 12. As for the amplitude, the  $v=6$  case is replotted from the BWT plot in the section 5 results (Figure 8). The  $v=1$  phase shift is the greatest, with up to a  $12^\circ$  difference between the phase shifts for the three levels. We have not plotted any results for large-scale waves, but for them the effect of quenching on  $\eta_v$  is smaller, being roughly limited to 5%.

An experiment which measures simultaneously OH Meinel bands originating from several vibrational levels  $v$  should be able to confirm the effect of quenching on the airglow response function  $\eta_v$  and observe the vibrational-level dependence discussed in this section and shown in Figures 11 and 12.

## 7. Effect of Standing Waves: Modified Hines Model

Another phenomenon which can have an appreciable effect on the airglow response to an IGW is the occur-

rence of standing waves. (When we compare our model to data in the next section, we will demonstrate that the model described so far is inadequate.) The simplest way to obtain standing waves within the framework of the current Hines [1960] isothermal model is to modify it slightly by assuming a downward propagating wave which is reflected from the ground ( $z=0$ ), leading to a standing wave. The presence of vertical standing waves can modulate the amplitude of the airglow response to an IGW by shifting the position of a wave node relative to the peak of the airglow layer. In addition, as was suggested by Hines and Tarasick [1993] and elaborated by us [Makhlouf et al., 1993; Picard et al., 1994], it can lead to large changes in the phase of the response function. Entirely similar behavior is seen when standing waves are formed by ducting of short-period waves, resulting from Doppler shifting by background winds and/or BV frequency variations with altitude in a non isothermal atmosphere. When comparing our model with airglow data, we find that traveling wave models are inadequate and that standing waves are essential to explain the phase of the response. This will be demonstrated in the next section.

The existence of reflection at a rigid ground boundary forces the vertical velocity fluctuation  $w(x, z, t)$  to be zero at the ground  $z=0$ . Under this condition, the linearized

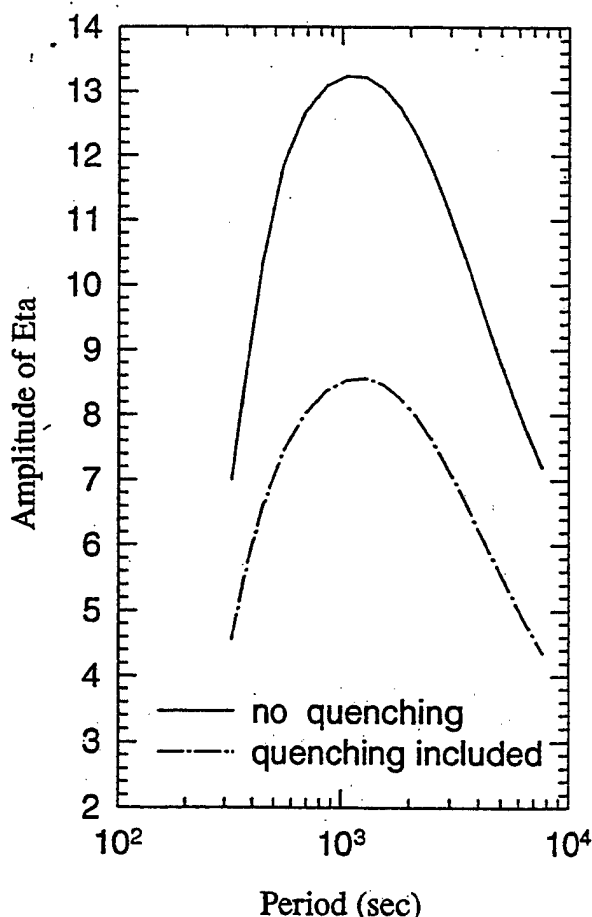
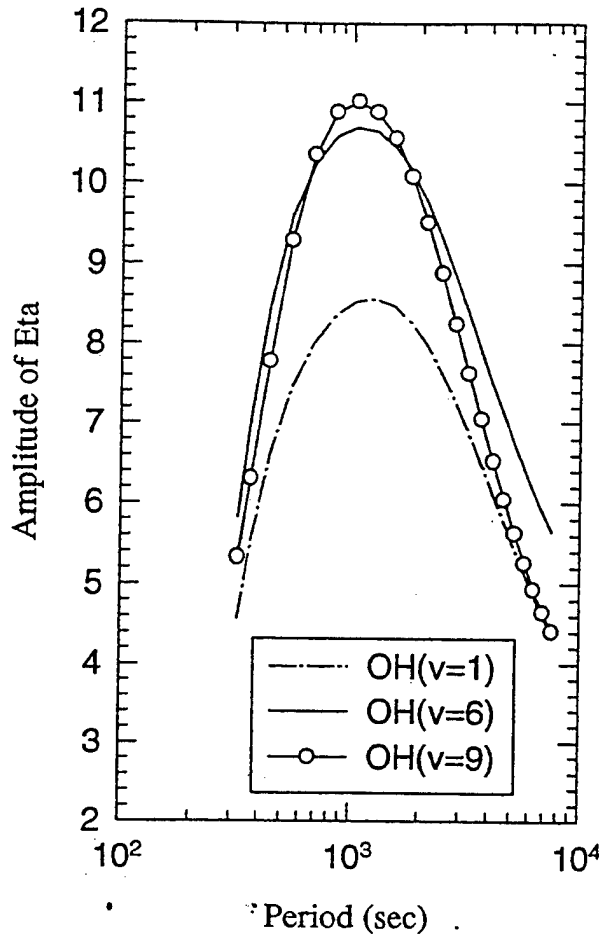


Figure 10. Effect of quenching on  $\eta_{v=1}$  as a function of period for the small-scale wave  $V_{phx}=40$  m/s. Neglect of quenching leads to a large increase in the amplitude.



**Figure 11.** Plots of  $\eta_v$  for  $v = 1, 6$ , and  $9$ , showing vibrational-level dependence of  $\eta_v$  resulting from quenching. The  $v = 1$  curve is the same as the "quenching included" curve of Figure 10, while the curve for  $v = 6$  is repeated from the BWT result in Figure 6.

hydrodynamic equations can be combined into a single second-order differential equation [Tuan and Tadic, 1982]:

$$\left[ \frac{d^2}{dz^2} + k_z^2 \right] \Psi = 0 \quad (31)$$

where  $\Psi(z) = \left( \omega / \rho_0^{1/2} \right) \Delta P e^{-i(\omega t - k_z x)}$  is the pressure fluctuation normalized to remove the exponential growth with altitude,  $\Delta P$  is the pressure fluctuation, and  $\rho_0$  is the steady state mass density. The rigid boundary condition can be written

$$\left. \frac{\partial \Psi}{\partial z} \right|_{z=0} = \chi \Psi|_{z=0} \quad (32)$$

where

$$\chi = -\frac{1}{2} \left( \frac{g}{c^2} - \frac{\omega_b^2}{g} \right)$$

The solution to equation (31), subject to the boundary condition of equation (32), is given in terms of the arbitrary constant wave amplitude  $C$  by

$$\Psi(z) = C \left[ (k_z + i\chi) e^{-ik_z z} + (k_z - i\chi) e^{ik_z z} \right] \quad (33)$$

From this solution and the linearized hydrodynamic equations the horizontal and vertical wave velocities, which are used in the linearized continuity equation (7), are obtained [Makhlof, 1989]:

$$u(x, z, t) = \frac{C k_x k_z}{\omega \rho_s^{1/2}} \left[ \cos k_z z + \frac{\chi}{k_z} \sin k_z z \right] e^{z/2H} e^{i(\omega t - k_x x)} \quad (34)$$

$$w(x, z, t) = \frac{iC}{\rho_s^{1/2}} (\sin k_z z) \frac{k_z^2 + \chi^2}{\omega_b^2 - \omega^2} e^{z/2H} e^{i(\omega t - k_x x)} \quad (35)$$

In equation (34) and (35),  $\rho_s = \rho_0(z=0)$ .

It is clear from equations (34) and (35) that the solutions are standing waves in the  $z$  direction and that  $w$  has a node at the ground.

In the next section we will compare results obtained using the isothermal model, both with and without standing waves, to data and to other models. We will demonstrate that the standing wave model is often necessary to reconcile theory and observations.

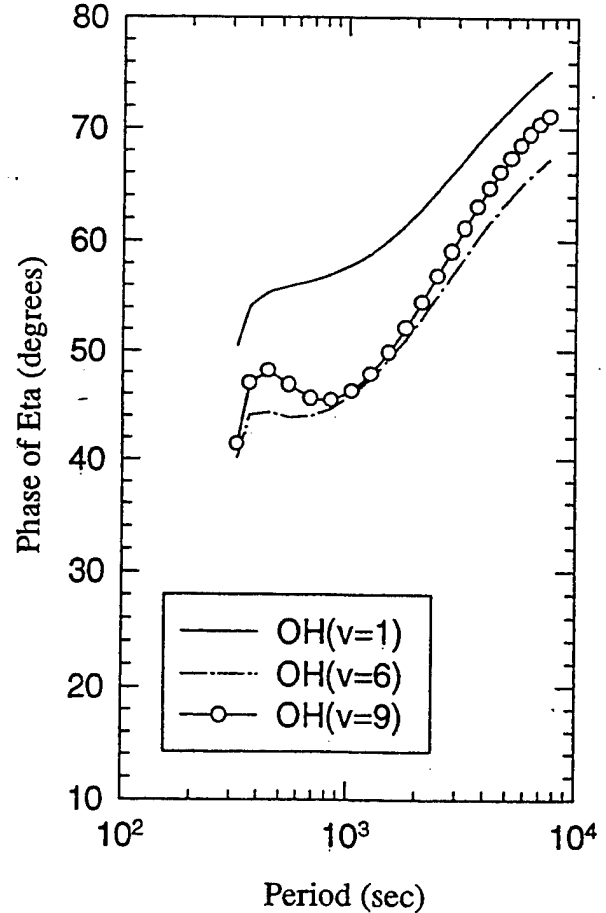


**Figure 12.** Phase of  $\eta_v$  for  $v = 1, 6$ , and  $9$ , corresponding to the amplitudes of the response function shown in Figure 11.

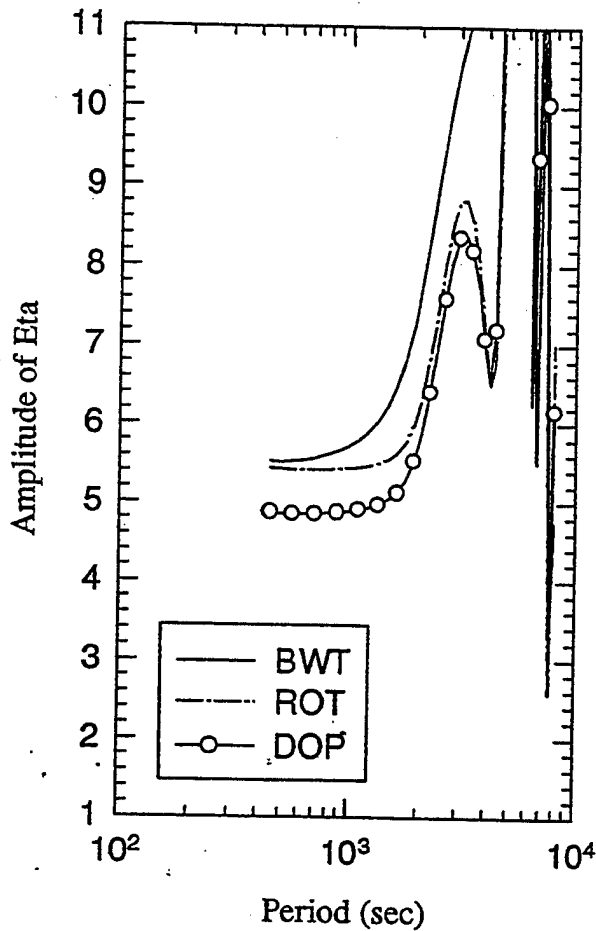


Figure 13. Amplitude of  $\eta_v$  for OH(6-2) band as a function of wave period for waves with constant horizontal wavelength  $\lambda_x = 100$  km. The result of using the same three effective temperatures used in Figure 3 in calculating  $\eta_v$  is shown, with the differences disappearing toward the right side of the figure as the vertical wavelength decreases and interference effects occur.

## 8. Discussion and Comparison With Experiment and Other Models

We have assumed that the dynamical perturbation of the atmosphere and of its airglow emission is due to a single monochromatic linear IGW. The wave parameters satisfy a dispersion relation [Hines, 1960], whereby we can express the wave frequency  $\omega = 2\pi/\tau$  in terms of  $V_{phx}$  and the vertical wavelength  $\lambda_z = 2\pi/k_z$  or, inverting this relation, express  $\lambda_z$  as a function of  $\omega$  and  $V_{phx}$ ,

$$\lambda_z = 2\pi \left( \frac{\omega_b^2 - \omega^2}{V_{phx}^2} - \frac{\omega_a^2 - \omega^2}{c^2} \right)^{-\frac{1}{2}} \quad (36)$$

where  $\omega_b$  is the BV frequency ( $\sim 2.05 \times 10^{-2} \text{ s}^{-1}$ ),  $\omega_a$  is the acoustic cutoff frequency ( $\sim 2.27 \times 10^{-2} \text{ s}^{-1}$ ), and  $c$  is the speed of sound ( $\sim 295 \text{ m/s}$ ). The numerical values are for typical mesopause conditions.

We see from equation (36) that in the gravity wave branch ( $\omega \leq \omega_b$ ) and for a fixed  $V_{phx}$ ,  $\lambda_z$  decreases as  $\tau$  increases. When  $\lambda_z$  is small enough to be comparable to the OH layer thickness (or 6-8 km FWHM, from Figure 4, with the smaller width applying to the lower vibrational levels), constructive and destructive interference between brightness fluctuations and between temperature fluctuations starts to occur. Then the fluctuation from one part of the layer can be out of phase with the fluctuation from another part of the layer, and hence cancellation can occur. Both the brightness and the temperature fluctuation can go through a series of maxima and minima as the vertical wavelength is reduced further. This can result both in very large and very small values of  $|\eta_v|$  and leads to oscillations in  $|\eta_v|$  as  $\lambda_z$  changes. These are accompanied by oscillations in the phase  $\phi_v$  of the response function.

However, we see no evidence of interference as the period increases in Figures 6-12. The reason is also apparent from the dispersion relation, where we see that when  $\omega \leq \omega_b$  and  $V_{phx}$  is fixed,  $\lambda_z$  varies only slowly with  $\omega$  unless  $\omega$  is very close to  $\omega_b$ . For example, in the large-scale wave case of Figures 7 and 9, where  $V_{phx} = 140 \text{ m/s}$ ,  $\lambda_z = 53 \text{ km}$  for a period of 16 min, while, for a period of 160 min,  $\lambda_z = 51 \text{ km}$ . So the vertical wavelength is much larger than the layer half-width and hardly

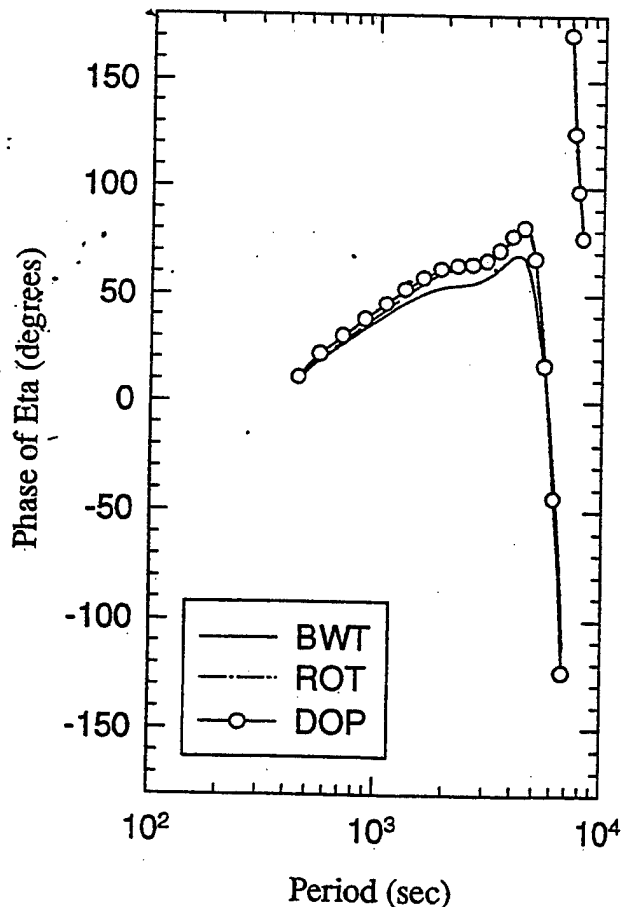
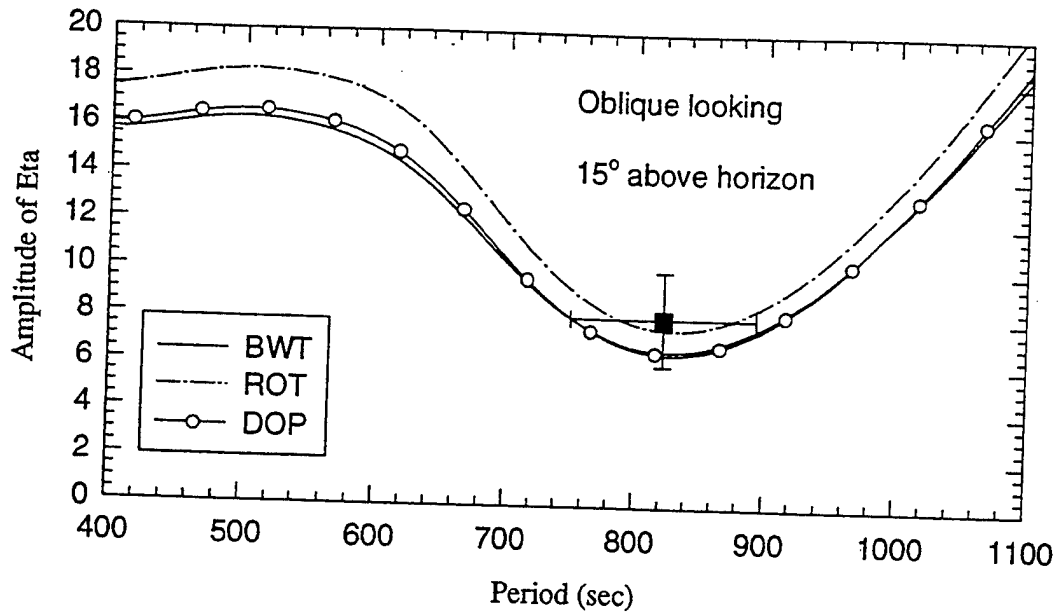


Figure 14. The phase of  $\eta_v$  corresponding to the amplitudes shown in Figure 13. The differences in this case are almost negligible.



**Figure 15.** Amplitude of response function  $\eta_{v=3}$  from PHD model as a function of period for an oblique line-of-sight at  $15^\circ$  elevation. Model is compared with data point corresponding to quasi-sinusoidal oscillation measured by *Taylor et al.* [1991] on OH(3-1) band from Sacramento Peak, New Mexico. The model phase speed  $V_{phx}$  is held constant at the observed value of 28 m/s.

changes with period, which is why one sees no interference effects in this case. The lack of interference effects makes it easier to see the effect of quenching and  $v$  dependence, as well as the effect of the definition of the (non isothermal atmosphere) effective temperature.

To see the interference effects which occur at small  $\lambda_z$ , one must keep  $\lambda_x$  fixed while evaluating the response function (rather than  $V_{phx}$ ). (See also *Schubert and Walterscheid* [1988] and *Schubert et al.* [1991].) Then, from equation (36), it is easily seen that  $\lambda_z$  decreases rapidly, in the gravity wave branch, as  $\tau$  increases. Figure 13 shows a plot of  $|\eta_v|$  as a function of period, once again for a vertical LOS, but now for a constant horizontal wavelength,  $\lambda_x = 100$  km. Over the range of periods plotted in Figure 13,  $\lambda_z$  is 75 km for  $\tau = 10$  min and 5 km when  $\tau = 100$  min. Maxima and minima due to the constructive and destructive interference become obvious in Figure 13 as  $\tau$  increases, beginning near  $\tau = 80$  min, where the vertical wavelength has decreased to about 6 km. We note that similar interference effects are evident in the  $\eta$  plots of *Hines and Tarasick* [1987], *Schubert and Walterscheid* [1988], and *Schubert et al.* [1991]. Figure 14 is a plot of the phase of  $\eta_v$  as a function of period for fixed  $\lambda_x = 100$  km, corresponding to the amplitude plot of Figure 13. Large phase-shift excursions also start to occur when  $\tau$  reaches 80 min, with the phase changing rapidly with increasing period. Notice also that the differences between the Krassovsky  $\eta$  values for the three effective temperature definitions disappear as  $\lambda_z$  decreases. This is due to two facts. (1) Differences between the three values of  $\eta_v$  are due entirely to the inhomogeneity of the atmospheric temperature. (2) When  $\lambda_z/2$  is less than the emission layer half width, only the homogeneity of the

temperature over a half wavelength counts. The discrepancies between the various response function definitions disappear as the half wavelength decreases and the temperature becomes effectively more homogeneous. We note that the interference effects seen here can be reduced markedly or eliminated if one has a finite duration wave train, or wave packet, as is invariably the case in reality. Then the response plotted in Figures 13 and 14 must be averaged appropriately over the frequency range present in the wave packet.

Effects such as interference show the importance of properly documenting the horizontal wave speed or the horizontal wavelength at the time of observation. When such information is lacking, comparing model results with experimental data can be very misleading. Often, a spectrum of waves with a distribution of wavelengths or phase speeds corresponding to a single dominant wave period will be simultaneously present in the atmosphere and modulating the atmospheric emissions. We will consider that situation in a future publication.

In the remainder of this section, we wish to begin comparing our model results against observations and other models. There exist in the literature several spectroscopic data sets for which Krassovsky ratios have been reported [*Sivjee and Hamwey*, 1987; *Viereck and Deehr*, 1989; *Swenson et al.*, 1990; *Taylor et al.*, 1991]. One of the most interesting observations by *Taylor et al.* [1991] at Sacramento Peak, New Mexico, showed a well-defined short-period, quasi-sinusoidal wave packet with an observed period of 13.7 min. The Utah State University infrared field-widened Michelson interferometer (IRFWI), looking at a  $15^\circ$  elevation angle, observed a time series of the OH(3-1) Meinel band spectrum, from

which a time series of the band radiance and the  $T_{rot}$  were extracted. Coaligned with the Michelson interferometer was a low-light-level television camera that detected a sharp structure in the OH layer moving with a horizontal phase speed of 28 m/s. Using the data from the television camera and the interferometer, the amplitude and phase of the Krassovsky ratio were calculated ( $|h| = 8$  and  $\phi = 48^\circ$ ) and plotted as the experimental points with error bars in Figures 15 and 16, respectively. The model values of  $\eta_{v=3}$  for  $V_{phx} = 28$  m/s are also shown in Figures 15 and 16 as a function of period. The measured Krassovsky ratio agrees with the model within the error bars. However, we note that background winds, which can Doppler shift the gravity wave frequency, were not measured, nor were they accounted for in the model. We have considered the effect of climatological background winds including tides [Makhlouf et al., 1991] and will publish this work in a future paper.

In Figure 17a, we compare the  $|h_{v=6}|$  values computed from our modified model, which includes standing waves due to a ground reflection, as described in section 7, with the data of Viereck and Deehr [1989]. These data were recorded at Longyearbyen, Svalbard ( $78^\circ\text{N}$ ), around winter solstice. The instrument used was an Ebert-Fastie spectrometer, set at  $30^\circ$  off zenith, which scanned from 820 nm to 875 nm every 30 s, covering the OH(6-2) band. The long uninterrupted nighttime conditions allow continuous measurements of the airglow to be made spanning several full days. No information is available about the existence of isolated quasi-sinusoidal waves in the data set, and no horizontal wavelength or phase speed measurements were made.

The data for the magnitude of  $\eta$  were compared against our model runs at constant  $V_{phx}$ . It was found that two large horizontal phase speeds had to be used to achieve model results comparable with the data. A value

of  $V_{phx} = 148.6$  m/s (solid line with plus signs) was required to approximate the short-period waves with  $\tau < 1$  hour. The trend of the model as a function of period agrees well with the trend seen in the data, although the uncertainties in the measurement preclude reading too much into this agreement. Nevertheless, it should be noted that none of the previous models [Schubert and Walterscheid, 1988; Schubert et al., 1991; Tarasick and Shepherd, 1992b] were able to obtain agreement with the data in this short-period region. The large-period waves with  $2 \text{ hours} < \tau < 4 \text{ hours}$  were compared to a standing-wave model calculation with a horizontal phase speed of 151.8 m/s (solid line). The model is in agreement with the data, with the same caveats given above. For  $\tau > 4$  hours, the model results are not in agreement with the data, but tidal effects should be taken into consideration, which we did not do in this paper. In addition, eddy viscosity, eddy thermal conduction, and inertial effects can play a role at the longer periods [Hickey, 1988a, b; Schubert et al., 1991]. In the latter studies it was shown that the Coriolis and eddy dissipation effects are generally unimportant at the scales we are considering except for periods greater than about 4 hours.

Of course, in addition, there is no reason why a single wave should be present in the data at any given period. Rather, the atmosphere can support a whole spectrum of different wavelengths simultaneously with the same period, and both observations and models [e.g., Dewan and Good, 1986] of gravity wave saturation effects seem to suggest that this is indeed the case. We will discuss such effects in a future publication.

In Figure 17b we overlay results from the other model calculations mentioned above [Schubert et al., 1991; Tarasick and Shepherd, 1992b] on the data of Viereck and Deehr and our model calculations both of which are repeated from Figure 17a. Each of the modelers has

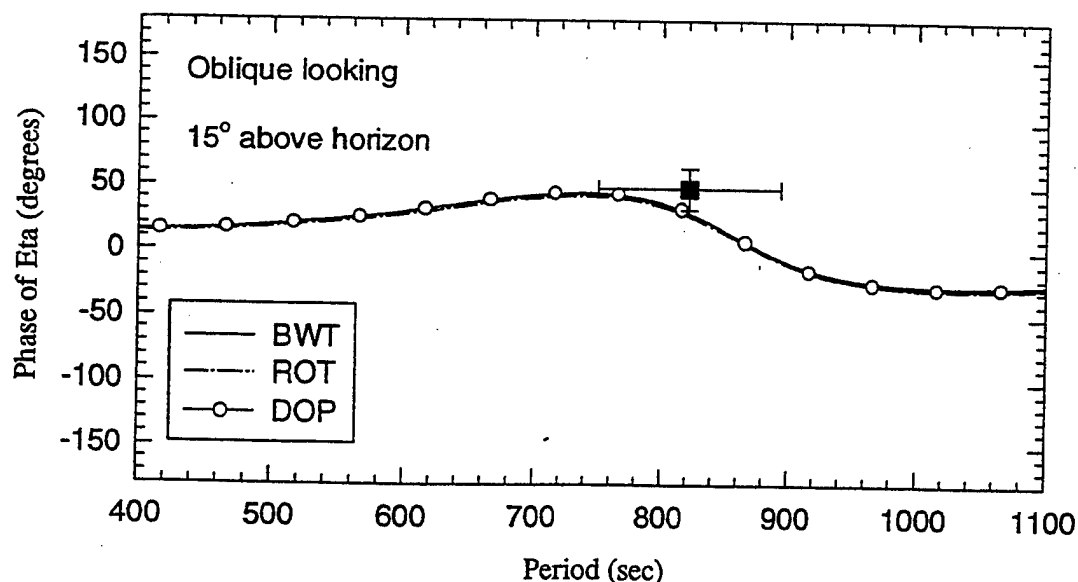


Figure 16. Phase of response function  $\eta_v$  corresponding to Figure 15, with data point of Taylor et al. [1991] shown.

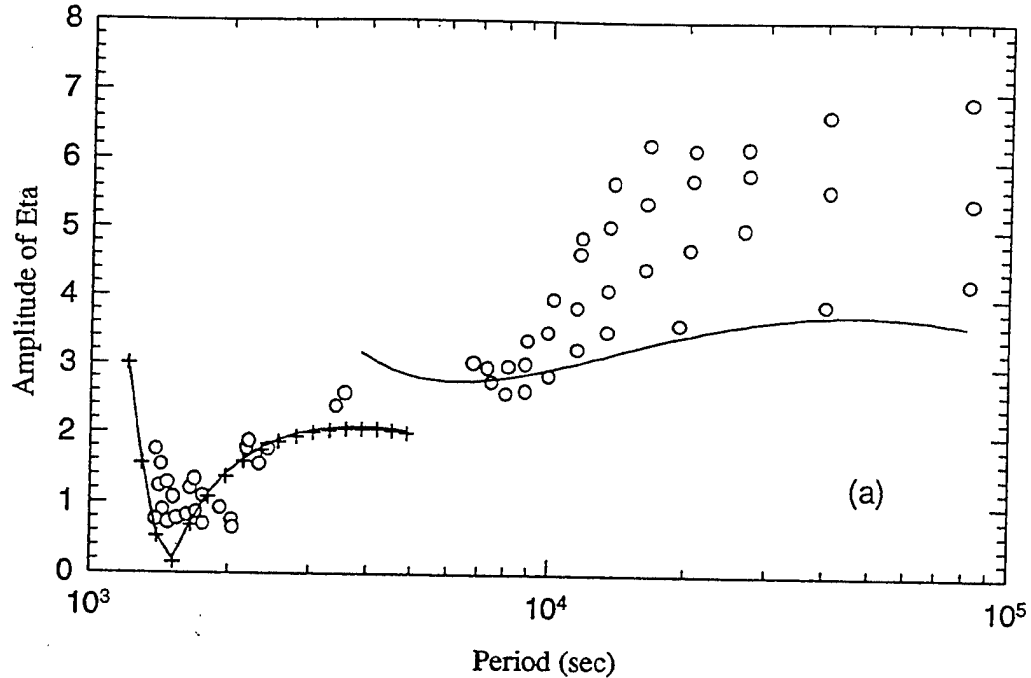


Figure 17(a). Amplitude of  $\eta$  for the OH Meinel (6-2) band from PHD model compared with measurements (open circles) by Viereck and Deehr [1989] from Svalbard. Two model curves having constant phase speed are shown, one with  $V_{phx}=151.8$  m/s (solid line), which is compared with the long-period data, and the other with  $V_{phx}=148.6$  m/s (solid line with +), which compares with the shorter-period data. Both model curves use the modified Hines model of Section 7 with a rigid ground boundary, leading to the presence of a pure standing waves, and assume a line-of-sight  $30^\circ$  off zenith.

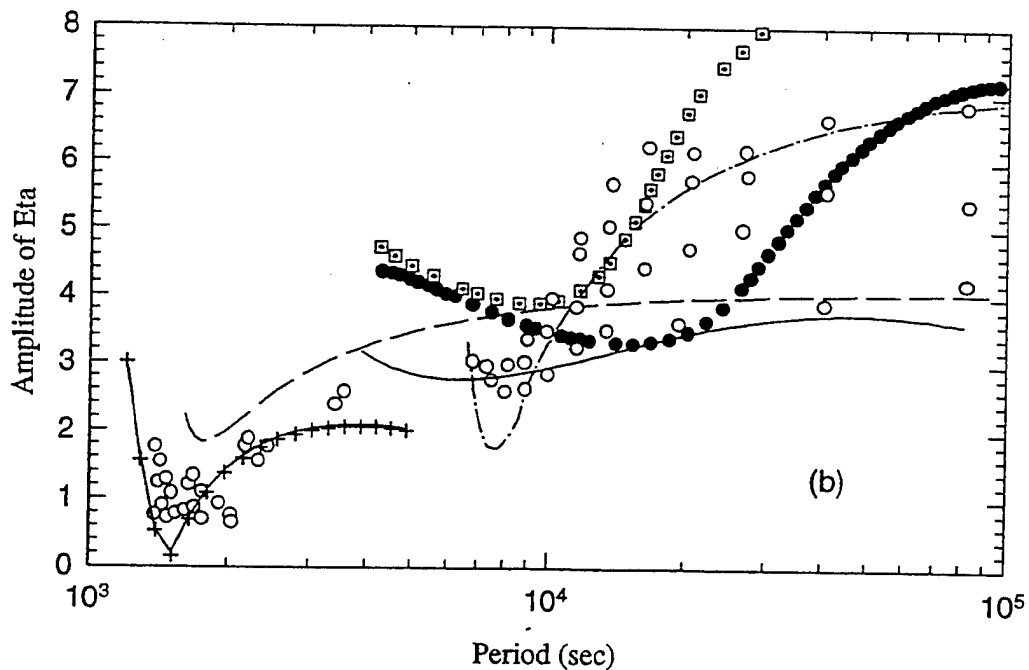


Figure 17(b). The data and model curves of (a), compared to other models having vertical traveling waves. These include model results (1) from Schubert *et al.* [1991], with constant horizontal wavelength  $\lambda_x = 500$  km (square-dot) and  $\lambda_x = 1000$  km (filled circles), and (2) from Tarasick and Shepherd [1992b], with constant phase speed  $V_{phx} = 125$  m/s (dashes) and  $V_{phx} = 65$  m/s (dash-dot). Both model results of Tarasick and Shepherd [1992b] assume a constant background wind of 100 m/s in the plane of the wave vector and the line-of-sight.

adjusted model parameters to match or span the range of the data. The model results of Schubert *et al.* [1991] are drawn for constant horizontal wavelengths,  $\lambda_x = 500$  km and 1000 km (dots and open circles, respectively), and are the only model results which include eddy viscosity and eddy thermal diffusivity. Hence they might be expected to give better agreement with the data at the longer periods. Tarasick and Shepherd [1992b] are the only modelers who added a background wind ( $V_0 = 100$  m/s, in the plane of the wave vector and the line of sight). Their model results are shown for two phase speeds,  $V_{phx} = 65$  m/s (dash-dot line) and 125 m/s (dashed line). Both the model of Schubert *et al.* and the model of Tarasick and Shepherd assume traveling waves in the vertical direction, unlike our model, which assumes standing waves due to a ground reflection. At short period the model of Schubert *et al.* is unable to obtain agreement with the data. Quenching, which reduces  $\eta$  and is included in an approximate way in the model of Tarasick and Shepherd and more exactly in our model, may help to explain the very small values of  $\eta$  observed by Viereck and Deehr at short period.

Figure 18 shows the model phase plot corresponding to Figure 17a, using the same symbols, along with Viereck and Deehr's [1989] data. The model phase results agree with the data for short-period waves, where the data tend to have phase shifts near zero. On the other hand, model phase results for our basic traveling-wave isothermal model without ground reflection (not shown) cannot be made to agree with the short-period data, yielding values greater than  $50^\circ$ . This is confirmed by the works of Schu-

bert *et al.* [1991] and of Tarasick and Shepherd [1992b], which were unable to achieve agreement with Viereck and Deehr's short-period phase data with traveling-wave models. We have plotted results for long period from our basic traveling-wave model in Figure 18 (solid line with filled circles). Here we have assumed a constant horizontal phase speed  $V_{phx} = 266.5$  m/s, and phases near  $14^\circ$ , in somewhat better agreement with the data, are obtained. Note that as was mentioned above, eddy viscosity and eddy thermal conductivity effects ignored in this model are important for periods longer than 4 hours. The traveling-wave model of Schubert *et al.* [1991], which includes eddy viscosity and eddy thermal conductivity, seems to agree rather well with the long-period phase data.

The way to achieve short-period phase results in agreement with data was suggested by the work of Hines and Tarasick [1987], which demonstrated that evanescent waves can lead to small phases. In addition, recent work by Hines and Tarasick [1994] supports the current study in showing that small phases (or alternately phases near  $180^\circ$ ) can result for any standing waves. With the ground reflection in our model, standing waves occur at all periods. However, for the long-period waves in the present example, there is a phase shift to near  $180^\circ$ , as is clear from Figure 18, in agreement with the prediction of Hines and Tarasick [1994]. We have found above that the model phase in the standing-wave isothermal model with ground reflection does not agree well with data for these long-period waves. However, we will show in a follow on publication that wave ducting in realistic non isothermal atmospheres can lead to phases which are only near zero

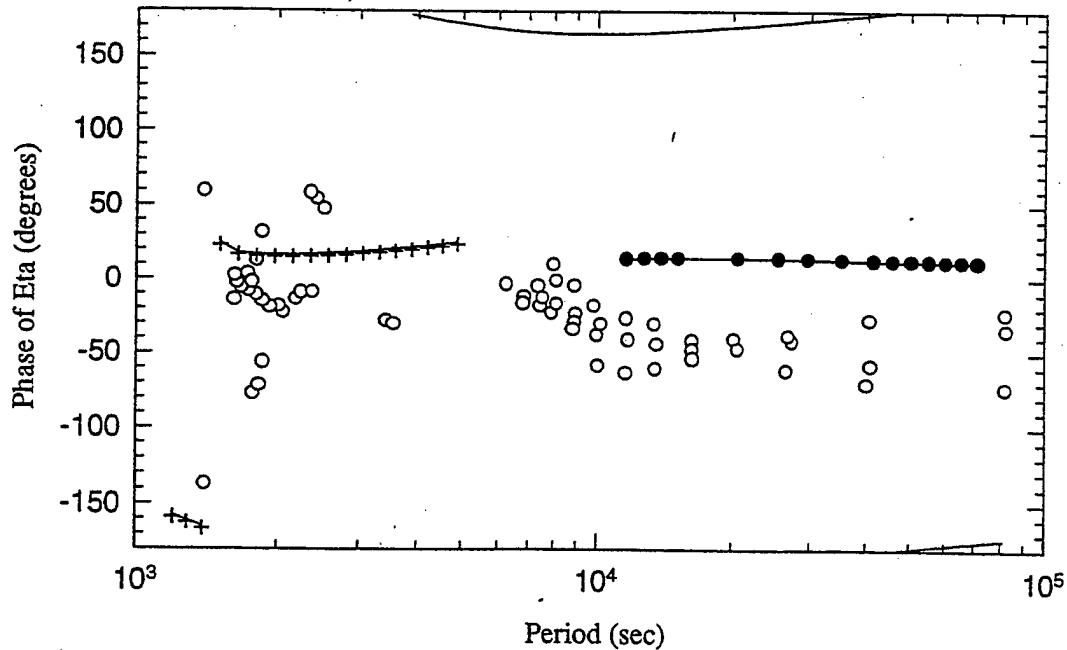


**Figure 18.** Data of Viereck and Deehr [1989] (open circles) for phase of  $\eta$  corresponding to the amplitudes shown in Figure 17(a), as compared to an isothermal standing-wave PHD model. As in Figure 17(a), two standing-wave model results for two different phase speeds are shown (solid line with +) for  $V_{phx} = 148.6$  m/s; (solid line) for  $V_{phx} = 151.8$  m/s. A traveling-wave PHD model result is also shown for a constant  $V_{phx} = 266.5$  m/s (filled circles).



(or 180°) at short periods, while the long-period phase can take on other values. This is to be expected since only short-period waves will be ducted by the thermal structure of the atmosphere and exist as standing waves.

## 9. Conclusion

We have developed a fully coupled photochemical-dynamical (PHD) model to study the structure in atmospheric emissions due to modulation by internal gravity waves and have applied this model to the OH Meinel band airglow. A number of effects in the real atmosphere and in real measurements have been shown to affect the magnitude and phase of the airglow linear response function, or Krassovsky  $\eta$  ratio. Since our model calculates modulation of the level populations rather than modulation of the production rate, it is fully capable of taking quenching into account. We have shown that quenching has a significant effect on the airglow response to an IGW. Not only does it have a large effect on the amplitude and phase of the response function  $\eta$ , but it also makes the response a vibrational-level-dependent quantity. Atmospheric temperature inhomogeneities were also shown to affect significantly the value of  $\eta$ , since they lead to different  $\eta$  values for different methods of inferring the effective temperature from the airglow emission. We have seen that  $\eta$  values determined from  $T_{rot}$  can differ from those determined from  $T_{Dop}$  and that both differ significantly from  $\eta$  calculated using the BWT, which is commonly used in model investigations. The differences between the various  $\eta$  disappear as the vertical wavelength becomes shorter and the atmospheric temperature becomes effectively more homogeneous.

We compared our model with the midlatitude off-zenith observations of Taylor *et al.* [1991] and with the high-latitude data of Viereck and Deehr [1989]. The model predicts well the value of  $\eta$  for an isolated short-period, quasi-sinusoidal wave which Taylor *et al.* observed. The agreement of the model  $|\eta|$  with Viereck and Deehr's data is also good, but there is some disagreement concerning the phase of  $\eta$ , especially for periods greater than 2 hours. Many of the zenith-looking observations show similar small differences in phase between the brightness fluctuations and those of the temperature, whereas the models show larger phase shifts. Standing waves are capable of yielding phases near zero, as we demonstrated by adding to the isothermal IGW model a ground reflection. In the real atmosphere, standing waves can result from atmospheric background winds and temperature variations, with consequent Doppler shifting and wave ducting. This wave ducting appears to be important in explaining observations, as will be discussed further in a follow-on publication.

## Appendix

Expanding the numerator of equation (15) to first order, one gets

$$B_a = B_{a0} + \Delta B_a$$

where  $B_{a0}$  is obtained from  $B_a$  by replacing  $N_v(x, z)$  by  $N_{v0}(z)$  and  $T(x, z)$  by  $T_0(z)$  in equations (15) and (16) and

$$\Delta B_a = A_a \int \Delta N_a(x, z) dl$$

Now  $\Delta N_a$  is determined by expanding equation (16) to first order, with the result

$$\frac{\Delta N_a(x, z)}{N_{a0}(z)} = \frac{\Delta N_v(x, z)}{N_{v0}(z)} + \frac{(E_a - \langle E \rangle) \Delta T(x, z)}{k_B T_0(z) T_0(z)}$$

where we have used

$$\frac{\Delta Z_v(T_0, \Delta T)}{Z_v[T_0(z)]} = \frac{\langle E \rangle}{k_B T_0(z)} \frac{\Delta T(x, z)}{T_0(z)}$$

and defined

$$\langle E \rangle = \frac{1}{Z_v[T_0(z)]} \sum g_a E_a \exp\left(-\frac{E_a}{k_B T_0(z)}\right)$$

**Acknowledgments.** This research has been sponsored by the Air Force Office of Scientific Research under the SOAR optical structure investigation program and has benefited from comments made by our colleagues during presentations at SOAR workshops. We are grateful for helpful discussions with W. R. Pendleton Jr., M. J. Taylor, R. P. Lowe, T. F. Tuan, and C. O. Hines. We would like to thank E.M. Dewan, J. O. Wise, and M. P. Hickey for reading the manuscript and making helpful suggestions and one of the reviewers for a very thoughtful and useful review. One of us (U. M.) would like to acknowledge the National Research Council Postdoctoral Research Associateship program, under whose support this research was begun, and the Air Force Office of Scientific Research's Geophysics Scholar program, administered by the Southeastern Center for Electrical Engineering Education, under which the work was continued. He is currently supported by Phillips Laboratory, Geophysics Directorate, under contract F19628-93-C-0165 with Utah State University.

## References

- Baker, D. J., Studies of atmospheric infrared emissions, *Rep. AFGL-TR-78-0251*, Air Force Geophys. Lab., Bedford, Mass., 1978.
- Bates, D. R., and M. Nicolet, Theoretical considerations regarding the altitude of the layer responsible for the nocturnal emission of the sodium D-lines, *J. Geophys. Res.*, **55**, 235-239, 1950.
- Chalamala, B. R., and R. A. Copeland, Collision dynamics of OH( $X^2\Pi, v=9$ ), *J. Chem. Phys.*, **99**, 5807-5811, 1993.
- Dewan, E. M., and R. E. Good, Saturation and the "universal" spectrum for vertical profiles of horizontal scalar winds in the atmosphere, *J. Geophys. Res.*, **91**, 2742-2748, 1986.
- Dodd, J. A., S. J. Lipson, and W. A. M. Blumberg, Vibrational relaxation of OH( $X^2\Pi, v=1-3$ ) by O<sub>2</sub>, *J. Chem. Phys.*, **92**, 3387-3393, 1990.
- Dodd, J. A., S. J. Lipson, and W. A. M. Blumberg, Formation and vibrational relaxation of OH( $X^2\Pi, v$ ) by O<sub>2</sub> and CO<sub>2</sub>, *J. Chem. Phys.*, **95**, 5752-5762, 1991.

- Garcia, R. R., and S. Solomon, The effects of breaking gravity waves on the dynamics and chemical composition of the mesosphere and lower thermosphere, *J. Geophys. Res.*, **90**, 3850-3868, 1985.
- Goody, R. M., and Y. L. Yung, *Atmospheric Radiation*, 2nd ed., Oxford University Press, New York, 1989.
- Hampson, R.F., and d. Garvin, Reaction rate and photochemical data for atmospheric chemistry, *NBS 513*, Natl. Inst. of Stand. and Technol., Gaithersburg, Md., 1977.
- Hernandez, G., Measurements of thermospheric temperatures and winds by remote Fabry-Perot spectrometry, *Opt. Eng.*, **19**, 518-532, 1980.
- Hernandez, G., *Fabry Perot Interferometers*, Cambridge University Press, New York, 1986.
- Hernandez, G., and J. L. Smith, Mesospheric wind determinations and the  $P_1(2)_{c,d}$  lines of the  $X^2\Pi$  OH (8-3) band, *Geophys. Res. Lett.*, **11**, 534-537, 1984.
- Hickey, M. P., Effects of eddy viscosity and thermal conduction and the Coriolis force in the dynamics of gravity wave driven fluctuations in the OH nightglow, *J. Geophys. Res.*, **93**, 4077-4088, 1988a.
- Hickey, M. P., Wavelength dependence of eddy dissipation and Coriolis force in the dynamics of the gravity wave driven fluctuations in the OH nightglow, *J. Geophys. Res.*, **93**, 4089-4101, 1988b.
- Hickey, M. P., G. Schubert, and R. L. Walterscheid, Seasonal and latitudinal variations of gravity wave-driven fluctuations in OH nightglow, *J. Geophys. Res.*, **97**, 14,911-14,922, 1992.
- Hickey, M. P., G. Schubert, and R. L. Walterscheid, Gravity wave-driven fluctuations in the  $O_2$  atmospheric (0-1) nightglow from an extended, dissipative emission region, *J. Geophys. Res.*, **98**, 13,717-13,729, 1993.
- Hines, C. O., Internal atmospheric gravity waves at ionospheric heights, *Can. J. Phys.*, **38**, 1441-1481, 1960.
- Hines, C. O., and D. W. Tarasick, On the detection and utilization of gravity waves in airglow studies, *Planet. Space Sci.*, **35**, 851-866, 1987.
- Hines, C. O., and D. W. Tarasick, Airglow response to ducted gravity waves (abstract), *Eos, Trans. A.G.U.*, **74**, (43), Fall Meeting suppl., 461, 1993.
- Hines, C. O., and D. W. Tarasick, Airglow response to vertically standing gravity waves, *Geophys. Res. Lett.*, **21**, 2729-2732, 1994.
- Jet Propulsion Laboratory, Chemical kinetics and photochemical data for use in stratospheric modeling, *JPL 90-1*, NASA Panel for Data Eval., Pasadena, Calif., 1990.
- Kaye, J. A., On the possible role of the reaction  $O + HO_2 \rightarrow OH + O_2$  in OH airglow, *J. Geophys. Res.*, **93**, 285-288, 1988.
- Klenerman, D., and I. W. M. Smith, Infrared chemiluminescence studies using a SISAM spectrometer. Reactions producing vibrationally excited OH, *J. Chem. Soc. Faraday Trans. 2*, **83**, 229-241, 1987.
- Knutsen, K., and R. A. Copeland, Vibrational relaxation of  $OH(X^2\Pi, v=7,8)$  by  $O_2$ ,  $N_2$ ,  $N_2O$  and  $CO_2$  (abstract), *Eos, Trans. A.G.U.*, (43) Fall Meeting Suppl., 472, 1993.
- Krassovsky, V. I., Infrasonic variations of OH emission in the upper atmosphere, *Ann. Geophys.*, **28**, 739-746, 1972.
- Krassovsky, V. I., B. P. Potapov, A. I. Seminov, M. V. Shagaev, N. H. Shefov, V. G. Sobolev and T. I. Toroshelidze, Internal gravity waves near the mesopause and the hydroxyl emission, *Ann. Geophys.*, **33**, 347-356, 1977.
- Le Texier, H., S. Solomon, and R. R. Garcia, Seasonal variability of the OH Meinel bands, *Planet. Space Sci.*, **35**, 977-989, 1987.
- Le Texier, H., S. Solomon, R.J. Thomas, and R. R. Garcia, OH\* (7,5) Meinel band dayglow and nightglow measured by the SME limb scanning near infrared spectrometer: Comparison of the observed seasonal variability with two-dimensional model simulations, *Ann. Geophys.*, **7**, 365-374 1989.
- Llewellyn, E. J., B. H. Long, and B. H. Solheim, The quenching of OH\* in the atmosphere, *Planet. Space Sci.*, **26**, 525-531 1978.
- López-Moreno, J. J., R. Rodrigo, F. Moreno, M. López-Puertas, and A. Molina, Altitude distribution of vibrationally excited states of atmospheric hydroxyl at levels  $v=2$  to  $v=7$ , *Planet. Space Sci.*, **35**, 1029-1038, 1987.
- Lunt, S. T., G. Marston, and R. P. Wayne, Formation of  $O_2(a^1\Delta_g)$  and vibrationally excited OH in the reaction between O atoms and  $HO_x$  species, *J. Chem. Soc. Faraday Trans. 2*, **84**, 899-912, 1988.
- Makhlouf, U. B., On the role of atmospheric gravity waves in mesospheric dynamics, Ph.D. Thesis, Univ. of Cincinnati, Cincinnati, Ohio, 1989.
- Makhlouf, U. B., R. H. Picard, and J. R. Winick, Modulation of the hydroxyl emission by a monochromatic gravity wave in a realistic non isothermal atmosphere (abstract), *Eos, Trans. A.G.U.*, **71**, (43), Fall Meeting suppl., 1496, 1990.
- Makhlouf, U. B., R. H. Picard, J. R. Winick, T. F. Tuan, and E. Ryan, Hydroxyl airglow fluctuations due to gravity waves propagating in a realistic atmosphere in the presence of background wind (abstract), *Eos, Trans. A.G.U.*, **72** (44) Fall Meeting suppl., 374, 1991.
- Makhlouf, U. B., R. H. Picard, J. R. Winick, T.F. Tuan, and E. Ryan, Response of the hydroxyl layer to small vertical scale gravity waves propagating in a realistic windy atmosphere (abstract), *Eos, Trans. A.G.U.*, **74**, (43), Fall meeting Suppl., 462, 1993.
- McDade, I. C., and E. J. Llewellyn, Kinetic parameters related to sources and sinks of vibrationally excited OH in the nightglow, *J. Geophys. Res.*, **92**, 7643-7650, 1987.
- Nelson, D. D., Jr., A. Schiffman, D. J. Nesbitt, J. J. Orlando, and J. B. Burkholder, H +  $O_3$  Fourier-transform infrared emission and laser absorption studies of  $OH(X^2\Pi)$  radical: An experimental dipole moment function and state-to-state Einstein A coefficients, *J. Chem. Phys.*, **93**, 7003-7019, 1990.
- Noxon, J. F., Effect of internal gravity waves upon night airglow temperatures, *Geophys. Res. Lett.*, **5**, 25-27, 1978.
- Peterson, A. W., and L. M. Kieffaber, Infrared photography of OH airglow structures, *Nature*, **242**, 321-322, 1973.
- Picard, R. H., U.B. Makhlouf, and J. R. Winick, Realistic photochemical-dynamical models for radiative response to acoustic-gravity waves (abstract), *International Conference on Gravity Waves in the Atmosphere: Program, Tutorial Notes, and Abstracts*, Canadian Network for Space Research, Calgary, Alta., 1994.
- Plane, J. M. C., and M. P. Hickey, A model of wave-driven fluctuations in the sodium nightglow and sodium layer (abstract), *Eos, Trans. A.G.U.*, **74**, (43), Fall Meeting suppl., 462, 1993.
- Rensberger, K. J., J. B. Jeffries and D. R. Crosley, Vibrational relaxation of  $OH(X^2\Pi, v=2)$ , *J. Chem. Phys.*, **90**, 2174-2181, 1989.

- Rogers, J. W., R. E. Murphy, A. T. Stair, Jr., J. C. Ulwick, K. D. Baker, and L. L. Jensen, Rocket-borne Radiometric measurements of OH in the auroral zone, *J. Geophys. Res.*, **78**, 7023-7031, 1973.
- Sappey, A. D., and R. A. Copeland, Collision dynamics of OH( $X^2\Pi$ ,  $v=12$ ), *J. Chem. Phys.*, **93**, 5741-5746, 1990.
- Schubert, G. and R. L. Walterscheid, Wave driven fluctuations in OH nightglow from an extended source region, *J. Geophys. Res.*, **93**, 9903-9915, 1988.
- Schubert, G., R. L. Walterscheid and M. P. Hickey, Gravity wave-driven fluctuations in OH nightglow from an extended, dissipative emission region, *J. Geophys. Res.*, **96**, 13,869-13,880, 1991.
- Shepherd, G. G., et al., WINDII, the wind imaging interferometer on the Upper Atmospheric Research Satellite, *J. Geophys. Res.*, **98**, 10,725-10,750, 1993.
- Sivjee, G. G., and R. M. Hamwey, Temperature and chemistry of the polar mesopause OH, *J. Geophys. Res.*, **92**, 4663-4672, 1987.
- Spencer, J. E., and G. P. Glass, Some reactions of OH( $v=1$ ), *Int. J. Chem. Kinet.*, **9**, 111-122, 1977.
- Stair, A. T., Jr., R. D. Sharma, R. M. Nadile, D. J. Baker and W. F. Grieder, Observations of limb radiance with cryogenic spectral infrared rocket experiment, *J. Geophys. Res.*, **90**, 9763-9775, 1985.
- Strobel, D. F., M. E. Summers, R. M. Bevilacqua, M. T. DeLand, and M. Allen, Vertical constituent transport in the mesosphere, *J. Geophys. Res.*, **92**, 6691-6698, 1987.
- Summers, M. E., Zonally averaged trace constituent climatology, *Tech. Pub. NRL/MR/7641--93-7416*, Nav. Res. Lab., Washington, D. C., 1993.
- Swenson, G. R., S. B. Mende, and S. P. Geller, Fabry-Perot imaging observations of OH(8-3): Rotational temperatures and gravity waves, *J. Geophys. Res.*, **95**, 12,251-12,263, 1990.
- Takahashi, H., P. P. Batista, Y. Sahai, and B. R. Clemesha, Atmospheric wave propagation in the mesopause region observed by the OH(8-3) band, NaD, O<sub>2</sub>A (8645 Å) band and OI (5577 Å) nightglow emissions, *Planet. Space Sci.*, **33**, 381-384, 1985.
- Tarasick, D. W., and C. O. Hines, The observable effects of gravity waves on airglow emissions, *Planet. Space Sci.*, **38**, 1105-1119, 1990.
- Tarasick, D. W., and G. G. Shepherd, Effects of gravity waves on complex airglow chemistries, 1, O<sub>2</sub>( $^1\Sigma_g^+$ ) emission, *J. Geophys. Res.*, **97**, 3185-3194, 1992a.
- Tarasick, D. W., and G. G. Shepherd, Effects of gravity waves on complex airglow chemistries, 2, OH emission, *J. Geophys. Res.*, **97**, 3195-3208, 1992b.
- Taylor, M. J., and M. J. Hill, Near infrared imaging of hydroxyl wave structure over an ocean site at low latitudes, *Geophys. Res. Lett.*, **18**, 1333-1336, 1991.
- Taylor, M. J., M. A. Hapgood, and P. Rothwell, Observations of gravity wave propagation in the OI (557.7 nm), Na (589.2 nm) and the near infrared OH airglow emissions, *Planet. Space Sci.*, **35**, 413-427, 1987.
- Taylor, M. J., P. J. Espy, D. J. Baker, R. J. Sica, P. C. Neal, and W. R. Pendleton Jr., Simultaneous intensity, temperature and imaging measurements of short period wave structure in the OH nightglow emission, *Planet. Space Sci.*, **39**, 1171-1188, 1991.
- Thuillier, G., and M. Hersé, Thermally stable field compensated Michelson interferometer for measurement of temperature and wind of the planetary atmospheres, *Appl. Opt.*, **30**, 1210-1220, 1991.
- Tuan, T. F., and D. Tadic, A dispersion formula for analyzing 'modal interference' among guided and free gravity wave modes and other phenomena in a realistic atmosphere, *J. Geophys. Res.*, **87**, 1648-1668, 1982.
- Turnbull, D. N., and R. P. Lowe, New hydroxyl transition probabilities and their importance in airglow studies, *Planet. Space Sci.*, **37**, 723-738, 1989.
- Viereck, R. A., and C. S. Deehr, On the interaction between gravity waves and the OH Meinel (6-2) and the O<sub>2</sub> atmospheric (0-1) bands in the polar night airglow, *J. Geophys. Res.*, **94**, 5397-5404, 1989.
- Walterscheid, R. L., G. Schubert, and J. M. Straus, A dynamical-chemical model of wave-driven fluctuations in the OH nightglow, *J. Geophys. Res.*, **92**, 8775-8780, 1987.
- Weinstock, J., Theory of the interaction of gravity waves with O<sub>2</sub>( $^1\Sigma$ ) airglow, *J. Geophys. Res.*, **83**, 5175-5185, 1978.
- Winick, J. R., Photochemical processes in the mesosphere and lower thermosphere, in *Solar-Terrestrial Physics*, edited by R. L. Carpvillano and J. M. Forbes, pp 677-732, D. Reidel, Norwell, Mass., 1983.
- Winick, J. R., R. H. Picard, R. D. Sharma, and R. M. Nadile, Oxygen singlet delta 1.58-micrometer (0-1) limb radiance in the upper stratosphere and lower mesosphere, *J. Geophys. Res.*, **90**, 9804-9814, 1985.
- Zhang, S. P., R. H. Wiens, and G. G. Shepherd, Gravity waves from O<sub>2</sub> nightglow during the AIDA '89 Campaign. II. Numerical modeling of the emission rate / temperature ratio,  $\eta$ , *J. Atmos. Terr. Phys.*, **54**, 377-395, 1993.

U. B. Makhlof, Stewart Radiance Laboratory, 139 The Great Rd., Bedford, MA 01730. (e-mail: makhlof@pldac.plh.af.mil)

R. H. Picard and J. R. Winick, Geophys. Directorate, Phillips Laboratory, Hanscom Air Force Base, MA 01731-3010.

(Received May 16, 1994; revised December 6, 1994; accepted December 8, 1994)

## Determination of horizontal and vertical structure of an unusual pattern of short period gravity waves imaged during ALOHA-93

M.J. Taylor

Space Dynamics Laboratory and Physics Department, Utah State University

D.C. Fritts and J.R. Isler

Laboratory for Atmospheric and Space Physics, University of Colorado

**Abstract.** An all-sky CCD imager has been used to measure the properties of short period gravity waves present over the Hawaiian Islands during the ALOHA-93 campaign. Observations of emissions from four different altitudes provided a capability to describe the vertical as well as the horizontal structure of the wave field. On several occasions during this campaign an unusual morphology wave pattern was detected that consisted of a group of small-scale waves oriented in the same direction. These were most noticeable in the OI (557.7 nm) emission, altitude ~96 km, and were usually observed in association with a larger scale gravity wave. This paper presents a preliminary analysis of data recorded on the night of 22 October during which both types of waves were prominent. The small-scale waves exhibited highly coherent phase structures at each emission altitude, consistent with a ducted wave motion. The spatial intensity and phase modulation of this display is indicative of interference between two waves with similar characteristics and slightly different propagation directions. The larger scale wave motion was observed to propagate perpendicular to the small-scale waves, and showed evidence of phase progression with altitude, implying upward energy propagation. These data have been interpreted in the context of simultaneous wind measurements from an MF radar.

### Introduction

Since gravity waves were first recognized as an important atmospheric phenomenon [Hines, 1960] considerable observational and theoretical research has ensued. These efforts have established the importance of such motions in driving the mean circulation and thermal structure of the mesosphere and lower thermosphere via wave energy and momentum transports [Fritts, 1989], yet the processes responsible for the variability, interactions and saturation of the gravity wave spectrum remain poorly understood at present. Images of the nightglow emissions from several different layers offer a unique three-dimensional measurement capability for quantifying the effects of small-scale wave motions on the upper mesosphere and lower thermosphere (~80-100 km). Most nightglow image measurements reported in the literature concern short-period motions (<1 hour) and fall into two distinct categories termed "bands" and "ripples". Bands are extensive, long-lasting wave patterns exhibiting horizontal wavelengths ( $\lambda_h$ ) of several tens of kilometers and horizontal phase velocities ( $v_h$ ) of up to 100  $\text{ms}^{-1}$  [Clairemidi et al., 1985]. These patterns have been attributed to vertically propagating

short-period gravity waves [Taylor et al., 1987]. Ripples are short-lived (<45 min) small-scale wave patterns ( $\lambda_h$  ~5-15 km), of restricted spatial extent [Peterson, 1979], and are thought to be generated in-situ by localized shear instabilities in the wind field [Taylor and Hapgood, 1990]. This paper describes an unusual morphology short-period wave pattern which appears to fall in between these two categories and was observed concurrently with a well-developed band display progressing on an almost orthogonal heading. Both wave motions occupied much of the visible sky at nightglow emission altitudes, but exhibited very different propagation characteristics.

### Nightglow and Radar Observations

During the ALOHA-93 campaign (6-23 October, 1993) a high-performance all-sky CCD imaging system was operated at Haleakala Crater (20.8°N, 156.2°W, 2970m) to measure gravity waves within a ~450 km radius of Maui, Hawaii. Sequential observations of the NIR OH(715-930 nm) and O<sub>2</sub>(0,1) At bands (centered at ~865 nm) and the OI(557.7 nm) and Na(589.2 nm) line emissions were recorded in a cycle time of ~9 min. Well-defined gravity wave bands and ripple events were observed on many occasions in each of these emissions [Taylor et al., 1995].

On several nights a most unusual wave pattern was imaged consisting of organized groups of small-scale waves, all oriented in the same direction and often extending over a large area of sky. In many cases these waves appeared in association with a set of larger scale bands oriented approximately orthogonal to the smaller-scale structures. This phenomenon was most pronounced on the night of 22 October. Correlative radar wind profiles were also obtained with the Hawaii MF radar located on Kauai, Hawaii (22°N, 160°W), ~375 km to the WNW of Maui. During ALOHA-93 the radar registered considerable amplitude variability of the diurnal tide [Isler and Fritts, 1995]. Here, the radar data have been used to define the average horizontal winds at nightglow altitudes. The winds were averaged over 3 hour intervals in order to focus on motions coherent over the horizontal distance separating the two sites.

### 22 October Nightglow Wave Display

All four nightglow emissions registered wave structure throughout this night, from 08:30 to 15:30 UT. Figure 1 shows four images of the OI(557.7 nm) nightglow emission illustrating the morphology of these waves at ~96 km altitude. They reveal a dramatic series of wave motions, with the dominant structures at early times consisting of several groups (rows) of small scale, ripple-like, waves but with a large  $\lambda_h$  of  $19 \pm 0.5$  km and lifetimes > 2 hours. Figure 2 plots the position and extent of this wave pattern at 09:27 UT in Figure 1a. Image sequences reveal a phase speed of ~40  $\text{ms}^{-1}$  towards the SE (azimuth ~137°) and an apparent drift of the wave group towards the NE (azimuth ~47°) at ~25  $\text{ms}^{-1}$ . Figure 1d shows a similar set of

Copyright 1995 by the American Geophysical Union.

Paper number 95GL02945

0094-8534/95/95GL-02945\$03.00

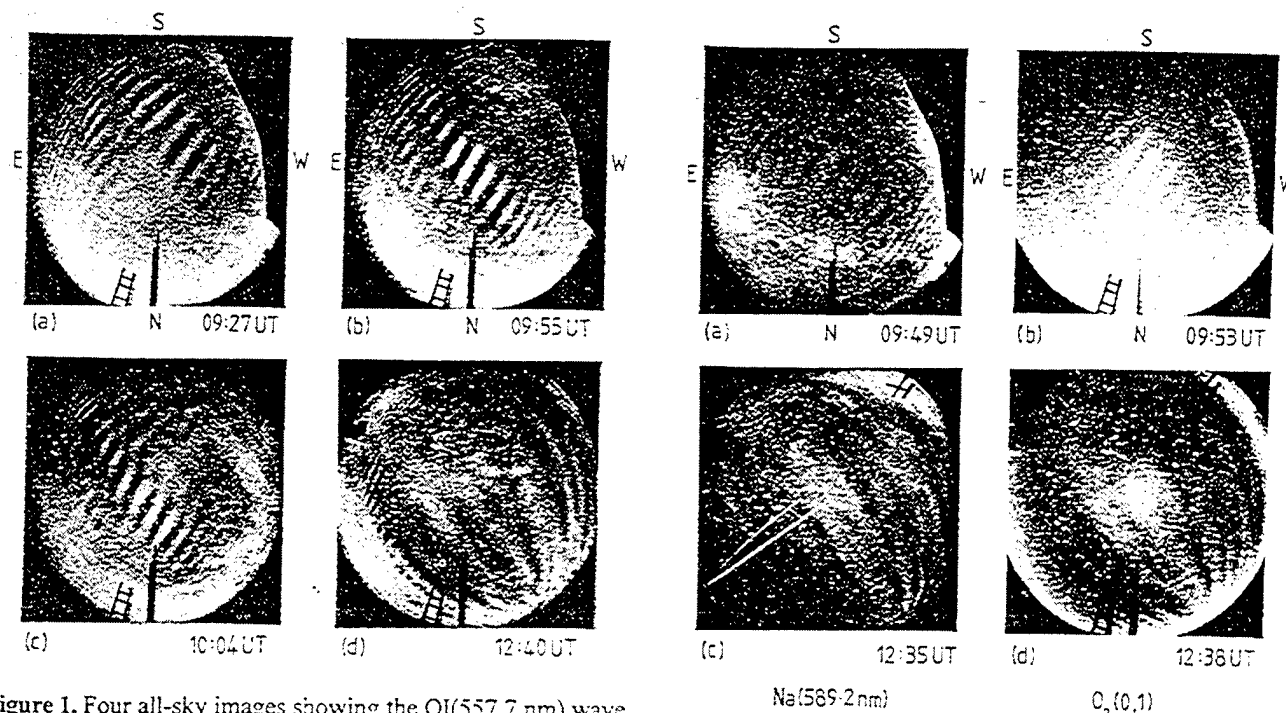


Figure 1. Four all-sky images showing the OI(557.7 nm) wave patterns (integration time 90s). Images a,b,c show the extent and apparent lateral motion of the small-scale wave pattern that was most conspicuous during the period 08:30–10:30 UT. Image d shows the morphology of the larger scale gravity wave at 12:40 UT.

small-scale waves (imaged ~3 hours later), superposed with an extensive, nearly orthogonal band pattern exhibiting a  $\lambda_b = 38 \pm 2$  km and  $v_b = 34 \pm 3$  ms<sup>-1</sup> moving towards the SW (azimuth ~234°). Figure 3 shows the Na(589.2 nm) and O<sub>2</sub>(0,1) data corresponding closely to the OI images at 09:55 UT and 12:40 UT. These emissions occur at ~90 and ~94 km altitudes respectively, and can be used to assess the vertical structure of the two wave motions.

#### MF Radar Wind Profiles

Figure 4 shows profiles of the horizontal winds obtained with the MF radar for 3-hour intervals centered at 09:30 UT and 12:30 UT

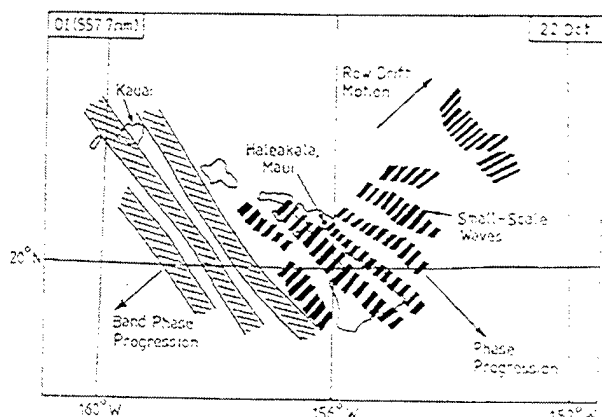


Figure 2. Map showing the horizontal scale size and geographical extent of the small-scale waves imaged at 09:27 UT (assuming an emission height of 96 km). The arrows indicate the observed phase progression towards the SE and the apparent drift motion of the rows towards the NE. For comparison three of the larger scale bands evident in Figure 1d are also plotted.

Figure 3. Four all-sky images showing wave structure in the Na and O<sub>2</sub> images at 09:50 UT and 12:40 UT.

and projected into the observed directions of motion of the two wave patterns of Figure 1 (i.e. toward the SE and SW). In Figure 4a winds of ~25 to 35 ms<sup>-1</sup> towards the NW existed over all emission altitudes, opposite to the direction of the small-scale wave motion, suggesting an intrinsic phase speed of ~70 ms<sup>-1</sup> and an intrinsic period of ~4.5 min. Winds toward the SW during this period were ≤10 ms<sup>-1</sup>. The profiles of Figure 4b reveal a mean wind towards the N, with a component directed opposite to the observed phase motion of the large scale wave of ~20–30 ms<sup>-1</sup>, implying an intrinsic phase speed of ~60 ms<sup>-1</sup> and an intrinsic period of ~10.6 min.

#### Implications for Wave Dynamics

##### Short Wavelength Motions

Inspection of the image data of Figures 1 and 3 reveals a number of interesting properties. One important feature is the high degree of correlation between the small-scale waves imaged at different altitudes. Comparison of the early OI, Na and O<sub>2</sub> (and OH) waves show close alignment at the zenith when compensation was made for the slightly different times of the three images. This suggests a wave motion with little or no phase variation with altitude, such as expected for motions ducted near a local maximum of horizontal velocity or stability [Chimonas and Hines, 1986; Fritts and Yuan, 1989]. Detailed analysis (not shown) also suggests a phase retardation of the upper layers relative to those below, which appears symmetric about the zenith, indicating that this wave motion was vertically coherent across the sky.

Vertical phase coherence by itself provides persuasive evidence for ducted gravity waves, but there are other data that further support this case. These are the radar wind profiles shown in Figure 4, the first of which indicates a large negative mean wind in the direction of phase progression below ~98 km. With a  $\lambda_b$  of 19 km, a scale height  $H \sim 6$  km and an assumed static stability  $N^2 \sim 2 \times 10^{-4}$  s<sup>-2</sup>, we infer from the Taylor-Goldstein equation a vertical wavenumber ( $m$ ) squared given by

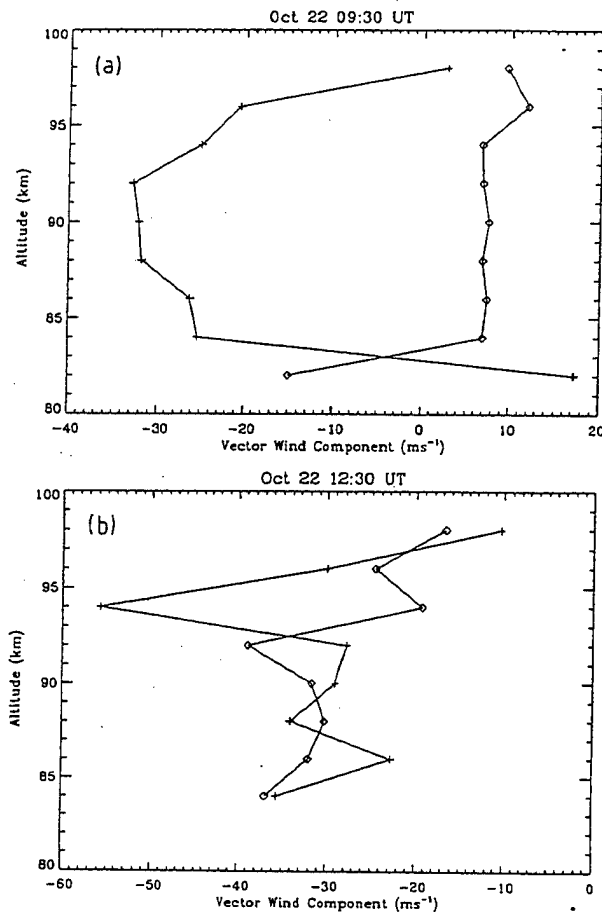


Figure 4. Time averaged wind measurements determined by the MF radar. The crosses show the SE-ward wind component in the direction of motion of the small-scale waves, and the diamonds the SW-ward wind component in the direction of motion of the bands.

$$m^2 = N^2/(c-u)^2 - k^2 - 1/4H^2 \quad (1)$$

where we have neglected shear and curvature effects of the mean wind profile and  $c$  is the observed phase speed,  $u$  is the mean wind in the direction of wave motion and  $k$  is the horizontal wave number. When  $m^2 > 0$  the motion is vertically propagating, when  $m^2 < 0$  the wave is vertically evanescent. Eq.(1) thus allows us to compute how large an intrinsic phase speed ( $c-u$ ) is required for evanescent (or ducted) behavior. In this case, a value of  $(c-u) \sim 50 \text{ ms}^{-1}$  or larger is required. However,  $(c-u)$  values below  $\sim 96 \text{ km}$  (where the emission layers occur) are typically  $70 \text{ ms}^{-1}$ . Thus, the suggestion that these motions represent ducted waves is also supported by the environmental data. A final feature of the observed structures supporting this interpretation is the intensity variation of the different nightglow features with height. This is shown in Figure 5 for the prominent small-scale waves observed around 09:55 UT. The larger response of the OI relative to the O<sub>2</sub> and Na features at lower altitudes is strongly suggestive of a wave duct at greater altitudes.

The morphology of these small-scale wave motions was most unusual and to our knowledge has not been previously reported [Taylor et al., 1995]. In particular, Figure 1 shows the wave forms to be staggered, with alternating bright and dark forms in adjacent rows (Figure 2). One possible explanation for this unusual pattern is the superposition of two band-type motions having similar characteristics, but slightly different directions of propagation i.e., similar periods, horizontal wavelengths and amplitudes, but somewhat

different azimuths. For example, two identical waves with horizontal wavelengths of  $\sim 19 \text{ km}$  propagating at phase speeds of  $\sim 40 \text{ ms}^{-1}$  and  $\sim 20^\circ$  apart, toward azimuths of  $125^\circ$  and  $145^\circ \text{ N}$ , would produce a row-like pattern having an apparent wavelength of  $19.3 \text{ km}$  and phase speed of  $40.6 \text{ ms}^{-1}$ . Such a superposition would also account for the staggering of bright and dark forms in adjacent rows because the superposed motions would generate an interference pattern with a fringe spacing of, in this case  $19 \text{ km}/2\sin 10^\circ = 55 \text{ km}$ , which is consistent with the observed separation between the bright forms in alternating rows. Furthermore, a slightly larger phase speed for the component propagating at  $145^\circ \text{ N}$  would easily account for the apparent drift motion of the wave group towards the NE.

### Long Wavelength Motions

The bands propagating towards the SW were evident for most of the night but were very prominent at later times. In this case, an intrinsic phase speed of  $\sim 60 \text{ ms}^{-1}$  combined with a larger horizontal wavelength ( $\sim 38 \text{ km}$ ) implies a large vertical wavelength ( $\lambda_z$ ) of  $\sim 40 \text{ km}$ . This wave is quite distinct from the evanescent character of the ducted wave discussed above and indicates a role for this motion in the vertical transport of energy and momentum. Further evidence of the vertical progression of this wave motion was again provided by the optical data which suggest a small phase shift with altitude consistent with a large  $\lambda_z$ . The orthogonal orientation of the smaller-scale waves to these bands is suggestive of a direct relationship between these two wave motions but the mechanism is not obvious. However, the horizontal wavelengths and lifetimes of the small-scale waves are too large to result from a convective instability induced by the long wavelength motion breaking as it propagated into the lower thermosphere [Fritts et al., 1993].

### Summary

We have presented a preliminary analysis of the wave motions observed in the OI, Na and O<sub>2</sub> nightglow emissions on 22 October, 1993. This night was selected because of the distinct wave structures present and the availability of correlative MF radar wind data. The coherence of the small-scale waves over  $\sim 80\text{--}100 \text{ km}$  altitude and their high intrinsic phase speed suggest a ducted motion

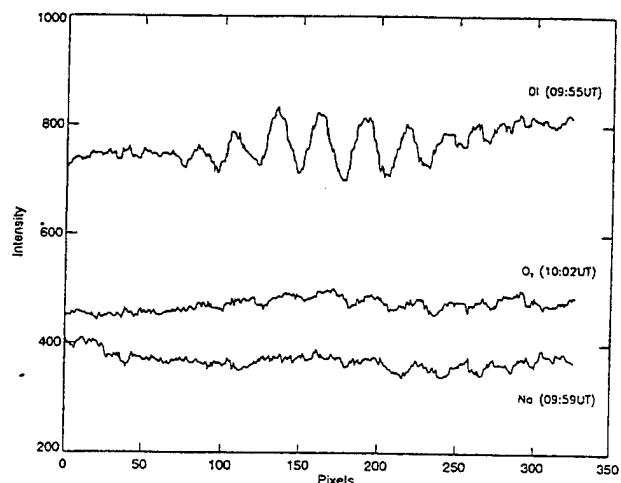


Figure 5. Intensity scan across the central, prominent, row around 09:55 UT for the OI, O<sub>2</sub> and Na emissions. The OI structures were most pronounced at  $\sim 7\%$  modulation, with  $\sim 3\%$  for the O<sub>2</sub> and only  $\sim 1\%$  for the Na (the OH wave modulation was barely detectable).

with a vertically evanescent character at nightglow altitudes. The unusual morphology of these patterns discriminates them from small-scale "ripple" events and in this case an explanation for their appearance may lie in the interference of two comparable band-type motions progressing at closely spaced azimuths. Similar type small-scale waves were observed on several occasions during this campaign (primarily at OI wavelengths), and their orientations were also found to be near perpendicular to that of a concurrent larger scale wave pattern. A detailed study on the role of the larger scale wave motions will be made in due course. Together, these observations suggest an important capability for quantitative gravity wave studies combining optical measurements of wave structure over an extended altitude with simultaneous ground-based wind measurements.

**Acknowledgments.** This research was funded by the National Science Foundation (NSF) grant Nos ATM-9118899, ATM-9301981 and ATM-9302844. Operational support for the MF radar was also provided by the NSF under grant NSF93-02050. Partial support for the image analysis was provided by the Geophysics Directorate, Air Force Phillips Laboratory, contract No F19628-93-C-0165. The assistance of J.A. Albettski and V. Taylor are gratefully acknowledged.

## References

- Chimonas, G., and C.O. Hines, Doppler ducting of atmospheric gravity waves, *J. Geophys. Res.*, **91**, 1219-1230, 1986.
- Clairemidi, J., M. Herse, and G. Moreels, Bi-dimensional observation of waves near the mesopause at auroral latitudes, *Planet. Space Sci.*, **33**, 1013-1022, 1985.
- Fritts, D.C., J.R. Isler, G. Thomas, and Ø. Andreassen, Wave breaking signatures in noctilucent clouds, *Geophys. Res. Lett.*, **20**, 2039-2042, 1993.
- Fritts, D.C., A review of gravity wave saturation processes, effects, and variability in the middle atmosphere, *Pageoph*, **130**, 343-371, 1989.
- Fritts and Yuan, An analysis of gravity wave ducting in the atmosphere: Eckart's resonances in thermal and Doppler ducts, *J. Geophys. Res.*, **94**, 18455-18466, 1989.
- Hines, C.O., Internal atmospheric gravity waves at ionospheric heights, *Can. J. Phys.*, **38**, 1441-1481, 1960.
- Isler, J.R., and D.C. Fritts, Mean winds and tidal and planetary wave motions over Hawaii during ALOHA-93, *Geophys. Res. Lett.*, this issue, 1995.
- Peterson, A.W., Airglow events visible to the naked eye, *Appl. Optics*, **22**, 3390-3393, 1979.
- Taylor, M.J., M. B. Bishop, and V. Taylor, All-sky measurements of short period waves imaged in the OI(557.7 nm), Na(589.2 nm) and near infrared OH and O<sub>2</sub>(0,1) nightglow emissions during the ALOHA-93 campaign, *Geophys. Res. Lett.*, this issue, 1995.
- Taylor, M.J., and M.A. Hapgood, On the origin of ripple-type wave structure in the OH nightglow emission, *Planet. Space Sci.*, **38**, 1421-1430, 1990.
- Taylor, M.J., M.A. Hapgood, and P. Rothwell, Observations of gravity wave propagation in the OI (557.7 nm), Na (589.2 nm) and the near infrared OH nightglow emission, *Planet. Space Sci.*, **35**, 413-427, 1987.
- M.J. Taylor, Space Dynamics Laboratory, Utah State University, Logan, UT 84322-4145 (e-mail: Taylor@psi.sci.sdl.usu.edu).
- D.C. Fritts and J.R. Isler, Laboratory for Atmospheric and Space Physics, Campus Box 392, University of Colorado, Boulder, CO 80309-0392 (e-mail: Dave@michelangelo.colorado.edu, and Joe@leonardo.colorado.edu).

(Received December 7, 1994; revised August 9, 1995; accepted August 25, 1995)



## Vibrational relaxation of $\text{NO}(v = 2, 3)$ by atomic oxygen

J.A. Dodd<sup>1</sup>, S.M. Singleton<sup>2</sup>, S.M. Miller, P.S. Armstrong<sup>1</sup>, W.A.M. Blumberg

*Phillips Laboratory / GPOS, Hanscom Air Force Base, MA 01731, USA*

Received 22 May 1996; in final form 27 June 1996

### Abstract

A two-laser, pump–probe arrangement has been used to measure room-temperature rate constants for the collision-induced relaxation of  $\text{NO}(v = 2, 3)$  by O atoms. The rate constants  $k_{\text{O}}(v)$  are equal to  $(2.2 \pm 0.2) \times 10^{-11}$  and  $(2.5 \pm 0.3) \times 10^{-11} \text{ cm}^3 \text{ s}^{-1}$  for  $v = 2$  and 3, respectively. These values are significantly lower than previously measured values for  $v = 1$ , but are in accord with model predictions assuming the role of a metastable  $\text{NO}_2^*$  intermediate. The NO self-relaxation rate constants  $k_{\text{NO}}(v)$  have been measured to be  $(3.2 \pm 0.3) \times 10^{-12}$  and  $(4.0 \pm 0.4) \times 10^{-12} \text{ cm}^3 \text{ s}^{-1}$  for  $v = 2$  and 3, respectively, in reasonable agreement with published results.

### 1. Introduction

The  $\text{NO } v = 1 \rightarrow 0$  vibrational transition constitutes an important background infrared emission source in the terrestrial thermosphere, and is also a significant thermospheric cooling mechanism. The efficient pumping of the  $\text{NO}(v = 1)$  level by oxygen atoms is a basic feature in standard models of the thermosphere, and has been confirmed in laboratory studies of  $\text{NO}(v)$  collisional relaxation [1–3]. In addition, spectral fits to high resolution thermospheric emission data have shown that the higher- $v$  levels are significantly populated [4]. It has been suggested that at least a portion of the population in  $\text{NO}(v \geq 2)$  levels arises from further vibrational excitation of  $\text{NO}(v = 1)$  in collisions with O atoms [5]. However, aside from the shock tube studies of  $\text{NO}(v = 1, 2)$  at 2700 K by Glanzer and Troe [3], vibra-

tional energy transfer rate constants for collisions of  $\text{NO}(v \geq 2)$  with O atoms have not been determined. These rate constants are necessary for the unambiguous identification of the source of the derived higher- $v$  thermospheric populations. In this work, we extend the laboratory measurements of the collisional relaxation of  $\text{NO}(v)$  by O to  $v = 2$  and 3.

### 2. Experiment

The primary experimental apparatus consisted of a 5 cm internal diameter stainless steel observation cell clamped to a 5 cm ID glass flow tube, together with two pulsed lasers to enable time-resolved excitation and probing of  $\text{NO}(v = 2, 3)$  populations. The interior surfaces of the observation cell and the flow tube were teflon-coated to reduce oxygen atom recombination. The flow tube was pumped by a Roots blower backed by a mechanical pump, with a butterfly valve adjusted to provide a linear flow speed of  $120 \text{ cm s}^{-1}$  at a pressure of 10 Torr. Gas flows were

<sup>1</sup> Stewart Radiance Laboratory, Bedford, MA.

<sup>2</sup> Phillips Laboratory Scholar.



controlled using factory-calibrated MKS controllers, and the total pressure measured using an MKS Baratron head. Partial pressures were calculated from the total pressure using the ratio of the corresponding individual flow rates to the total flow rate. All experimental runs were performed at ambient temperature, approximately 295 K.

The observation cell had removable side arms with Brewster angle window mounts for the introduction of laser pulses, along with windows flush-mounted on the top and bottom of the cell for chemiluminescence and laser-induced fluorescence (LIF) detection. The cell was also fitted with two teflon rings concentric with the longitudinal axis of the tube, located upstream and downstream of the side arm window positions. Each ring supported a grid of fine nickel wire biased at 0 and +45 V, respectively, to enable multiphoton ionization (MPI) detection. During operation of the experiment, transient signals (on the order of  $10^{-9}$ – $10^{-8}$  A) were amplified using an Ithaco 1211 current amplifier.

Argon was used as the buffer gas, with small amounts of NO, N<sub>2</sub>O, and NO<sub>2</sub> added for particular aspects of the experiment. Prior to entering the flow tube, Ar was passed through a copper coil cooled to  $-90^{\circ}\text{C}$  to minimize any water or hydrocarbon impurities. Nitric oxide was purified by flowing the commercially obtained gas through a copper coil cooled to  $-125^{\circ}\text{C}$ , then stored at 1000 Torr in a glass bulb. The resultant NO purity was verified through MPI spectra using the A–X 0–0  $\gamma$ -band, and also through visual inspection of the purified gas, which was completely colorless if NO<sub>2</sub> impurity was efficiently removed. The NO<sub>2</sub> was purified using a freeze–pump–thaw cycle at  $-40^{\circ}\text{C}$ . Titration results obtained using NO<sub>2</sub> purified in this manner and those obtained using NO<sub>2</sub> directly from the cylinder were the same within error. Nitrous oxide (Matheson, 99.99% stated purity) was used as obtained from the vendor.

Tunable infrared laser pulses at 2.7 and 1.8  $\mu\text{m}$  for pumping of the NO 2–0 and 3–0 vibrational overtone transitions, respectively, were generated by mixing dye laser output with residual Nd:YAG fundamental output in a LiNbO<sub>3</sub> crystal (Quanta-Ray DCR-2A, PDL-2, IR WEX). Pulses of approximately 400  $\mu\text{J}$  at 2.7  $\mu\text{m}$  and 5 mJ at 1.8  $\mu\text{m}$  were generated in this manner, with a laser bandwidth of

1.1  $\text{cm}^{-1}$  and a temporal width of about 10 ns. Ultraviolet probe pulses were produced by doubling the output of a dye laser in a KD\*P crystal, then mixing the doubled light with residual Nd:YAG fundamental output in a KDP crystal, yielding 1–2 mJ, 10 ns pulses with a bandwidth of  $1.4 \text{ cm}^{-1}$  (Quanta-Ray DCR-2A, PDL-1, WEX-1). Probe pulses were delayed relative to pump pulses using an SRS DG535 digital delay generator, with the observed time separation jitter of 0.5  $\mu\text{s}$  limited by the triggering circuitry of the two 10 Hz repetition rate Nd:YAG lasers. The pump and probe pulses were weakly focused to give approximate diameters of 1.5 mm and 4 mm, respectively, in the detection region. The two beams were counterpropagated and overlapped within the cell.

Oxygen atoms were formed in a microwave discharge through an Ar/N<sub>2</sub>O gas mixture. Ar(1000 sccm) and N<sub>2</sub>O (3–30 sccm) and N<sub>2</sub>O (3–30 sccm) were flowed through a magnesium oxide tube, which protruded into the larger diameter glass flow tube. An additional 500 sccm of unexcited Ar was flowed through a glass loop injector upstream of the magnesia tube outlet in order to entrain the discharge product and carry it down the flow tube. Unlike an O<sub>2</sub> discharge, the N<sub>2</sub>O discharge minimizes the production of O<sub>2</sub>( $\Delta$ ) and O<sub>3</sub> metastable species which could compete with O atoms in NO( $\nu$ ) relaxation [6]. Piper et al. [6] detail a method whereby the N<sub>2</sub>O flow is adjusted to optimize the O-atom production while essentially eliminating the formation of N atoms and NO as well as oxygen metastables.

The oxygen atom concentration was determined by titrating with NO<sub>2</sub>, providing absolute number densities to within a few percent accuracy [2]. The chemiluminescent NO<sub>2</sub><sup>\*</sup> produced in the titration was observed 7.5 cm downstream of the NO<sub>2</sub> glass loop injector using a phototube and a 580 nm bandpass filter. The O-atom yield was observed to be about 10%, calculated based on a comparison of the effective O-atom throughput (0.3–3 sccm) to the N<sub>2</sub>O flow introduced into the microwave discharge tube. The relative O-atom density was monitored using LIF by pumping the O 2p<sup>3</sup>3p <sup>3</sup>P–2p<sup>4</sup> <sup>3</sup>P two-photon transition at 225.6 nm with a weakly focused UV pulse, then detecting the 844.7 nm fluorescence with an RCA 31034A phototube equipped with an 850 nm bandpass filter. Addition of NO into the cell

region for the purposes of the pump/probe study resulted in a 5% decrease in the O-atom density, owing to a small amount of  $\text{NO} + \text{O} + \text{M} \rightarrow \text{NO}_2 + \text{M}$  recombination. For a given microwave power, the derived O-atom concentrations were reproducible to within  $\pm 5\%$  in the day-to-day operation of the experiment.

Because the derived rate constants  $k_{\text{O}}(v)$  rely on the accuracy of the O-atom concentration measurement, an alternative O-atom source was used as a consistency check. A known concentration of oxygen atoms was generated through photolysis of  $\text{NO}_2$  at 355 nm using the tripled output of a Nd:YAG laser, telescoped down to 1.4 mm diameter. The resultant O atoms were detected via LIF using a focused UV laser beam to probe a small portion of the pump laser volume. Unit photodissociation of the  $\text{NO}_2$  in the pump volume was ensured by varying the pump laser fluence and observing a constant LIF signal, consistent with the  $\text{NO}_2$  absorption cross section  $\sigma_{355} = 4.7 \times 10^{-19} \text{ cm}^2$  and quantum photolysis yield  $\Phi_{355} = 0.986$  [7], together with the estimated pump laser fluence of  $1 \times 10^{19} \text{ photons cm}^{-2}$ . The signal was compared to that obtained with the microwave O-atom source, using the same probe laser power and geometry. The normalized LIF signals were found to agree to within 20%, corroborating the  $\text{NO}_2$  titration results.

### 3. Results and discussion

The NO  $v' = 2$  and 3 levels were populated by pumping various  $(\Omega, v', J') \rightarrow (\Omega, 0, J'')$  overtone rotational transitions. The NO  $v$  level populations were probed using two-photon MPI, taking advantage of the strong 2–2 and 3–3 vibrational bands in the NO A–X  $\gamma$ -band system, with wavelengths near 221.9 and 219.7 nm, respectively. The MPI signals were maximized by tuning the probe laser wavelength to correspond to one of the A–X band head positions. The IR and UV laser powers did not drift appreciably over the course of a scan. The rotational and spin–orbit state populations in the excited  $v$  level were collisionally equilibrated on a timescale very short compared to vibrational relaxation, as evidenced by the fact that the decay rates did not depend on the particular levels being pumped or

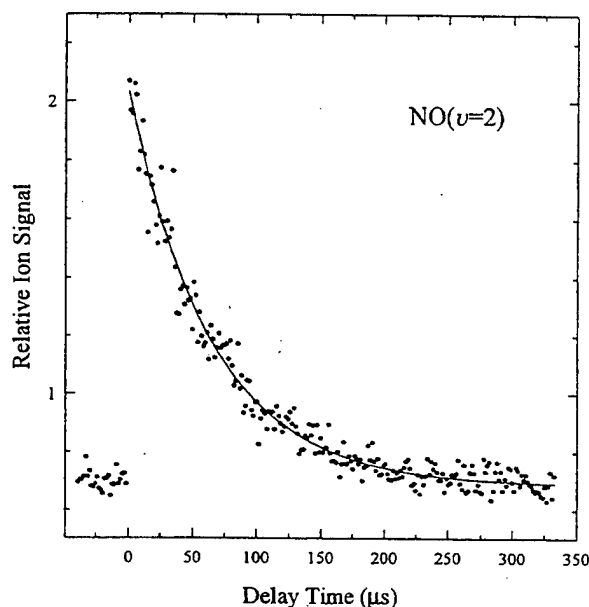


Fig. 1. Time dependence of the  $\text{NO}(v=2)$  MPI signal arising from the UV probe laser pulse, both before and after the firing of the IR pump laser at  $t=0 \text{ } \mu\text{s}$ . Conditions: 8.25 Torr total pressure, with densities of Ar ( $2.6 \times 10^{17} \text{ cm}^{-3}$ ),  $\text{N}_2\text{O}$  ( $5.2 \times 10^{15} \text{ cm}^{-3}$ ), and NO ( $1.7 \times 10^{14} \text{ cm}^{-3}$ ). An O-atom density of  $5.1 \times 10^{14} \text{ cm}^{-3}$  is also present, formed from a 110 W microwave discharge.

probed. For each delay time the ion signal was averaged over 10 laser shots. A LeCroy 9310AM oscilloscope was used to digitize the transient signals, with further off-line numerical processing performed on a PC.

Fig. 1 shows a typical decay curve for  $\text{NO}(v=2)$  and  $[\text{O}] = 5.1 \times 10^{14} \text{ cm}^{-3}$ , with the IR excitation pulse occurring at  $t=0 \text{ } \mu\text{s}$ . Following excitation, the temporal profile of the ion signal is well described by the equation

$$I(t) = I_0 \exp(-bt) + c, \quad (1)$$

to within the S/N limits of the run, which varied between 10 and 200. The ion signal baseline was negligible in the absence of the microwave discharge, but became more important as the discharge power was increased. This background signal arose from partial photodissociation of the small amount of  $\text{NO}_2$  present (via  $\text{NO} + \text{O}$  recombination) to form additional  $\text{NO}(v)$ , which was ionized within the same laser pulse [8]. However, any nascent  $\text{NO}(v)$  photolysis product would have insufficient time to collisionally deactivate on the timescale of a single

laser pulse. Thus, the ion background did not affect the measurement of the NO decay kinetics.

Non-exponential decay profiles were observed when high IR beam fluences were employed, i.e. with the IR beam focused at the cell. Wysong [9,10] details kinetic modeling which suggests that a proportion greater than  $10^{-3}$  of NO in the vibrationally excited state can lead to second-order decay kinetics through  $\text{NO}(v)\text{--NO}(v')$  collisions. Saupe et al. [11] have observed an anharmonic vibration–vibration pumping mechanism in NO which can produce very high vibrational excitation. Under the present conditions, we estimate maximum  $\text{NO}(v=2)/\text{NO}$  and  $\text{NO}(v=3)/\text{NO}$  population ratios of  $7 \times 10^{-4}$  and  $2 \times 10^{-4}$ , respectively, based on the effective laser fluence and the NO absorption line strengths [12]. No attempts were made to model non-exponential decay curves in this work.

### 3.1. NO / O-atom relaxation

Figs. 2 and 3 show Stern–Volmer plots for the measured decay rates of NO  $v=2$  and  $v=3$ , respectively, as a function of O-atom concentration. The different symbols represent results obtained on different days, indicating good reproducibility. Weighted least-squares fits to the measured rates were used to determine the rate constants  $k_{\text{O}}(v)$ . The y-intercept values are consistent with the additive loss of  $\text{NO}(v)$  arising from several mechanisms, including diffusion of excited species out of the UV probe field of view, linear transport out of the field of view owing to the bulk flow, and, to a lesser extent, radiative relaxation and collisional relaxation by the Ar buffer gas. In the case of the O-atom quenching experiments, the intercept also includes small contributions from NO and  $\text{NO}_2$  collisional quenching.

Table 1 presents the derived rate constants  $k_{\text{O}}(v=2, 3)$ , along with literature values for comparison. The  $k_{\text{O}}(v=2, 3)$  are about a factor of 2–3 lower than previously measured values of  $k_{\text{O}}(v=1)$ . Fernando and Smith [2] and Lilenfeld [1] used  $\text{NO}(v=1-0)$  IR fluorescence as the probe of the  $\text{NO}(v=1)$  time-dependent populations. In their measurement, Fernando and Smith [2] formed  $\text{NO}(v=1)$  using energy transfer from  $\text{HCl}(v=1)$  in a slowly flowing gas mixture, with the HCl initially excited by a

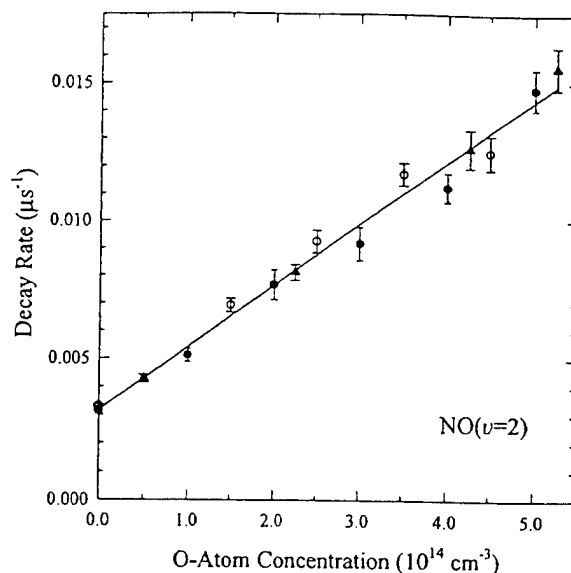


Fig. 2. Stern–Volmer plot of  $\text{NO}(v=2)$  disappearance rates as a function of O-atom concentration. The different symbols represent data obtained on different days; each point is the average of 3–7 determinations, with the  $2\sigma$  error bars indicated. Conditions: 8.15–8.35 Torr total pressure, with densities of Ar ( $\approx 2.6 \times 10^{17} \text{ cm}^{-3}$ ),  $\text{N}_2\text{O}$  ( $(1.8\text{--}5.2) \times 10^{15} \text{ cm}^{-3}$ ), and NO ( $\approx 1.7 \times 10^{14} \text{ cm}^{-3}$ ). The microwave power was adjusted between 10 and 110 W, with the  $\text{N}_2\text{O}$  flow optimized at each setting as described in Piper et al. [6].

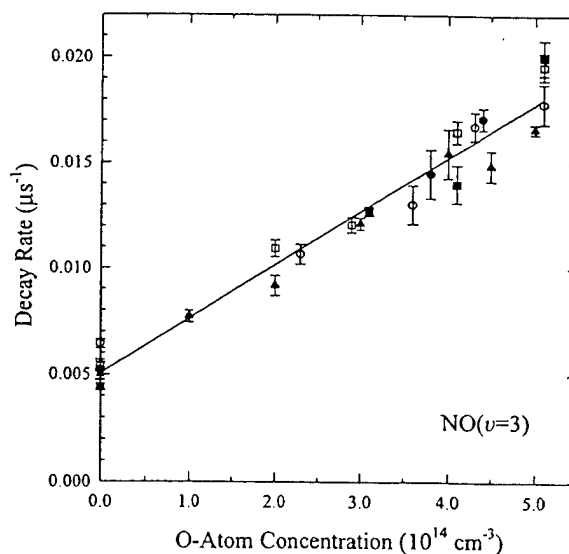


Fig. 3. Stern–Volmer plot of  $\text{NO}(v=3)$  disappearance rates as a function of O-atom concentration. The different symbols represent data obtained on different days; each point is the average of 3–7 determinations, with the  $2\sigma$  error bars indicated. The experimental conditions are similar to those described in the Fig. 2 caption.

Table 1

Rate constants  $k_O(v)$  for the room-temperature relaxation of  $\text{NO}(v=1-3)$  by O atoms (units of  $10^{-11} \text{ cm}^3 \text{ s}^{-1}$ ). Error bars listed for the present work represent two standard deviations in the scatter in the measured rates

$v=1$	$v=2$	$v=3$	Ref.
	$2.2 \pm 0.2$	$2.5 \pm 0.3$	present work
$5 \pm 1$			Lilenfeld [1]
$6.5 \pm 0.7$			Fernando and Smith [2]
1.7	2.1		Quack and Troe [13]

chemical laser. In the Lilenfeld [1] measurement,  $\text{NO}(v=1)$  was formed by pumping  $\text{NO}(v=0)$  with a near-resonant CO laser line. Unfortunately, we are not at present equipped to excite the  $v=1$  level to permit a more direct comparison with these studies, although it seems unlikely that the rate constants would decrease so markedly from  $v=1$  to 2. The fact that the measured  $k_O(v=2, 3)$  values are significantly lower than the  $k_O(v=1)$  literature values suggests a possible bias resulting from an overestimate of the O-atom concentration. However, such a bias was not evident in either of the O-atom measurements detailed in Section 2.

Glanzer and Troe [3] performed the only previous experimental measurement of  $k_O(v)$  for  $v \geq 2$ , in a shock tube with an effective temperature of 2700 K. They obtained  $k_O(v) = (3.7 \pm 1.7) \times 10^{-11}$  and  $(4.0 \pm 1.7) \times 10^{-11} \text{ cm}^3 \text{ s}^{-1}$  for  $v=1$  and 2, respectively, which for  $v=2$  is almost a factor of two larger than the present measurement. The Glanzer and Troe  $v=2$  result can also be compared with the present result using the corresponding cross sections  $\sigma_O(v=2)$ , obtained from the rate constants by dividing by the relative velocity of NO and O. This yields  $\sigma_O(v=2) = 1.7 \times 10^{-16}$  and  $2.9 \times 10^{-16} \text{ cm}^2$  at 2700 and 295 K, respectively, implying a high-temperature cross section that is about 40% smaller than the room-temperature cross section.

The efficiency of the  $\text{O} + \text{NO}(v)$  vibrational relaxation process suggests the role of a metastable  $\text{NO}_2^*$  intermediate. If the reaction proceeds through such an intermediate, the rate constant  $k_O(v)$  can be approximated by

$$k_O(v) = k_c \chi(v), \quad (2)$$

where  $k_c$  is the second-order rate constant for complex formation, and  $\chi(v)$  represents the fraction of

complexes which dissociate to yield a lower NO  $v$  level [13]. The quantity  $k_c$  can be approximated by the high-pressure limit of the  $\text{NO} + \text{O} + \text{M} \rightarrow \text{NO}_2 + \text{M}$  recombination rate constant  $k_{\text{rec}}^\infty$ , equal to  $(3 \pm 1) \times 10^{-11} \text{ cm}^3 \text{ s}^{-1}$  in air [7]. Various statistical theories can be used to calculate values of  $\chi(v)$ . Fernando and Smith [2] discuss three such approaches in the calculation of  $\chi(v=1)$ , yielding values ranging from 0.88 to 0.95. Quack and Troe [14] present a simplified form of their statistical adiabatic channel model which predicts  $\chi(v) = 0.88, 0.95$ , and  $0.97$  for  $v=1-3$ , respectively. Assuming that the complex formation rate constant is independent of  $v$  [13], these values can be used to predict  $k_O(v) \approx 2.6 \times 10^{-11}, 2.9 \times 10^{-11}$ , and  $2.9 \times 10^{-11} \text{ cm}^3 \text{ s}^{-1}$  for  $v=1-3$ , respectively, in reasonable agreement with the present data.

A more sophisticated prediction can be obtained from the complete statistical adiabatic channel model of Quack and Troe [13], whose calculated rate constants for O-atom-induced relaxation of  $\text{NO}(v=1, 2)$  are listed in Table 1. The theoretical value for  $k_O(v=2)$  is the sum of rate constants calculated for relaxation of NO  $v=2$  into  $v=1$  and 0, and is seen to be in excellent agreement with the present result. For 2100 K, Quack and Troe predict  $k_O(v) = 1.2 \times 10^{-11}$  and  $1.6 \times 10^{-11} \text{ cm}^3 \text{ s}^{-1}$  for  $v=1$  and 2, respectively, about 25% lower than the room-temperature predictions and in significant disagreement with the larger values measured by Glanzer and Troe [3] at 2700 K. However, the predicted negative temperature dependence is consistent with the formation of an intermediate complex.

### 3.2. NO self-relaxation

To help benchmark the O-atom decay measurements, rate constants were determined for the self-relaxation of  $\text{NO}(v=2, 3)$  by NO. Table 2 presents the derived rate constants, which were obtained from Stern–Volmer plots similar to those shown in Figs. 2 and 3. Values of  $k_{\text{NO}}(v=2)$  spanning more than a factor of two have been reported by various groups (see Table 1 in Wysong [9]). Many of the measurements, however, suffer from experimental complications that could significantly reduce the accuracy of the derived relaxation rate constants [9]. More recently, Wysong [9] and Islam et al. [15] have inde-

Table 2

Rate constants  $k_{\text{NO}}(v)$  for the room-temperature relaxation of  $\text{NO}(v=2, 3)$  by  $\text{NO}$  (units of  $10^{-12} \text{ cm}^3 \text{ s}^{-1}$ ). Error bars listed for the present work represent two standard deviations in the scatter in the measured rates

$v = 2$	$v = 3$	Ref.
$3.2 \pm 0.3$	$4.0 \pm 0.4$	present work
$3.10 \pm 0.16$		Wysong [9]
	$3.26 \pm 0.24$	Wysong [10]
$2.44 \pm 0.3$	$2.22 \pm 0.2$	Islam et al. [15]

pendently measured  $k_{\text{NO}}(v=2)$  using laser IR pump/UV probe techniques similar to ours. The Wysong measurement is in excellent agreement with the present result, while the Islam et al. value is somewhat lower. Wysong separated the measured  $k_{\text{NO}}(v=2)$  disappearance rate constant into vibration–vibration and vibration–translation components; Table 2 reports the total disappearance rate in order to be consistent with this work.

Wysong [10] and Islam et al. [15] have also measured  $k_{\text{NO}}(v=3)$  values using laser pump/probe techniques. As shown in Table 2, the Wysong result is in fair agreement with the present measurement, while the Islam et al. value is almost a factor of two lower. These differences persist despite the similarity of the experimental methods and data reduction procedures. We can offer no explanation for the discrepancies at this time.

#### 4. Summary

Room-temperature rate constants for the quenching of  $\text{NO}(v=2, 3)$  by O atoms and by NO have been determined. The self-quenching values are in reasonable accord with previous results. The rate coefficients for O-atom quenching are about a factor of 2–3 lower than previous measurements for  $v=1$ , but agree well with a statistical adiabatic channel model prediction. The high relaxation efficiency and lack of a significant  $v$  dependence are consistent with the formation of an  $\text{NO}_2^*$  metastable intermediate.

#### Acknowledgement

SMS acknowledges the support of a Phillips Laboratory Scholarship, administered by the Northeast Consortium for Engineering Education and funded by the Air Force Office of Scientific Research. We thank S.J. Lipson, R.B. Lockwood, and J.R. Winick for helpful discussions. The SRL authors performed this work under Contract F19628-93-C-0165 with Phillips Laboratory. Funding was provided by AFOSR under Task 2303EP1/PL007.

#### References

- [1] H.V. Lilenfeld, PL-TR-94-2180, Phillips Laboratory Final Report (1994).
- [2] R.P. Fernando and I.W.M. Smith, *J. Chem. Soc. Faraday II* 75 (1979) 1064.
- [3] K. Glanzer and J. Troe, *J. Chem. Phys.* 63 (1975) 4352.
- [4] P.S. Armstrong, S.J. Lipson, J.A. Dodd, J.R. Lowell, W.A.M. Blumberg and R.M. Nadile, *Geophys. Res. Lett.* 21 (1994) 2425.
- [5] S.J. Lipson, W.A.M. Blumberg, R.B. Lockwood, J.R. Lowell, R.M. Nadile, P.S. Armstrong and J.A. Dodd, *Eos Trans. AGU* 76 (1995) F439.
- [6] L.G. Piper, W.T. Rawlins and R.A. Armstrong, AFGL-TR-83-0031, Air Force Geophysics Laboratory Tech. Rep. (1983).
- [7] W.B. DeMore, S.P. Sander, D.M. Golden, M.J. Molina, R.F. Hampson, M.J. Kurylo, C.J. Howard and A.R. Ravishankara, *JPL Pub.* 90-1 (1990).
- [8] T.G. Slanger, W.K. Bischel and M.J. Dyer, *J. Chem. Phys.* 79 (1983) 2231.
- [9] I.J. Wysong, *J. Chem. Phys.* 101 (1994) 2800.
- [10] I.J. Wysong, *Chem. Phys. Lett.* 227 (1994) 69.
- [11] S. Saupe, I. Adamovich, M.J. Grassi, J.W. Rich and R.C. Bergman, *Chem. Phys.* 174 (1993) 219.
- [12] B. Schurin and R.E. Ellis, *J. Chem. Phys.* 45 (1966) 2528.
- [13] M. Quack and J. Troe, *Ber. BunsenGes. Phys. Chem.* 79 (1975) 170.
- [14] M. Quack and J. Troe, *Ber. BunsenGes. Phys. Chem.* 81 (1977) 160.
- [15] M. Islam, I.W.M. Smith and J.W. Wiebrecht, *J. Phys. Chem.* 98 (1994) 9285.

# Fractional population of NO( $v - 1$ ) from vibrational relaxation of NO( $v = 2, 3$ ) by O and NO

James A. Dodd,<sup>a\*</sup> Ronald B. Lockwood,<sup>b</sup> Steven M. Miller<sup>b</sup> and William A. M. Blumberg<sup>b</sup>

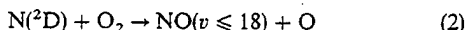
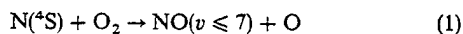
<sup>a</sup> Stewart Radiance Laboratory, 139 Great Road, Bedford, Massachusetts 01730 USA

<sup>b</sup> Phillips Laboratory/GPOC, Hanscom Air Force Base, Massachusetts 01731 USA

Significant populations of NO in excited vibrational levels  $v \geq 2$  have recently been observed in the lower thermosphere, for which the relaxation rates and pathways are largely governed by collisions with O atoms. Laboratory experiments can provide accurate kinetic parameters for modelling and interpreting such steady-state  $v$ -dependent population distributions. In this study, a two-laser, pump-probe arrangement has been used to measure the fractional population of NO( $v - 1$ ) arising from the collision-induced relaxation of NO( $v = 3$ ) by O atoms and, in an ancillary experiment, NO( $v = 2, 3$ ) by NO. The branching fraction  $\chi_O(v = 3 \rightarrow 2) = 0.35 \pm 0.12$  for O-atom collisions. The  $\chi_O$  value is consistent with a long-lived NO<sub>2</sub> collision complex, in which the total energy is randomly distributed among the internal degrees of freedom prior to dissociation, and agrees with a recent quasiclassical trajectory calculation. For collisions with NO,  $\chi_{NO}(v = 3 \rightarrow 2) = 0.73 \pm 0.19$ , indicating a significant multi-quantum component. The branching fraction  $\chi_{NO}(v = 2 \rightarrow 1) = 1.19 \pm 0.31$  can be considered an effective value only, since its interpretation relies on an assumption regarding the relaxation mechanism. The rate constants  $k_O(v = 3) = (3.0 \pm 0.6) \times 10^{-11} \text{ cm}^3 \text{ s}^{-1}$  for the vibrational relaxation of NO( $v = 3$ ) by O atoms, and  $k_{NO}(v = 2) = (2.7 \pm 0.5) \times 10^{-12} \text{ cm}^3 \text{ s}^{-1}$  and  $k_{NO}(v = 3) = (3.4 \pm 0.7) \times 10^{-12} \text{ cm}^3 \text{ s}^{-1}$  for the relaxation of NO( $v = 2, 3$ ) by NO have also been obtained, and are in good agreement with previous results from this laboratory.

## 1 Introduction

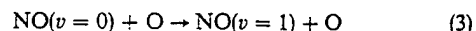
A great deal of attention has recently been focused on the chemical sources and sinks of NO in the lower thermosphere. Reactions (1) and (2) constitute the dominant NO production mechanisms:<sup>1-4</sup>



Reactions (1) and (2), in conjunction with other NO formation reactions, can clearly give rise to a large degree of vibrational excitation in the NO product, consistent with laboratory measurements.<sup>5</sup> Evidence that excited  $v$ -level populations of NO are present in the thermosphere is exemplified by recent observations of NO( $v \geq 2$ ) fundamental band radiance in high-resolution earthlimb emission data from the CIRRIS 1A mission.<sup>6,7</sup> Excited NO( $v$ ) populations are especially prevalent in auroras, for which the NO production rate can be vastly increased. NO populations up to  $v = 5$  were detected in CIRRIS 1A measurements of naturally occurring auroras,<sup>6</sup> and up to  $v = 12$  in the EXCEDE III space-based artificial aurora experiment.<sup>8</sup> The decay pathways of the vibrationally excited NO populations will partially govern the resultant infrared background radiance and the extent to which the initial chemical energy is converted into thermal heating. Kinetic models for the production and decay of NO vibrational levels have been developed,<sup>9,10</sup> but need to be updated and enhanced with more accurate input parameters.

Vibrational energy transfer in thermospheric NO is dominated by collisions with oxygen atoms, since both N<sub>2</sub> and O<sub>2</sub> are inefficient relaxers.<sup>11-13</sup> However, relatively little is known concerning the rates and pathways of NO( $v$ )/O vibrational excitation or relaxation. In 1979 Fernando and Smith<sup>14</sup> performed a landmark measurement of the room-temperature rate constant  $k_O(v = 1)$  for NO( $v = 1$ ) vibrational relaxation by oxygen atoms. Their measurement is particularly important, since it is related through detailed balance to the vibra-

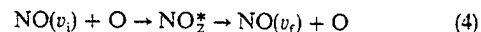
tional uppumping reaction



Reaction (3) is a primary mechanism for lower thermospheric cooling through the conversion of kinetic energy into NO( $v = 1 \rightarrow 0$ ) fundamental band emission, which largely escapes into space. The temperature dependence of  $k_O(v = 1)$  in the 500–1200 K range has not been empirically determined, increasing the uncertainty with which the Fernando and Smith measurement can be applied to models of the lower thermosphere.

Our group has recently examined the analogous process for NO( $v = 2, 3$ ),<sup>15</sup> providing the only determination of the O-atom-induced quenching rates for NO( $v \geq 2$ ), aside from a shock-tube measurement of NO( $v = 2$ ) relaxation at 2700 K.<sup>16</sup> The determination of additional  $v$ -dependent relaxation rate constants and single/multi-quantum relaxation pathways would be of great use in modelling the dynamics of nascently-formed high- $v$  NO in the thermosphere. The problem is potentially very similar to that of OH( $v \leq 9$ ) collisional quenching at the mesopause,<sup>17</sup> in which the question of collision-induced single- vs. multi-quantum decay remains largely unanswered.

In this paper we extend our earlier work on the relaxation of NO( $v = 2, 3$ ) by O and NO, and report measurements of the branching fractions of initially populated NO( $v = 2, 3$ ) into the lower  $v - 1$  level. In the case of O-atom relaxation, this represents the first measurement of a detailed vibrational relaxation pathway. The results can be compared with the statistical models of Quack and Troe,<sup>18,19</sup> who calculated pathways based on the presence of a long-lived NO<sub>2</sub> intermediate, viz.



The measurements can also be compared with the more recent semiclassical trajectory calculations of Duff and Sharma<sup>20</sup> on the same system. All of these studies are in general agreement that the final vibrational state populations are approximately equal, i.e. independent of  $v_i$ .

## 2 Experimental

The experimental apparatus and methodology were very similar to that used in our previous study of  $\text{NO}(v = 2, 3)$  vibrational relaxation<sup>15</sup> (see Fig. 1). The primary apparatus consisted of a 2 in (in = 2.54 cm) internal diameter glass flow tube, coated on its internal surfaces with halocarbon wax in order to minimize oxygen-atom recombination. Clamped to the flow tube was the detection cell, which consisted of a stainless-steel cube bored through to give the same 2 in internal diameter, and Teflon-coated on its internal surfaces. Two 10 cm long side-arms containing a series of black anodized aluminium light baffles were attached at right angles to the flow tube axis, in order to pass laser light through Brewster-angle windows. The cell provided the capability for multi-photon ionization (MPI) and laser-induced fluorescence (LIF) detection of trace species in the gas flow. Vibrational level populations of NO were probed in the previous study using 1 + 1 resonance-enhanced MPI; in this study we used the LIF technique as described in the following.

Fig. 2 shows an example schematic of the IR pump-UV probe methodology for initial excitation of  $\text{NO}(v = 2)$ .  $\text{NO}(v = 2, 3)$  rotational levels were populated using tunable IR laser pulses, generated by mixing visible dye laser output with the 1.06  $\mu\text{m}$  Nd:YAG fundamental in a  $\text{LiNbO}_3$  crystal. Residual visible and 1.06  $\mu\text{m}$  radiation was eliminated by passing the mixed output through a silicon window at Brewster's angle (for 1.8  $\mu\text{m}$ ), and additionally through a germanium window, also at Brewster's angle (for 2.7  $\mu\text{m}$ ). Laser pulse energies in the 2.7  $\mu\text{m}$  region with frequencies corresponding to several of the  $v = 0 \rightarrow 2$ ,  $J'' \rightarrow J'' + 1$  R-branch transitions were found to vary by a factor of three owing to varying absorption by water vapour in room air. The 2-0  $R(J'' = 6.5)$  and 3-0  $R(J'' = 7.5)$  transitions were used in the two cases, with a fractional excitation of ca.  $10^{-5}$ – $10^{-4}$  of the total NO population (*vide infra*). The IR pulse was weakly focused using a 500 mm  $\text{CaF}_2$  lens positioned 370 mm before the cell, giving a  $1/e^2$  Gaussian beam diameter of ca. 3 mm.

$\text{NO}(v = 1-3)$  time-dependent populations were detected using LIF and various bands in the A-X  $\gamma$ -band system. To generate the detection laser wavelengths, an Inrad Autotracker II was used to frequency-double laser light from a Nd:YAG-pumped dye laser. The detection beam was shaped

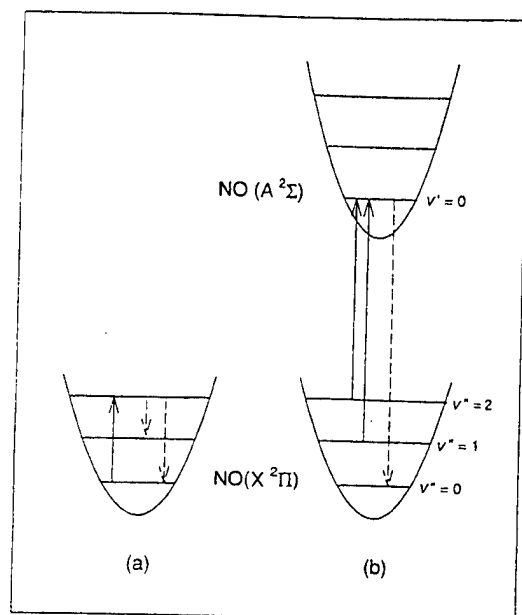


Fig. 2 Schematic of laser excitation/detection methodology. In (a), a tunable IR laser excites a small fraction of the  $\text{NO } v = 0$  population to  $v = 2$ . Collisions with relaxer species then transfer the initially excited population to lower  $v$  levels on a timescale of tens of  $\mu\text{s}$ . In (b), a UV laser is used to probe either the initially excited  $v = 2$  level, or the  $v = 1$  level which is populated by collisional relaxation. Detection is accomplished using the  $\gamma(0-0)$  band, which occurs at a shorter wavelength. Detection via the  $\gamma(2-v'')$  bands is performed in a similar manner. Note that the separation between the A and X levels is not drawn to scale.

into a circular cross-section using a pair of cylindrical lenses, then sent through a pair of 1 mm diameter irises prior to entry into the cell in order to precisely maintain its position relative to the larger IR beam. UV pulse fluences were kept very low (1–10  $\mu\text{J}$ ) to avoid saturation of the strong  $\gamma$ -band transitions. A Burleigh WA-5500 pulsed wavemeter was used to monitor both the IR and UV dye laser frequencies to be certain they were not drifting off resonance. While we did observe inaccuracies in these measurements consistent with the instrument

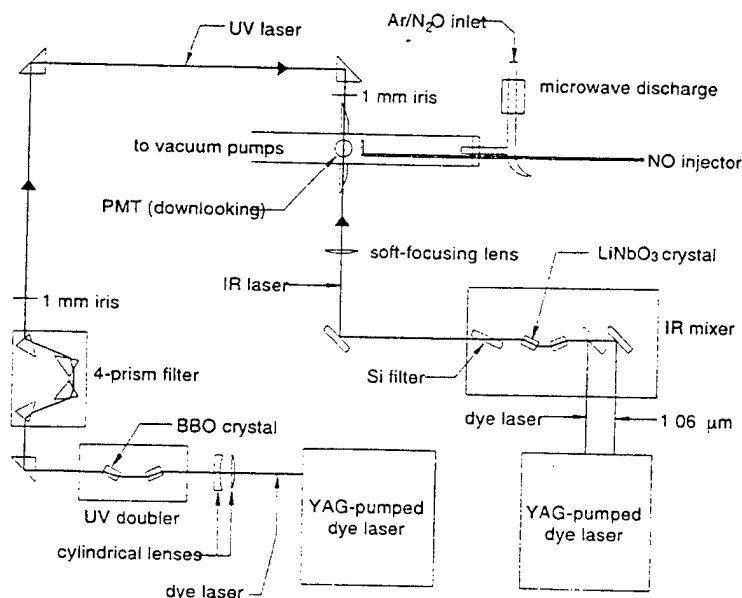


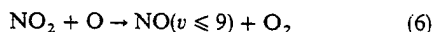
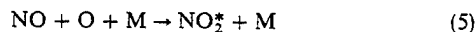
Fig. 1 Experimental apparatus. See text for discussion.

specification (e.g.  $\pm 0.1 \text{ cm}^{-1}$  at 600 nm,  $\pm 0.2 \text{ cm}^{-1}$  at 300 nm), the reading remained stable over the course of several days in the absence of optics readjustment.

The NO  $\gamma$ -band fluorescence was detected at a shorter wavelength than the pump wavelength, largely eliminating background arising from laser light scatter off the windows, the microwave discharge, and from  $\text{NO}_2^+$  fluorescence, which extends from 400 nm into the near-IR. In many cases it was easy to detect the  $\text{NO}(v)$  under photon-counting conditions, although the fluorescence signals were typically much stronger. Two  $\gamma$ -band series were used, the  $\gamma(2-v'')$  series, in which the  $\gamma(2-2)$  and  $\gamma(2-3)$  bands at 222 and 231 nm were pumped, and the  $\gamma(2-0)$  band at 205 nm detected, and the  $\gamma(0-v'')$  series, in which the  $\gamma(0-1)$  and  $\gamma(0-2)$  bands at 237 and 247 nm were pumped, and the  $\gamma(0-0)$  band at 227 nm detected. The  $\gamma(2-0)$  detection method gave rise to about a factor-of-two better S/N, owing to more favourable A-X Franck-Condon factors. Fluorescence was detected by a Hamamatsu R166 solar-blind PMT, in conjunction with 10 nm FWHM bandpass filters (Corion Corp., Andover Corp.) centred at 206.5 and 224.4 nm, respectively. In each case the use of the same upper state allowed relative  $v''$  population measurements to be accomplished without needing to account for such factors as detector wavelength response and  $\text{NO}(A, v)$  fluorescence lifetime.

Between 8 and 32 laser shots were averaged for each time element, resulting in typical run times of between 3 and 13 min for 250 time values. At each time delay the integrated LIF signal and the UV and IR laser fluences were separately averaged on digital oscilloscopes, and the averaged values stored on a laboratory computer. In the data workup the LIF signals were ratioed by 50 point running averages of the IR and UV laser fluences to account for long-term drift, which was generally  $< 10\%$ . These ratioed signals were then converted to relative populations of the  $\text{NO}(v)$  populations by dividing by the product of the appropriate Boltzmann population factor and line strength<sup>22</sup> of the rotational level probed, and by the  $v'' \rightarrow v'$  Franck-Condon factor.<sup>23</sup> In each case a rotational transition was chosen that was separated from its nearest neighbours by more than the FWHM bandwidth ( $0.7 \text{ cm}^{-1}$ ) of the UV laser.

A mixture of ca. 25 sccm  $\text{N}_2\text{O}$  in 1100 sccm Ar was flowed through a McCarroll cavity microwave discharge in order to form O atoms. A 0.5 in od. Pyrex tube was used instead of the magnesium oxide tube used previously. The discharge region was followed by a Woods horn and a right angle in order to minimize stray light in the fluorescence detection region. An additional 425 sccm Ar was introduced through a loop injector just upstream of the discharge effluent in order to minimize turbulence. One sccm NO was introduced a few mm upstream of the detection region, through an injector formed from a 1 in long, 0.125 in od Teflon tube aligned along the laser axis, with about ten small holes pointing downstream. This arrangement was found to minimize mixing of the injected NO with oxygen atoms prior to the laser pump-probe sequence. Reactions (5) and (6) reduce the O-atom concentration, and give rise to  $\text{NO}(v)$  background through the sequence



with rate constants  $k_5 = 2.4 \times 10^{-14} \text{ cm}^3 \text{ s}^{-1}$  (at 8.5 Torr) and  $k_6 = 9.7 \times 10^{-12} \text{ cm}^3 \text{ s}^{-1}$ .<sup>21</sup> The observed NO LIF background was linear in laser power, consistent with the presence of a small amount of  $\text{NO}(v)$  created through reactions (5) and (6). Conceivably, photolysis of  $\text{NO}_2$  followed by detection of product  $\text{NO}(v)$  in the same laser pulse could also give rise to a background signal, though such a process would have a quadratic laser power dependence at the low probe fluences used. In our previous study we found that reactions (5) and (6)

reduced the O-atom density by about 5% upon the addition of NO. The chemiluminescent  $\text{NO}_2^+$  formed in reaction (5) was used to advantage in adjusting the various flow rates to minimize the turbulence in the cell region. The microwave discharge was operated at ca. 110 W. The O-atom density was measured to be  $1.8 \times 10^{15} \text{ cm}^{-3}$  through  $\text{NO}_2$  titrations,<sup>24</sup> about a factor of three higher than densities achieved in our previous study employing the magnesium oxide discharge tube.<sup>15</sup>

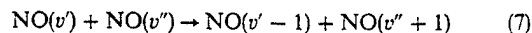
For the  $\text{NO}(v = 2, 3)$ -NO self-relaxation studies, the microwave discharge and the  $\text{N}_2\text{O}$  flow were turned off, and mixtures of either 50 sccm  $\text{NO}$ -1525 sccm Ar or 10 sccm  $\text{NO}$ -215 sccm Ar were used, corresponding to NO number densities of  $8.6 \times 10^{15} \text{ cm}^{-3}$  and  $1.2 \times 10^{16} \text{ cm}^{-3}$ , respectively. For both flow rates the total pressure was set to ca. 8.5 Torr by throttling the downstream vacuum pump, giving rise to linear flow velocities of 120 and  $17 \text{ cm s}^{-1}$ , respectively. The measured branching fractions did not depend on the flow speed. In general, the observed  $\text{NO}(v)$  decay rates were dominated by O-atom- and NO-induced collisional relaxation, respectively. The collision-induced decay rates of  $\text{NO}(v = 2, 3)$  by Ar and  $\text{N}_2\text{O}$  were  $< 100 \text{ s}^{-1}$ , and the  $\text{NO}(v = 2, 3)$  radiative decay rates are ca.  $30 \text{ s}^{-1}$ . The transport loss rate of  $\text{NO}(v)$  from the laser field of view is accounted for in the kinetic equations outlined below.

### 3 Data interpretation and reduction

Rotational energy transfer in NO in general occurs at or near gas kinetic rates,<sup>25-27</sup> with little dependence on the initially excited  $J$  level. The 8.5 Torr Ar bath gas gives rise to an NO rotational energy transfer timescale of ca. 10–20 ns, based on the  $\text{NO}(v = 2, 3; J)$  removal rate constants of ca.  $2-3 \times 10^{-10} \text{ cm}^3 \text{ s}^{-1}$  measured by Islam *et al.*<sup>25</sup> In addition, Islam *et al.*<sup>27</sup> have recently measured a large number of state-to-state rovibronic rate coefficients for collisions of initially created  $\text{NO}(v = 2, \Omega, J)$  with NO, He and Ar. It was found the  $\Omega$ -changing collisions of NO with Ar occur at no greater than 10% of the rate for  $\Omega$ -preserving collisions,<sup>27</sup> which places a lower limit of 100 ns on the timescale for  $\Omega$ -changing collisions. However, these rotational and spin-orbit equilibration time scales are still about a factor of 100–1000 times smaller than the timescale for NO vibrational decay in our experiment.

Fig. 3 shows a series of  $\text{NO}(v = 3)$  LIF spectra, obtained at various times following IR excitation, along with a synthetic spectrum calculated assuming a room-temperature distribution of rotational populations. The  $v = 0 \rightarrow 3$ ,  $R(J' = 7.5) F_1$  and  $F_2$  vibrational overtone transitions are separated by only  $0.07 \text{ cm}^{-1}$ , far less than the IR laser bandwidth of  $1.1 \text{ cm}^{-1}$ , and both the  $F_1$  and  $F_2$   $J' = 8.5$  levels are initially populated in the upper vibrational state. Each of the two excited rotational populations gives rise to four resolved emission lines shortly after the IR pump pulse (Fig. 3). The entire  $v = 3$  manifold is seen to fill in and approximate the predicted room-temperature spectrum after  $< 100 \text{ ns}$ , consistent with the rotational energy transfer timescales estimated above. Thus, since the rotational level populations reequilibrate on a timescale short compared to vibrational relaxation, the vibrational populations can be probed using any one of a number of  $\gamma$ -band rotation-vibration transitions.

Too high a concentration of vibrationally excited NO can lead to 'ladder-climbing' effects, in which the excited species exchange energy in an efficient, near-resonant process<sup>28</sup>



Wysong,<sup>11,29</sup> in previous measurements of  $\text{NO}(v = 2, 3)$  self-quenching rates, found that  $\text{NO}(v)$  fractions  $> \text{ca. } 10^{-3}$  of the total NO concentration led to discernible second-order effects in model calculations of  $\text{NO}(v)$  vibrational relaxation. It is



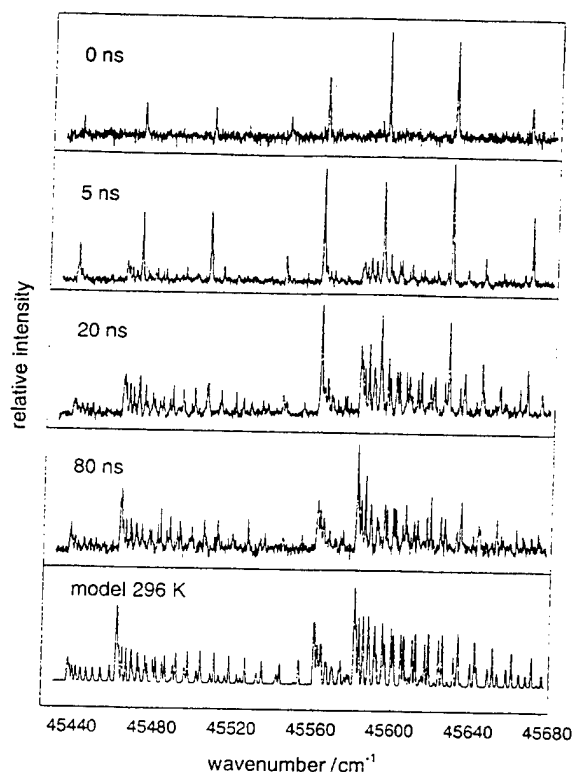


Fig. 3 Time series of NO  $\gamma(3, 3)$  laser-induced fluorescence spectra following IR excitation of NO( $v = 3$ ) at  $t = 0$  ns. Collisions with Ar bath gas molecules efficiently transfer the initially formed  $F_1$  and  $F_2$   $v = 3$ ,  $J' = 8.5$  populations to other rotational levels. After ca. 100 ns the rotational level populations are equilibrated at ambient temperature.

straightforward to estimate the excited fraction by comparing the maximum NO( $v = 2$ ) population to the background NO( $v = 1$ ) population, where both are obtained from normalized LIF signals. The Boltzmann equilibrium  $v = 1$  background population is equal to a  $1.1 \times 10^{-4}$  fraction of the  $v = 0$  population at 295K. From observations of several data sets, the initially pumped NO( $v = 2$ ) population was found to equal about one-half of the ambient  $v = 1$  population, a  $5 \times 10^{-5}$  fraction of the total NO. The maximum NO( $v = 3$ ) population is estimated to be about one-half that of NO( $v = 2$ ), based on relative IR laser fluences and bandwidths, and absorption coefficients and Doppler linewidths of the NO(X) 3–0 and 2–0 overtone bands.

In a typical experiment the UV laser was first tuned to detect the initially populated NO( $v$ ) level, and several NO( $v$ ) time series obtained. The UV laser frequency was then adjusted to detect NO( $v - 1$ ), and again several time series accumulated. Data on several different days were obtained in this manner for each different excited species–quencher pair. For  $v = 3 \rightarrow 2$  relaxation this was relatively straightforward, owing to negligible population of the lower  $v$  level in room-temperature NO. For  $v = 2 \rightarrow 1$  relaxation, however, the ca.  $10^{-4}$  fraction of the total NO concentration in  $v = 1$  resulted in a large background signal in the absence of IR excitation. This background signal dominated the noise observed on the  $v = 1$  signals. For NO( $v = 2$ ) self-relaxation the noise could be sufficiently reduced through signal averaging to obtain a branching fraction  $\chi_{\text{NO}}(v = 2 \rightarrow 1)$ . For NO( $v = 2, 3$ )–O relaxation the combination of reactions (5) and (6) gave rise to an additional source of background signal for NO( $v = 1$ ), and to a lesser extent for NO( $v = 2$ ).<sup>30</sup> These complications obviated an acceptable measurement of  $\chi_{\text{O}}(v = 2 \rightarrow 1)$ .

Fig. 4 shows time-dependent NO( $v$ ) populations and a model fit for a sample NO( $v = 3$ )–O-atom run. The rate pro-

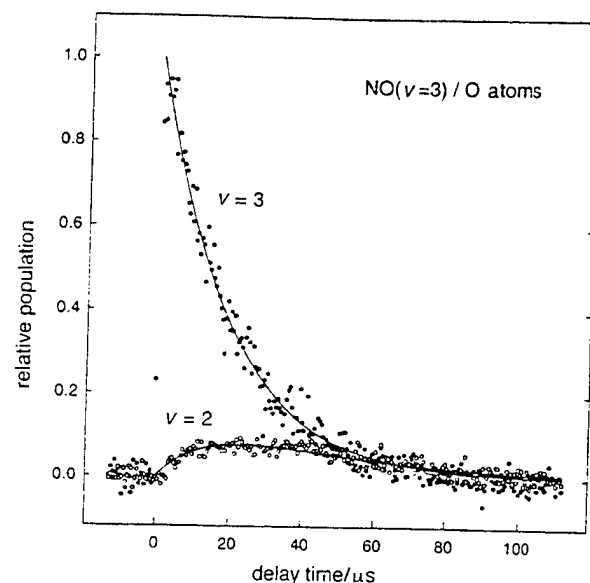
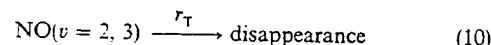
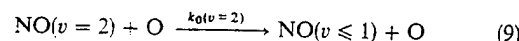
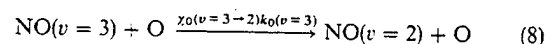


Fig. 4 Quenching of NO( $v = 3$ ) by O atoms. The IR laser fires at  $t = 0$ , which populates the  $v = 3$  level. NO( $v = 3$ ) decays exponentially, while NO( $v = 2$ ) grows in over time according to the branching fraction  $\chi_{\text{O}}(v = 3 \rightarrow 2)$  and the relaxation rate constants  $k_{\text{O}}(v)$ . The NO( $v = 2$ ) population builds up only modestly because  $\chi_{\text{O}}(v = 3 \rightarrow 2)$  is relatively small, and  $k_{\text{O}}(v = 2) \approx k_{\text{O}}(v = 3)$ . The NO( $v = 2, 3$ ) background LIF signals have been subtracted; the background signals are about  $6 \times (v = 2)$  and  $0.5 \times (v = 3)$  the magnitude of the transient signals.

cesses governing the relaxation of initially excited NO( $v = 3$ ) are written



In eqn. (8)–(10),  $k_{\text{O}}(v)$  is the rate constant for O-atom-induced relaxation of NO( $v$ ),  $\chi_{\text{O}}(v = 3 \rightarrow 2)$  is the branching fraction for single-quantum decay, and  $r_{\text{T}}$  is the transport loss rate out of the UV laser field of view. The transport loss rate has both convective and diffusive components under the present conditions, and can be estimated as  $5 \times 10^3 \text{ s}^{-1}$  based on the observed decay rate of NO( $v = 1$ ) (*vide infra*), i.e. ca. 10% of the O-atom-induced decay rate. Reactions (8)–(10) were modelled using the coupled differential equations

$$\frac{d[\text{NO}(v = 3)]}{dt} = -[\text{NO}(v = 3)]\{r_{\text{T}} + k_{\text{M}}(v = 3)[\text{M}]\} \quad (\text{I})$$

$$\begin{aligned} \frac{d[\text{NO}(v = 2)]}{dt} = & -[\text{NO}(v = 2)]\{r_{\text{T}} + k_{\text{M}}(v = 2)[\text{M}]\} \\ & + [\text{NO}(v = 3)]\{\chi_{\text{M}}(v = 3 \rightarrow 2)k_{\text{M}}(v = 3)[\text{M}]\} \end{aligned} \quad (\text{II})$$

In eqn. (I) and (II) [NO( $v$ )] and [M] refer to time-dependent species concentrations, with M being the identity of the chief quencher species, i.e. O atoms or NO as appropriate. Trial integrations performed on a PC showed second-order reactions such as eqn. (7) to be unimportant owing to the very small amount of excited level populations present.

Fig. 5 and 6 show time-dependent NO( $v$ ) populations and model fits for sample NO( $v = 3$ )–NO and NO( $v = 2$ )–NO runs, respectively. The NO( $v = 3$ )–NO kinetics are governed

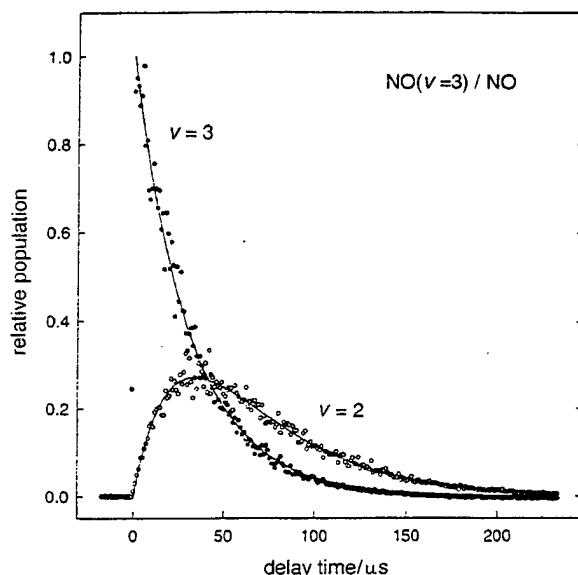


Fig. 5 Quenching of  $\text{NO}(v=3)$  by  $\text{NO}$ . The larger build-up of  $\text{NO}(v=2)$  relative to the  $\text{NO}(v=3)$ -O system shown in Fig. 4 is due mostly to the larger branching coefficient  $\chi_{\text{NO}}(v=3 \rightarrow 2)$ .

by a set of equations very similar to those given in eqn. (I) and (II), except for the identity of the relaxing species. The  $\text{NO}(v=2)$ -NO system, however, follows a somewhat different scheme. Two relaxation pathways are possible, depending on whether the relaxation of an initially excited  $\text{NO}(v=2)$  molecule gives rise to a pair of  $\text{NO}(v=1)$  molecules through the efficient near-resonant vibration-to-vibration (V-V) energy-transfer process<sup>31</sup>



or to a single  $\text{NO}(v=1)$  molecule through a vibration-to-translation (V-T) process, generally assumed to be much

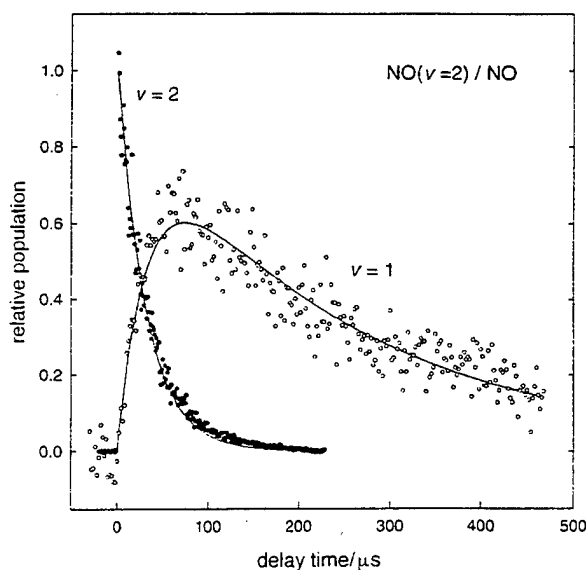
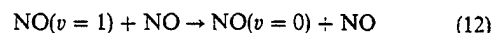


Fig. 6 Quenching of  $\text{NO}(v=2)$  by  $\text{NO}$ . The  $\text{NO}(v=1)$  population build-up is substantial due to the large branching fraction  $\chi_{\text{NO}}(v=2 \rightarrow 1)$  (see text), and to the slow decay of  $\text{NO}(v=1)$ , which is governed by the transport loss rate  $r_T$  out of the detection laser field of view. The  $\text{NO}(v=1)$  background LIF signal is about twice that of the transient signal, and has been subtracted.

slower due to the large energy defect:



Either reaction would be followed by the slow quenching of  $\text{NO}(v=1)$ ,



with  $k_{\text{NO}}(v=1) = 7 \times 10^{-14} \text{ cm}^3 \text{ s}^{-1}$ , or *ca.*  $700 \text{ s}^{-1}$  under the present conditions. Reactions (11) and (12) were modelled *viz.*

$$\frac{d[\text{NO}(v=2)]}{dt} = -[\text{NO}(v=2)]\{r_T + k_{\text{NO}}(v=2)[\text{NO}]\} \quad (III)$$

$$\begin{aligned} \frac{d[\text{NO}(v=1)]}{dt} = & -[\text{NO}(v=1)]\{r_T + k_{\text{NO}}(v=1)[\text{NO}]\} \\ & + [\text{NO}(v=2)]\{\chi_{\text{NO}}(v=2 \rightarrow 1)k_{\text{NO}}(v=2)[\text{NO}]\} \end{aligned} \quad (IV)$$

In eqn. (III) and (IV),  $k_{\text{NO}}(v=1, 2)$  are the appropriate disappearance rate constants, and  $\chi_{\text{NO}}(v=2 \rightarrow 1)$  is the observed fractional population of  $\text{NO}(v=1)$  upon decay of  $\text{NO}(v=2)$ . Since the observed decay rate of product  $\text{NO}(v=1)$  is dominated by transport loss,  $r_T$  can be determined directly through least-squares fitting. In this case accounting for transport loss increased the best-fit  $\chi_{\text{NO}}$  value by *ca.* 40%.

Eqn. (I) and (II) were used to model the population time evolution in the  $\text{NO}(v=3)$ -O and  $\text{NO}(v=3)$ -NO systems, and eqn. (III) and (IV) in the  $\text{NO}(v=2)$ -NO system. In each case the appropriate differential equations were numerically integrated using trial kinetic parameters to generate a solution against which the data could be compared. A non-linear least-squares fitting routine was used to determine the best fit through the automatic adjustment of the kinetic parameters. In general, a total of four parameters was allowed to vary in the fits: the decay rates  $k_M(v)[M]$  for the upper and lower  $v$  level populations, the branching coefficient  $\chi_M(v \rightarrow v-1)$ , and an arbitrary scaling parameter. While not the object of this study, the best-fit  $\text{NO}(v)$  decay rates were found to be consistent with previous measurements<sup>11,15,25,29</sup> and are reported below. For O-atom quenching the decay constant  $k_O(v=2)[O]$  could not be accurately determined due to poor S/N. Instead,  $k_O(v=2)$  was held equal to  $k_O(v=3)$ , consistent with the published values in Dodd *et al.*<sup>15</sup> Also, for  $\text{NO}(v=2)$  relaxation the decay of  $\text{NO}(v=1)$  is dominated by transport loss, as described above.

## 4 Results and Discussion

The least-squares fitting results were averaged to yield the branching fractions  $\chi$  shown in Tables 1 and 2. The scatter in the best-fit  $\chi$  values gave rise to standard deviations of 5–10% for relaxation by NO, and *ca.* 20% for relaxation by O atoms. The error bars quoted in Tables 1 and 2 include these errors, with an additional 25% of the best-fit result added in quadrature to account for the estimated systematic error in the

Table 1 Branching fractions  $\chi_O(v \rightarrow v-1)$  for relaxation of  $\text{NO}(v)$  by  $\text{O}^a$

$v=2 \rightarrow 1$	$v=3 \rightarrow 2$	ref.
	$0.35 \pm 0.12$	present work, decay rates varied
	$0.35 \pm 0.12$	present work, decay rates fixed
0.37		Quack and Troe <sup>18</sup>
0.43	0.29	Duff and Sharma <sup>20</sup>

<sup>a</sup> Values of  $\chi_O$  from the present work were obtained either by allowing the  $\text{NO}(v)$  decay rates to vary in the fit, or by fixing them using known parameters. See text for discussion.

**Table 2** Branching fractions  $\chi_{\text{NO}}(v \rightarrow v-1)$  for relaxation of  $\text{NO}(v)$  by  $\text{NO}^a$ 

$v = 2 \rightarrow 1$	$v = 3 \rightarrow 2$	ref.
$1.19 \pm 0.31^b$	$0.73 \pm 0.19$	present work, decay rates varied
$1.11 \pm 0.30^b$	$0.74 \pm 0.19$	present work, decay rates fixed

<sup>a</sup> Values of  $\chi_{\text{NO}}$  from the present work were obtained either by allowing the  $\text{NO}(v)$  decay rates to vary in the fit, or by fixing them using known parameters. See text for discussion. <sup>b</sup> Observed fractional population of  $v = 1$ , for which the interpretation depends on an assumption regarding the reaction mechanism. See text for discussion.

experiment. The non-linear least-squares fits used to determine the branching fractions  $\chi$  were also performed by fixing the  $\text{NO}(v = 2, 3)$  decay rates using the known O and NO number densities and the rate constants measured by Dodd *et al.*<sup>15</sup> The resultant branching fractions are also given in Tables 1 and 2, and are seen to be in excellent agreement with the  $\chi$  values obtained when the rates are adjusted in the fit. This agreement is consistent with the good agreement between the best-fit rate constants  $k_{\text{M}}(v = 2, 3)$  obtained in the present work and those obtained previously.<sup>15</sup> The rate constant results are discussed below, with the best-fit  $k_{\text{NO}}(v = 2, 3)$  from the present work given in Table 3.

### $\text{NO}(v = 3)\text{-O}$

In Table 1, the measured branching fraction  $\chi_{\text{O}}(v = 3 \rightarrow 2) = 0.35 \pm 0.12$  is seen to be in good agreement with the prediction of 0.29 made by the recent quasiclassical trajectory calculation of Duff and Sharma<sup>20</sup> (DS). A second calculation highlighted in Table 1 is taken from the statistical adiabatic channel model of Quack and Troe<sup>18</sup> (QT), which was originally developed to model the rates of unimolecular dissociation. The latter model calculates the rate of dissociation of a strongly bound 'activated complex', taking into account the coupling of initial and final state angular momenta. It is ideally suited for the  $\text{NO}(v)\text{-O}$  system, given the 3 eV binding energy available to an  $\text{NO}_2^*$  intermediate.

The QT and DS calculations both predict NO final vibrational state  $v_f$  population distributions that are approximately independent of  $v_i$ . For the initially populated level  $v_i = 2$ , both models predict final state populations that are weighted slightly toward  $v_f = 0$  (Table 1). The DS study predicts that for higher  $v_i$  levels this proclivity toward low- $v$  final states disappears, and that the final state populations are divided equally among the levels  $v_f < v_i$ . This distribution is consistent with a long-lived  $\text{NO}_2^*$  intermediate [reaction (4)], as are the large relaxation rate coefficients.<sup>11</sup>

QT predict from first principles a room-temperature  $k_{\text{O}}(v = 2)$  value which is in good agreement with that recently measured by Dodd *et al.*<sup>15</sup> It is likely, however, that the QT calculation underestimates the actual rate constant, since it considers only one of the two attractive potential-energy surfaces that arise in the interaction of ground-state NO and O. The DS trajectory calculation uses both attractive ( $1^2A' + 1^2A''$ ) surfaces, resulting in a  $k_{\text{O}}(v = 2)$  value which is ca. 50% higher than the QT result, and ca. 30–40% higher

**Table 3** Rate constants  $k_{\text{NO}}(v)$  for the relaxation of  $\text{NO}(v = 2, 3)$  by NO at ca. 295 K (units of  $10^{-12} \text{ cm}^3 \text{ s}^{-1}$ )<sup>a</sup>

$v = 2$	$v = 3$	ref.
$2.7 \pm 0.5$	$3.4 \pm 0.7$	present work
$3.2 \pm 0.3$	$4.0 \pm 0.3$	Dodd <i>et al.</i> <sup>15</sup>
$2.72 \pm 0.15^a$	$3.26 \pm 0.24$	Wysong <sup>11,29</sup>
$2.44 \pm 0.3$	$2.22 \pm 0.2$	Islam <i>et al.</i> <sup>25</sup>

<sup>a</sup> The measured value of  $k_{\text{NO}}(v = 2)$  (ref. 11) was listed incorrectly in Table 2 of ref. 15, and is given correctly here.

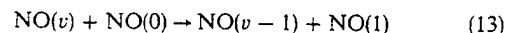
than the empirical result.<sup>15</sup> However, the DS paper points out the complexity inherent in a system with a total of 18 adiabatic doubly degenerate electronic states. The only existing *ab initio* calculation of the  $\text{O}(^3\text{P}) + \text{NO}(X^2\Pi)$  potential-energy surfaces does not include the effects of non-adiabatic coupling.<sup>32</sup> Clearly more effort is needed in both the experimental and theoretical areas in order to resolve the discrepancies and further understanding of the  $\text{NO}(v)\text{-O}$  system.

There exist at least two worthwhile extensions to the experiments described herein. First, it would be useful to measure the temperature dependence of the branching fractions in the 500–1200 K range, *i.e.* for thermospheric temperatures, albeit these measurements may be difficult using the present apparatus due to the increased ambient population of excited  $v$  levels and the resultant LIF background. Alternatively, a photolytic source of  $\text{NO}(v)$  such as  $\text{NO}_2$ <sup>30</sup> could be employed in order to mitigate the background NO signal. Some temperature-dependent rate coefficients for  $\text{NO}(v = 2, 3)$  relaxation by NO and other stable species have been measured,<sup>11,25</sup> though it is difficult to predict the effect of temperature on the  $\text{NO}(v_i \rightarrow v_f)$  branching fractions in the absence of detailed experimental or theoretical information. The  $\text{NO}(v)\text{-O}$  system in particular is lacking in information.

A second extension is suggested by the observations of Lipson *et al.*<sup>33</sup> and Sharma *et al.*,<sup>34</sup> who independently derived steady-state  $\text{NO}(v = 1)$  spin-orbit populations from high-resolution earthlimb IR emission data. The spin-orbit populations were found to depart strongly from local thermodynamic equilibrium, favouring the lower  $F_1$  component. Effective spin-orbit temperatures of ca. 200 K at higher altitudes were derived,<sup>33,34</sup> in contrast to the kinetic temperature of ca. 900 K inferred from the  $\text{NO}(v = 1)$  rotational distribution observed simultaneously. It has been proposed<sup>33</sup> that the subthermal spin-orbit distribution results from selective formation of the  $v = 1$   $F_1$  spin-orbit level in upumping collisions of  $\text{NO}(v = 0)$  with O. Thus, measurements of the spin-orbit dependence of  $\text{NO}(v)$  relaxation rate constants would be valuable, as well as measurements of  $\text{NO}(v = 1, 2)$  final state propensities in the upumping of  $\text{NO}(v = 0)$  by O. These experiments may require a molecular beam apparatus instead of the cell arrangement used here, due to the efficiency with which collider species (*e.g.* He and Ar) interconvert the NO spin-orbit components.<sup>27</sup>

### $\text{NO}(v = 3)\text{-NO}$

The branching fraction  $\chi_{\text{NO}}(v = 3 \rightarrow 2) = 0.73 \pm 0.19$  listed in Table 2 is significantly lower than the value of unity predicted assuming a single-quantum relaxation mechanism, but instead indicates some degree of multiquantum behaviour. It is generally accepted that NO vibrational self-relaxation proceeds *via* the resonant V–V transfer mechanism (13) for the lower  $v$  levels.<sup>25,35,36</sup>



As  $v$  increases reaction (13) gradually becomes more endothermic owing to a small degree of vibrational anharmonicity, ca.  $28 \text{ cm}^{-1}$  per  $v$  level, which slows the reaction. The reaction endothermicity exceeds the room-temperature  $kT$  value at  $v = 9$ , and Yang *et al.*<sup>36</sup> have suggested that the V–V mechanism (13) is unimportant for  $v \geq 8$ . For  $v \geq 13$  the  $k_{\text{NO}}(v)$  values increase rapidly, which the authors attribute at least partially to the onset of multiquantum relaxation pathways. In one experiment, Yang *et al.* populated  $\text{NO}(v = 19)$ , then monitored  $\text{NO}(v = 17\text{--}19)$  populations as a function of delay time in a manner very similar to the present work. They determined  $\chi_{\text{NO}}(v = 19 \rightarrow 18) = 0.47$ ,  $\chi_{\text{NO}}(19 \rightarrow 17) = 0.33$ , and  $\chi_{\text{NO}}(18 \rightarrow 17) = 0.48$ ,<sup>36</sup> consistent with a high degree of multiquantum behaviour.

## NO( $v = 2$ )-NO

The measured branching fraction  $\chi_{\text{NO}}(v = 2 \rightarrow 1) = 1.19 \pm 0.31$  is also listed in Table 2. Unfortunately, the NO( $v = 2$ )-NO measurement performed here does not unambiguously identify the reaction mechanism. Such an identification requires determining (1) the relative contributions of single- and double-quantum relaxation, and (2) for the single-quantum component, the relative contributions of the V-V process (11a) and the V-T process (11b). Thus, the measured  $\chi_{\text{NO}}(v = 2 \rightarrow 1)$  value is consistent with an effective single-quantum branching fraction of 0.5–1.0, depending on the contributions of (11a) and (11b) to the single-quantum component. We note, however, that all interpretations of  $\chi_{\text{NO}}(v = 2 \rightarrow 1)$  are in disagreement with the expectation of a negligible V-T contribution to the overall disappearance rate.<sup>36</sup> Clearly a more definitive experiment could be used to determine the precise mechanism of the NO( $v = 2$ )-NO relaxation process. For instance, a small amount of admixed isotopically labelled NO\* in unlabelled NO could be excited to  $v = 2$ , followed by observing the population time evolution of both NO\*( $v = 1$ ) and NO( $v = 1$ ).

Wysong<sup>11,29</sup> performed semiquantitative measurements of the extent of single-quantum behaviour in NO( $v = 2$ ) self-relaxation. The NO( $v = 2$ ) population was excited via tunable IR laser excitation of ambient NO, using an apparatus very similar to that of the present work. Transient population of NO( $v = 1$ ) was measured to be 'about twice' that of initially excited NO( $v = 2$ ), consistent with the single-quantum V-V transfer mechanism governed by eqn. (13).

Stephenson<sup>31</sup> performed a landmark measurement of the rate constant for reaction (14a) by measuring the rate of appearance of NO( $v = 2$ ):



As pointed out by Hopkins and Chen,<sup>37</sup> who pioneered the measurement technique and data interpretation in the analogous process in HCl( $v$ ), the necessary simplification of the kinetic equations can lead to an overestimate of  $k_{14a}$  by as much as 25%. The rate constant  $k_{14a}$  can be related to  $k_{14b}$  through detailed balance; at room temperature,  $k_{18b} = 0.87k_{14a}$ . Thus, assuming that reaction (14b) proceeds wholly as shown, measurements of the vibrational relaxation of  $v = 2$  can be related to Stephenson's measurement. Subsequent determinations of the rate constant for reaction (14b) are lower than that derived from Stephenson's work by factors ranging from 1.3 to 2.4,<sup>11,15,35,38,39</sup> with the later, more reliable measurements<sup>11,15,35</sup> in good agreement with each other and with the Stephenson value, albeit just within the combined error bars.

It is important to note that despite the degree of effort in measuring the disappearance rates of NO( $v$ ) in collisions with itself and with other species, we are unaware of any explicit measurements of the relaxation pathways aside from the NO( $v = 19$ ) study of Yang *et al.*<sup>36</sup> The  $v = 4$ –8 region is particularly open to investigation at this juncture, although it is not easily accessible using either the stimulated emission pumping technique of Yang *et al.*, nor the IR pumping technique owing to rapidly decreasing 0– $v'$  absorption coefficients. Yang *et al.*<sup>36</sup> predict that the relaxation proceeds via a single-quantum mechanism for  $v$  levels as high as  $v = 14$ ; this has not been experimentally verified.

## NO( $v = 2, 3$ ) Disappearance rate constants

The best-fit NO( $v = 2, 3$ ) decay rates can be combined with the known quencher species concentrations to determine relaxation rate constants. The rate constants result essentially from one- or two-point Stern-Volmer plots, and thus have

lower precision than the values measured previously in this laboratory;<sup>15</sup> here we quote ca. 20% error bars. Using the measured O-atom density of  $1.8 \times 10^{15} \text{ cm}^{-3}$ , the rate coefficient  $k_{\text{O}}(v = 3)$  was determined to be  $(3.0 \pm 0.6) \times 10^{-11} \text{ cm}^3 \text{ s}^{-1}$ . This result agrees well with the value of  $(2.5 \pm 0.3) \times 10^{-11} \text{ cm}^3 \text{ s}^{-1}$  reported by Dodd *et al.*,<sup>15</sup> in which NO( $v = 2, 3$ ) time-dependent populations were detected using MPI, and the maximum O-atom density was much lower, ca.  $0.5 \times 10^{15} \text{ cm}^{-3}$ . Thus the current measurement provides a valuable corroboration of the previously measured  $k_{\text{O}}(v = 2, 3)$ .

For NO self-quenching, the relaxation rate constants were determined to be  $k_{\text{NO}}(v = 2) = (2.7 \pm 0.5) \times 10^{-12}$  and  $k_{\text{NO}}(v = 3) = (3.4 \pm 0.7) \times 10^{-12} \text{ cm}^3 \text{ s}^{-1}$ . The  $k_{\text{NO}}(v = 2)$  value is average of  $2.5 \times 10^{-12}$  and  $2.9 \times 10^{-12} \text{ cm}^3 \text{ s}^{-1}$  obtained from analyzing the decay of initially excited NO( $v = 3$ ) and NO( $v = 2$ ), respectively. The rate constants  $k_{\text{NO}}(v = 2, 3)$  are compared in Table 3 with values measured using similar laser IR pump-UV probe experiments. The two sets of values are seen to be in general agreement with the exception of the Islam *et al.*<sup>25</sup> measurement of  $k_{\text{NO}}(v = 3)$ , which is about 40% lower than the mean of the other three values and outside the error bars of any of them. While the Islam *et al.*  $k_{\text{NO}}(v = 2)$  measurement is also lower than the others, it is in good agreement with two of them and just outside the error bars of the third.

## 5 Summary

We have measured the fractional population of NO( $v = 1$ ) arising from the collision-induced relaxation of NO( $v = 3$ ) by O atoms and NO( $v = 2, 3$ ) by NO. The branching fraction  $\chi_{\text{O}}(v = 3 \rightarrow 2)$  is consistent with the existence of a long-lived NO\* collision complex, and agrees well with the results of a recent quasiclassical trajectory study<sup>20</sup> of NO( $v = 3$ )-O-atom collisions on a calculated potential-energy surface. The  $\chi_{\text{NO}}(v = 3 \rightarrow 2)$  value is significantly lower than the value of unity arising from a V-V, single-quantum relaxation mechanism, and suggests a multiquantum component. For NO( $v = 2$ ) self-relaxation the  $\chi_{\text{NO}}(v = 2 \rightarrow 1)$  value cannot be used to unambiguously assign the mechanism, owing to the possible, unknown contribution of resonant uppumping of NO( $v = 0$ ) to NO( $v = 1$ ) in the relaxation process. Both NO self-relaxation results imply a significant V-T component to the quenching process, contrary to the relatively low rate for NO( $v = 1$ ) self-relaxation. Rate constants for the vibrational relaxation of NO( $v = 3$ ) by O and NO( $v = 2, 3$ ) by NO were obtained in the course of fitting for the branching fractions, and are consistent with previous results from this laboratory.

This work has the strongest application in improving the accuracy of auroral models, in which the NO production rate is greatly enhanced over the quiescent atmosphere. Auroral energy deposition is typically a maximum in an altitude region where the O-atom density is also high, i.e. in the lower thermosphere near 100 km. Thus, O atoms play a key role in determining the NO( $v$ ) population distribution.<sup>9</sup> The recent measurements of NO( $v \geq 2$ ) fundamental band radiance in the quiescent atmosphere<sup>6,7</sup> also point up the need for more accurate energy-transfer parameters for the NO( $v$ )-O system. Finally, the observation of subthermal NO spin-orbit distributions in the lower thermosphere<sup>33,34</sup> suggests the need for additional measurements and theory concerning final state propensities in NO( $v, J, \Omega$ ) collisions with O atoms.

We thank Steven J. Lipson of Phillips Laboratory/GPOC for insights into the atmospheric implications of this work, and Richard A. Copeland of SRI for valuable discussions regarding experimental techniques in the laser detection of NO. We would also like to acknowledge one of the referees for a number of helpful comments. J.A.D. performed this work

## References

- 1 C. A. Barth, *Planet. Space Sci.*, 1992, **40**, 315.
- 2 D. W. Rusch, J.-C. Gerard and C. G. Fesen, *J. Geophys. Res.*, 1991, **96**, 11331.
- 3 J.-C. Gerard, D. V. Bisikalo, V. I. Shematovich and J. W. Duff, *J. Geophys. Res.*, 1997, **102**, 285.
- 4 R. D. Sharma, V. A. Kharchenko, Y. Sun and A. Dalgarno, *J. Geophys. Res.*, 1996, **101**, 275.
- 5 W. T. Rawlins, M. E. Fraser and S. M. Miller, *J. Phys. Chem.*, 1989, **93**, 1097.
- 6 P. S. Armstrong, S. J. Lipson, J. A. Dodd, J. R. Lowell, W. A. M. Blumberg and R. M. Nadile, *Geophys. Res. Lett.*, 1994, **21**, 2425.
- 7 R. D. Sharma, H. Dothe, F. von Esse, V. A. Kharchenko, Y. Sun and A. Dalgarno, *J. Geophys. Res.*, 1996, **101**, 19707.
- 8 P. S. Armstrong, J. A. Dodd, S. J. Lipson, W. A. M. Blumberg, R. B. Lockwood, J. R. Lowell, R. M. Nadile, D. E. Paulsen, R. E. Murphy, W. T. Rawlins, M. E. Fraser and B. D. Green, *Eos Trans. AGU*, 1995, **76**, F439.
- 9 G. E. Caledonia and J. P. Kennealy, *Planet. Space Sci.*, 1982, **30**, 1043.
- 10 T. C. Degges, *Appl. Opt.*, 1971, **10**, 1856.
- 11 I. J. Wysong, *J. Chem. Phys.*, 1994, **101**, 2800.
- 12 R. E. Murphy, E. T. P. Lee and A. M. Hart, *J. Chem. Phys.*, 1975, **63**, 2919.
- 13 B. D. Green, G. E. Caledonia, R. E. Murphy and F. X. Robert, *J. Chem. Phys.*, 1982, **76**, 2441.
- 14 R. P. Fernando and I. W. M. Smith, *Chem. Phys. Lett.*, 1979, **66**, 218.
- 15 J. A. Dodd, S. M. Singleton, S. M. Miller, P. S. Armstrong and W. A. M. Blumberg, *Chem. Phys. Lett.*, 1996, **260**, 103.
- 16 K. Glanzer and J. Troe, *J. Chem. Phys.*, 1975, **63**, 4352.
- 17 D. V. Shalashilin, A. V. Michtchenko, S. Ya. Umanskii and Yu. M. Gershenzon, *J. Phys. Chem.*, 1995, **99**, 11627.
- 18 M. Quack and J. Troe, *Ber. Bunsen-Ges. Phys. Chem.*, 1975, **79**, 170.
- 19 M. Quack and J. Troe, *Ber. Bunsen-Ges. Phys. Chem.*, 1977, **81**, 160.
- 20 J. W. Duff and R. D. Sharma, *J. Chem. Soc., Faraday Trans.*, 1997, **93**, 2645.
- 21 W. B. DeMore, S. P. Sander, C. J. Howard, A. R. Ravishankara, D. M. Golden, C. E. Kolb, R. F. Hampson, M. J. Kurylo and M. J. Molina, *Chemical Kinetics and Photochemical Data for Use in Stratospheric Modeling*, Eval. No. 11, 1994, JPL Publ. 94-26.
- 22 L. T. Earls, *Phys. Rev.*, 1935, **48**, 423.
- 23 R. W. Nicholls, *J. Res. Nat. Bur. Stand.*, 1964, **68A**, 535.
- 24 R. P. Fernando and I. W. M. Smith, *J. Chem. Soc., Faraday Trans. 2*, 1979, **75**, 1064.
- 25 M. Islam, I. W. M. Smith and J. W. Wiebrecht, *J. Phys. Chem.*, 1994, **98**, 9285.
- 26 Aa. S. Sudbo and M. M. Loy, *J. Chem. Phys.*, 1982, **76**, 3646.
- 27 M. Islam, I. W. M. Smith and J. W. Wiebrecht, *J. Chem. Phys.*, 1995, **103**, 9676.
- 28 S. Saupe, I. Adamovich, M. J. Grassi, J. W. Rich and R. C. Bergman, *Chem. Phys.*, 1993, **174**, 219.
- 29 I. J. Wysong, *Chem. Phys. Lett.*, 1994, **227**, 69.
- 30 I. W. M. Smith, R. P. Tuckett and C. J. Whitham, *Chem. Phys. Lett.*, 1992, **200**, 615.
- 31 J. C. Stephenson, *J. Chem. Phys.*, 1973, **59**, 1523.
- 32 H. Katagiri and S. Kato, *J. Chem. Phys.*, 1993, **99**, 8805.
- 33 S. J. Lipson, P. S. Armstrong, J. A. Dodd, J. R. Lowell, W. A. M. Blumberg and R. M. Nadile, *Geophys. Res. Lett.*, 1994, **21**, 2421.
- 34 R. D. Sharma, H. Dothe and F. von Esse, *J. Geophys. Res.*, 1996, **101**, 17129.
- 35 M. J. Frost, M. Islam and I. W. M. Smith, *Can. J. Chem.*, 1994, **72**, 606.
- 36 X. Yang, E. H. Kim and A. M. Wodtke, *J. Chem. Phys.*, 1992, **96**, 5111.
- 37 B. J. Hopkins and H.-L. Chen, *J. Chem. Phys.*, 1972, **57**, 3816.
- 38 H. Horiguchi and S. Tsuchiya, *Jpn. J. Appl. Phys.*, 1979, **18**, 1207.
- 39 R. G. Macdonald and F. C. Sopchysyn, *Chem. Phys.*, 1985, **94**, 455.

Paper 7/01534H; Received 4th March, 1997

# A model for the response of the atomic oxygen 557.7 nm and the OH Meinel airglow to atmospheric gravity waves in a realistic atmosphere

U. B. Makhlof

Stewart Radiance Laboratory, Utah State University, Bedford, Massachusetts

R. H. Picard and J. R. Winick

Geophysics Directorate, Phillips Laboratory, Hanscom Air Force Base, Massachusetts

T. F. Tuan

Physics Department, University of Cincinnati, Cincinnati, Ohio

**Abstract.** We describe a model for the response of atomic oxygen and hydroxyl airglow to a gravity wave. The airglow models use a realistic atmospheric-gravity-wave model, describing the wave velocity and pressure fluctuations in the presence of a nonisothermal background temperature profile and background winds. The gravity-wave model is coupled to the OH photochemical model of Makhlof *et al.* [1995] and to a simple chemical model for the 557.7 nm airglow as described below. It is shown that the chemistry of the 557.7 nm airglow does not affect the phase of the Krassovsky  $\eta$ , due to the short chemical lifetime of the  $O(^1S)$  and the  $O_2(c^1\Sigma_u^-)$  precursor states, whereas for the OH airglow the chemistry and dynamics couple for wave periods of 10-25 min, and chemistry does affect the phase of  $\eta$ . The effect of standing waves and traveling waves on the phase of  $\eta$  is shown to be different, and this behavior can be used to differentiate between freely propagating waves and ducted waves. These effects are illustrated by applying the model to examples of Airborne Lidar and Observations of Hawaiian Airglow (ALOHA-93) campaign data. A combination of model prediction and ground-based measurements from the ALOHA-93 campaign are used to estimate the vertical eddy diffusivity  $D_{zz}$  due to nonlinear gravity waves following the formulation of Weinstock [1976]. The estimated values of  $D_{zz}$  vary between  $1.0 \times 10^2$  and  $5.0 \times 10^3$  m<sup>2</sup>/s, which is in the range of measured and inferred values.

## 1. Introduction

In a previous paper by Makhlof *et al.* [1995], hereinafter referred to as MPW, a photochemical-dynamical model for the OH Meinel airglow was developed and used to study the fluctuations in the OH airglow emissions. These fluctuations were assumed to be due to the passage of internal gravity waves (IGW) from low-altitude sources through the OH layer. In that study, the IGW was assumed to propagate in an isothermal atmosphere, which allows for an analytic solution of the fluid-dynamic equations [Hines, 1960]. Traveling-wave solutions of the dynamical equations were used to drive a simple photochemical model for the odd-oxygen and odd-hydrogen species, from which OH Meinel-band emission rates were calculated. We studied the behavior of the Krassovsky ratio  $\eta$  [Krassovsky, 1972], which is a measure of the airglow response to a periodic dynamical perturbation such as an IGW, relating the observed relative fluctuations in the airglow brightness to the relative fluctuations in the temperature. The traveling-wave solution was found not to be satisfactory for short-period waves, since it could not predict a zero phase for  $\eta$ , as observed in many of the measurements [Viereck and Deehr, 1989; Hecht *et al.*, 1987].

Hence, following up on a suggestion of Hines and Tarasick [1994], standing-wave solutions were also studied in MPW by forcing the vertical velocity fluctuation at the ground to be zero, ensuring an IGW node there. This led to a bi stable phase of 0° or 180° for  $\eta$ , with a rather sharp transition region between the two states.

Another way to produce standing waves is to assume a realistic nonisothermal atmosphere which, while producing traveling waves at long periods, will naturally lead to standing waves at short periods due to Brunt-Väisälä ducting [e.g., Wang and Tuan, 1988]. The short-period waves are reflected from the temperature gradient in the lower thermosphere occurring when the wave frequency approaches the local Brunt-Väisälä frequency. This ducting will be modified and accentuated by the presence of winds (Brunt-Doppler ducting), which can Doppler shift the wave frequency to the local Brunt-Väisälä frequency [Pitteway and Hines, 1965].

In the current paper, a nonisothermal dynamical model of this type is developed and applied to both the 557.7 nm atomic oxygen green-line emission and to the OH airglow. The fluctuations are again due to IGW, which now are propagating in the presence of a background temperature profile and background winds. The wind profile is taken from the model of Hedin [1996], modified to match measurements whenever actual wind measurements exist. The fluid-dynamic equations are solved numerically, and the solutions are used to calculate the Krassovsky ratio for the green-line and the OH Meinel emission. The Krassovsky ratio is a response, or transfer, function measuring the response of airglow to a dynamical per-

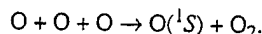
Copyright 1998 by the American Geophysical Union.

Paper number 97JD03082.  
0148-0227/98/97JD-03082\$09.00

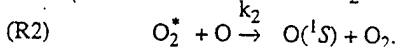
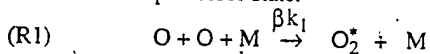
turbation. We calculate another transfer function  $\tau$ , which is defined as the ratio of the relative brightness fluctuation to the relative density fluctuation, finding that  $\tau$  is especially useful to describe green-line response. This transfer function is used to estimate the vertical eddy diffusivity  $D_{zz}$  arising from nonlinear wave interaction, following the method of *Weinstock* [1976]. A preliminary application of this method is described by *Makhlof et al.* [1997]. However, in this paper, we will use the Doppler lineshape to obtain the brightness fluctuation as discussed by MPW, and then the transfer function  $\tau$  is calculated to estimate  $D_{zz}$ , while *Makhlof et al.* [1997] used the brightness-weighted method to estimate  $\tau$ .

## 2. The $O(^1S)$ Chemical Kinetics

The kinetic mechanism of the production of the  $O(^1S)$ , which is the source of the 557.7 nm green line, has been widely debated in the literature. *Chapman* [1931] first proposed that the  $O(^1S)$  state is formed by a three-body reaction of ground-state atomic oxygen,  $O(^3P)$ , namely



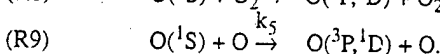
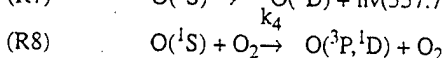
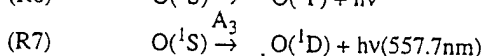
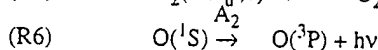
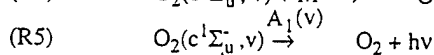
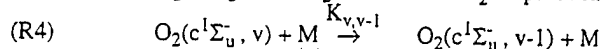
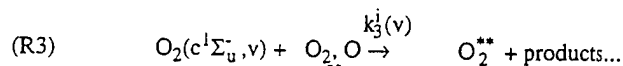
*Barth* [1961] suggested that the  $O(^1S)$  state is not formed by a Chapman-type reaction, but is formed by a two-stage mechanism that involves a precursor state.



Both in situ observation [*Thomas et al.*, 1979; *Thomas and Young*, 1981] and theoretical considerations [*Bates*, 1981, 1992] strongly favored the Barth-type mechanism. The question then is, What is the identity of the precursor? Through a process of elimination, *Thomas* [1981] concluded that the precursor is most likely to be either  $O_2(A^3\Delta_u)$  or  $O_2(c^1\Sigma_u^-)$ . A spectrum of the Venus nightglow obtained by *Venera 9* [*Krasnopolsky et al.*, 1976], showed emissions from only  $v=0$  of  $O_2(A^3\Sigma_u^+)$ ,  $O_2(A')$ , and  $O_2(c)$ , but no 557.7 nm airglow from  $O(^1S)$ . The quenching of  $O_2(A)$  and  $O_2(A')$

at  $v=0$  is exothermic for the  $O(^1S)$  state while the quenching of  $O_2(c)$  is endothermic for  $v \leq 2$ . So *Krasnopolsky* [1981] concluded that the Barth precursor must be  $O_2(c)$  and must be in a vibrationally excited state  $v \geq 3$ .

Using a Barth-type mechanism with  $O_2^* = O_2(c)$  as the precursor to  $O(^1S)$  in reaction (R2), a model scheme to calculate the 557.7 nm airglow emission is developed as follows:



This reaction set includes collisional removal of the precursor by  $O_2$  and by  $O$  (R3), vibrational deactivation of the precursor (R4), radiative relaxation of the precursor and of  $O(^1S)$  (R5)-(R7), and quenching of  $O(^1S)$  (R8)-(R9). In (R3),  $O_2^{**}$  is an electronic state other than the  $c$  state. Electronic quenching of  $O_2(c)$  by  $N_2$  was neglected due to lack of sufficient data. One recent measurement reported collisional quenching of  $O_2(c, v=9)$  by  $N_2$  [*Copeland et al.*, 1996], but no information is available on the quenching by  $N_2$  of other vibrational levels.

In reaction (R1), it is assumed that the  $O_2(c)$  is produced in high vibrational levels,  $v > 10$ . Single-quantum vibrational deactivation then takes place to lower vibrational levels through collisions with  $O_2$ . The vibrational deactivation rates  $K_{v,v-1}$  are derived based on the Schwartz, Slawsky, and Herzfeld (SSH) theory [*Schwartz et al.*, 1952] for the transition probabilities of an anharmonic oscillator. Using this theory and some approximations from *Degen's* [1972] model, the vibrational deactivation rate constants are expressed as

Table 1. Reaction and Transition Rates Used

Rate Constant	Value	Comments and References
$\beta k_1$	$\beta 4.7 \times 10^{-33} (300/T)^2 \text{ cm}^6 \text{ s}^{-1}$ $\beta = 0.04$	<i>Campbell and Gray</i> [1973] <i>Bates</i> [1992]
$k_2$	$2.5 \times 10^{-12} \text{ cm}^3 \text{ s}^{-1}$	<i>Bates</i> [1992]
$k_3^j(v)$	$z(v)K_{1,0}$ for $i=O_2$ $5z(v)K_{1,0}$ for $i=O$ $K_{1,0} = x 10^{-14} \text{ cm}^3 \text{ s}^{-1}$	$z(v)=[7, 12, 16, 29, 33, 37, 38, 41, 45, 59, 88, 167, 274, 426, 647, 921, 1269]$ for $v=0, 16$
$A_1(v)$	Values from <i>Bates</i> [1989], reduced by a factor of 3.	Reduction based on private communication with D. L. Huestis, [1994].
$A_2$	$0.17 \text{ s}^{-1}$	<i>Nicolauides et al.</i> [1971]
$A_3$	$1.18 \text{ s}^{-1}$	<i>Nicolauides et al.</i> [1971]
$k_4$	$4.9 \times 10^{-12} \exp(-850/T) \text{ cm}^3 \text{ s}^{-1}$	<i>Atkinson and Welge</i> [1972]
$k_5$	$2 \times 10^{-14} \text{ cm}^3 \text{ s}^{-1}$	<i>Krauss and Neumann</i> [1975]

$$K_{v,v-1} = v \left( \frac{\Delta E_{v,v-1}}{\Delta E_{1,0}} \right)^{\frac{4}{3}} e^{-\sigma K_{1,0}}, \quad (1)$$

where  $v$  is the vibrational level number,  $\Delta E_{v,v'}$  is the energy difference between levels  $v$  and  $v'$ ,

$$\sigma = \left[ \frac{c_1}{T} (\Delta E_{v,v-1})^2 \right]^{\frac{1}{3}} - \left[ \frac{c_1}{T} (\Delta E_{1,0})^2 \right]^{\frac{1}{3}} + \left[ \frac{\Delta E_{1,0} - \Delta E_{v,v-1}}{2kT} \right],$$

$c_1$  is a constant that depends on the collisional partners, and  $T$  is the kinetic temperature.

Knowing the two constants  $K_{1,0}$  and  $c_1$ , one can calculate all the vibrational deactivation rates for the  $O_2(c)$  vibrational levels. Lopez-Gonzalez *et al.* [1992] fit data taken on the Herzberg II bands (which originate in the  $c$  state) and obtained  $K_{1,0} = 9 \times 10^{-14} \text{ cm}^3/\text{s}$  and  $c_1 = 2.0 \text{ K}/(\text{cm}^{-1})^2$  as best fits, and these values are used in our calculations. Table 1 summarizes all the reaction and transition rates used. The function  $z(v)$  is chosen to give the best fit to the vibrational-distribution measurement of Slinger and Huestis [1981] and is forced to give the exact measured rates of Copeland *et al.* [1994, 1996] for  $v=9, 10$  and 11. The rate  $k_3^1(v)$  of quenching by  $[O]$  is assumed to be five times the rate of quenching by  $O_2$ , based on Krasnopolsky's [1986] analysis of the Herzberg II band measurements by Thomas [1981].

The minor-species profiles that are used in the  $O(^1S)$  kinetic model are generated from the one-dimensional diurnal model described by MPW, which uses the climatological model of Summers [1993] as an input. Using reactions (R1)–(R9), and the reaction rates in Table 1, the  $O(^1S)$  density is calculated assuming it is in a photochemical equilibrium state where the production is equal to the loss. Figure 1 shows the steady state  $O(^1S)$  number density as obtained from the above chemical scheme. OH vibrational level

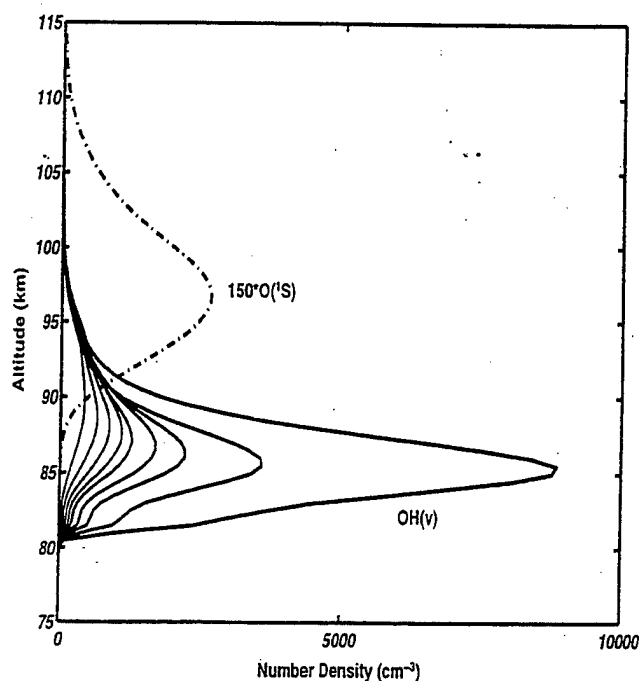


Figure 1. Steady state  $O(^1S)$  and  $OH(v)$  number densities ( $v=1,9$ ) calculated for the ALOHA-93 conditions.

profiles output by the diurnal model and OH vibrational population model (see MPW) are also shown in Figure 1.

### 3. Nonisothermal Gravity Wave Model and Airglow Response

We start with the equations of fluid motion in the atmosphere, assuming that motions are adiabatic and neglecting eddy viscosity, eddy thermal conductivity, and the coriolis force. The coriolis and eddy dissipation effects are generally unimportant at the scales we are considering here and become important only for wave periods greater than 4 hours [Hickey, 1988a, b; Schubert *et al.*, 1991]. The dissipationless fluid equations are then:

$$\frac{D\rho}{Dt} + \rho \nabla \cdot \mathbf{u} = 0 \quad (2)$$

$$\rho \frac{D\mathbf{u}}{Dt} = \rho \mathbf{g} - \nabla p \quad (3)$$

$$\frac{Dp}{Dt} = \frac{\gamma p D\rho}{\rho Dt} \quad (4)$$

$$p = \rho RT, \quad (5)$$

where

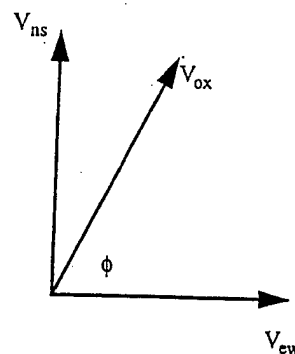
$$\frac{D}{Dt} = \frac{\partial}{\partial t} + \mathbf{u} \cdot \nabla$$

is the convective derivative;  $\rho$ ,  $p$ , and  $T$  are the density, pressure, and temperature;  $\mathbf{g} = (0, 0, -g)$  is the acceleration due to gravity;  $\mathbf{u} = (u, 0, w)$  is the velocity field;  $\gamma$  is the ratio of specific heats; and  $R$  is the universal gas constant.

The thermodynamic quantities  $\rho$ ,  $p$ , and  $T$  and the velocity  $\mathbf{u}$  are measured quantities that contain a perturbation component due to IGW propagating in the atmosphere. These perturbations are deviations from the mean quantities  $\rho_0$ ,  $p_0$ , and  $\mathbf{u}_0$  (the background winds). In this model we will account for the effects of mean zonal winds ( $V_{ew}$ ) and meridional winds ( $V_{ns}$ ), while mean vertical winds are negligible and are ignored. The  $z$  direction is taken to be vertical and the perturbations are assumed to vary harmonically in time and in  $x$ , where the  $x$  direction is taken along the wave vector; that is,

$$\begin{aligned} \rho &= \rho_0(z) + \rho'(z) \exp(i\omega t - ik_x x), \\ p &= p_0(z) + p'(z) \exp(i\omega t - ik_x x), \\ T &= T_0(z) + T'(z) \exp(i\omega t - ik_x x), \\ u &= V_{ox}(z) + u'(z) \exp(i\omega t - ik_x x), \\ w &= w'(z) \exp(i\omega t - ik_x x), \end{aligned} \quad (6)$$

where primes denote perturbed wave quantities,  $\omega$  = intrinsic frequency,  $k_x$  = horizontal wave number, and  $V_{ox} = V_{ew} \cos \phi + V_{ns} \sin \phi$  is the background wind speed along the wave direction, where  $\phi$  is the angle between the eastward direction and the wave vector.





Substituting the variables in equation (6) into the hydrodynamic equations, equations (2)-(5) and neglecting terms of second order and higher in the wave amplitude, we obtain a set of linearized hydrodynamic equations

$$i\Omega p' + w' \frac{\partial p_o}{\partial z} - ik_x p_o u' + \rho_o \frac{\partial w'}{\partial z} = 0 \quad (7)$$

$$i\Omega \rho_o u' + \rho_o \frac{\partial V_{ox}}{\partial z} w' = ik_x p' \quad (8)$$

$$i\Omega \rho_o w' = -g p' - \frac{\partial p'}{\partial z} \quad (9)$$

$$i\Omega p' + w' \frac{\partial p_o}{\partial z} = i\Omega c^2 \rho' + c^2 w' \frac{\partial \rho_o}{\partial z} \quad (10)$$

$$\frac{T'}{T_o} = \frac{p'}{p_o} - \frac{\rho'}{\rho_o} \quad (11)$$

where  $\Omega = \omega - k_x V_{ox}$  is the Doppler-shifted frequency and  $c$  is the speed of sound.

There are several approaches to simplifying the linearized fluid equations, equations (7)-(11) which are summarized in standard references [e. g., *Gossard and Hooke*, 1975; *Tuan and Tadic*, 1982; *Holton*, 1992]. We choose to follow a slightly different procedure. Using simple algebra, we eliminate variables and obtain two coupled differential equations in  $z$  for the scaled pressure perturbation  $\Psi = \omega p_o^{-1/2} p'$  and the scaled vertical velocity  $\Phi = \rho_o^{1/2} w'$ . The variables  $\Psi$  and  $\Phi$  are scaled to remove the effect of the quasi-exponential variation of the background atmospheric density. The result is

$$\frac{\partial \Psi}{\partial z} - \Gamma \Psi = i\Omega \left( \frac{\omega_b^2}{\omega^2} - \Omega^2 \right) \Phi \quad (12)$$

$$\frac{\partial \Phi}{\partial z} + \left[ \Gamma + \frac{k_x}{\Omega} \frac{\partial V_{ox}}{\partial z} \right] \Phi = i\Omega \left[ \frac{k_x^2}{\Omega^2} - \frac{1}{c^2} \right] \Psi \quad (13)$$

where  $\omega_b$  = Brunt-Väisälä frequency and

$$\Gamma = -\frac{1}{2} \left( \frac{g}{c^2} - \frac{\omega_b^2}{g} \right)$$

is the negative of Eckart's coefficient [*Gossard and Hooke*, 1975]. Elimination of  $\Phi$  from these equations leads to a single second-order equation for  $\Psi$  which is equivalent to the Sturm-Liouville equation of *Tuan and Tadic* [1982]. Alternatively, eliminating  $\Psi$  leads to a second-order equation for  $\Phi$  which is a scaled version of the Taylor-Goldstein equation for  $w'$  [*Gossard and Hooke*, 1975].

Equations (12) and (13) are solved numerically using a Runge-Kutta-Fehlberg (RKF) algorithm of fourth order [See, e. g., *Burden et al.*, 1981]. The integration step size was chosen to be 0.5 km, and a tolerance of  $1 \times 10^{-6}$  was used for the truncation error, so that the solution remained stable and convergence was ensured.

We solve the coupled equations subject to the Dirichlet boundary condition where we specify a value for  $\Psi$  and  $\Phi$  at the lower boundary. A vertical velocity equal to zero at the ground ( $z=0$ ) implies that the waves are standing waves for any frequency, with upgoing and downgoing waves of equal amplitudes at  $z=0$ . See also equation (33) of MPW.

The other fluid variables of interest are determined simply from the solutions  $\Psi(z)$  and  $\Phi(z)$ . The pressure perturbation  $p'(z)$  and vertical velocity  $w'(z)$  are deduced directly by unscaling  $\Psi$  and  $\Phi$ . Equation (9) then allows the density perturbation  $\rho'(z)$  to be deter-

mined. From equations (7)-(11), relative temperature fluctuation  $T'(z)$  can be expressed in terms of  $\Psi$  as

$$\frac{T'}{T} = \frac{\omega_b^2}{\omega g \sqrt{\rho_o}} \frac{1}{\omega_b^2 - \Omega^2} \left\{ \frac{\partial \Psi}{\partial z} - \left[ \Gamma + \frac{g(1-\gamma)}{c^2} \left( \frac{\omega_b^2 - \Omega^2}{\omega_b^2} \right) \right] \Psi \right\} \quad (14)$$

Finally, the horizontal velocity fluctuation  $u'(z)$  is obtained from equation (7) by substituting the values for  $w'$  and  $\rho'$ .

The next task is to determine the response to the IGW of minor species and airglow emissions. The minor-species number densities satisfy the Eulerian continuity equation,

$$\frac{\partial N_i}{\partial t} = Q_i - L_i N_i - \nabla \cdot (N_i \mathbf{u}), \quad (15)$$

where  $N_i$ ,  $Q_i$ , and  $L_i$  are, the number density, photochemical production rate, and photochemical loss frequency, respectively, for the  $i^{\text{th}}$  species.

We assume that a monochromatic IGW perturbs the photochemical system described in section 2. We further assume that the IGW amplitude is small enough so that the wave and the corresponding airglow response can be treated in the linear approximation. We expand the variables in the continuity equation, equation (15), to first order about their steady state values by writing  $X = X_o + \Delta X$  for a generic variable  $X$  ( $X_o$  = steady state value, and  $\Delta X$  = wave perturbation) and assume that  $\Delta X$  varies sinusoidally in  $x$  and  $t$  as in equation (6). The linearized form of equation (15) is then:

$$(L_{io} + i\Omega) \frac{\Delta N_i}{N_{io}} = \frac{\Delta Q_i}{N_{io}} - \Delta L_i + ik_x u' - \frac{\partial w'}{\partial z} \frac{1}{N_{io}} \frac{\partial N_{io}}{\partial z} w'. \quad (16)$$

The density of the background atmosphere  $\rho$  is assumed to change negligibly due to the photochemistry and to be affected only by the IGW perturbation. We have already made this assumption tacitly in writing the continuity equation for the total atmospheric mass density above in equation (2) or (8). For the case of  $O(^1S)$  green-line emission, we insert production and loss processes from reactions (R1)-(R9) into equation (16), obtaining three coupled linear algebraic equations for the relative fluctuations in the three species number densities  $[O]$ ,  $[O(^1S)]$  and  $[O_2(c)]$ . Solving these three equations, we obtain the fluctuations  $\Delta[O]$ ,  $\Delta[O(^1S)]$ , and  $\Delta[O_2(c)]$  due to the IGW.

A convenient and commonly used response, or transfer, function for airglow modulation by an IGW is Krassovsky's ratio  $\eta$  [*Krassovsky*, 1972], as mentioned in section 1. The denominator of  $\eta$  consists of the relative temperature perturbation  $\Delta T/T_o$ . We assume that the required temperature is inferred remotely from airglow measurements. In the case of the 557.7 nm airglow, temperature can only be inferred from the width of the emission line, assumed to be Doppler, using a spectral instrument of high resolving power such as a Fabry-Pérot interferometer. We assume that the instrument is ground-based, although the method can be modified easily to accommodate a space-based instrument. The measured spectral brightness  $B(v)$  has two components, a background emission  $B_o(v)$  and a fluctuation part  $\Delta B(v)$  due to the IGW, which are given by

$$B_o(v) = \int I_o(v, z) dz \quad (17)$$

$$\Delta B(v) = \int \Delta I(v, x, z) dz. \quad (18)$$

Here

$$I(v, x, z) = I_o(v, z) + \Delta I(v, x, z) \quad (19)$$

Table 2. Gravity Wave Parameters and Eddy Diffusion

	Wave Events		
	1	2	3
Day, UT	283	292	295
Time, UT	1100	0923	1255
Apparent phase speed, m/s	77.0	60.9	34.0
Wind speed along wave direction, m/s	17.0	30.0	-22.2
Direction of propagation of the wave counterclockwise from east	320	250	220
Horizontal wavelength $\lambda_x$ , km	20.1	14.6	38.0
Apparent wave period $T_{obs}$ , min	4.4	4.0	18.6
Intrinsic wave period $T_{int}$ , min	5.6	7.9	11.3
$\Delta B/B_o$ , %	9.8	7.2	5.5
Eddy diffusivity using brightness-weighted method, $m^2/s$	$1.5 \times 10^2$	$4.5 \times 10^3$	$9.2 \times 10^2$
Eddy diffusivity using Doppler line and background winds $m^2/s$	$0.13 \times 10^2$	$4.0 \times 10^3$	$0.69 \times 10^2$

$$= \frac{A_3 [O(^1S)](x, z)}{\sqrt{\pi} \alpha(x, z)} \exp \left[ -\left( \frac{v - v_o}{\alpha(x, z)} \right)^2 \right]$$

is the spectral volume emission rate, separated into a steady state part  $I_0$  and a perturbation  $\Delta I$ ,  $dl = dz \sec \theta$  ( $\theta$  = angle of line of sight from the zenith) is the element of photon path,  $v$  is the photon frequency,  $v_o$  is the center frequency of the emission line, and  $\alpha$  is the Doppler line width (line center to  $1/e$  point) given by

$$\alpha(x, z) = \frac{v_o}{c_L} \sqrt{\frac{2k_B T(x, z)}{m}} \quad (20)$$

(Note that the full width at half-maximum (FWHM) is  $2(\ln 2)^{1/2} \alpha$ ). In equation (20),  $c_L$  is the speed of light, and  $m$  is the molecular mass of the emitting species.

From MPW, the relative fluctuation in the Doppler temperature  $\Delta T_D/T_{Do}$ , as inferred from the path-integrated Doppler line, is given by

$$\frac{\Delta T_D}{T_{Do}} = \frac{\frac{\Delta B(v_1)}{B_o(v_1)} - \frac{\Delta B(v_o)}{B_o(v_o)}}{\ln \left( \frac{B_o(v_o)}{B_o(v_1)} \right)} \quad (21)$$

where  $v_1$  is an arbitrary frequency in the emission line. Using equations (17), (18), and (21), the Krassovsky ratio  $\eta$  can be calculated as

$$\eta = \frac{(\Delta B/B_o)}{(\Delta T_D/T_{Do})} \quad (22)$$

Using the green-line photochemical model described in section 2 above and the hydroxyl photochemical model described by MPW, coupled with the dynamical model, the Krassovsky  $\eta$  was calculated for three quasi-sinusoidal wave events recorded by Tay-

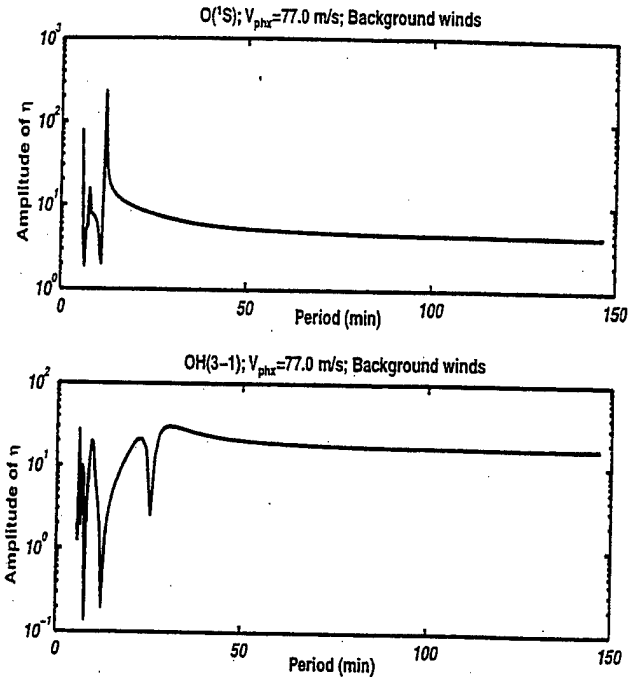


Figure 2. Comparison between the amplitude of  $\eta$  as a function of period for the  $O(^1S)$  and  $OH(3-1)$  emission and a constant horizontal phase speed of 77.0 m/s. A standing-wave solution at all periods, brought about by a ground reflection, and Doppler temperature measurements are assumed.

lor et al. [1995a, b, c] during the Airborne Lidar and Observations of Hawaiian Airglow (ALOHA-93) campaign [Gardner, 1995]. The characteristics of the waves measured by the instrument complex, consisting of CCD imager, OH Michelson interferometer, sodium wind/temperature lidar, and MF radar, are summarized in Table 2.

We use these data for ALOHA cases 1-3 to infer some of the characteristics of the airglow response to an IGW in a nonisother-

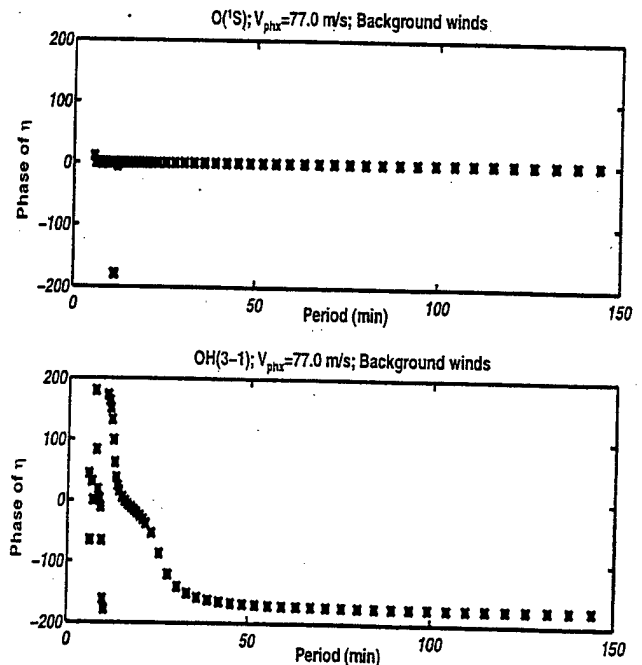


Figure 3. Same comparison as Figure 2, but for the phase of  $\eta$ .

mal windy atmosphere. Figure 2 shows a plot of the amplitude of  $\eta$  versus period for a constant apparent horizontal wave phase speed of 77.0 m/s, as measured in ALOHA wave event 1. The top panel shows  $|\eta|$  for green-line airglow, and the bottom panel shows it for the OH(3-1) band emission, using the OH(3-1) Doppler temperature to calculate  $\eta$  in the latter case. The structure in the amplitude of  $\eta$  at the short-period end of the spectrum is due to changes in the standing wave relative to the emission layer as the period changes. Two types of changes are relevant, (1) vertical displacements of the standing-wave nodes relative to the emission layer peak and (2) changes in the vertical wavelength, which alter the way in which the relatively broad airglow layer low-pass filters the wave. The vertically standing short-period waves become evanescent (usually in the lower thermosphere) when  $\Omega(z) = \omega_b(z)$ .

In Figure 3 the phases of  $\eta$  corresponding to the amplitudes in Figure 2 are plotted. Notice that sharp maxima or minima of  $|\eta|$  in Figure 2 are associated with  $180^\circ$  phase jumps in Figure 3. One interesting feature of the 557.7 nm airglow IGW response is that the phase is always zero or  $180^\circ$ ; that is, the brightness fluctuations are either in phase or completely out of phase with the temperature fluctuations. Keep in mind that the solution in this case is forced to be a vertically standing wave for any period due to the reflection condition at the ground boundary. The behavior of the green-line phase agrees with the argument of Hines and Tarasick [1994], who consider a case where the species reacting to produce the radiating excited state are passive tracers not subject to chemical effects. They showed that, subject only to dynamical influences, the phase is always zero or  $180^\circ$  for vertically standing waves. We have included the effects of chemistry in our  $O(^1S)$  calculation, with no effect on the phase of  $\eta$ . The reason for this is that the chemical lifetimes of the  $O(^1S)$  and the precursor species  $O_2(c)$  are less than 0.8 s in the upper mesosphere and the lower thermosphere, which is negligibly small compared to the Brunt period. The OH(v) airglow case is quite different, and the results in Figure 3 reflect this difference, showing the occurrence of phases other than zero and

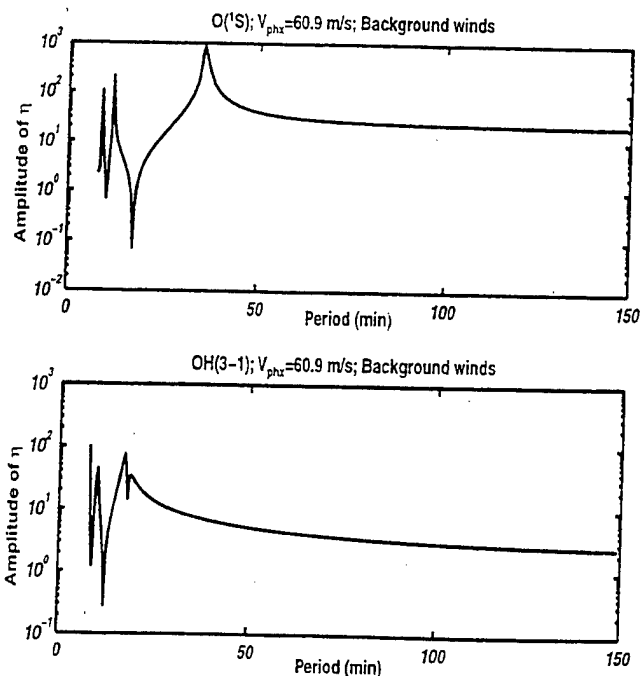


Figure 4. Same as Figure 2, except for wave event 2, where the horizontal phase speed is 60.9 m/s.

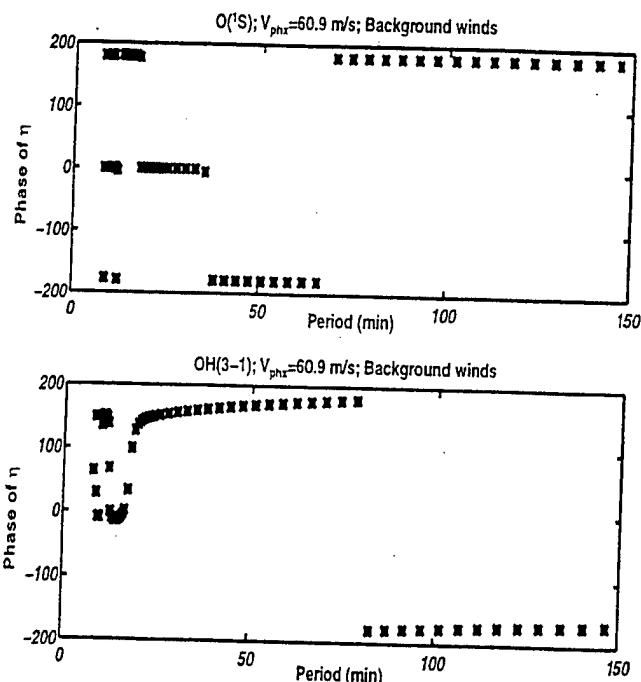


Figure 5. Same as Figure 3, except for wave event 2, where the horizontal phase speed is 60.9 m/s.

$180^\circ$ . Here there is coupling between chemistry and dynamics, since the chemical lifetime of ozone which is the main source of excited OH through the  $H+O_3$  reaction is of the order of 10-25 min in the region of the OH Meinel emission layer (see MPW).

In Figures 4 and 5, we have carried out calculations similar to those of Figures 2 and 3, except that the characteristics of the wave in ALOHA case 2 (Table 2) are used. In particular, the wave has an

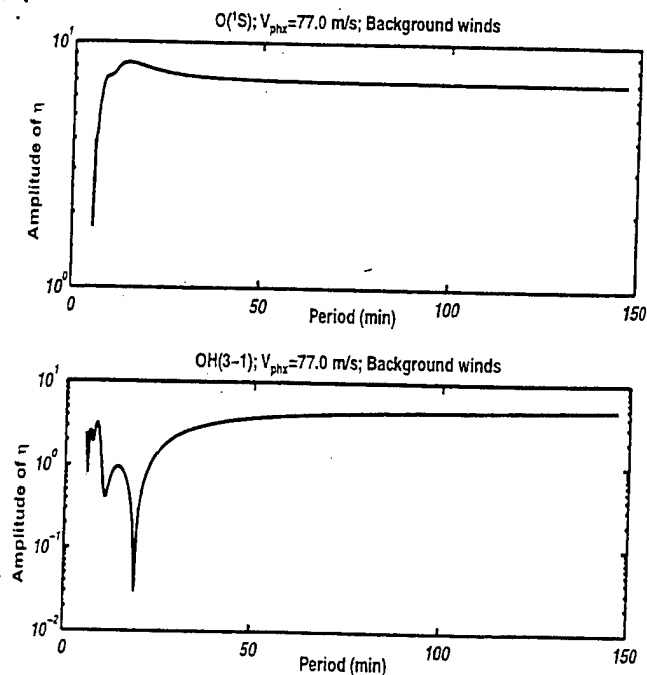


Figure 6. Comparison between the amplitude of  $\eta$  as a function of period for the  $O(^1S)$  and OH(3-1) emission and a constant horizontal phase speed of 77.0 m/s, but for no ground reflection leading to a traveling-wave solution except at short periods.

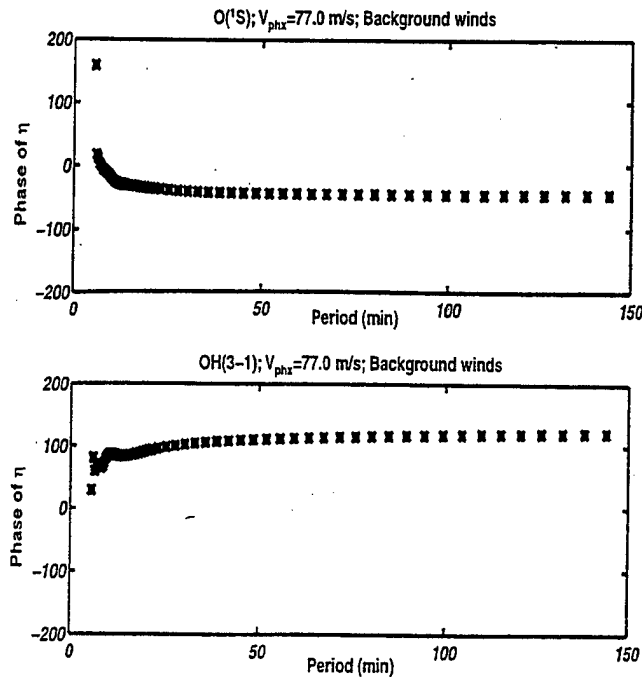


Figure 7. Comparison between the phase of  $\eta$  corresponding to Figure 6.

apparent phase speed of 60.9 m/s. The results are quite similar to those for case 1, with considerable structure in  $|\eta|$  (Figure 4) associated with  $180^\circ$  phase jumps (Figure 5).

One benefit of studying the 557.7 nm airglow is that for short-period waves (period less than 30 min), the airglow response can be used to distinguish between standing and traveling waves, since a measured phase value other than  $0^\circ$  and  $180^\circ$  for  $\eta$  unequivocally indicates a traveling wave.

Next, we solved the coupled fluid differential equations, equations (12) and (13), once again for the wave of case 1 without forc-

ing the wave vertical velocity to be zero at  $z=0$ ; that is, we sought a traveling-wave solution this time. The results are shown in Figures 6 and 7, where we plot the amplitude and phase, respectively, of  $\eta$  for the  $O(^1S)$  and  $OH(3-1)$  emissions using this solution. One notices that, indeed, for periods greater than 10 min, the amplitudes and phases of  $\eta$  are featureless, with the phases nearly constant at some value other than  $0^\circ$  or  $180^\circ$ . As the wave period is decreased, the wave can become ducted from the temperature structure or from the wind structure. For periods less than 10 min, there is sharp structure in  $|\eta|$  associated with phases which tend to zero or  $180^\circ$ .

#### 4. Vertical Diffusion and Alternate Response (Transfer) Function

In the middle-atmosphere models, the effect of turbulence and interacting wave processes on constituent transport is often parametrized in terms of an effective eddy diffusivity [e. g., *Winick*, 1983]. This procedure is based on applying a closure hypothesis to the fluid equations which results in a relation between the eddy flux and the gradient of the average concentration by an eddy diffusion coefficient, in analogy to the Fickian diffusion equation. This eddy diffusivity often becomes a freely adjustable parameter in models without explicit reference to the underlying physical processes responsible for it. In the current study we attempt to obtain the eddy diffusivity resulting from one physical process, namely nonlinear interaction of IGW, using IGW parameters from actual ALOHA observations. In so doing, we follow a method proposed by *Weinstock* [1976]. The nonlinear interaction causes the particles to drift away from a pure sinusoidal motion, causing spreading, and this results in diffusion when viewed over a sufficiently long temporal scale.

Since *Weinstock's* [1976] method is based on the knowledge of  $\Delta\rho$  rather than  $\Delta T$ , it is convenient to introduce an alternate response, or transfer, function to use instead of  $\eta$ . This function, which we call  $\tau$  and which is defined by

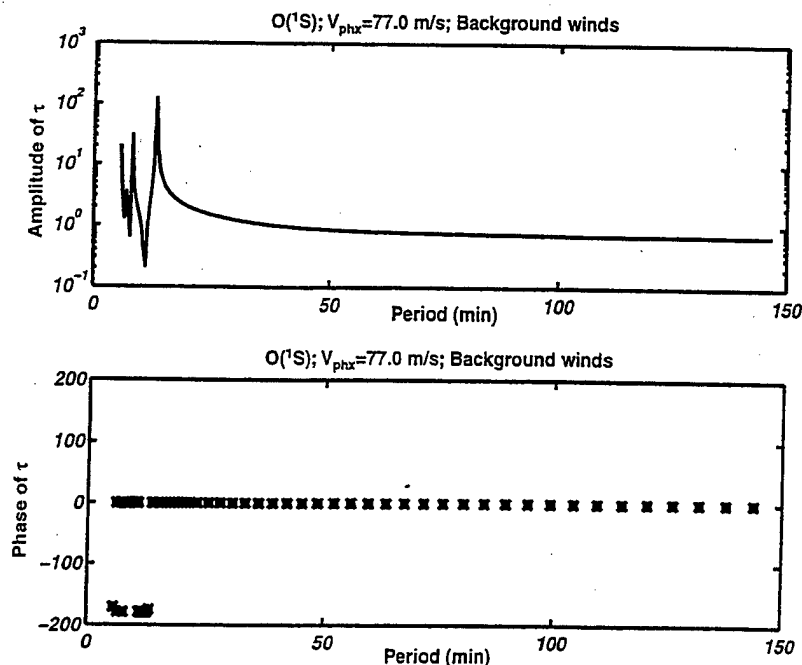


Figure 8. Amplitude and phase of the transfer function  $\tau$  in the 557.7 nm airglow for the ALOHA case number 1.

$$\tau = \frac{(\Delta B/B_o)}{(\Delta \rho/\rho_o)}, \quad (23)$$

is a function similar to the Krassovsky  $\eta$ , except that its denominator consists of the relative density fluctuation rather than the relative temperature fluctuation. Using the model described above to predict  $\tau$ , we can then estimate the relative density fluctuation from a measurement of the relative brightness fluctuation along with the IGW parameters. Figure 8 shows the amplitude and phase of the transfer function  $\tau$  obtained for the 557.7 nm airglow for the case of ALOHA event 1 (Table 2). Calculating the relative density fluctuation  $\Delta \rho/\rho_o$  from the transfer function  $\tau$ , one can then estimate the vertical diffusion coefficient  $D_{zz}$ , in the region where the particular airglow emission resides, using the formula derived by *Weinstock* [1976]

$$D_{zz} = A \left[ \frac{\lambda_x \zeta (4\pi^2 \zeta^2 \lambda_x^2 + (\gamma - 1)^2 g^2 T_w^4 T_b^2)}{T_w^3 (\zeta^2 T_b^2 \lambda_x^2 + 4\pi^2 T_w^4 H^2)} \right] \left| \frac{\Delta \rho}{\rho_o} \right|^2, \quad (24)$$

where  $A = HT_b^3 / 16(\gamma - 1)^2 \pi^2$ ,  $\lambda_x = 2\pi/k_x$  is the horizontal wavelength,  $\zeta = (T_w^2 - T_b^2)^{1/2}$ ,  $T_w = 2\pi/\omega$  is the wave period,  $T_b = 2\pi/\omega_b$  is the Brunt period, and  $H$  is the atmospheric scale height.

*Makhlof et al.* [1997] gave a complete description of how this method was applied to some of the ALOHA-93 data. In that calculation, the transfer function  $\tau$  was calculated using a nonisothermal atmosphere with no background winds and using a brightness-weighted method to calculate  $\tau$  instead of a more experimentally realistic one which in this case is using the Doppler line shape. The last two rows of Table 2 compare  $D_{zz}$  obtained from a brightness weighted temperature to the current calculation using the Doppler lineshape method, where the background winds are incorporated into the model. In the three cases one notices a reduction in the value of  $D_{zz}$  when the Doppler line calculation is implemented. The reduction in the  $D_{zz}$  is due to the reduction in the estimated relative density fluctuation  $\Delta \rho/\rho_o$ .

## 5. Summary and discussion

In this paper, we have presented a model for airglow response to IGW traveling in a realistic nonisothermal atmosphere with winds. This model can be used in conjunction with ground-based or space-based observation of airglow emissions to enhance our understanding of the dynamics of the mesosphere and lower thermosphere region. Calculations of IGW response are carried out using this model for three cases of sinusoidal waves observed in the ALOHA-93 campaign, with and without a reflecting boundary condition at the ground, which leads to standing waves at all periods. For short-period waves, the model yields values of the phase of Krassovsky's  $\eta$  which agree, for the case of  $O(^1S)$ , with the analytical formula derived by *Hines and Tarasick* [1994] which ignores chemical effects. For the case of OH airglow, deviations from the analytical formula are seen due to the much longer chemical lifetimes involved.

The model is also applied to estimating the effective vertical diffusion coefficient  $D_{zz}$  due to nonlinear wave processes for the three ALOHA-93 cases following the method of *Weinstock* [1976].  $D_{zz}$  is an important parameter in atmospheric numerical models, where it is usually treated as a free parameter to be adjusted in order to achieve agreement between model predictions and observations. Figure 9 shows a profile of the range of values of  $D_{zz}$  required in the one-dimensional photochemical model of MPW in order to

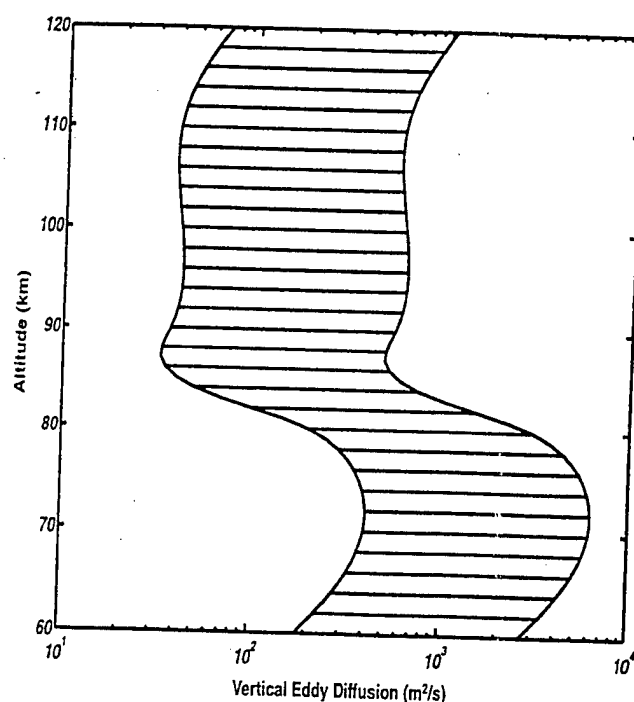


Figure 9. The range of values of  $D_{zz}$  used in the one-dimensional photochemical model of *Ulwick et al.* [1994]. These values were used in order to obtain a good fit between resonance fluorescence measurements during the Dynamic Adapted Network for the Atmosphere (DYANA) campaign and the model output.

obtain a good fit between model predictions and a series of high-latitude rocketborne resonance-fluorescence measurements of atomic oxygen [*Ulwick et al.*, 1994]. These numbers are comparable or lower than the values of  $D_{zz}$  derived for the ALOHA cases. However, the numbers in Figure 9 represent values appropriate to high latitude, where the latter measurements took place in Kiruna, Sweden (67.9° latitude). The values listed in Table 2 are for measurements over Maui, Hawaii (20.8° latitude). *Ebel* [1980] developed an empirical model which shows the value of  $D_{zz}$  at low and midlatitudes to exceed the values at high latitude in all seasons by as much as a factor of 4. The  $D_{zz}$  values obtained here from the green-line emission, especially wave number two, agree with the *Ebel* [1980] assessment.

Many researchers have tried to directly measure  $D_{zz}$  using rockets, [e. g., *Zimmerman and Keneshea*, 1981], others have tried to use averaged meteorological quantities like wind variance to develop a model for eddy diffusion in the mesosphere and lower thermosphere regions [*Ebel*, 1980]. In this method, we are attempting to infer  $D_{zz}$  indirectly using a modeled transfer function  $\tau$  in conjunction with the theoretical formula derived by *Weinstock* [1976]. The values of  $D_{zz}$  derived from this ALOHA-93 data vary from  $1.0 \times 10^2$  to  $5.0 \times 10^3$  m<sup>2</sup>/s, which also agree with the range of values derived by *Weinstock* [1976]. However, these values are preliminary, and much more data from different locations and times and for different airglow emitters need to be analyzed to build a statistical database of  $D_{zz}$  and to put a bound on the variability of  $D_{zz}$  used in numerical models.

**Acknowledgments.** The authors appreciate the funding of this research by the NSF CEDAR Program under grant ATM-9415764 and by the Phillips Laboratory and the Air Force Office of Scientific Research under contract F19628-93-C-0165 as part of the SOAR program.

## References

- Atkinson, R., and K. H. Welge, Temperature dependence of  $O(^1S)$  deactivator by  $CO_2$ ,  $O_2$ ,  $N_2$  and Ar., *J. Chem. Phys.*, **57**, 3689, 1972.
- Barth, C. A., The 5577-Ångstrom airglow, *Science*, **134**, 1426, 1961.
- Bates, D. R., The green light of the night sky, *Planet. Space Sci.*, **29**, 1061, 1981.
- Bates, D. R., Oxygen band system transition arrays, *Planet. Space Sci.*, **37**, 881, 1989.
- Bates, D. R., Nightglow emissions from oxygen in the lower thermosphere, *Planet. Space Sci.*, **40**, 211, 1992.
- Burden, R. L., J. D. Faires, and A. C. Reynolds, *Numerical Analysis 2nd ed.*, Prindle, Weber and Schmidt, Boston, Mass., 1981.
- Campbell, I. M., and C. N. Gray, Rate constants for  $O(^3P)$  recombination and association with  $N(^4S)$ , *Chem. Phys. Lett.*, **8**, 259, 1973.
- Chapman, S., Some phenomena of the upper atmosphere, *Proc. R. Soc. London Ser. A*, **132**, 353, 1931.
- Copeland, R. A., K. Knutsen, M. E. Onishi and T. Yalcin, Laboratory investigation of collisional energy transfer in the  $O_2(c^1\Sigma_u^-)$  Herzberg state, *Eos Trans. AGU*, **75**(44), Fall Meet. Suppl. 496, 1994.
- Copeland, R. A., K. Knutsen, M. E. Onishi and T. Yalcin, Collisional removal of  $O_2(c^1\Sigma_u^-)$ ,  $v=9$  by  $O_2$ ,  $N_2$ , and He, *J. Chem. Phys.*, **105**, 10349, 1996.
- Degen, V., Excitation of the Herzberg bands of the  $O_2$  in laboratory afterglow and night airglow, *J. Geophys. Res.*, **77**, 6213, 1972.
- Ebel, A., Eddy diffusion models for the mesosphere and lower thermosphere, *J. Atmos. Terr. Phys.*, **42**, 617, 1980.
- Gardner, C. S., Introduction to ALOHA/ANLC-93: The 1993 airborne lidar and observations of the Hawaiian airglow / airborne noctilucent cloud campaigns, *Geophys. Res. Lett.*, **22**, 2789-2792, 1995.
- Gossard, E. E., and W. H. Hooke, *Waves in the Atmosphere*, Elsevier, New York, 1975.
- Hecht, J. H., R. L. Walterscheid, G. G. Sivjee, A. B. Christensen and J. B. Pranke, Observations of wave-driven fluctuations of OH nightglow emission from Sondre Stromfjord, Greenland, *J. Geophys. Res.*, **92**, 6091, 1987.
- Hedin, A. E., Empirical wind model for the upper, middle, and lower atmosphere, *J. Atmos. Terr. Phys.*, **58**, 1421, 1996.
- Hickey, M. P., Effects of eddy viscosity and thermal conduction and the coriolis force in the dynamics of gravity wave driven fluctuations in the OH nightglow, *J. Geophys. Res.*, **93**, 4077, 1988a.
- Hickey, M. P., Wavelength dependence of eddy dissipation and coriolis force in the dynamics of the gravity wave driven fluctuations in the OH nightglow, *J. Geophys. Res.*, **93**, 4089, 1988b.
- Hines, C. O., Internal atmospheric gravity waves at ionospheric heights, *Can. J. Phys.*, **38**, 1441, 1960.
- Hines, C. O., and D. W. Tarasick, Airglow response to vertically standing waves, *Geophys. Res. Lett.*, **21**, 2729, 1994.
- Holton, J. R., An Introduction to Dynamic Meteorology 3rd. ed., Academic, San Diego, Calif. 1992.
- Krasnopolsky, V. A., A. A. Krysko, V. N. Rogachev and V. A. Pachev, Spectroscopy of the night-sky luminescence of Venus from the interplanetary spacecraft Venera 9 and Venera 10 (in Russian), *Kosm. Issled.*, **14**, 789, 1976. (*Cosmic Res., Engl. Transl.*, **14**, 705, 1977.)
- Krasnopolsky, V. A., Excitation of oxygen emissions in the night airglow of the terrestrial planets, *Planet. Space Sci.*, **29**, 925, 1981.
- Krasnopolsky, V. A., Oxygen emissions in the airglow of Earth, Venus and Mars, *Planet. Space Sci.*, **34**, 511, 1986.
- Krasnovsky, V. I., Infrasonic variations of OH emission in the upper atmosphere, *Ann. Geophys.*, **28**, 739, 1972.
- Krauss, M., and D. Neuman, On the interaction of  $O(^1S)$  with  $O(^3P)$ , *Chem. Phys. Lett.*, **36**, 372, 1975.
- López-Gonzalez, M. J., J. J. López-Moreno and R. Rodrigo, Altitude and vibrational distribution of the  $O_2$  ultraviolet nightglow emissions, *Planet. Space Sci.*, **40**, 913, 1992.
- Makhlouf, U. B., R. H. Picard, and J. R. Winick, Photochemical-dynamical modeling of the measured response of airglow to gravity waves, 1, Basic model for OH airglow, *J. Geophys. Res.*, **100**, 11,289, 1995.
- Makhlouf, U. B., R. H. Picard, M. J. Taylor and J. R. Winick, Gravity waves and vertical diffusion in the lower thermosphere from 557.7 nm airglow, *Adv. Space Res.*, **19**, 583, 1997.
- Nicolaides, G., O. Sinanoglu and P. Westhaus, Theory of atomic structure including electron correlation, IV, Method for forbidden-transition probabilities with results for OI, OII, OIII, NI, NII, and CI, *Phys. Rev. A*, **4**, 1400, 1971.
- Pitteway, M. L. V., and C. O. Hines, The reflection and ducting of atmospheric acoustic-gravity waves, *Can. J. Phys.*, **43**, 2222, 1965.
- Schubert, G., R. L. Walterscheid and M. P. Hickey, Gravity wave-driven fluctuations in OH nightglow from an extended, dissipative emission region, *J. Geophys. Res.*, **96**, 13,869, 1991.
- Schwartz, R. N., Z. I. Slawsky and K. F. Herzfeld, Calculation of vibrational relaxation times in gases, *J. Chem. Phys.*, **20**, 1591, 1952.
- Slangor, T. G., and D. H. Huestis,  $O_2(c^1\Sigma_u^- \rightarrow X^3\Sigma_g^-)$  emission in the terrestrial nightglow, *J. Geophys. Res.*, **86**, 3551, 1981.
- Summers, M. E., Zonally averaged trace constituent climatology, *Rep. NRL/MR/7641-93-7416*, Naval Res. Lab., Washington, D. C., 1993.
- Taylor, M. J., D. N. Turnbull, and R. P. Lowe, Spectrometric and imaging measurements of a spectacular gravity wave event observed during the ALOHA-93 campaign, *Geophys. Res. Lett.*, **22**, 2849, 1995a.
- Taylor, M. J., Y. Y. Gu, X. Tao, C. S. Gardner, and M. B. Bishop, An investigation of intrinsic gravity wave signatures using coordinated lidar and nightglow image measurements, *Geophys. Res. Lett.*, **22**, 2853, 1995b.
- Taylor, M. J., D. C. Fritts and J. R. Isler, Determination of horizontal and vertical structure of an unusual pattern of short period gravity waves imaged during ALOHA-93, *Geophys. Res. Lett.*, **22**, 2837, 1995c.
- Thomas, L., R. G. H. Greer and P. H. G. Dickinson, The excitation of the 557.7 nm line and Herzberg bands in the nightglow, *Planet. Space Sci.*, **27**, 925, 1979.
- Thomas, R. J., Analysis of atomic oxygen, the green line and Herzberg bands in the lower thermosphere, *J. Geophys. Res.*, **86**, 206, 1981.
- Thomas, R. J., and R. A. Young, Measurement of atomic oxygen and related airglows in the lower thermosphere, *J. Geophys. Res.*, **86**, 7389, 1981.
- Tuan, T. F., and D. Tadic, A dispersion formula for analyzing "modal interference" among guided and free gravity wave modes and other phenomena in a realistic atmosphere, *J. Geophys. Res.*, **87**, 1648-1668, 1982.
- Ullwick, J. C., A. J. Ratkowski, and U. B. Makhlouf, Twilight rocket measurements of high-latitude atomic oxygen density during the DYANA campaign, *J. Atmos. Terr. Phys.*, **56**, 1871-1883, 1994.
- Viereck, R. A., and C. S. Deehr, On the interaction between gravity waves and the OH Meinel (6-2) and the  $O_2$  atmospheric (0-1) bands in the polar night airglow, *J. Geophys. Res.*, **94**, 5397-5404, 1989.
- Wang D. Y., and T. F. Tuan, Brunt-Doppler ducting of small-period gravity waves, *J. Geophys. Res.*, **93**, 9916, 1988.
- Weinstock, J., Nonlinear theory of acoustic-gravity waves, 1, Saturation and enhanced diffusion, *J. Geophys. Res.*, **81**, 633, 1976.
- Winick, J. R., Photochemical processes in the mesosphere and lower thermosphere, in *Solar-Terrestrial Physics*, edited by R. L. Carovillano and J. M. Forbes, D. Reidel, Norwell, Mass., 677-732, 1983.
- Zimmerman, S. P., and T. J. Keneshea, Turbulent heating and transfer in the stratosphere and upper mesosphere, in *Middle Atmosphere Program Handbook*, p. 311, SCOSTEP Sec., Univ. of Ill., Urbana, 1981.

U. B. Makhlouf, SRL, Utah State University, 139 The Great Road, Bedford, MA 01730. (e-mail: makhlouf@pld.ac.ph.af.mil)

R. H. Picard and J. R. Winick, Geophysics Directorate, Phillips Laboratory, Hanscom AFB, MA 01731.

T. F. Tuan, Physics Department, University of Cincinnati, Cincinnati, OH 45221.

(Received January 24, 1997; revised October 3, 1997; accepted October 9, 1997.)